Spring 1-1-2017

Search for Supersymmetry in Hadronic Final States

Troy Mulholland
University of Colorado at Boulder, mulholland.troy.d@gmail.com

Search for Supersymmetry in Hadronic Final States

by

Troy Mulholland

B.S., St. Bonaventure University, 2011

M.S., University of Colorado Boulder, 2014

A thesis submitted to the

Faculty of the Graduate School of the

University of Colorado in partial fulfillment

of the requirements for the degree of

Doctor of Philosophy

Department of Physics

2017

This thesis entitled:
Search for Supersymmetry in Hadronic Final States
written by Troy Mulholland
has been approved for the Department of Physics

Prof. Kevin Stenson

Prof. William Ford

Date

The final copy of this thesis has been examined by the signatories, and we find that both the content and the form meet acceptable presentation standards of scholarly work in the above mentioned discipline.

Mulholland, Troy (Ph.D., Physics)

Search for Supersymmetry in Hadronic Final States

Thesis directed by Prof. Kevin Stenson and Prof. William Ford

We present a search for supersymmetry in purely hadronic final states with large missing transverse momentum using data collected by the CMS detector at the CERN LHC. The data were produced in proton-proton collisions with center-of-mass energy of $\sqrt{s} = 13$ TeV and correspond to an integrated luminosity of 35.9 fb^{-1}. Data are analyzed with variables defined in terms of jet multiplicity, bottom quark tagged jet multiplicity, the scalar sum of jet transverse momentum, the magnitude of the vector sum of jet transverse momentum, and angular separation between jets and the vector sum of transverse momentum. We perform the search on the data using two analysis techniques: a boosted decision tree trained on simulated data using the above variables as features and a four-dimensional fit with rectangular search regions. In both analyses, standard model background estimations are derived from data-driven techniques and the signal data are separated into exclusive search regions. The observed yields in the search regions agree with background expectations. We derive upper limits on the production cross sections of pairs of gluinos and pairs of top squarks at 95% confidence using simplified models with the lightest supersymmetric particle assumed to be a weakly interacting neutralino. Gluinos as heavy as 1960 GeV and top squarks as heavy as 980 GeV are excluded. The limits significantly extend the exclusions obtained from previous results.

Acknowledgments

The work presented here is a culmination of the trials and tribulations of collaborators, friends, and family. It wouldn't be possible to suitably acknowledge all of the individuals who helped me in this endeavor, but I will try.

For the content of my thesis and for my development as a scientist, I owe the biggest debt of gratitude to Bill Ford and Kevin Stenson. I could not have asked for more supportive and helpful advisers. Thank you, Bill, for your mentorship and wisdom. Your vision helped guide me throughout my career in graduate school. Thank you, Kevin, for challenging me. Your presence accelerated my progress in particle physics. I would also like to thank the faculty, staff, and graduate students of CU's physics department, especially the members of my committee: Alysia Marino, Oliver DeWolfe, and Michael Shull. I want to send a special thanks to Frank Jensen for the comradery which helped to alleviate the grind of graduate school.

I would like to thank the past and present members of the CMS collaboration and all those who contributed to the design, construction, and operation of the Large Hadron Collider. I am amazed at the outstanding level of perfection these machines perform at and the quality of the physics data. Thanks to the professors, post-docs, and graduate students involved with the search for supersymmetry presented here. This thesis would not have been possible without all of your hard work, expertise, technical support, and collaborative spirit.

Thank you, Mom and Dad, for your unwavering support. Your belief in me was indispensable; I would not have finished without it. Thank you, Shawn, Tim, and Jordan, for the encouragement and advise. I aspire to be like all of you. I also want to thank Ed and Mary for your goodwill and honesty. I'm lucky to have a great family.

Most of all I would like to thank my wife, Paula. Anything I have or ever will accomplish is because of your love and support. I cannot express enough gratitude for your patience and companionship. I dedicate this thesis to you.

Contents

Tables

Table

Figures

Figure

Chapter 1

Introduction and Theory

Understanding the fundamental constituents of matter and their interactions is the basic goal of particle physics. Through the combination of theory and experiment, we've discovered an enormously successful description of the nature of subatomic particles. This theory includes all observed particles and their electromagnetic, weak, and strong interactions. The theory was built to explain natural phenomena, and it has produced testable predictions later confirmed by experiment. There are, however, reasons to believe the picture we have is incomplete. It is the subject of this thesis to investigate a potential link between the standard model and a more general theory of nature.

An effective technique for probing the physics of fundamental particles is through the use of high energy particle collisions. By examining the products of these collisions, we are able to find evidence for interactions and resonances. In 2015 the Large Hadron Collider (LHC), a 27 kilometer in circumference proton-proton collider, broke the world record for highest energy collisions with a center-of-mass energy of 13 TeV. Another record was broken in 2016 with the largest data sample of hadron collisions ever recorded [1]. This sample of high energy proton collisions gives us insight into the frontier of particle physics.

The Compact Muon Solenoid (CMS) and A Toroidal LHC Apparatus (ATLAS) detectors are two experiments designed to observe particles produced in LHC collisions. In 2012, the CMS and ATLAS experiments jointly announced the discovery of a boson with mass near 125 GeV [2, 3]. The properties of this particle have been measured to be consistent with that of the Higgs particle [4].

In the theoretical treatment, the scalar Higgs boson receives divergent corrections to its mass, requiring a severely unnatural fine-tuning. Fine-tuning of model parameters is often a symptom of an incomplete theory.

In this Chapter, we examine our basic theoretical understanding of particle physics and our motivations for the subject of this search. In Section 1.1, we describe the standard model of particle physics, including the successes and limitations of the theory. In Section 1.2, we examine the theory of supersymmetry (SUSY). We discuss the basic framework that SUSY is built upon and the reasons SUSY is seen as an attractive extension to the standard model.

Chapter 2 describes the experimental apparatus, and Chapter 3 describes the data and simulated samples used in this thesis. In Chapter 4, we describe the process of transforming raw data into observable physics objects, and Chapter 5 describes how data are selected for analysis. Two overlapping searches for SUSY are presented in Chapters 6 and 7. The analysis described in Chapter 6 utilizes eight observables to separate SUSY signal from standard model background with a boosted decision tree, a multivariate discriminant. The analysis described in Chapter 7 represents a wider CMS effort to search, with similar data selection as the analysis in Chapter 6, without any model dependence. A comparison of the two analyses is given in the summary, Chapter 8.

1.1 The Standard Model

The gauge symmetry group of the standard model (SM), a quantum field theory in a four-dimensional Minkowski space, is given by

$$\mathrm{SU}_c(3) \times \mathrm{SU}_L(2) \times \mathrm{U}_Y(1), \tag{1.1}$$

where c stands for color, L refers to the left-handed fermions with weak isospin, and Y denotes weak hypercharge [5]. The $\mathrm{SU}_c(3)$ group governs the strong interaction and is described in Section 1.1.1. Electroweak theory, discussed in Sections 1.1.2 and 1.1.3, describes the weak and electromagnetic interactions and is based on the $\mathrm{SU}_L(2)$ and $\mathrm{U}_Y(1)$ gauge groups.

Table 1.1: The integer spin particles of the standard model [6].

	Name	Symbol	Charge	Mass	Interaction
Vector bosons	Photon	γ	0	-	Electromagnetic
	W boson	W	± 1	80.385 ± 0.015 GeV	Weak
	Z boson	Z	0	91.1876 ± 0.0021 GeV	Weak
	gluon	g	0	-	Strong
Scalar bosons	Higgs	H	0	125.7 ± 0.4 GeV	-

The most general Lagrangian density that describes the standard model is:

$$\mathcal{L}_{\text{SM}} = \mathcal{L}_{\text{Gauge}} + \mathcal{L}_{\text{Matter}} + \mathcal{L}_{\text{Higgs}} + \mathcal{L}_{\text{Yukawa}}, \tag{1.2}$$

where $\mathcal{L}_{\text{Gauge}}$ describes the massless spin 1 gauge bosons, $\mathcal{L}_{\text{Matter}}$ describes the massless spin 1/2 fermions, $\mathcal{L}_{\text{Higgs}}$ describes the Higgs potential, and $\mathcal{L}_{\text{Yukawa}}$ contains the terms describing the coupling between the fermion fields and the Higgs field.

1.1.1 Quantum Chromodynamics

The eight generators of the $\text{SU}_c(3)$ symmetry group are the gluon fields $G^{\alpha}_{\mu}(x)$, where $\alpha = 1, \ldots, 8$ [5]. Excitations in the $G^{\alpha}_{\mu}(x)$ fields are the spin 1 massless gluons, given in Table 1.1. Any particle which carries color is said to be strongly interacting. In addition to mediating the strong force, gluons carry color.

Hadrons, such as the proton, are bound states of the spin 1/2 particles that carry color, known as quarks: u, d, s, c, b, and t. Properties of the quarks are given in Table 1.2. In this thesis, we denote the lightest four quarks (u, d, s, and c) collectively as q. The Weyl fermion fields, and

Table 1.2: The spin 1/2 particles of the standard model [6].

	Name	Symbol	Charge	Mass	Generation
Leptons	electron	e	± 1	0.511 MeV	1
	electron neutrino	ν_{e}	0	< 2 eV	1
	muon	μ	± 1	106 MeV	2
	muon neutrino	ν_μ	0	< 2 MeV	2
	tau	τ	± 1	1.78 GeV	3
	tau neutrino	ν_τ	0	< 20 MeV	3
Quarks	up	u	$\pm 2/3$	$2.3^{+0.7}_{-0.5}$ MeV	1
	down	d	$\pm 1/3$	$4.8^{+0.5}_{-0.3}$ MeV	1
	charm	c	$\pm 2/3$	1.275 ± 0.025 GeV	2
	strange	s	$\pm 1/3$	95 ± 5 MeV	2
	top	t	$\pm 2/3$	$173.21 \pm 0.51 \pm 0.71$ GeV	3
	bottom	b	$\pm 1/3$	4.18 ± 0.03 GeV	3

transformation properties, that describe these spin 1/2 particles are given in Equations 1.3–1.5:

$$Q_i = \begin{pmatrix} \mathrm{u} \\ \mathrm{d} \end{pmatrix}, \begin{pmatrix} \mathrm{c} \\ \mathrm{s} \end{pmatrix}, \begin{pmatrix} \mathrm{t} \\ \mathrm{b} \end{pmatrix} \qquad \text{transforms as } \left(\mathbf{3}, \mathbf{2}, +\frac{1}{6}\right) \tag{1.3}$$

$$U_i = \bar{\mathrm{u}},\ \bar{\mathrm{c}},\ \bar{\mathrm{t}} \qquad \left(\bar{\mathbf{3}}, \mathbf{1}, -\frac{2}{3}\right) \tag{1.4}$$

$$D_i = \bar{\mathrm{d}},\ \bar{\mathrm{s}},\ \bar{\mathrm{b}} \qquad \left(\bar{\mathbf{3}}, \mathbf{1}, +\frac{1}{3}\right), \tag{1.5}$$

where we have suppressed the color index. Here, Q_i is a left-handed quark weak-isospin doublet field, U_i is a right-handed up field, and D_i is a right-handed down field. In the transformation equations, the first number gives the $\mathrm{SU}_c(3)$ representation, the second number gives the $\mathrm{SU}_L(2)$ representation, and the third number is the eigenvalue of the weak hypercharge.

1.1.2 Electroweak Theory

The gauge group

$$\mathrm{SU}_L(2) \times \mathrm{U}_Y(1), \tag{1.6}$$

of the standard model, unifies the electromagnetic and weak interactions [7, 8, 9]. The three generators of the $\mathrm{SU}_L(2)$ symmetry group are W_μ^a, where $a = 1, 2, 3$, and the generator of $\mathrm{U}_Y(1)$ symmetry group is B_μ. The W^+, W^-, Z, and γ particles, listed in Table 1.1, are excitations of linear combinations of the W_μ^a and B_μ fields. These linear combinations are given in Equations 1.7-1.9:

$$\mathrm{W}_\mu^\pm = (\mathrm{W}_\mu^1 \mp i\mathrm{W}_\mu^2)/\sqrt{2}, \tag{1.7}$$

$$\mathrm{Z}_\mu = \cos\theta_w \mathrm{W}_\mu^3 - \sin\theta_w \mathrm{B}_\mu, \tag{1.8}$$

$$\mathrm{A}_\mu = \sin\theta_w \mathrm{W}_\mu^3 + \cos\theta_w \mathrm{B}_\mu \tag{1.9}$$

where θ_w is the Weinberg angle. The photon mediates the electromagnetic force and the W^+, W^-, and Z mediate the weak force. Table 1.1 gives properties of the electroweak gauge bosons.

The electroweak fermions of generation are described by the fields

$$L_i = \begin{pmatrix} \nu_\mathrm{e} \\ \mathrm{e} \end{pmatrix}, \begin{pmatrix} \nu_\mu \\ \mu \end{pmatrix}, \begin{pmatrix} \nu_\tau \\ \tau \end{pmatrix}, \qquad \text{transforms as } \left(\mathbf{1}, \mathbf{2}, -\frac{1}{2}\right) \tag{1.10}$$

$$E_i = \bar{\mathrm{e}},\ \bar{\mu},\ \bar{\tau} \qquad (\mathbf{1}, \mathbf{1}, +1) \tag{1.11}$$

where L_i describes the left-handed lepton and neutrino doublet fields and E_i describes the right-handed lepton singlet fields. The transformation properties follow the same convention as that described in Section 1.1.1. The leptons are charged particles that do not carry color. The three generations of leptons described by the SM are the electron, muon and tau. Each generation of lepton has a corresponding left-handed neutrino. Properties of these particles are summarized in Table 1.2.

1.1.3 Electroweak Symmetry Breaking and the Higgs Mechanism

The standard model generates masses for physical particles through spontaneous symmetry breaking of $\mathrm{SU}_L(2) \times \mathrm{U}_Y(1)$. This mechanism is accomplished by minimizing the scalar Higgs potential

$$V(\phi) = -\mu^2\phi^\dagger\phi + \lambda\left(\phi^\dagger\phi\right)^2, \tag{1.12}$$

where constants μ^2 and λ are required to be positive. The Higgs field is described by the complex scalar doublet given, with transformation properties, by

$$\phi = \begin{pmatrix} \phi^+ \\ \phi^0 \end{pmatrix}, \qquad \text{transforms as } \left(\mathbf{1}, \mathbf{2}, +\frac{1}{2}\right). \tag{1.13}$$

The Higgs potential is minimized at a nonzero value of the Higgs field. The Higgs field in this ground state, or vacuum expectation value (VEV), may be chosen such that the nonzero component is real and neutral:

$$\langle\phi\rangle = \frac{1}{\sqrt{2}} \begin{pmatrix} 0 \\ v \end{pmatrix}, \tag{1.14}$$

with $v^2 = \mu^2/\lambda$. The VEV is responsible for spontaneous symmetry breaking, which allows the electroweak boson fields to mix. In this process, the subsequent fields, given in Equations 1.7-1.8, acquire mass, while the photon field, given by Equation 1.9, remains massless. Meanwhile, the fermions acquire mass through Yukawa couplings after shifting the scalar field by v.

1.1.4 Open Questions

To date, there are no significant deviations from the predictions of the standard model. In fact, the theory has been tested to unrivaled precision [11]. As shown in Figure 1.1, the observed production rates of various SM processes agree with the theoretical prediction. Despite the resounding success of the standard model, limitations and unanswered questions exist, providing inspiration for new discoveries. Quantum corrections to the standard model computation of the Higgs mass are unstable. As we will see in Section 1.2.1, this results in an unnatural fine-tuning without the addition of new physics. This unnaturalness is often referred to as the hierarchy problem [12].

Additionally, there is theoretical and empirical evidence that suggest the standard model is incomplete. Many Grand Unified Theories (GUT) predict a simplified description only directly observable at the Λ_{GUT} scale, where Λ_{GUT} is thought to be around 10^{16} GeV. Empirically, observations of galactic rotation curves, redshift survey results detailing the large-scale structure of the universe, and gravitational lensing observations all appear to suggest the existence of mass that

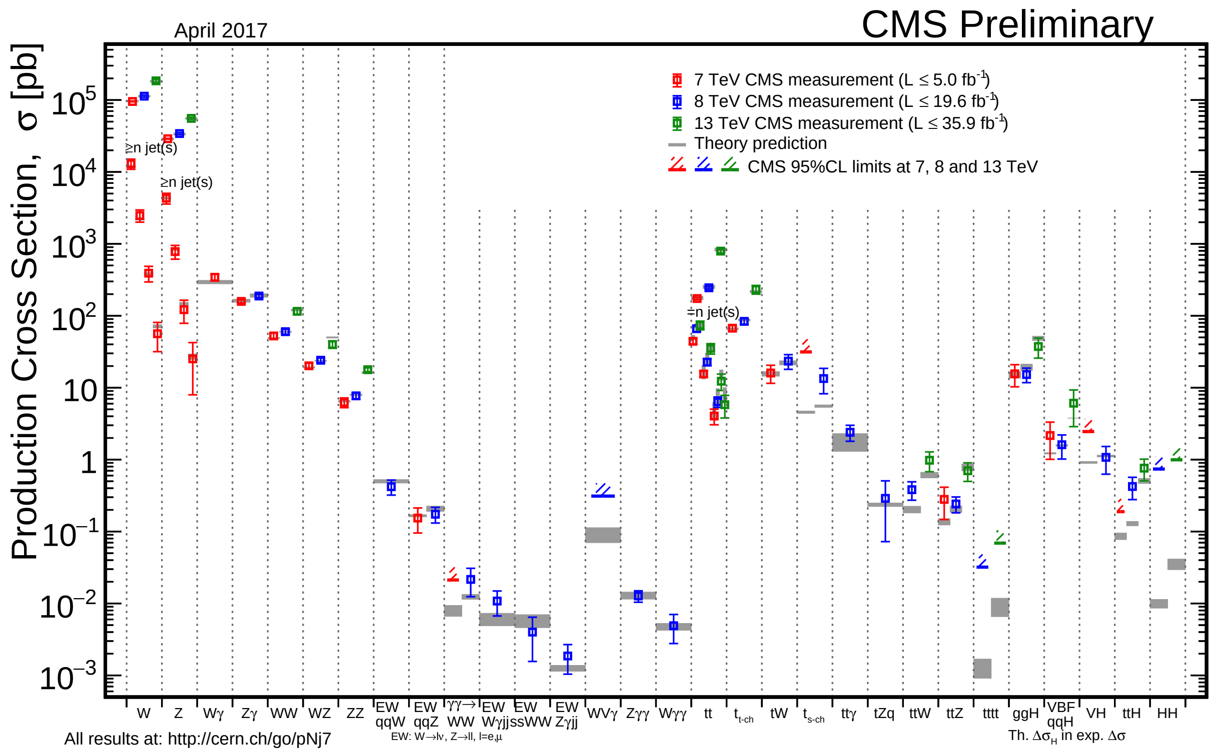

Figure 1.1: Cross section theoretical prediction and observation with uncertainties from CMS of standard model processes [10].

cannot be accounted for by ordinary baryonic matter. Estimates of the abundance in the observable universe of dark matter place the fractional percentage of the matter at approximately 84% [13]. While attempts have been made at explaining dark matter within the context of the standard model, the most widely accepted hypothesis is the existence of weakly interacting massive particles (WIMPs), for which the standard model has no candidates. A WIMP is a hypothetical particle whose only interactions include the weak force and gravity. The only two standard model particles that satisfy this criterion are the neutrino, which is much too light to be a plausible candidate, and the highly unstable Z boson.

1.2 Supersymmetry

SUSY is a hypothetical symmetry of nature that provides a symmetry between the two classes of fundamental particles: Bosons $\longleftrightarrow$ Fermions. The operator, Q, generates the SUSY

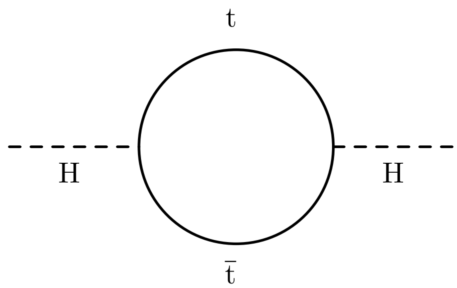

Figure 1.2: The top-loop correction to the Higgs mass.

transformations such that

$$Q\,|\text{boson}\rangle = |\text{fermion}\rangle \qquad\qquad Q\,|\text{fermion}\rangle = |\text{boson}\rangle. \tag{1.15}$$

Before we further describe SUSY, the fine-tuning problem is revisited to provide motivation for such a symmetry.

1.2.1 The Problem of Fine-Tuning

The heart of the fine-tuning problem lies at the instability of the VEV. Fundamental scalar fields lead to quadratic and logarithmic divergences with the introduction of a finite cut-off [14]. We will see that the VEV is highly unstable under quantum loop corrections and that these corrections enter as divergences in the value of the Higgs mass. The largest SM correction to the Higgs mass is from the top quark loop shown in Figure 1.2. The coupling of the Higgs to the top quark is given by

$$\mathcal{L}_{\text{Yukawa}} = -\frac{y_{\rm t}}{\sqrt{2}}\mathrm{H}^0\,\bar{\mathrm{t}}_L\mathrm{t}_R + h.c., \tag{1.16}$$

where $y_{\rm t}$ is the top Yukauwa coupling, t_L and t_R are the left- and right-handed components of the top quark, and $h.c.$ is the hermitian conjugate. We express the top mass as

$$m_{\rm t} = \frac{y_{\rm t} v}{\sqrt{2}}. \tag{1.17}$$

Then, we can evaluate the top-loop contribution to the square of the Higgs mass:

$$\delta m_{\rm h}^2|_{\rm top} \;\; = \;\; -\frac{3|y_{\rm t}|^2}{8\pi^2}\left[\Lambda^2 - 3m_{\rm t}^2 \ln\left(\frac{\Lambda^2 + m_{\rm t}^2}{m_{\rm t}^2}\right)\right], \tag{1.18}$$

where we have imposed a hard momentum cutoff (Λ^2). Since we are only concerned with the asymptotic behavior of $\delta m_{\rm h}^2$, we've dropped terms in Eq. 1.18 that are finite in the limit $\Lambda \to \infty$. It's useful to subdivide Equation 1.18 into

$$\delta m_{\rm h}^2|_{\rm top}^{\Lambda^2} = -\frac{3|y_{\rm t}|^2}{8\pi^2}\Lambda^2 \text{ and} \tag{1.19}$$

$$\delta m_{\rm h}^2|_{\rm top}^{\rm ln} = \frac{9m_{\rm t}^2|y_{\rm t}|^2}{8\pi^2}\ln\left(\frac{\Lambda^2+m_{\rm t}^2}{m_{\rm t}^2}\right). \tag{1.20}$$

Here, we have split the correction to the Higgs mass from the top-loop into its quadratic (Equation 1.19) and logarithmic (Equation 1.20) parts, such that $\delta m_{\rm h}^2|_{\rm top} = \delta m_{\rm h}^2|_{\rm top}^{\Lambda^2} + \delta m_{\rm h}^2|_{\rm top}^{\rm ln}$.

To quantify the fine-tuning, we define the amount f as

$$\frac{m_{\rm h}^2}{\delta m_{\rm h}^2} \equiv \frac{1}{f}, \tag{1.21}$$

where $m_{\rm h} = m_0 + \delta m_{\rm h}$, and m_0 is the Higgs bare mass. We've defined f such that $f \leq 1$ implies no fine-tuning, and $f > 1$ gives the degree of fine-tuning of m_0. If we use $m_{\rm h} = 125$ GeV and $\Lambda = \Lambda_{GUT}$, we see from Equation 1.19 that m_0 must be adjusted to around 27 orders of magnitude to achieve $f = 1$. This is the so called fine-tuning problem, and despite the above discussion only considering the leading contribution to the Higgs mass, the problem persists even under the most rigorous treatment [12].

1.2.2 A Natural Solution to Fine-Tuning with SUSY

Suppose we have a scalar partner of the top quark, denoted $\widetilde{\rm t}$, with the same color content, called a top squark or stop, with interactions described by

$$\mathcal{L}_{\rm stop} = -\frac{\tilde{\lambda}({\rm h}^0)^2}{2}\left(|\widetilde{\rm t}_L|^2 + |\widetilde{\rm t}_R|^2\right) - {\rm h}^0\left(\tilde{\mu}_L|\widetilde{\rm t}_L|^2 + \tilde{\mu}_R|\widetilde{\rm t}_R|^2\right) - m_{\widetilde{\rm t}_L}|\widetilde{\rm t}_L|^2 - m_{\widetilde{\rm t}_R}|\widetilde{\rm t}_R|^2. \tag{1.22}$$

If we assume for the moment that $\tilde{\lambda} = |y_{\rm t}|^2$ and calculate the quadratic contribution to the Higgs mass from the leading order loop diagrams given in Figure 1.3 we find

$$\delta m_{\rm h}^2|_{\rm stop}^{\Lambda^2} = \frac{3|y_{\rm t}|}{8\pi^2}\Lambda^2, \tag{1.23}$$

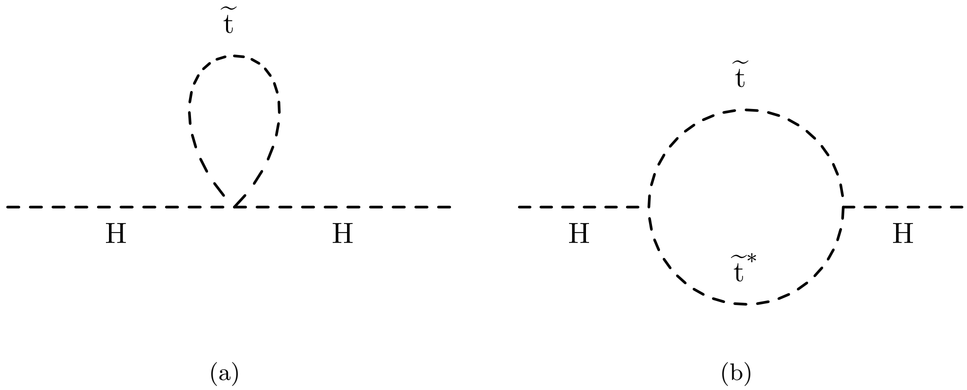

Figure 1.3: The stop-loop corrections to the Higgs mass.

which precisely cancels the quadratic contribution from the top quark loop. To illuminate logarithmic cancellations, we also assume that $\tilde{\mu}_L = \tilde{\mu}_R = 2\tilde{\lambda} m_{\mathrm{t}}^2$ and a small perturbation to the left and right handed component of the stop mass relative to m_{t}, which we express as $m^2_{\widetilde{\mathrm{t}}_L} = m_{\mathrm{t}}^2 + m^2_{\delta_L}$ and $m^2_{\widetilde{\mathrm{t}}_R} = m_{\mathrm{t}}^2 + m^2_{\delta_R}$. Then the logarithmic contributions from the stop-loops are found to be

$$\begin{aligned}\delta m_{\mathrm{h}}^2|_{\mathrm{stop}}^{\ln} = -\frac{9|y_{\mathrm{t}}|}{16\pi^2}\Bigg[&\left(m_{\mathrm{t}}^2 + m_{\delta_R}^2\right)\ln\left(\frac{\Lambda^2 + m_{\mathrm{t}}^2 + m_{\delta_R}^2}{m_{\mathrm{t}}^2 + m_{\delta_R}^2}\right)\\ &+ \left(m_{\mathrm{t}}^2 + m_{\delta_L}^2\right)\ln\left(\frac{\Lambda^2 + m_{\mathrm{t}}^2 + m_{\delta_L}^2}{m_{\mathrm{t}}^2 + m_{\delta_L}^2}\right)\Bigg]. \qquad (1.24)\end{aligned}$$

As $m^2_{\delta_L}$, $m^2_{\delta_R} \to 0$, we see that $\delta m_{\mathrm{h}}^2|_{\mathrm{top}}^{\ln} + \delta m_{\mathrm{h}}^2|_{\mathrm{stop}}^{\ln} = 0$. In other words, the fine-tuning resulting from the top-loop corrections can be resolved by introducing a scalar particle with identical couplings, provided the mass difference is small.

1.2.3 SUSY Algebra

More formally, Q_α and $Q_{\dot\alpha}^\dagger$ are the spin 1/2 Weyl spinors[1] which are the generators of the SUSY transformations and are described by the relations [15]

$$\{Q_\alpha, Q_\beta\} = \{Q^\dagger_{\dot\alpha}, Q^\dagger_{\dot\beta}\} = 0 \qquad (1.25)$$

$$\{Q_\alpha, Q^\dagger_{\dot\alpha}\} = 2\sigma^\mu_{\alpha\dot\alpha} P_\mu \qquad (1.26)$$

$$\left[P_\mu, Q_\alpha\right] = \left[P_\mu, Q^\dagger_{\dot\alpha}\right] = 0 \qquad (1.27)$$

[1] The SUSY algebra presented here assumes no extra dimensions.

where σ^μ are the Pauli spin matrices, P_μ is the spacetime translations generator, and α, $\dot{\alpha} = 1, 2$ are the Weyl spinor indices.

Supermultiplets form single particle states of the SM and SUSY partners. Since Q_α commutes with the generators of gauge transformations, it follows that partner particles in a supermultiplet must have the same electric charges, weak isospin, and color degrees of freedom. For unbroken SUSY, the commutation relations given in Equation 1.27 indicate the individual superparter masses must be equal to the SM counterpart.

1.2.4 The Minimal Supersymmetric Standard Model

The Minimal Supersymmetric Standard Model (MSSM) is the minimal extension to the standard model that incorporates SUSY [15]. In the MSSM, the SM gauge and fermion fields have superpartners with spin that differs by a half unit. Gauge supermultiplets are formed by pairing each SM gauge field with a spin 1/2 gaugino field. Gluons are partnered with gluinos, denoted as $\widetilde{\mathrm{g}}$, with corresponding fields described by $\widetilde{G}^\alpha_\mu(x)$, for $\alpha = 1, \ldots, 8$. Likewise, electroweak gauge supermultiplets contain the three wino fields, $\widetilde{\mathrm{W}}^a_\mu$, and the bino field, $\widetilde{\mathrm{B}}_\mu$.

The Higgs sector is modified in the MSSM. The complex scalar field ϕ is replaced by two scalar doublet fields H_u and H_d that transform as $(\mathbf{1}, \mathbf{2}, 1/2)$ and $(\mathbf{1}, \mathbf{2}, -1/2)$, respectively. These fields can be decomposed into $\mathrm{H}_u = (\mathrm{H}^+_u, \mathrm{H}^0_u)$ and $\mathrm{H}_d = (\mathrm{H}^0_d, \mathrm{H}^-_d)$. Chiral supermultiplets pair spin 0 fields with spin 1/2 fields. The Higgs scalar doublet fields form a chiral supermultiplet field with the Higgsino fields $\widetilde{\mathrm{H}}_u = (\widetilde{\mathrm{H}}^+_u, \widetilde{\mathrm{H}}^0_u)$ and $\widetilde{\mathrm{H}}_d = (\widetilde{\mathrm{H}}^0_d, \widetilde{\mathrm{H}}^-_d)$. Likewise, each SM fermion field is paired with a complex scalar field to form a chiral supermultiplet in the MSSM. These SUSY partners of SM fermions are named by prepending an *s* to the corresponding fermion name, i.e., squarks and sleptons.[2]

Since we have not observed any SUSY particles, the masses must be different than the SM particles and therefore SUSY must be a broken symmetry. The details of the symmetry breaking

[2] When referring to specific SUSY flavors, we often transfer the *s* from quark to the particle flavor. That is, top squark, stop quark, and stop all refer to the same SUSY particle.

Table 1.3: The undiscovered particles of the MSSM [15].

Names	Spin	P_R	Gauge Eigenstates	Mass Eigenstates
Higgs boson	0	+1	$\mathrm{H}_u^0\ \mathrm{H}_d^0\ \mathrm{H}_u^+\ \mathrm{H}_d^-$	$\mathrm{h}^0\ \mathrm{H}^0\ \mathrm{A}^0\ \mathrm{H}^\pm$
squarks	0	-1	$\widetilde{\mathrm{u}}_L\ \widetilde{\mathrm{u}}_R\ \widetilde{\mathrm{d}}_L\ \widetilde{\mathrm{d}}_R$	(same)
	0	-1	$\widetilde{\mathrm{s}}_L\ \widetilde{\mathrm{s}}_R\ \widetilde{\mathrm{c}}_L\ \widetilde{\mathrm{c}}_R$	(same)
	0	-1	$\widetilde{\mathrm{t}}_L\ \widetilde{\mathrm{t}}_R\ \widetilde{\mathrm{b}}_L\ \widetilde{\mathrm{b}}_R$	$\widetilde{\mathrm{t}}_1\ \widetilde{\mathrm{t}}_2\ \widetilde{\mathrm{b}}_1\ \widetilde{\mathrm{b}}_2$
sleptons	0	-1	$\widetilde{\mathrm{e}}_L\ \widetilde{\mathrm{e}}_R\ \widetilde{\nu}_{\mathrm{e}}$	(same)
	0	-1	$\widetilde{\mu}_L\ \widetilde{\mu}_R\ \widetilde{\nu}_\mu$	(same)
	0	-1	$\widetilde{\tau}_L\ \widetilde{\tau}_R\ \widetilde{\nu}_\tau$	$\widetilde{\tau}_1\ \widetilde{\tau}_2\ \widetilde{\nu}_\tau$
neutralinos	1/2	-1	$\widetilde{\mathrm{B}}^0\ \widetilde{\mathrm{W}}^0\ \widetilde{\mathrm{H}}_u^0\ \widetilde{\mathrm{H}}_d^0$	$\widetilde{\chi}_1^0\ \widetilde{\chi}_2^0\ \widetilde{\chi}_3^0\ \widetilde{\chi}_4^0$
charginos	1/2	-1	$\widetilde{\mathrm{W}}^\pm\ \widetilde{\mathrm{H}}_u^+\ \widetilde{\mathrm{H}}_d^-$	$\widetilde{\chi}_1^\pm\ \widetilde{\chi}_2^\pm$
gluino	1/2	-1	$\widetilde{\mathrm{g}}$	same
goldstino (gravitino)	1/2 (3/2)	-1	$\widetilde{\mathrm{G}}$	same

mechanism are unknown, but SUSY breaking scenarios that prevent fine-tuning can be expressed as

$$\mathcal{L}_{\mathrm{MSSM}} = \mathcal{L}_{\mathrm{SUSY}} + \mathcal{L}_{\mathrm{soft}}, \tag{1.28}$$

where the gauge and Yukawa interactions are contained within $\mathcal{L}_{\mathrm{SUSY}}$ and we parameterize our ignorance about SUSY breaking in $\mathcal{L}_{\mathrm{soft}}$, which contains around 100 free parameters such as the mass splittings between SM and SUSY particles. SUSY breaking allows for mixing between the gauge eigenstates. Neutralinos, denoted $\widetilde{\chi}_i^0$ with $i = 1, \ldots, 4$, are linear combinations of $\widetilde{\mathrm{H}}_u^0$, $\widetilde{\mathrm{H}}_d^0$, $\widetilde{\mathrm{W}}^0$, and $\widetilde{\mathrm{B}}^0$. Three of the eight degrees of freedom from the two Higgs doublet fields are absorbed by the $\mathrm{W}^\pm$ and the Z. The remaining five degrees of freedom become five mass eigenstates of the MSSM Higgs sector. These include two scalar Higgs particles, h^0 and H^0, a pseudoscalar Higgs, A^0, and two charged Higgs particles, $\mathrm{H}^\pm$. Another consequence of SUSY breaking is the addition of a neutral, massless fermion which we call the goldstino. Accounting for gravity introduces the massless spin 3/2 gravitino, which pairs with the massless spin 2 graviton into a third type of supermultiplet [15]. As SUSY is spontaneously broken, the gravitino acquires mass by absorbing the goldstino. A list of particles introduced in the MSSM is given in Table 1.3.

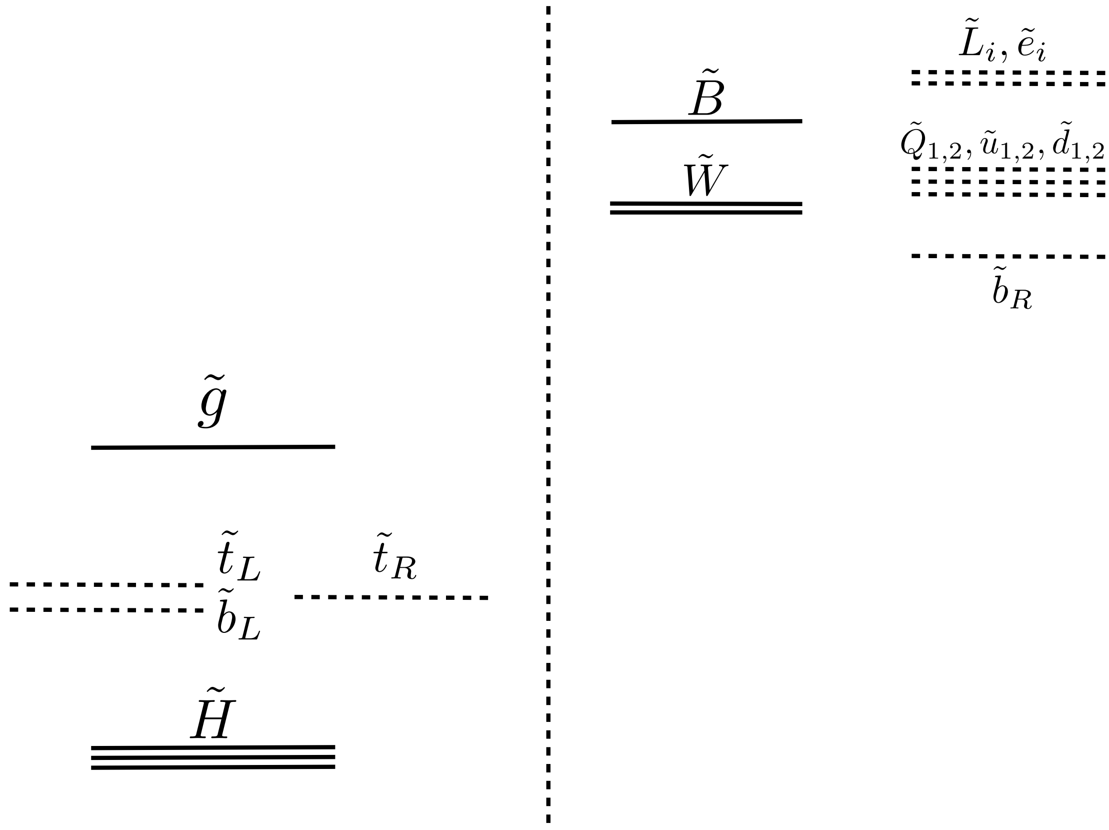

Figure 1.4: A generic spectrum of masses for natural SUSY [16]. The vertical axis represents mass with SUSY particles on the left of the dashed line favored to be light.

Returning to the concept of naturalness, we note that while model parameter freedom can blur specific statements about SUSY particle mass and fine-tuning, general statements can still be made with modest assumptions. We have already seen that the stop quark must be relatively light to satisfy naturalness. Because the gluino and left-handed sbottom are strongly coupled to the stop quark, these particles enter as radiative corrections to the stop mass. This results in restrictions on $m_{\tilde{g}}$ and $m_{\tilde{b}_L}$ in the context of naturalness. The same parameter that sets the approximate scale for the lightest neutral Higgs particle also scales the Higgsino particles. This requires the Higgsino masses to be not much heavier than the lightest Higgs boson. Heavier and charged Higgs particles can be arbitrarily massive. Generally speaking, the sleptons and the first and second generation squarks are not required to be very light in natural SUSY models. Figure 1.4 depicts key features in the mass spectrum requirements in natural SUSY. References [16] and [17] provide a more quantitative analysis on f (Equation 1.21). Using 1% fine-tuning as a benchmark, we should expect to find the stop and left-handed sbottom masses no greater than around 1 TeV and the gluino mass no greater than around 1.5-2 TeV. Figure 1.5a shows the functional form of f^{-1} against SUSY mass scale for a generic set of SUSY model parameters.

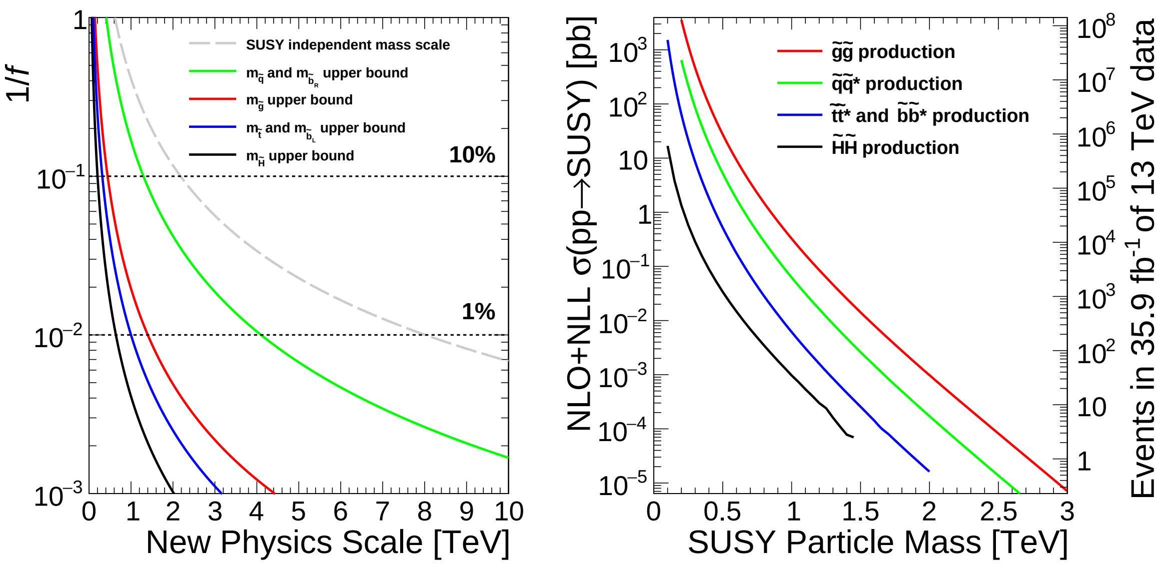

(a) (b)

Figure 1.5: The degree of fine-tuning needed for a 125 GeV Higgs, plotted as a function of the scale at which new physics exists (a) [17, 18], and SUSY production cross section and event rate for proton-proton collisions at 13 TeV vs sparticle mass (b) [19]. Here, $\tilde{q}$ refers to $\tilde{u}$, $\tilde{d}$, $\tilde{c}$, and $\tilde{s}$, collectively.

The naturalness spectrum serves as a guide for designing searches for direct SUSY production at hadron colliders, like the search presented in this thesis. However, analyses targeting SUSY must also consider the production cross section of SUSY pairs. Gluinos have the largest cross sections, making direct gluino pair production an attractive target for searches for SUSY at the LHC. Figure 1.5b shows the pair production cross section vs SUSY particle mass. While direct stop pair production yields a smaller cross section, a tighter restriction on stop mass from naturalness considerations implies that stop searches can also be fruitful. Figures 1.6 and 1.7 show the leading pair production diagrams for gluinos and squarks (such as stops), respectively.

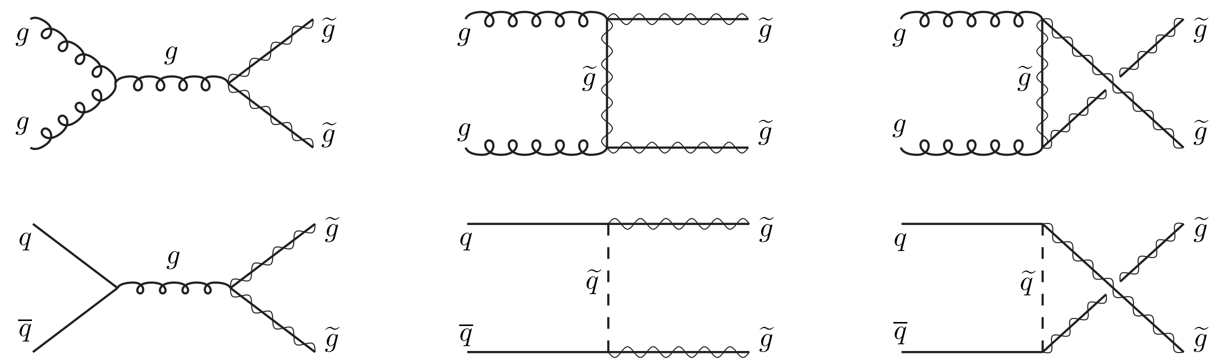

Figure 1.6: The leading gluino pair production diagrams [15].

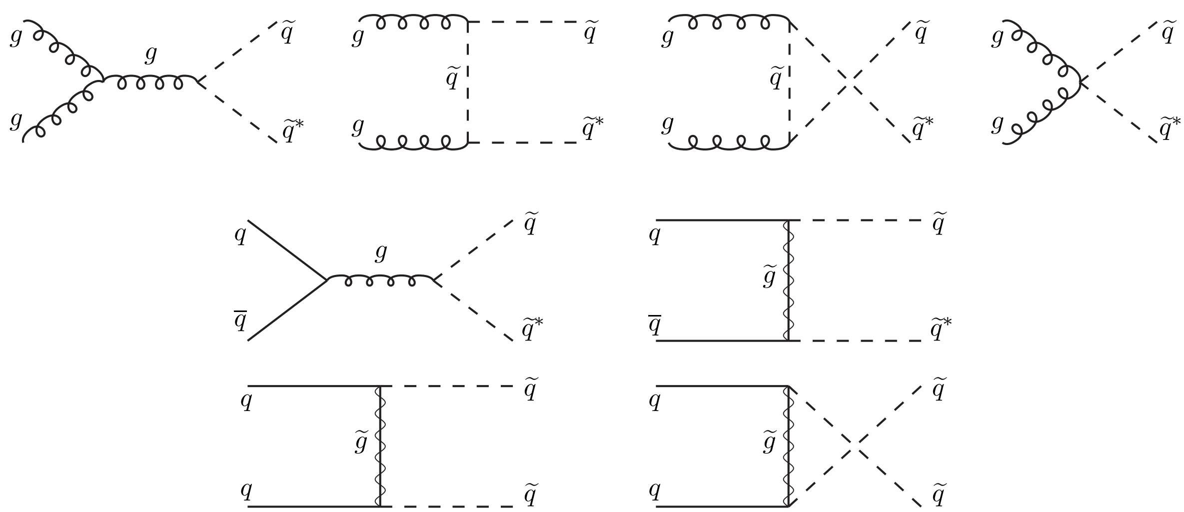

Figure 1.7: The leading squark pair production diagrams [15].

1.2.5 Gauge Coupling Unification

In addition to providing a solution to the hierarchy problem, the MSSM has an attractive feature related to the convergence of the running strengths of the gauge couplings. This feature of SUSY also relies on relatively light partner masses. In fact, it is remarkable that the naturalness scale requirement of $\mathcal{O}(1$ TeV$)$ is also the approximate SUSY scale required to achieve gauge coupling unification.

The apparent regularity across the gauge groups of the standard model has lead to speculation of unification in the form of a single gauge group, speculation that has persisted since the formulation of the SM itself [20]. Important to this concept is the weakening of the $\mathrm{SU}_c(3)$ coupling constant with energy scale, as unification is only possible if all effective theory gauge-group coupling constants converge to a single value. However, extrapolation of each of the gauge couplings using beta functions calculated in the SM do not intersect at a single point, as shown in Figure 1.8a. If, instead, we extrapolate with beta functions calculated in the MSSM, the slope of the gauge couplings vs the logarithm of the energy scale deviates upon the introduction of a scale at which SUSY contributes, m_{SUSY}. Figure 1.8 gives the gauge coupling constants in the MSSM for $m_{\mathrm{SUSY}} = m_{\mathrm{Z}}$. Coupling constants converge to within uncertainties for $m_{\mathrm{SUSY}} \lesssim 1$ TeV.

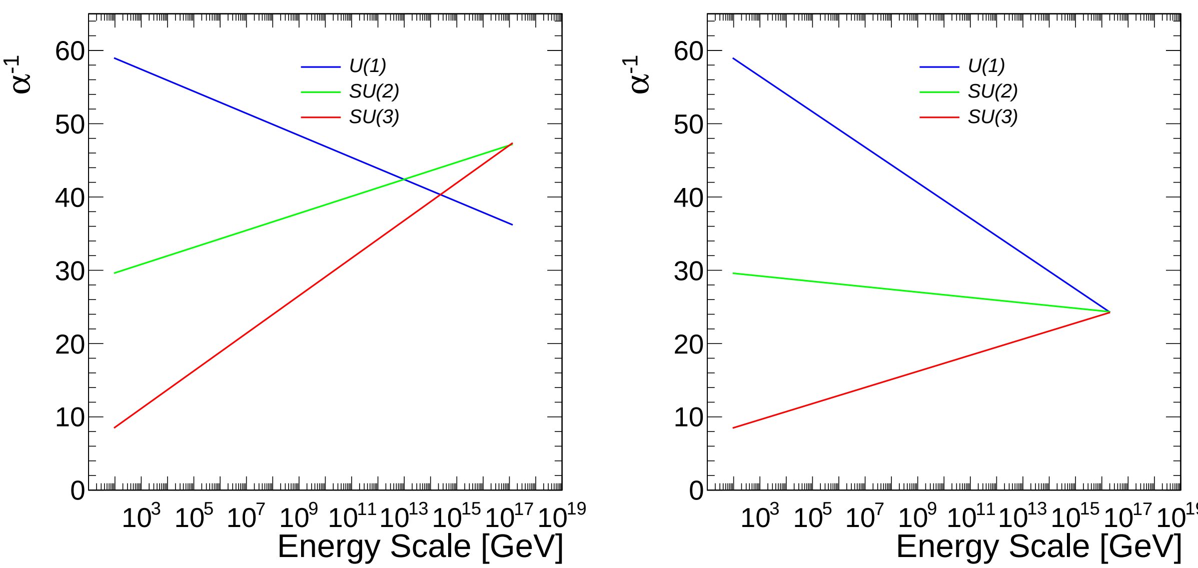

(a) (b)

Figure 1.8: The running couplings vs energy scale for SM (a) and MSSM (b).

1.2.6 R-Parity Conserving SUSY

An important concept in SUSY is R-parity:

$$P_R = (-1)^{3B+L+2s}, \tag{1.29}$$

where B is baryon number, s is spin, and L is lepton number.[3] It is very useful to consider R-parity conserving SUSY models because such models can stabilize the lifetime of the proton [21]. R-parity is a discrete symmetry with the following transformation properties:

$$\begin{aligned}
\text{(SM particle)} &\longrightarrow \text{(SM particle)},\\
\text{(superpartner)} &\longrightarrow -\text{(superpartner)}.
\end{aligned}$$

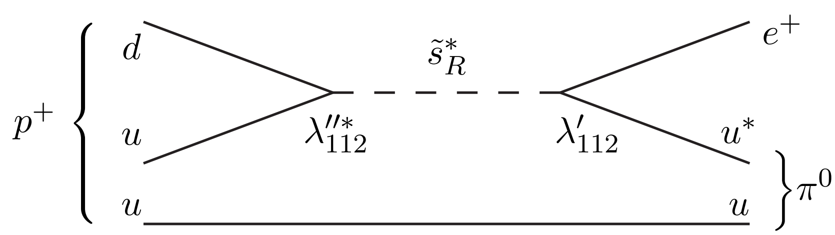

Figure 1.9: Without P_R conservation, the proton is free to decay. The above example shows $\mathrm{p} \to \mathrm{e}^+\pi^0$ mediated by a strange anti-squark, denoted by $\tilde{\mathrm{s}}^*_R$ [15]. In the diagram, u^* denotes an up anti-quark.

If we assume R-parity conservation, we are led to two important phenomenological consequences:

- SUSY particles are always produced in pairs.
- The lightest SUSY particle (LSP) is stable, and all other SUSY particles will decay into an odd number of LSPs.

[3] Baryon number is defined as $B = \frac{1}{3}(n_\mathrm{q} - n_{\bar{\mathrm{q}}})$, where n_q, $n_{\bar{\mathrm{q}}}$ is the (s)quark, anti-(s)quark multiplicity, and lepton number is defined as $L = n_\ell - n_{\bar{\ell}}$, where n_ℓ, $n_{\bar{\ell}}$ is the (s)lepton, anti-(s)lepton multiplicity.

These consequences restrict the available model topologies in proton-proton collisions. While R-parity-violating models are targeted in some SUSY searches [22, 23], for reasons discussed above and below, this dissertation will focus on P_R-conserving SUSY models.

While, dynamically speaking, the LSP is not required to be free of color or electric charge, a stable SUSY particle with nonzero color or electric charge should already have been observed [24]. This leaves the neutralino, gravitino, and sneutrino as prime LSP candidates. Gravitinos and sneutrinos generally are disfavored as a result of cosmological inconsistencies [15, 25] and experimental exclusions [6]. Therefore, we will assume that the LSP is the lightest neutralino.

Here enters yet another promising result of generic supersymmetry: the weakly interacting massive LSP is a dark matter candidate. While SUSY is not unique in providing an extension to the standard model that purports to explain the composition of dark matter, it is clearly an attractive side effect that is difficult to ignore when considering motivations for physics beyond the standard model. The search for SUSY presented in this thesis will not make any assumptions on the mass of $\widetilde{\chi}_1^0$, or assert that it be consistent with dark matter. SUSY might only partially account for dark matter or not at all, and there are no *a priori* dark matter considerations in building any SUSY models considered in the search.

1.3 Supersymmetry Event Topologies Expected from TeV Collisions

In designing a search for direct production of SUSY there are three main criteria that need to be considered: production rate, expected mass sensitivity of SUSY particle candidates, and final state topologies. As shown in Figure 1.5b, sparticles that carry color have the largest production cross section at the LHC. To satisfy naturalness, the gluino and heavy flavor squarks should be relatively light. Therefore, an understanding of the final state topologies of gluino and squark production, with particular attention to processes involving heavy flavor, is essential for a generic search for SUSY.

If we focus our attention on the colored sector, the full parameter space of the MSSM is more detailed and complex than needed. In the MSSM, the leading diagram for gluino decay is given in

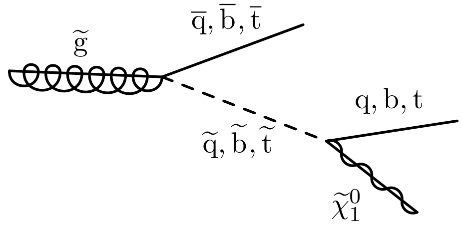

Figure 1.10: Dominant gluino decay channel.

Figure 1.10 [15]. Per gluino, we have three different scenarios that lead to final states with either two light flavored quarks, two bottom quarks, or two top quarks. Since P_R conserving models require SUSY particles be produced in pairs, the final state we would find in pp collisions would double the number of final state quarks in Figure 1.10.

1.3.1 Simplified Models

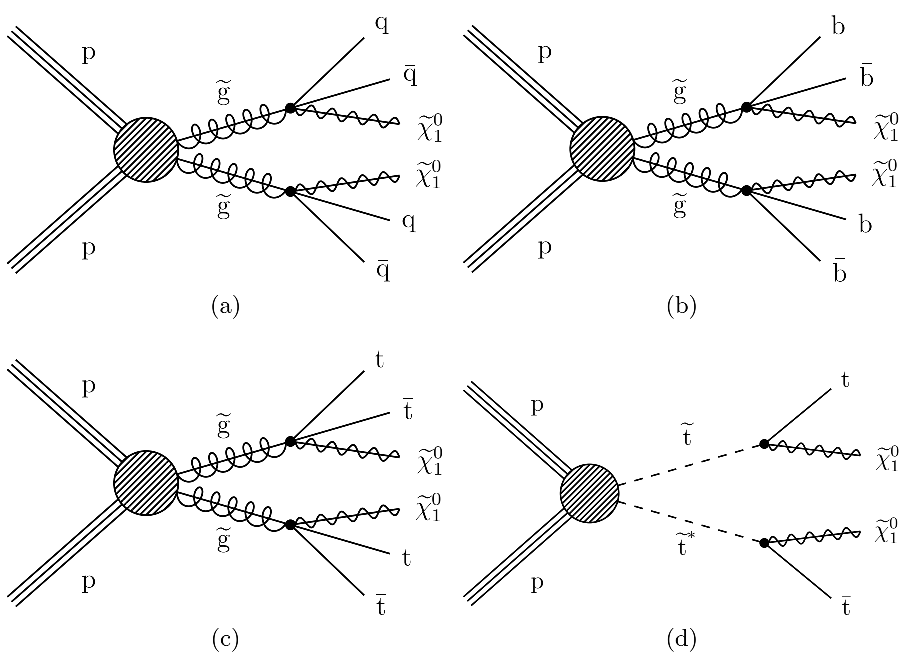

Figure 1.11: Simplified SUSY diagrams considered for this search. We refer to each model individually: T1qqqq (a), T1bbbb (b), T1tttt (c), and T2tt (d).

Targeting a full SUSY model, such as the MSSM, for a search for new physics is less desirable because of the multitude of parameters that add complexity to the signal generation and that interpretations can be too model specific, making it difficult to draw general conclusions. Simplified SUSY models are designed to involve only a few SUSY particles, setting the remaining particle masses out of the reach of the LHC. Simplified models are limits to more general SUSY models and exhibit final states that can be virtually indistinguishable to a wide range of parameter space for a number of SUSY models [26, 27]. For instance, the squarks in the gluino decay given in Figure 1.10 can be either on-shell or virtual. If the stop is the only squark available at LHC energies, then the $\widetilde{g} \rightarrow t\widetilde{t}$ will dominate [15]. Therefore, we consider simplified models given in Figures 1.11a-1.11c for targeting gluino pair production. Similarly, squark decays given by $\widetilde{q} \rightarrow q\widetilde{\chi}_1^0$ are always kinematically favored and may be the dominant decay channel [15]. This process is identical to the simplified model shown in Figure 1.11d, for the case of top squark production. In other words, we are sensitive to a wide range of SUSY scenarios by focusing our search on final state topologies with two undetected neutralinos and, often many, SM quarks.

Chapter 2

Physics at TeV Scale Particle Collisions

High energy particle collisions provide direct evidence to study elementary particles in the laboratory. The interaction occurring from the result of a collision is referred to as an *event*. We often look for high mass resonances. Therefore, we aim for large total energy of the colliding initial particles, and this is maximized if the center-of-mass frame of the particle collisions is at rest with respect to the laboratory. To increase the energies of the colliding particles we accelerate particles using electric fields. By assembling our accelerators in ring like structures, we are able to reuse accelerating cavities, further increasing the accelerated particle energy.

In this chapter, we introduce the physics involved with colliding high energy protons. Then, the apparatus used to supply these proton collisions, the Large Hadron Collider, and the tool to analyze the product of these collections, the Compact Muon Solenoid experiment, are described.

2.1 Proton Collisions at the High Energy Frontier

In this section, we introduce some concepts needed to understand the physics involved in high energy proton collisions. The nature of the strong interaction presents challenges, both in our ability to calculate measurable quantities and in our ability to identify particles. More complete descriptions of hadron collider physics can be found in References [28, 29].

2.1.1 Proton Structure

An understanding of the proton structure is necessary to characterize the physics involved with proton collisions. The proton, denoted as p, is a composite particle, including three valence quarks (u, u, and d) and a sea of gluons and quark-antiquark pairs. These partons carry momentum fraction ξ of the total proton momentum. We can factorize the parton distribution function (PDF), which characterizes the long-distance behavior of the proton, from the hard scatter process:

$$\sigma(\mathrm{pp} \to X) = \int_0^1 dx_1 \int_0^1 dx_2 \sum_{a,b} f_a(x_1, \mu_F^2) f_b(x_2, \mu_F^2) \hat{\sigma}^{ab \to X}(Q^2, \mu_F^2). \tag{2.1}$$

Here, $\sigma(\mathrm{pp} \to X)$ is the total production cross section of some physical final state process X, $\hat{\sigma}^{ab\to X}$ is the hard scatter cross section between parton a from one proton and parton b from another, $f_a(\xi, \mu_F^2)$ is the PDF of parton a, Q is the energy scale, and μ_F is the factorization scale, which sets the boundary at which the hard physics factorizes from the PDF. At leading order, the probability of finding a parton a with momentum fraction ξ within the proton is described by the PDF.

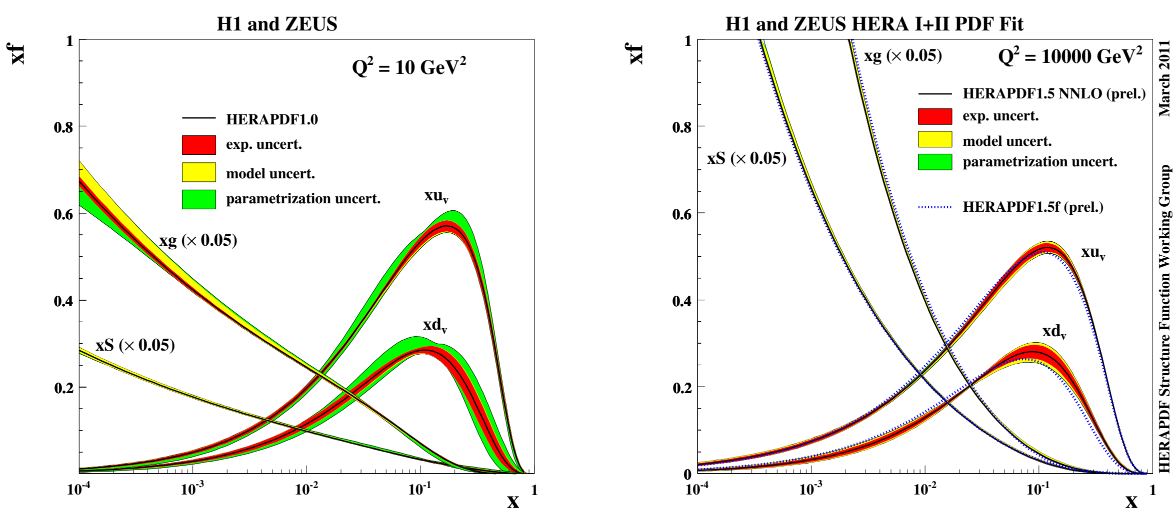

(a) (b)

Figure 2.1: The PDFs for the proton at $Q^2 = 10$ GeV^2 (a) and at $Q^2 = 10000$ GeV^2 (b) as measured by the H1 and Zeus collaborations. In both plots, the gluon and sea distributions are scaled down by a factor of 20 [30].

The PDF absorbs divergences from collinear and soft emissions below μ_F. PDFs are measured experimentally, mainly from deep inelastic scattering experiments, for a given scale and are used as input when simulating pp collisions. Figure 2.1 gives PDFs for two different scales from the H1 and ZEUS Collaborations [30]. The choice of μ_F introduces model uncertainty for a given PDF. The functional behavior of the PDF against μ_F^2 is given by the DGLAP [31] equation

$$\mu_F^2 \frac{\partial f_a(\xi, \mu_F^2)}{\partial \mu_F^2} = \sum_b \frac{\alpha_s(\mu_F^2)}{2\pi} \int_\xi^1 \frac{dz}{z} P_{ab}(z) f_b(\xi/z, \mu_F^2), \tag{2.2}$$

where $P_{ab}(z)$ is the probability of parton a to split $a \to bc$ with longitudinal momentum $p_b = zp_a$.

2.1.2 Hard Scatter, Parton Shower, and Hadronization

The calculation of the hard scatter interaction is accomplished with perturbation theory. If the precision of the calculation includes loop contributions, integration over the loop momenta can lead to divergences. Unlike the divergences considered in Chapter 1 regarding the calculation of the Higgs mass, hard scatter divergences are unphysical artifacts from the perturbation expansion, and are controlled with a cutoff scale, μ_R, called the renormalization scale [32]. No physical observables depend on μ_R and associated theory uncertainties must be accounted for when comparing observation directly with theoretical calculations.

Color confinement prevents free quarks or gluons from exceeding a separation distance of order 10^{-15} m. However, in conjunction with hard scatter partons in pp collisions is a cascade of radiation, called a parton shower, through the production of quark-antiquark pairs and gluon radiation. Parton showers occurring before the hard interaction are called initial state radiation (ISR), while parton showers occurring after the hard interaction are called final state radiation (FSR). During the parton shower, the strong coupling constant is large and the partons begin to form hadrons through a process called hadronization. The cluster of hadronic and electromagnetic energy surrounding this process is called a jet. Jets can come from a parton shower or a hard scatter of a parton.

It's generally understood that color neutral hadrons are formed and unstable hadrons subsequently decay into stable hadrons, leptons, and photons. However, perturbative QCD is unable to accurately describe hadronization, and so we must rely on phenomenological models. Two commonly used models of hadronization are the cluster and string models, illustrated in Figure 2.2. In the string model, the color field between $q\overline{q}$ pairs is assumed to be a string of uniform density at the end of a parton shower [29]. Hard gluons are modeled as *kinks* in the string, and the string breaks through $q\overline{q}$ pair creation. Simulations used in this thesis utilize the string model of hadronization. An alternate model is called the cluster model, which requires all gluons at the end of a shower to split into $q\overline{q}$ pairs, and subsequent clusters are formed from neighboring quark singlets. Clusters can decay to lighter clusters if energy thresholds are met, and hadrons are formed from the final cluster in the decay chain.

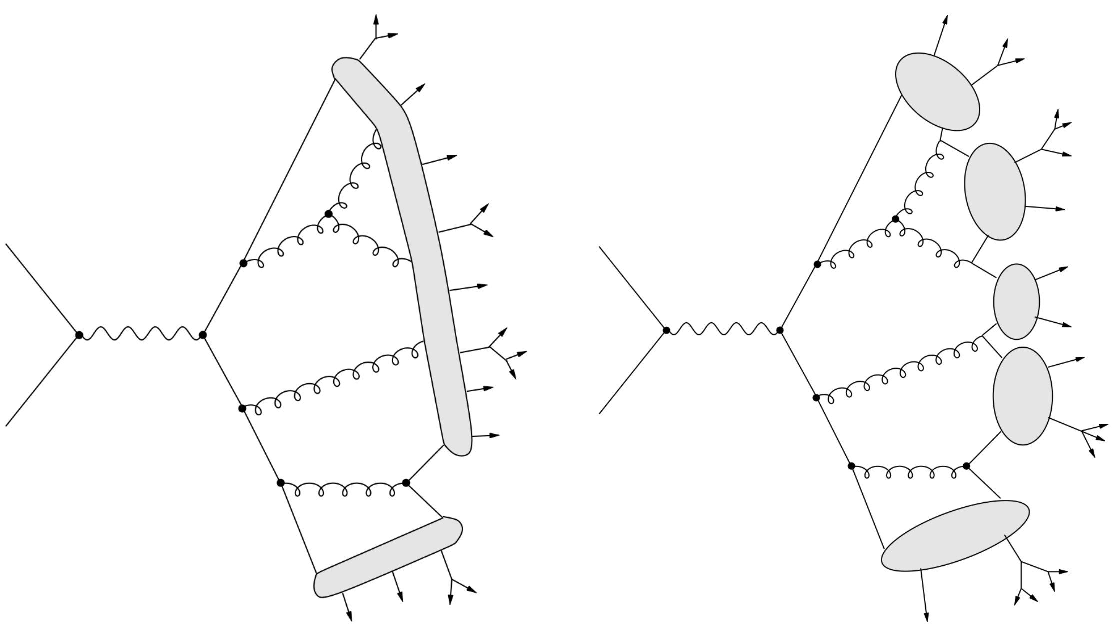

(b)

(b)

Figure 2.2: Illustrations of the String (a) and Cluster (b) models of hadronization [29].

2.2 The Large Hadron Collider

The LHC is a synchrotron currently operating with a proton beam energy of 6.5 TeV. The main ring straddles the border between Switzerland and France, is roughly 100 m underground, and is about 26.7 km in circumference [33]. There are four LHC collision points, one of which is at the CMS detector described in Section 2.3.

Table 2.1: The stages of proton acceleration before reaching peak proton energy [33].

Stage	Accelerator Apparatus	Initial Energy	Final Energy
1	Linac2	0	50 MeV
2	Proton Synchrotron Booster (PSB)	50 MeV	1.4 GeV
3	Proton Synchrotron (PS)	1.4 GeV	26 GeV
4	Super Proton Synchrotron (SPS)	26 GeV	450 GeV
5	LHC	450 GeV	6.5 TeV

Protons are ionized from hydrogen and are eventually injected into the LHC at 450 GeV in energy after being accelerated in stages given in Table 2.1, with the accelerator complex shown in Figure 2.3. While accelerated by the Proton Synchrotron, the beam is split into proton bunches with a separation between bunches of 25 ns.

For a given physical process, the number of events produced in a time interval is given by the production cross section times the luminosity integrated over that interval:

$$N(\mathrm{pp} \to X) = \sigma(\mathrm{pp} \to X) \int \mathcal{L}\, dt. \tag{2.3}$$

To increase the event rate, we then attempt to maximize the instantaneous luminosity, $\mathcal{L}$. To a very good approximation, the proton beam follows a gaussian distribution with the instantaneous luminosity expressed as,

$$\mathcal{L} = \frac{N_{\mathrm{p}}^2 n_b f_{\mathrm{rev}}}{4\pi\epsilon_n\beta^*} F. \tag{2.4}$$

Here F is a small reduction factor to account for the crossing angle and f_{rev} is the revolution frequency determined by the LHC circumference. The remaining parameters and definitions in Equation 2.4 are given in Table 2.2. The bunch spacing, $\tau_b = 25$ ns, and the number of gaps

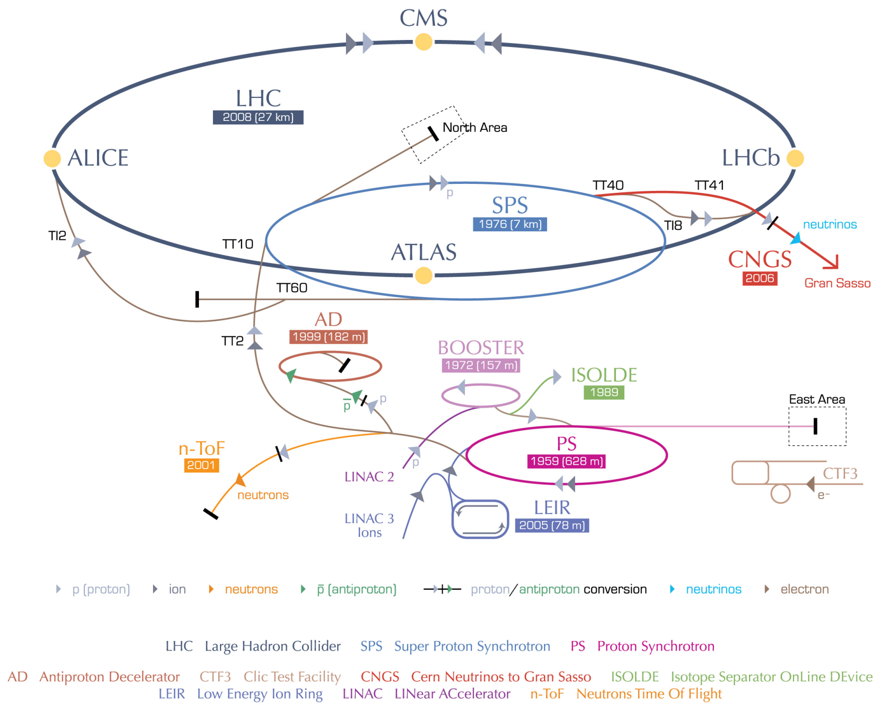

Figure 2.3: A schematic view of the injector complex and LHC at CERN [34, 35].

determine n_b, and the injection kicker limits the bunch population, N_p [36]. The LHC injector complex limits the normalized transverse beam emittance, ϵ_n, and the mechanical aperture limits the beta function at the interaction point, β^* [37].

The powerful superconducting dipole magnets, illustrated in Figure 2.4, bend the protons along the path of the LHC. There are a total of 1,232 dipole magnets which also function to sort the protons according to individual momentum. Beam focusing and stabilization is accomplished using a number of quadrupole magnets with alternating focusing and defocusing fields. The beam cross sectional area is focused to be minimized at the interaction point. The electric fields that accelerate the protons and separate them into bunches are generated from 400 MHz radio frequency (RF) cavities. The number of collisions per bunch crossing is called pileup and depends on the parameters given in Table 2.2. A typical bunch crossing during the 2016 run produced 40 interactions.

Table 2.2: LHC operating parameters for 2016 RunII data taking [1, 35].

Parameter	
Total center-of mass energy ($\sqrt{s}$)	13 TeV
Circumference	26659 m
Number of bending magnets	1232
Maximum field in bending magnets	8.3 T
Bunch spacing (τ_b)	25 ns
Bunch population (N_{p})	1.15×10^{11}
Beta function at interaction point (β^*)	40 cm
Normalized transverse beam emittance (ϵ_n)	2.0 μm
Number of colliding bunches per beam (n_b)	2220
Maximum stored energy (E_s)	265 MJ
Peak instantaneous luminosity ($\mathcal{L}$)	1.4×10^{34} cm$^{-2}s^{-1}$

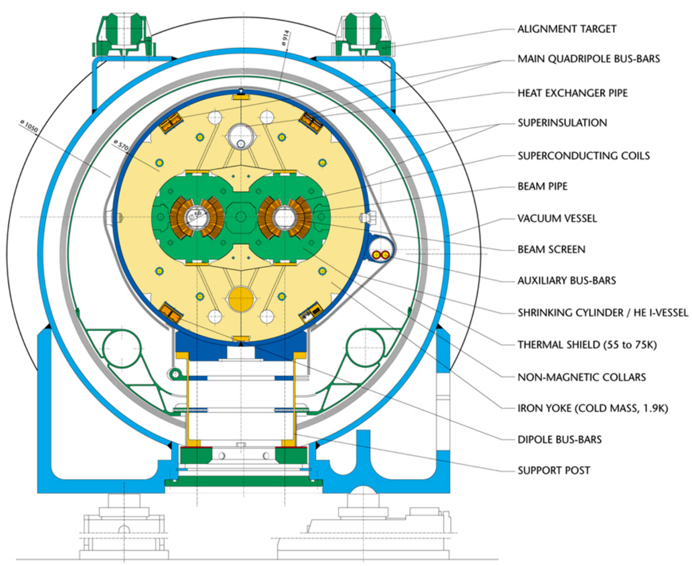

Figure 2.4: Cross sectional view of the LHC dipole magnets [37].

2.3 The Compact Muon Solenoid Experiment

The CMS experiment is a nearly hermetic, general purpose detector at the LHC [38]. Several subdetectors that comprise CMS are designed to measure and absorb products of the delivered pp collisions. To a good approximation, these subdetectors are cylindrically arranged and centered around the P5 interaction point of the LHC, with the length of the cylinder aligned with the beam axis. During operation, the subdetectors are situated within a 3.8 T magnetic field generated by a solenoidal magnet described in Section 2.3.2. The solenoid and cylindrical subdetectors form layers around the interaction point. A cutaway view of the full detector is shown in Figure 2.5. The first condition to select data for analyzing is the passing of a fast, hardware-level processing system in some of the CMS subdetectors. This system is known as the Level-1 (L1) trigger and it is designed to be highly efficient in selecting interesting events while balancing throughput limitations. Events that pass the L1 trigger decision are read out to the CMS Data Acquisition (DAQ) system described in Section 2.3.8. The subcomponent systems of the detector are described in detail in the following sections.

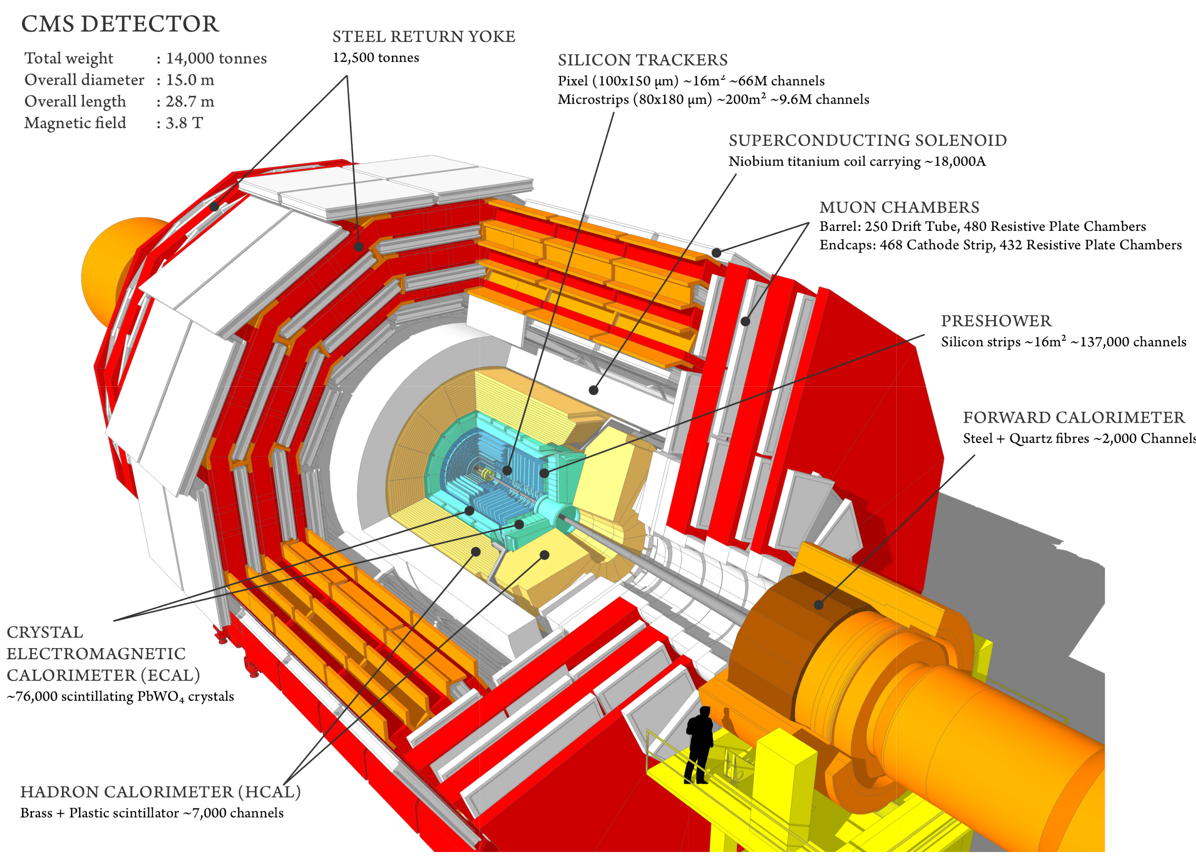

Figure 2.5: Cutaway view of the CMS detector. Image: CERN.

2.3.1 Coordinate System

The origin of the adopted CMS coordinate system is chosen to be at the nominal interaction point. The x–axis points radially inward toward the center of the LHC and the y–axis points vertically upward. The z–axis points along the beam direction, such that the coordinate system is right-handed. The x–y plane is referred to as the transverse plane, with azimuthal angle, ϕ, taken with respect to the x–axis. The radial direction is denoted r. To describe a particle's direction from the collision vertex, we use ϕ and pseudorapidity, defined as $\eta = -\ln\tan(\theta/2)$, where θ is the polar angle measured with respect to the z–axis. A vector pointing perpendicular to the beam axis corresponds to $\eta = 0$. As we will see later in this chapter, particles with $|\eta|$ larger than around 2.4 are very forward relative to many of our subdetectors. Thus, we lose some ability to identify particles with $|\eta| \gtrsim 2.4$. CMS derives its clock by synchronizing with the LHC collisions.

2.3.2 Superconducting Solenoid Magnet

Large magnetic bending strength is needed to precisely measure the momentum of charged particles. For muons, this is the only measurement we have of the particle's momentum. The design requirement of a bending power of 12 Tm requires a superconducting solenoid. The CMS superconducting solenoid magnet weighs 220 metric tons and is 13 m long, with an inner diameter of 6 m. The strength of the magnetic field throughout the detector from the superconducting niobium-titanium coils is 3.8 T. An artists view of the magnet is given in Figure 2.6.

An iron yoke, composed of five barrel wheels and six endcap disks, returns the magnetic field. There are three layers in each barrel wheel and endcap disk. The yoke is 14 m in diameter, is 13 m in length, and has total weight of 10,000 metric tons. Inside the solenoid lie the tracker, electromagnetic calorimeter, and hadronic calorimeter described in Sections 2.3.3, 2.3.4, and 2.3.5, respectively. The yoke is interlaced with the muon system described in Section 2.3.6.

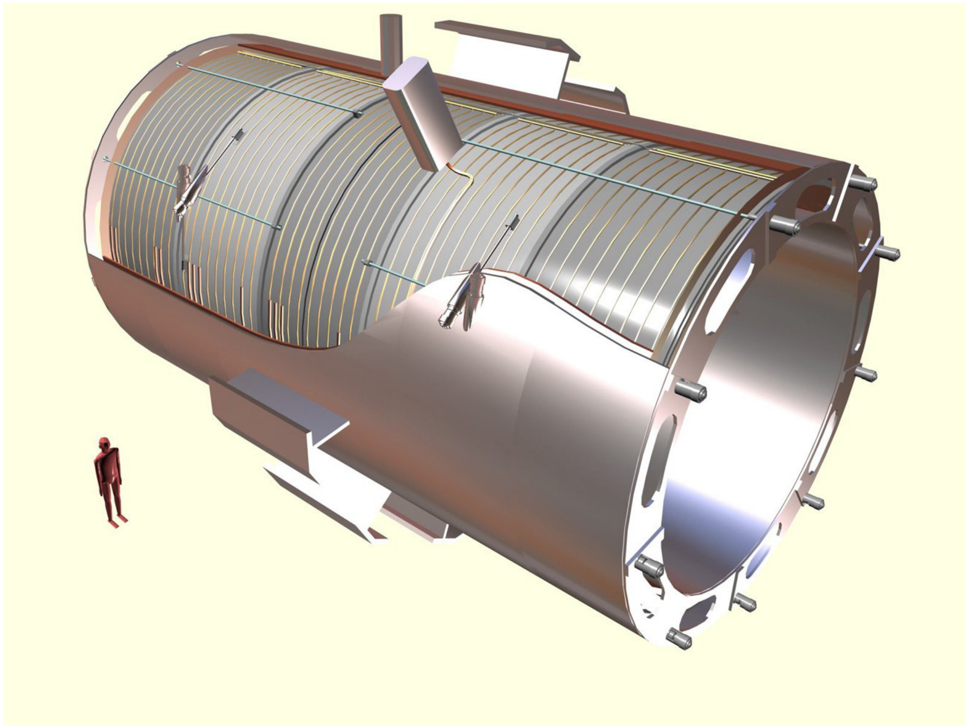

Figure 2.6: Artist's depiction of the CMS superconducting solenoid magnet [38].

2.3.3 Tracking

The purpose of the CMS tracking system is to provide precise vertexing and reconstruction of the trajectories of the charged particles that emerge from the pp collisions. The tracker is 5.8 m long and 2.5 m in diameter. It is composed of a pixel detector, described in Section 2.3.3.1, and a strip tracker, described in Section 2.3.3.2. The magnetic field throughout the tracker is a homogeneous 3.8 T. Tracking at CMS is crucial, not only to identify and reconstruct charged particles, but also to mitigate the effects of pileup. To meet requirements on radiation hardness, speed, and granularity, a silicon based tracker was chosen for both the pixel and strip systems. The momentum resolution for charged particles in the barrel region ($|\eta| < 1.6$) is around 2% or less for a charged particle with $p_{\mathrm{T}} = 100$ GeV [39].

2.3.3.1 Pixel Detector

The pixel system is the innermost subdetector of CMS and is responsible for the most precise vertexing and best impact parameter resolution. The detector consists of 1,440 silicon modular detector units (modules) placed on carbon fiber support ladders [40]. The pixel detector consists of barrel and endcap sections as shown in Figure 2.7a. Each of the three barrel layers of the pixel detector is 53.3 cm long with radii 4.4 cm, 7.3 cm, and 10.2 cm, with a total of 47,923,200 pixels. The four endcap disks sit at $z = \pm 35.5$ cm and $z = \pm 48.5$ cm with radii extending from 6 cm to 15 cm, with a total number of 17,971,200 pixels. The pixel detector covers $|\eta|$ up to 2.5.

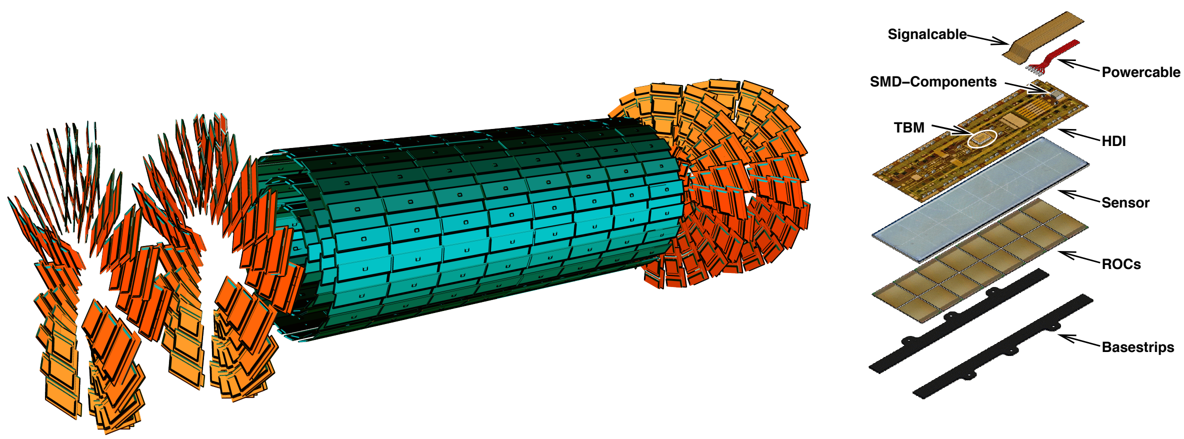

(a) (b)

Figure 2.7: Perspective view of the CMS pixel detector within the tracker (a) and exploded view of pixels showing the silicon sensor and readout chip (b) [40].

The barrel modules, shown in Figure 2.7b, include 16 or 8 readout chips (ROC), each serving a 52×80 array of pixels. The pixels themselves are 150 μm $\times$ 100 μm. Signals from ROC hits are time-stamped corresponding to the bunch crossing and are fed into the CMS data acquisition system.

2.3.3.2 Silicon Strip Tracker

Surrounding the pixel detector lies the CMS strip tracker, which consists of 9.3 million p-on-n type silicon micro-strip sensors [41, 38]. As shown in Figure 2.8, there are four main subsystems of the silicon strip tracker: the Tracker Inner Barrel (TIB), the Tracker Inner Disks (TID), the Tracker Outer Barrel (TOB), and the Tracker End Caps (TEC). There are four and six layers parallel to the beam line in the TIB and TOB, respectively. In the TID and TEC, the disks run perpendicular to the beam line. On each side of the interaction point, there are three disks in the TID and nine disks in the TEC. The TIB and TID both cover a radial distance of 20 cm to 55 cm and the TOB extends the tracker barrel coverage to $r = 116$ cm. The total active area of the strip detector is 198 m^2. Like the pixel detector, the strip tracker covers $|\eta| < 2.5$.

The TOB and TIB strips run parallel to z, providing hit measurements in the r–ϕ plane. The radial TID and TEC strips allow measurements in ϕ and z. Each subsystem of the strip tracker has a subset of layers with an additional layer mounted at an angle of 100 mrad. This feature is present in the first two layers of the TOB and TIB, and parts of the TID and TEC. The stereo angle allows for z measurement in the barrel strips and r measurement in the disks.

A custom APV25 chip provides readout by amplifying and shaping the analog pulses from the strips [42]. Optical links connect the APV25 chip to the front end driver (FED) where data rate gets reduced from several GB/s to roughly 50 MB/s before the data are sent to the DAQ.

2.3.4 Electromagnetic Calorimeter

The CMS electromagnetic calorimeter (ECAL) is divided into a barrel (EB) and endcap (EC) as shown in Figure 2.9. The ECAL is designed to absorb and measure the energy from high momentum electrons, positrons, and photons. It functions on the Bremsstrahlung principle and photon pair production. Therefore, a homogeneous ECAL made of lead tungstate ($PbWO_4$) exhibits desirable characteristics of high density (8.28 g/cm^3), short radiation length (0.89 cm), and small Molière radius (2.2 cm). In addition, $PbWO_4$ is radiation hard, reducing the need for large cali-

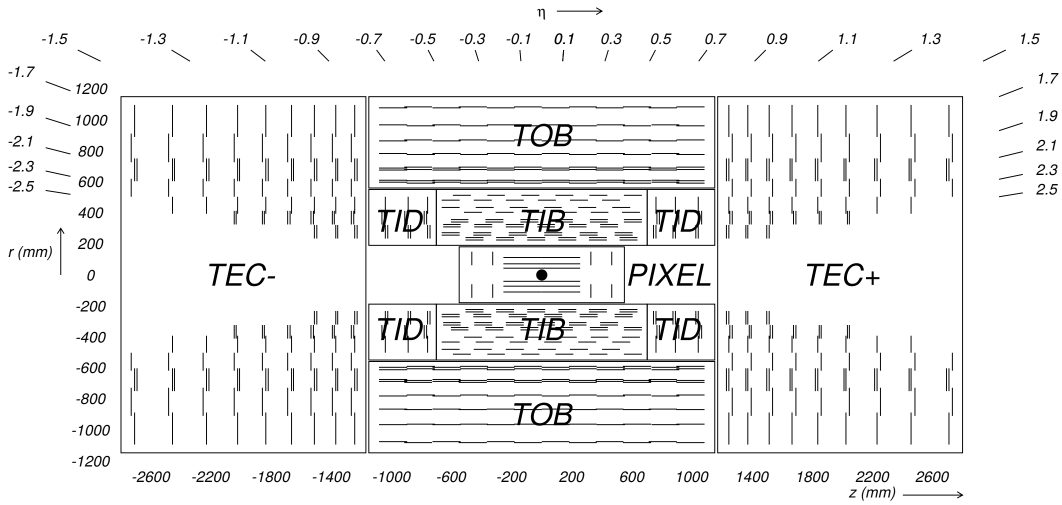

Figure 2.8: Cross sectional view of the CMS tracker in the r–z plane with strip layout shown [38].

brations to correct for radiation damage. The short radiation length ensures small transverse radii of electromagnetic showers, thereby improving position resolution and reducing overlap with concurrent showers. However, the light yield for $PbWO_4$ is relatively low. Thus, special attention to efficiency in the collection of light must be considered. The crystals are kept at 18 ± 0.05°C to control for the temperature dependence in light yield.

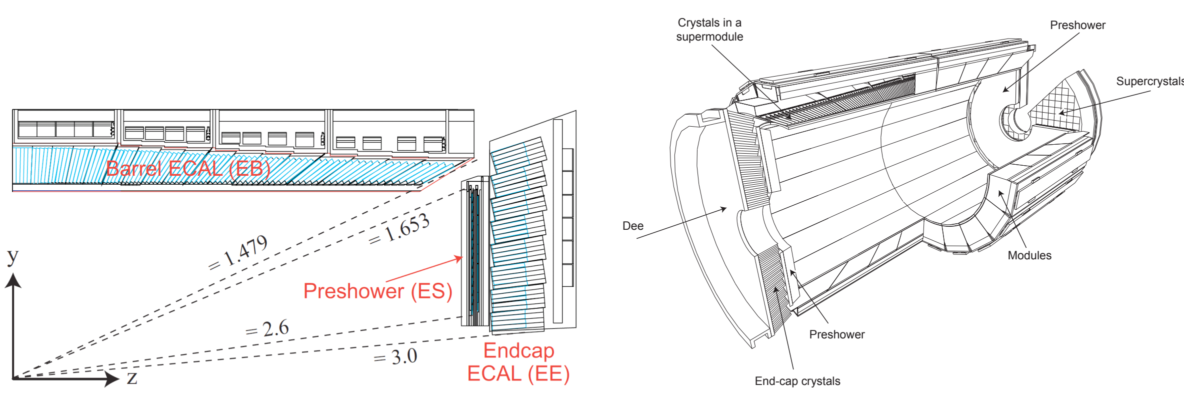

(a) (b)

Figure 2.9: Geometric view of one electromagnetic calorimeter quadrant [43] and a schematic view of the ECAL layout [38].

There are $61,200$ crystals in the EB and $7,524$ crystals in the EE. In the EB, the crystals are approximately $22 \times 22\,\mathrm{mm}^2$ on the face nearest the interaction point and $26 \times 26\,\mathrm{mm}^2$ on the opposing face. Each EB crystal is 230 mm in length. The EB covers a region of $|\eta| < 1.479$ and each crystal is approximately aligned with a value of constant η as shown in Figure 2.9a. This is to minimize shower energy loss in the regions between crystals. EE crystals are 220 mm in length with $28.62 \times 28.62\,\mathrm{mm}^2$ on the front face and $30 \times 30\,\mathrm{mm}^2$ on the opposing face. The EE covers a region of $1.479 < |\eta| < 3.0$. Light from each crystal is collected with a pair of avalanche photodiodes (APDs) and a 25 mm diameter vacuum phototriode (VPT) for the EB and EE, respectively.

The readout of the ECAL follows paths to both the L1 trigger and the CMS DAQ. Amplification, shaping, and digitization of the ECAL readout data are all done with on-detector electronics. In the L1 trigger path, the on-detector electronics sum the samples from a *trigger tower*, which are groups of 25 crystals. The sum is then sent to a Trigger Concentrator Card (TCC), which computes a trigger primitive of the total transverse energy of the energy deposited and the lateral profile of the electromagentic shower. The trigger primitive is then sent to the L1 trigger. The data sent to the CMS DAQ first go through a Data Concentrator Card (DCC), where data are reduced from around 2 MB per event to around 100 kB.

2.3.4.1 Preshower

The ES is a two-layer sampling calorimeter consisting of two layers of lead radiators and two planes of silicon strip sensors. The ES is 20 cm thick and is located between the EE and the TEC. The lead radiator initiates electromagetic showers before the showers are sampled by the strips. The first lead radiator is two radiation lengths in thickness, while the second radiator has a thickness of one radiation length. The strips are orthogonal to one another, each with a thickness of 320 μm.

A custom front-end ASIC, known as the PACE3, provides amplification, shaping, and sampling of the readout data. Three consecutive samples, time centered around the peak signal, are sent to an ES DCC. The ES DCC then zero suppresses the data before being sent to the CMS

DAQ system.

2.3.5 Hadronic Calorimeter

Like the ECAL, the hadronic calorimeter has barrel (HB) and endcap (HE) subsystems [38, 44]. Constraints on the available space between the ECAL and the solenoid lead to the necessity of an additional calorimeter system beyond the solenoid in the outer barrel (HO). The HB and HO roughly cover $|\eta| < 1.3$, while the HE coverage includes $1.3 < |\eta| < 3.0$. Finally, in the very forward region of the detector sits the forward calorimeter (HF). The HF extends calorimetery coverage to the range $3.0 < |\eta| < 5.2$ and is important for studies involving missing energy signatures, like the analysis described in this thesis. A view of one quadrant of the CMS detector with all four HCAL subsystems labeled is given in Figure 2.10.

The HCAL detects ionizing radiation via scintillating material. Hybrid photodiodes (HPDs) and PMTs collect measured light created in the detector subsystems. The analog signals are digitized with non-linear charge-integrating analog-to-digital converters (ADCs). The HCAL Trigger/Read-out (HTR) boards receive the digital signals via optical links. Trigger primitives are calculated from the HTRs and are sent to the L1 trigger. Triggered event data and trigger primitives are sent to HCAL DCCs followed by the CMS DAQ.

2.3.5.1 Barrel Calorimeter

The HB is a sampling calorimeter with 16 steel and brass absorber layers and 17 active scintillator layers. The absorber layers nearest and farthest from the interaction point are steel plates with a thickness of 40 mm and 75 mm, respectively. The remaining absorber layers are brass plates, eight of which have a thickness of 50.5 mm; the other six have a thickness of 56.5 mm. The first active layer, made of 9-mm-thick Bicron BC408, sits between the ECAL and the nearside steel layer of the HCAL [45]. The last active layer is made of 9-mm-thick Kuraray SCSN81, and it sits between the farthest steel plate and the magnetic solenoid [46]. The remaining active layers are also made of Kuraray SCSN81 but are 3.7 mm in thickness. These scintillators are interlaced with

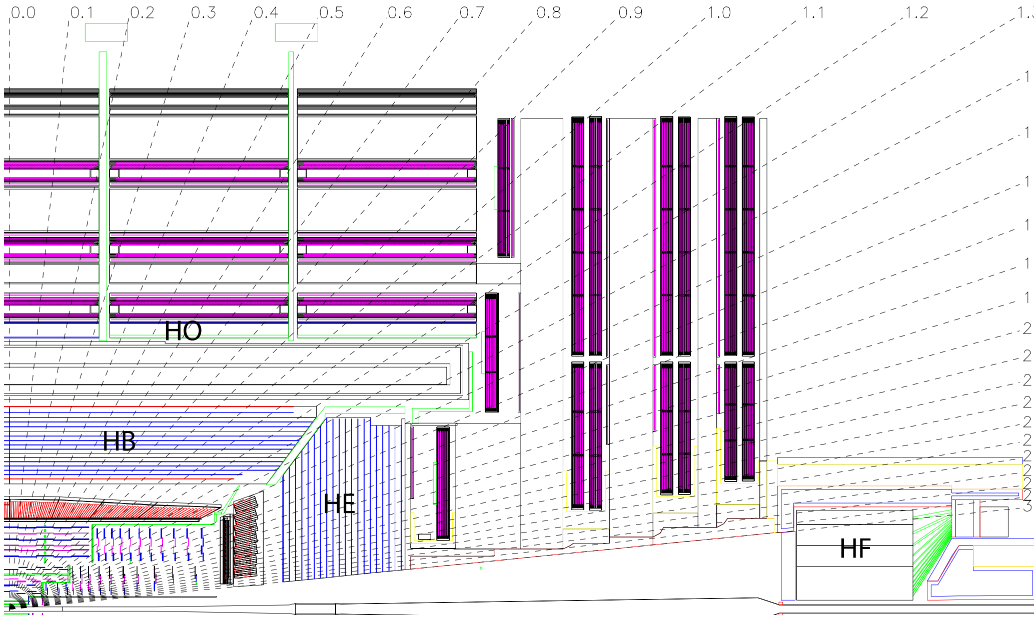

Figure 2.10: One quadrant of the CMS detector with the HB, HO, HE, and HF of the hadronic calorimeter labeled with the η coverage shown [38].

the absorber layers. The width in both η and ϕ of the HB scintillator segments is 0.087. Light from individual segments are collected with wavelength-shifting fibers spliced to clear fibers before being sent to an HPD.

2.3.5.2 Endcap Calorimeter

Similar to the HB, the HE contains 18 brass absorber layers. Each absorber layer in the HE is 79 mm thick. Likewise, the first scintillating layer in the HE is 9-mm-thick Bicron BC408. The following 17 active layers consist of 3.7-mm-thick Kuraray SCSN81. For $|\eta| < 1.6$, the segment width in both η and ϕ is 0.087 again, while the segment width for $|\eta| > 1.6$ is 0.17. The readout system for the HE is schematically the same as the HB.

2.3.5.3 Outer Calorimeter

The purpose of the HO is to sample hadronic showers that extend beyond the outermost layer of the HB. It consists of two layers of 10-mm-thick Bicron BC408 straddling the innermost layer of the iron yoke. The outermost HO layer does not extend beyond the central barrel wheel. Segmentation of the HO roughly corresponds to the HB, and HPDs collect the HO scintillation light.

2.3.5.4 Forward Calorimeter

The HF is exposed to large doses of highly energetic particles in the very forward region of the detector. Therefore, the active region in the HF must be radiation hard. This makes quartz fibers with fused-silica cores and polymer hard-cladding an appropriate choice for forward calorimetery. The individual fibers are 600 μm in diameter. The passive material of the HF is steel, and the fibers collect Cherenkov light produced from showers. Photons and electrons can be distinguished from hadrons by the depth of the shower, the latter of which deposit energy more uniformly. The width of the fiber bundles is approximately 0.175 in both η and ϕ. Fiber readout is accomplished with conventional PMTs.

2.3.6 Muon System

The muon is around 200 times more massive than the electron and, therefore, does not radiate enough energy to induce showers required for calorimetry in CMS. Instead, a dedicated muon tracking system is used to provide identification and additional momentum information. The CMS muon system consists of three subdetectors installed in the gaps throughout the iron yoke [38, 47]. Each of these subdetectors operate on the principle of gas ionization. In the barrel region of the muon system is the Drift Tube (DT) detector, and the Cathode Strip Chambers sit in the endcap. The third subdetector, the Resistive Plate Chamber (RPC), covers both barrel and endcap muons. These three subdetectors of the muon system are shown in Figure 2.11. Apart from punch through of hadronic showers and beam halo particles, only muons are left to interact with these subdetectors.

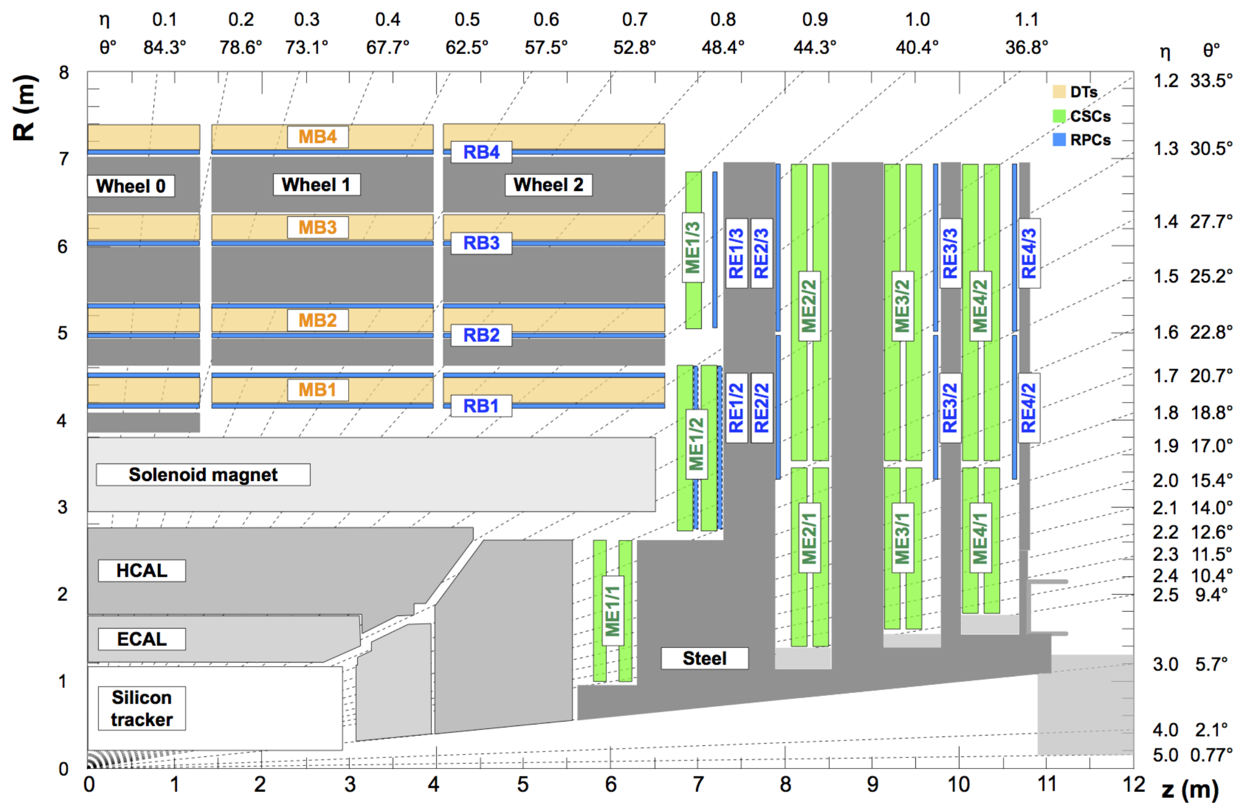

Figure 2.11: A view of one quadrant of the CMS detector showing the complete muon system [47].

2.3.6.1 Drift Tubes

The DT detector covers $|\eta| < 1.2$ and is made up of drift cells, each with dimensions $13 \times 42\,\mathrm{mm}^2$. A cross sectional view of a drift cell is depicted in Figure 2.12. These dimensions limit the occupancy of a given cell and give rise to a maximum drift path of 21 mm and a maximum drift time of 380 ns. The field is shaped by a +3.6 kV anode wire, two +1.8 kV electrode strips, and two −1.2 kV cathodes. The 1 atm gaseous mixture contains 85% Ar and 15% CO_2.

We stagger four layers of drift cells to form a super layer (SL). Two or three SLs comprise a chamber, and each barrel wheel contains four rings of chambers. In each ring there are two SLs with anode wire parallel to z, allowing measurements in r–ϕ. The inner three rings have one orthogonal

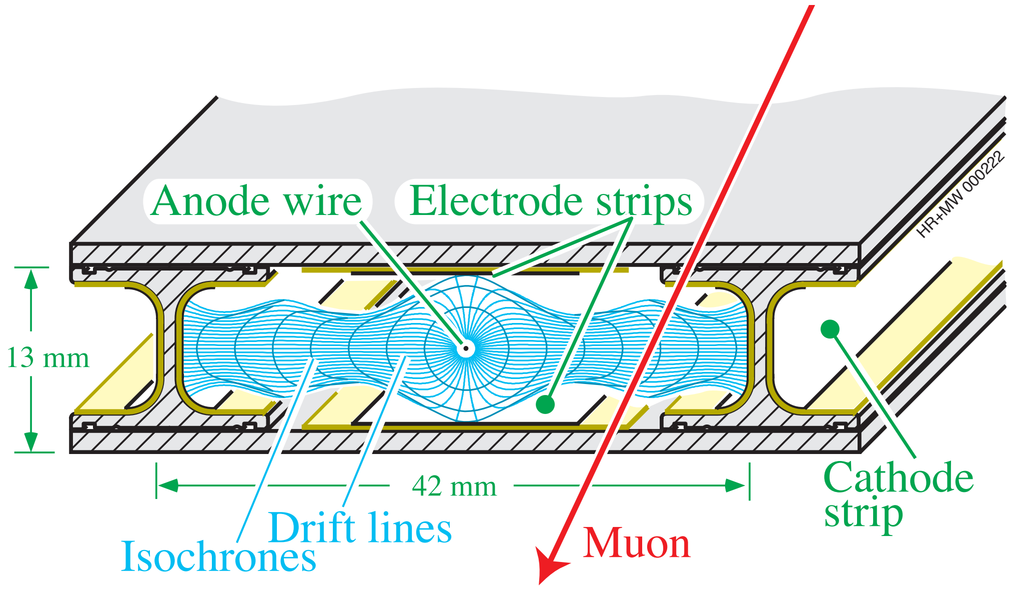

Figure 2.12: Cross sectional view of a drift tube cell [47].

SL that gives measurements in z.

Inside each chamber are front end electronics that shape and amplify the signals and split them to a trigger path and a path to the CMS DAQ. Preliminary tracking is performed in the trigger path, and the best two tracks are selected for the L1 trigger. Time digitization is performed in the path to the CMS DAQ. A second set of electronics merges signals from the entire wheel before being sent to the L1 trigger and CMS DAQ.

2.3.6.2 Cathode Strip Chambers

The CSC detector module is designed to be fast, highly segmented, and insensitive to magnetic field non-uniformity. These properties are needed in the endcap region of the detector where we naturally have a non-uniform magnetic field and a high radiation flux. The CSC modules are multi-wire proportional counters with alternating layers of cathode strips and anode wires used for readout. Each module includes six layers of cathode strips and six layers of anode wires. A diagram of the CSC module is shown in Figure 2.13a. The gaseous composition within the chamber is 40% Ar, 50% CO_2, and 10% CF_4. The CSC coverage includes $0.9 < |\eta| < 2.4$.

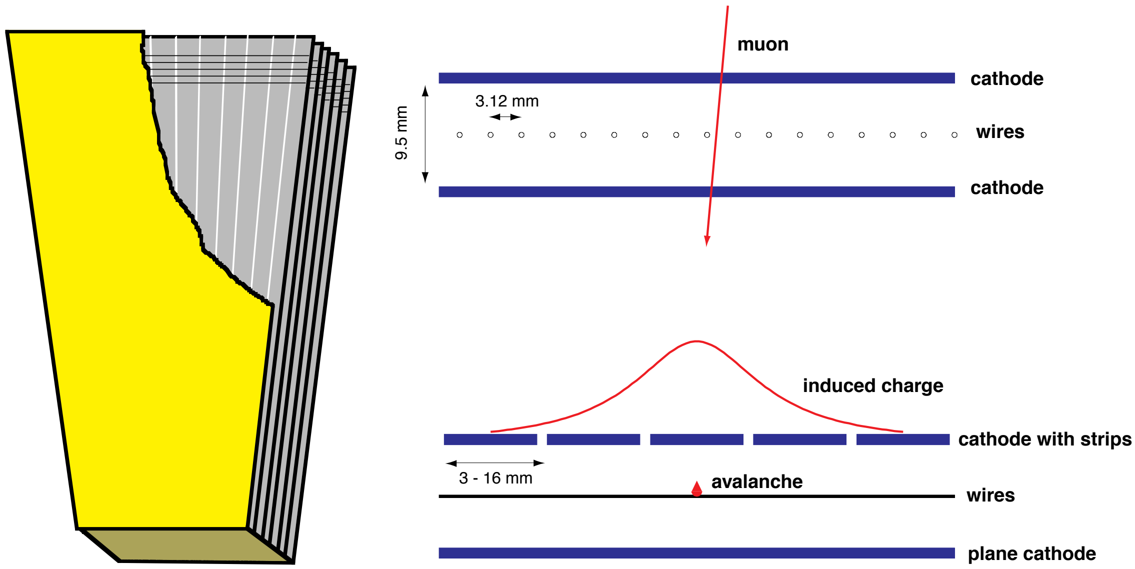

(a) (b)

Figure 2.13: A cut-away diagram of a CSC module (a) and schematic of the CSC electronics with charge projection (b) [47].

The CSCs are oriented such that the wires run radially outward, providing a measurement of ϕ and z. We can achieve good precision through avalanche induced charge interpolation depicted in Figure 2.13b. We can also use the anode wires to obtain a coarse measurement in r. The four CSC stations are shown in Figure 2.11, including the extended fourth station which was installed during an upgrade before 13 TeV collisions.

Signals from cathode strips and anode wires are amplified and shaped. The requirement of hits in at least four layers of the CSC module must be met before trigger primitives are built. Trigger primitives combine cathode strip and anode wire signals and are fed into the L1 trigger. Depending on the trigger decision, hits are then sent to the CMS DAQ.

2.3.6.3 Resistive Plate Chambers

The RPC detector provides supporting trigger information for the muon system. Its design allows for excellent time resolution so that muons can be associated with an identified bunch crossing. The RPC includes four stations, each with six layers of chambers, in the barrel region and four stations, each with three layers, in the endcap region. The fourth endcap station was added during an upgrade before 13 TeV data taking. Gas in the chambers consists of 95.2% Freon, 4.5% isobutane, and 0.3% hexafluoride.

2.3.7 Trigger

In general, the collision rate delivered by the LHC is high (up to 40 MHz), which we must reduce to around 1 kHz. To achieve this large rate reduction while keeping interesting events with high efficiency, CMS uses a two-level trigger system to quickly make decisions using raw information from subdetectors [48, 49]. The L1 trigger is the first-level trigger and is implemented in hardware electronics built into subdetector systems. The L1 trigger reduces the rate to about 100 kHz. The second-level trigger is called the High-Level Trigger (HLT) and is software based with the full set of data from all subdetectors. A more thorough description of the CMS trigger system is given in Reference [50]. Significant upgrades to the trigger system were implemented before the start of 13 TeV collisions [51, 52].

Calorimeter and muon detectors contribute to the L1 trigger. Hardware based algorithms make decisions on local subsystems within a subdetector, e.g. local DT trigger, then on regional subdetectors, e.g. global muon detector, then globally which includes all muon and calorimeter L1 trigger information. In the L1 calorimeter trigger, primitives combine to form estimates of energy sums, jet multiplicity, and energy imbalance. The muon part of the L1 trigger generates trigger primitives from DT, CSC, and RPC detectors. From these primitives, L1 tracks are built, and the four best muon candidate tracks are sent to the global L1 trigger. Each L1 trigger decision is made in less than a few μs. A computing farm with approximately 10,000 processors runs the software used to make HLT decisions. Several software based HLT decision paths, called HLT triggers or just triggers, are developed with specific final state topologies in mind. These triggers use physics objects available from the full set of subdetector data. Event processing time is restricted to $\mathcal{O}(100)$ ms.

2.3.8 Data Acquisition

Events that pass the L1 trigger decision are further processed by the CMS DAQ [38]. The DAQ receives event fragments from the CMS subdetectors each with an average size of 2 kB. Event fragments are assembled to form 72 super-fragments. A complete event is formed from assembled super-fragments. Each event at CMS is around 1-2 MB in size. Events that pass an HLT decision are processed and stored at the CERN computing center. Final reconstruction is accomplished and data are distributed to CMS institutions.

Chapter 3

Data and Simulation

The nature of the strong force makes it difficult to simulate large datasets of proton-proton collisions. We therefore rely heavily on data control samples to test our understanding of the products of these collisions. At minimum, however, simulation is essential support in two experimental challenges: a guide for designing our analyses and for interpreting the observed data in the context of a signal model. In Section 3.1 we discuss the simulation used for these purposes, and in Section 3.2 we describe the data samples used in this analysis.

3.1 Simulation

Monte Carlo (MC) methods are used to generate both simulated SM and SUSY samples. For both MC samples, we use the MadGraph [53] or powheg [54] event generators to simulate the hard interaction, pythia [55] for parton shower hadronization, and the geant [56] package to model the detector response. Some ISR partons in the event can be generated in the MadGraph or powheg calculation at a computational cost. All additional partons in the event are generated using the pythia package, and a matching scheme is utilized to ensure proper merging without double counting [57].

Samples are generated with an average pileup distribution of 20 interactions per bunch crossing and a bunch spacing interval of 25 ns. For SM samples, the number of pp interactions per bunch is reweighted so that the pileup matches the observed distribution in data. We do not apply pileup reweighting to signal MC since the effect on the signal efficiency is small. The NNPDF3.0

PDFs are used for all generated MC samples [58]. As described in Section 4.10.1, scale factors are applied to all MC samples to account for mismodeling of the observed heavy flavor content of the jets. We also improve the description of ISR jets for signal and SM $\mathrm{t\bar{t}}$ samples by comparing MadGraph to data in dileptonic events with two jets identified as coming from a b–quark. The implication then is that all remaining jets in the event are ISR jets.

3.1.1 Standard Model Simulation

Standard model simulations are used for roughly understanding our background composition and for validating our data-driven background estimation techniques. The production of $\mathrm{t\bar{t}}$, Z, W, γ, and QCD processes are generated at leading order (LO), that is, matrix elements are computed at tree level only. The $\mathrm{t\bar{t}}$, Z, W, γ, and QCD samples are all generated in bins of $\mathrm{H_T}$ which are given in Tables 3.1 and 3.2. Here, $\mathrm{H_T}$ is defined as the scalar sum of parton p_T. In addition to $\mathrm{H_T}$ binned samples, we also use inclusive, semileptonic, and fully leptonic $\mathrm{t\bar{t}}$ samples. Tables 3.1 and 3.2 give the sample production cross section, either as computed by the respective generators or by scaling the production cross section by a phenomenological ratio, called a k-factor, which is derived from a sample generated at higher order. For the $\mathrm{t\bar{t}}$ and W processes, k-factors are computed to scale the production cross sections to next-to-leading order (NLO), which include one loop matrix element contributions. The $\mathrm{t\bar{t}}$ sample configurations include up to three additional matrix element partons, while the Z, W, γ, and QCD samples include up to four additional partons.

The rare SM background MC samples are given in Table 3.3. These samples are all generated at NLO and include di- and tri-boson production, single-top production, $\mathrm{t\bar{t}t\bar{t}}$, and $\mathrm{t\bar{t}V}$, where V indicates W, Z, or, γ. Except for the dileptonic decay of WW production, which is generated with powheg [59], all of the rare backgrounds are MadGraph samples. The NNLO two loop matrix element level accuracy k-factors are computed for all rare backgrounds except for single-top.

Table 3.1: Standard model simulated samples used in the analysis. Asterisk indicates matrix element calculation at LO accuracy with k-factor at NLO accuracy.. The sample cross section, σ, is given in pb and an equivalent sample integrated luminosity, $\int \mathcal{L}\,dt$, given in fb^{-1}, takes into account σ and the number of generated events.

Sample	Generator	Generator Selection	σ [pb]	$\int \mathcal{L}\,dt$ [fb^{-1}]
$\mathrm{pp} \to \mathrm{t\bar{t}}$	MadGraph (NLO*)	–	831.76	12.34
$\mathrm{pp} \to \mathrm{t\bar{t}}$	MadGraph (NLO*)	$\mathrm{W}^+ \to \ell^+\overline{\nu}_\ell$	182.72	283.90
$\mathrm{pp} \to \mathrm{t\bar{t}}$	MadGraph (NLO*)	$\mathrm{W}^- \to \ell^-\nu_\ell$	182.72	326.48
$\mathrm{pp} \to \mathrm{t\bar{t}}$	MadGraph (NLO*)	$\mathrm{W}^+ \to \ell^+\overline{\nu}_\ell$, $\mathrm{W}^- \to \ell^-\nu_\ell$	88.34	346.25
$\mathrm{pp} \to \mathrm{t\bar{t}}$	MadGraph (NLO*)	$600 \leq \mathrm{H_T} \leq 800$	2.734	5231.81
$\mathrm{pp} \to \mathrm{t\bar{t}}$	MadGraph (NLO*)	$800 \leq \mathrm{H_T} \leq 1200$	1.121	9416.61
$\mathrm{pp} \to \mathrm{t\bar{t}}$	MadGraph (NLO*)	$1200 \leq \mathrm{H_T} \leq 2500$	0.198	14819.34
$\mathrm{pp} \to \mathrm{t\bar{t}}$	MadGraph (NLO*)	$\mathrm{H_T} \geq 2500$	0.002	221088.29
$\mathrm{pp} \to \mathrm{W} \to \ell\nu_\ell$	MadGraph (NLO*)	$100 \leq \mathrm{H_T} \leq 200$	1627.45	18.16
$\mathrm{pp} \to \mathrm{W} \to \ell\nu_\ell$	MadGraph (NLO*)	$200 \leq \mathrm{H_T} \leq 400$	435.24	45.88
$\mathrm{pp} \to \mathrm{W} \to \ell\nu_\ell$	MadGraph (NLO*)	$400 \leq \mathrm{H_T} \leq 600$	59.18	123.64
$\mathrm{pp} \to \mathrm{W} \to \ell\nu_\ell$	MadGraph (NLO*)	$600 \leq \mathrm{H_T} \leq 800$	14.58	221.32
$\mathrm{pp} \to \mathrm{W} \to \ell\nu_\ell$	MadGraph (NLO*)	$800 \leq \mathrm{H_T} \leq 1200$	6.66	1123.13
$\mathrm{pp} \to \mathrm{W} \to \ell\nu_\ell$	MadGraph (NLO*)	$1200 \leq \mathrm{H_T} \leq 2500$	1.608	153.44
$\mathrm{pp} \to \mathrm{W} \to \ell\nu_\ell$	MadGraph (NLO*)	$\mathrm{H_T} \geq 2500$	0.039	6497.28
QCD	MadGraph (LO)	$200 \leq \mathrm{H_T} \leq 300$	1735000	0.03
QCD	MadGraph (LO)	$300 \leq \mathrm{H_T} \leq 500$	366800	0.16
QCD	MadGraph (LO)	$500 \leq \mathrm{H_T} \leq 700$	29370	1.95
QCD	MadGraph (LO)	$700 \leq \mathrm{H_T} \leq 1000$	6524	6.68
QCD	MadGraph (LO)	$1000 \leq \mathrm{H_T} \leq 1500$	1064	12.62
QCD	MadGraph (LO)	$1500 \leq \mathrm{H_T} \leq 2000$	121.5	32.63
QCD	MadGraph (LO)	$\mathrm{H_T} \geq 2000$	25.42	239.30
$\mathrm{pp} \to \mathrm{Z} \to \nu\overline{\nu}$	MadGraph (LO)	$100 \leq \mathrm{H_T} \leq 200$	344.3	54.21
$\mathrm{pp} \to \mathrm{Z} \to \nu\overline{\nu}$	MadGraph (LO)	$200 \leq \mathrm{H_T} \leq 400$	95.23	209.12
$\mathrm{pp} \to \mathrm{Z} \to \nu\overline{\nu}$	MadGraph (LO)	$400 \leq \mathrm{H_T} \leq 600$	13.19	77.25
$\mathrm{pp} \to \mathrm{Z} \to \nu\overline{\nu}$	MadGraph (LO)	$600 \leq \mathrm{H_T} \leq 800$	3.221	1754.33
$\mathrm{pp} \to \mathrm{Z} \to \nu\overline{\nu}$	MadGraph (LO)	$800 \leq \mathrm{H_T} \leq 1200$	1.474	1462.80
$\mathrm{pp} \to \mathrm{Z} \to \nu\overline{\nu}$	MadGraph (LO)	$1200 \leq \mathrm{H_T} \leq 2500$	0.359	1018.45
$\mathrm{pp} \to \mathrm{Z} \to \nu\overline{\nu}$	MadGraph (LO)	$\mathrm{H_T} \geq 2500$	0.00820	49463.85

Table 3.2: Standard model samples primarily used for validation of the $Z \to \nu\overline{\nu}$ estimation procedure. The sample cross section, σ, is given in pb and an equivalent sample integrated luminosity, $\int \mathcal{L}\,dt$, given in fb^{-1}, takes into account σ and the number of generated events.

Sample	Generator	Generator Selection	σ [pb]	$\int \mathcal{L}\,dt$ [fb^{-1}]
$\mathrm{pp} \to \mathrm{Z}/\gamma^* \to \ell^+\ell^-$	MadGraph (LO)	$100 \leq \mathrm{H_T} \leq 200$	225.5	47.57
$\mathrm{pp} \to \mathrm{Z}/\gamma^* \to \ell^+\ell^-$	MadGraph (LO)	$200 \leq \mathrm{H_T} \leq 400$	62.02	155.7
$\mathrm{pp} \to \mathrm{Z}/\gamma^* \to \ell^+\ell^-$	MadGraph (LO)	$400 \leq \mathrm{H_T} \leq 600$	8.59	1170
$\mathrm{pp} \to \mathrm{Z}/\gamma^* \to \ell^+\ell^-$	MadGraph (LO)	$600 \leq \mathrm{H_T} \leq 800$	2.07	4010
$\mathrm{pp} \to \mathrm{Z}/\gamma^* \to \ell^+\ell^-$	MadGraph (LO)	$800 \leq \mathrm{H_T} \leq 1200$	0.953	2800
$\mathrm{pp} \to \mathrm{Z}/\gamma^* \to \ell^+\ell^-$	MadGraph (LO)	$1200 \leq \mathrm{H_T} \leq 2500$	0.229	2600
$\mathrm{pp} \to \mathrm{Z}/\gamma^* \to \ell^+\ell^-$	MadGraph (LO)	$\mathrm{H_T} \geq 2500$	0.00540	74100
$\mathrm{pp} \to \gamma$	MadGraph (LO)	$100 \leq \mathrm{H_T} \leq 200$	5390	2.74
$\mathrm{pp} \to \gamma$	MadGraph (LO)	$200 \leq \mathrm{H_T} \leq 400$	1168	42.44
$\mathrm{pp} \to \gamma$	MadGraph (LO)	$400 \leq \mathrm{H_T} \leq 600$	132.5	88.15
$\mathrm{pp} \to \gamma$	MadGraph (LO)	≥ 600	44.05	264.2

Table 3.3: SM diboson, triboson, $t\bar{t}V$, where V stands for vector boson, and other rare process MC samples used in the analysis. Asterisk indicates matrix element calculation at NLO accuracy with k-factor at NNLO accuracy. The sample cross section, σ, is given in pb and an equivalent sample integrated luminosity, $\int \mathcal{L}\,dt$, given in fb^{-1}, takes into account σ and the number of generated events.

Sample	Generator	Generator Selection	σ [pb]	$\int \mathcal{L}\,dt$ [fb^{-1}]
$pp \to t$	MadGraph (NLO)	s–channel	3.340	72.39
$pp \to t$	MadGraph (NLO)	t–channel	136.02	494.35
$pp \to \bar{t}$	MadGraph (NLO)	t–channel	80.95	479.44
$pp \to t$	MadGraph (NLO)	tW–channel	19.4674	586.01
$pp \to \bar{t}$	MadGraph (NLO)	tW–channel	19.4674	582.80
$pp \to t\bar{t}t\bar{t}$	MadGraph (NNLO*)	–	0.009	2013.86
$pp \to t\bar{t}Z$	MadGraph (NNLO*)	$Z \to \ell^+\ell^-$, $Z \to \nu\bar{\nu}$	0.253	795.96
$pp \to t\bar{t}Z$	MadGraph (NNLO*)	$Z \to q\bar{q}$	0.530	145.57
$pp \to t\bar{t}W$	MadGraph (NNLO*)	$W \to \ell\nu_\ell$	0.204	3517.87
$pp \to t\bar{t}W$	MadGraph (NNLO*)	$W \to q\bar{q}$	0.403	285.02
$pp \to t\bar{t}\gamma$	MadGraph (NNLO*)	–	3.697	135.42
$pp \to WW$	MadGraph (NNLO*)	$WW \to \ell\nu_\ell q\bar{q}$	50.00	25.00
$pp \to WW$	powheg (NNLO*)	$WW \to \ell\nu_\ell\ell\nu_\ell$	12.18	164.15
$pp \to WZ$	MadGraph (NNLO*)	$W \to \ell\nu_\ell$, $Z \to q\bar{q}$	10.71	440.86
$pp \to WZ$	MadGraph (NNLO*)	$W \to \ell\nu_\ell$, $Z \to \nu\bar{\nu}$	3.058	94.18
$pp \to ZZ$	MadGraph (NNLO*)	$ZZ \to \nu\bar{\nu}q\bar{q}$	4.040	1723.65
$pp \to ZZ$	MadGraph (NNLO*)	$ZZ \to \ell^+\ell^-q\bar{q}$	3.220	1199.40
$pp \to WWZ$	MadGraph (NNLO*)	–	0.165	1052.70
$pp \to WZZ$	MadGraph (NNLO*)	–	0.056	2988.21
$pp \to ZZZ$	MadGraph (NNLO*)	–	0.014	11158.63

3.1.2 Signal Simulation

We target pair production of gluinos and stops with the following three body and two body decays:

- $\widetilde{g} \rightarrow q\overline{q}\widetilde{\chi}_1^0$, $\widetilde{g} \rightarrow b\overline{b}\widetilde{\chi}_1^0$, $\widetilde{g} \rightarrow t\overline{t}\widetilde{\chi}_1^0$
- $\widetilde{t} \rightarrow t\widetilde{\chi}_1^0$

The kinematics of the model largely depend on the mass of the LSP ($\widetilde{\chi}_1^0$ here) and that of either the gluino or the squark, depending on the mediating sparticle. We therefore must generate a scan of MC samples in a two dimensional mass plane, which can be very computationally taxing. The bulk of the computational expense comes in the form of detector geometry and material budget modeling. Therefore, we develop a simplified description of the detector, called FastSim, that greatly reduces the time needed to generate a sample [60, 61, 62, 63]. To guard against biases introduced in FastSim, we generate a few benchmark points with the full detector simulation (FullSim) for comparison. We find excellent agreement between samples, but we generate a separate set of b–quark jet scale factors and a jet identification scale factor applied to FastSim only. Tables 3.4 and 3.5 show the gluino and squark mediated MC samples, respectively.

Both the FullSim and FastSim samples are generated with MadGraph at LO with up to two additional partons in the matrix element calculation. However, the production cross sections of the signal MC are determined at an accuracy of NLO plus next-to-leading-logarithm (NLL) [64, 65, 66, 67].

Table 3.4: Gluino mediated simulated signal samples used in the analysis. The sample cross section, σ, is given in pb and an equivalent sample integrated luminosity, $\int \mathcal{L}\,dt$, given in fb^{-1}, takes into account σ and the number of generated events.

Decay Mode	SMS Name	Generator	$m_{\widetilde{\mathrm{g}}}$ [GeV]	$m_{\widetilde{\chi}_1^0}$ [GeV]	σ [pb]	$\int \mathcal{L}\,dt$ [fb^{-1}]
$\widetilde{\mathrm{g}} \to \mathrm{t\bar{t}}\widetilde{\chi}_1^0$	T1tttt	FullSim	2000	100	9.81×10^{-4}	52342
$\widetilde{\mathrm{g}} \to \mathrm{t\bar{t}}\widetilde{\chi}_1^0$	T1tttt	FullSim	1200	800	8.56×10^{-2}	1715
$\widetilde{\mathrm{g}} \to \mathrm{t\bar{t}}\widetilde{\chi}_1^0$	T1tttt	FastSim	600–2300	0–1600	varies	varies
$\widetilde{\mathrm{g}} \to \mathrm{b\bar{b}}\widetilde{\chi}_1^0$	T1bbbb	FullSim	1500	100	1.42×10^{-2}	3697
$\widetilde{\mathrm{g}} \to \mathrm{b\bar{b}}\widetilde{\chi}_1^0$	T1bbbb	FullSim	1000	900	0.325	438.5
$\widetilde{\mathrm{g}} \to \mathrm{b\bar{b}}\widetilde{\chi}_1^0$	T1bbbb	FastSim	600–2300	0–1600	varies	varies
$\widetilde{\mathrm{g}} \to \mathrm{q\bar{q}}\widetilde{\chi}_1^0$	T1qqqq	FullSim	1400	100	2.53×10^{-2}	2026
$\widetilde{\mathrm{g}} \to \mathrm{q\bar{q}}\widetilde{\chi}_1^0$	T1qqqq	FullSim	1000	800	0.325	283.0
$\widetilde{\mathrm{g}} \to \mathrm{q\bar{q}}\widetilde{\chi}_1^0$	T1qqqq	FastSim	600–2300	0–1600	varies	varies

Table 3.5: Stop mediated simulated signal samples used in the analysis. The sample cross section, σ, is given in pb and an equivalent sample integrated luminosity, $\int \mathcal{L}\,dt$, given in fb^{-1}, takes into account σ and the number of generated events.

Decay Mode	SMS Name	Generator	$m_{\widetilde{\mathrm{t}}}$ [GeV]	m_{LSP} [GeV]	σ [pb]	$\int \mathcal{L}\,dt$ [fb^{-1}]
$\widetilde{\mathrm{t}} \to \mathrm{t}\widetilde{\chi}_1^0$	T2tt	FullSim	850	100	1.90×10^{-2}	12395
$\widetilde{\mathrm{t}} \to \mathrm{t}\widetilde{\chi}_1^0$	T2tt	FullSim	650	350	0.107	935
$\widetilde{\mathrm{t}} \to \mathrm{t}\widetilde{\chi}_1^0$	T2tt	FullSim	500	325	0.518	767
$\widetilde{\mathrm{t}} \to \mathrm{t}\widetilde{\chi}_1^0$	T2tt	FullSim	425	325	1.31	120
$\widetilde{\mathrm{t}} \to \mathrm{t}\widetilde{\chi}_1^0$	T2tt	FastSim	150–1200	0–650	varies	varies

3.2 Data

This search is performed on data collected in 2016 from April 22 to October 27. During this period, the LHC delivered a record setting 41.07 fb^{-1} of integrated luminosity, nearly ten times larger than the 13 TeV collision data delivered in 2015 and a little less than twice as large as the 8 TeV data delivered during the 2012 run, as shown in Figure 3.1. A subset of 37.82 fb^{-1} of data were collected while the CMS detector was fully operational. Physics runs separated by LHC maintenance or machine developments are called *run eras*. There were 7 run eras during the 2016 campaign of data collection. The run-by-run data, given in Table 3.6, are examined for data certification by the sub-detector and physics object groups to ensure sufficient data quality. Data quality checks include object and conditions consistency, detector hardware status, and validating calibration results [68, 69]. The certified data collected is measured to correspond to 35.9 fb^{-1} using the BRIL work suite [70, 71].

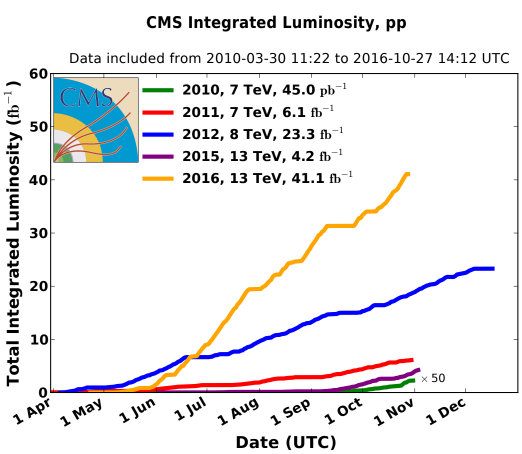

(a)

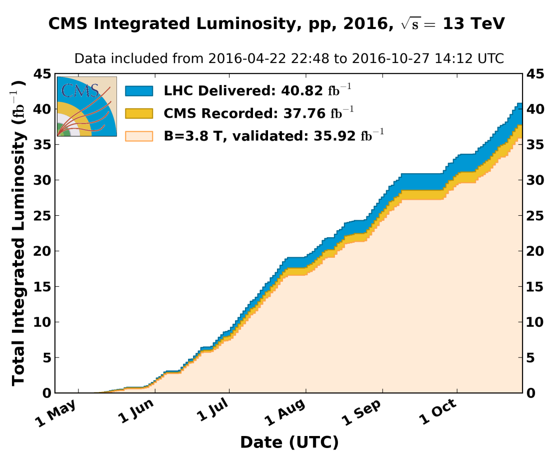

(b)

Figure 3.1: Integrated luminosity delivered vs year (a) and recorded by CMS (b) [70].

Primary datasets contain groups of data with similar event selection requirements. Information stored in primary datasets include high-level physics objects, particle tracks and associated hits, calorimetric clusters, and interaction vertices. For this analysis, we use the *MET, Single-*

Muon, SingleElectron, and *SinglePhoton* primary datasets. As described in Chapter 6, the *MET* dataset is split into disjoint control and signal samples, while the *SingleMuon, SingleElectron,* and *SinglePhoton* samples are used exclusively as control samples.

Table 3.6: The run range and integrated luminosity for data runs 2016B–2016H.

Run Era	Run Range	reconstruction	$\int \mathcal{L}\, dt$ [fb^{-1}]
2016B	273158–275376	reprocessed	5.784
2016C	275657–276283	reprocessed	2.573
2016D	276315–276811	reprocessed	4.248
2016E	276831–277420	reprocessed	4.009
2016F	277981–278808	reprocessed	3.102
2016G	278820–280385	reprocessed	7.540
2016H	281613–284044	prompt	8.606
Total	273158–284044	–	35.862

Chapter 4

Event Reconstruction

We understand the underlying event from the collected data by translating the hits in the subdetectors into well defined physics objects. This involves identifying tracks and the associated interaction vertices, described in Sections 4.1 and 4.3. Stable particle identification is accomplished with the CMS Particle-Flow (PF) algorithm, described in Section 4.5. The remainder of the chapter is devoted to describing the reconstruction of specific physics objects, such as muons, electrons, photons, jets, and missing transverse energy.

4.1 Track Reconstruction

The CMS tracker is designed to trace charged particle trajectories and use this information to obtain particle charge and momentum. Pileup results in roughly 1,000 charged particles in the inner tracker for every bunch crossing [39]. High track density is a challenging problem, particularly when experimental demands place strict requirements on track efficiency, fake rate, and momentum resolution.

Before we can algorithmically isolate individual tracks, pixel and strip hits are clustered into *local hits*. Positions of local hits are determined through a clustering algorithm. The Combinatorial Track Finder (CTF) algorithm runs on local hits and reconstructs tracks in four steps [72]:

(1) Seed generation: Track *seeds* are short track candidates using 2-3 local hits that define initial trajectory parameters and associated uncertainties of candidate tracks. Helical trajectories are assumed and the parameters needed to define the track trajectory are derived

from the local hits of the seed and a constraint of track origin near the region in which the proton bunches collide, called the *beamspot*. Very loose requirements on the track p_T and impact parameter with respect to the interaction region reduce the track seed multiplicity to a manageable value.

(2) Track finding: After the event seeds are generated, track candidates are filtered using the Kalman method [73]. During this step, tracks are found by extrapolating the track trajectory of each track seed and adding hits from successive layers that are compatible with the track parameters. While helical parameters are retained, additional parameters are considered to account for particle interaction with detector material. All local hits within three standard deviations of the extrapolated track are considered. Tracks are dropped if quality criteria are not met or if duplicate tracks are found.

(3) Track fitting: Once the relevant tracks have been reconstructed, the track parameters are refit to avoid seed bias. This involves the removal of the requirements on track p_T and impact parameter applied during the seed generation step. The Kalman method is then applied outward starting with the innermost local hits. A set of fitted tracks from iterating the Kalman method over all local hits in the track candidate are then averaged, resulting in a smoothed set of track parameters.

(4) Track selection: Finally, quality cuts are applied to smoothed tracks to reduce the track fake rate. These cuts include criteria such as the number of hits, number of layers with hits, χ^2 per degree of freedom, and impact parameter significance.

We repeat the CFT algorithm a total of six times. In the subsequent iterations, hits from reconstructed tracks are removed. At each iteration, seed generation criteria on p_T and impact parameter are loosened, but track finding criteria are made more stringent. After the sixth iteration, a full set of tracks is defined for the event.

4.2 Standalone Muon Tracks

Muon tracks reconstructed from hits in the muon system only are called *standalone muon* tracks. These tracks are also reconstructed using the Kalman filter method [74]. Seeds for the standalone muon track reconstruction are selected from track segments in the innermost muon chambers. The filter is run outward and then inward combining track segments from the DT and hits from the CSC and RPC detectors. Selecting only hits with compatible χ^2 rejects bad hits resulting from showers, delta rays, and pair production.

4.3 Primary Vertices

We call a vertex *primary* if it coincides with a point at which beam protons collide, including the interactions of interest as well as pileup. We find primary vertices by mapping all vertices from tracks compatible with the beamspot, called *prompt* tracks. The criterion of small transverse impact parameter significance is used to determine if a track is prompt. Additionally, we require sufficient track hit multiplicity in both the pixel and strip detectors and require the track to be high quality.

After selecting prompt tracks for primary vertex reconstruction, we cluster tracks into groups of common primary vertices. The basis for clustering is determined by comparison of the track z-coordinate at the point of closest approach to the beamspot. The *deterministic annealing* (DA) algorithm for track clustering is used to determine the tracks associated to a given vertex [75]. The final step in the primary vertex reconstruction is to fit the tracks for a given PV with the Adaptive Vertex Fitter (AVF) [76]. In the AVF, PV parameters, such as position, are determined with an iterative Kalman filter. At each iteration, the PV parameters get updated and more compatible tracks enter the parameter determination with higher weight. The primary vertex resolution for events we consider in this search is around 10 μm.

4.4 Calorimeter Clusters

Cells in the calorimeter system are clustered in the EB, EE, HB, HE, and first and second layer of the ES, while each cell in the HF is considered a cluster. The three steps in clustering are as follows:

- **Cluster seeds** are local cell maxima required to be above a threshold dependent on the calorimeter system.
- **Topological clusters** result from adding cells adjacent to the cluster seed with energy above an electronic noise threshold. A topological cluster may contain more than one seed.
- **Cluster formation** is accomplished by dividing the energy from each cell across the cluster seeds for a given topological cluster. This is accomplished iteratively whereby the cluster location is recalculated at each iteration, and the process stops once the cluster location change is less than a small fraction of the position resolution.

4.5 Particle Flow

We identify individual particles, such as photons, charged hadrons, neutral hadrons, electrons, or muons, with the PF algorithm using information from all subdetectors in the CMS experiment [77, 78]. It is from these particles that we build compound objects, such as jets and missing transverse energy. Tracks, standalone muon tracks, and calorimeter clusters serve as input *elements* in particle flow.

Elements are paired to form *links*, each with an associated parameter that represents the quality of the link. For instance, a track in the inner tracker may be linked to a standalone muon track. The list of possible links in the particle flow algorithm are given in Figure 4.1.

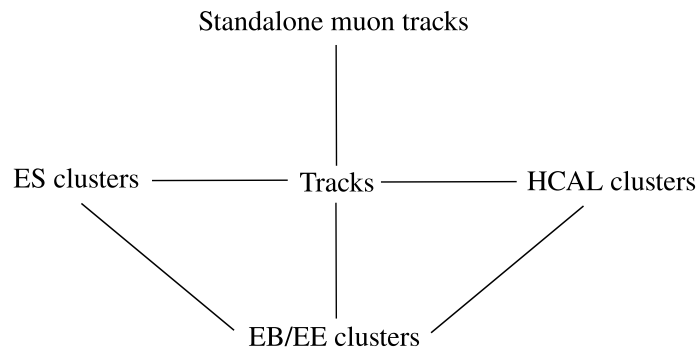

Figure 4.1: Illustration of links formed in the PF algorithm.

In linking tracks with a calorimeter cluster, a track is extrapolated into the calorimeter systems. A cluster is linked to a track if the extrapolated track is within the cluster envelope, which can be enlarged by up to the size of a cell to account for cluster size uncertainty. Links between two calorimeter clusters result when the more granular calorimeter is within the less granular cluster envelope in the η-ϕ plane. Again, uncertainty in the cluster envelope size is considered when cluster overlap is determined. A standalone muon track linked with an inner tracker track becomes a *global muon*. The individual track χ^2 are compared to determine the quality of the link.

Finally, groups of linked elements form *blocks*, which serve as the foundation for which quasi-stable particles are reconstructed and identified by the PF algorithm. Typically, blocks consist of only one, two, or three elements. As a naming convention, particles identified by the PF algorithm receive the PF- prefix, e.g., PF muon.

4.6 Muon Reconstruction

A global muon becomes a PF muon if the global muon is within three standard deviations of both tracks within the link. The tracks in the link are then removed from the event to prevent further processing of the PF muon hits. In addition to the muon PF status, important parameters related to muon quality are considered for offline muon reconstruction. These include *position match*, *kink*, and *segment compatibility*. Position match is a χ^2 comparison between the tracker muon and the standalone muon. Kink finder algorithms reject non-prompt muons from pion and kaon decays. Finally, segment compatibility is a measure of how well individual segments within the object are compatible with the muon hypothesis.

4.7 Electron Reconstruction

Electrons[1] produce tracks in the inner tracker and clusters in the ECAL. Therefore, PF electrons consist of a track and an ECAL *supercluster*, which is a group of ECAL cells. A Gaussian sum filter (GSF) takes into account energy loss due to bremsstrahlung photon emission to reconstruct the electron trajectory [79]. When the GSF fit recognizes a bremsstrahlung photon, the ECAL cluster from the photon is linked to the PF electron and is included in the estimate of the electron momentum. All PF electron hits are removed before the PF algorithm proceeds.

Important parameters for electron reconstruction include $\sigma_{i\eta i\eta}$ and H/E. The shower shape width parameter, $\sigma_{i\eta i\eta}$, rejects fake electrons that yield wider shower shapes than electrons. The ratio H/E is also used to reject fake electrons and is a comparison of the ECAL deposit from a candidate electron with a nearby HCAL energy deposit.

4.8 Photon Reconstruction

Photons do not leave hits the inner tracker but do result in ECAL clusters. Therefore, photon reconstruction is based on the signal from the ECAL superclusters. Clusters in the ECAL that are not linked to a track are identified as PF photons. This is often how isolated photons are identified. Moreover, photons within jets often share ECAL superclusters with other electromagnetic energy in the event. Therefore, when the ECAL supercluster energy exceeds the linked track momentum beyond the expected calorimeter energy resolution, a PF photon is identified with the remaining supercluster energy. Photons interacting with the material of the tracker can result in conversion to e^+e^- pairs. We can recover these photons by reconstructing electron pairs that are consistent with a photon conversion candidate.

[1] Here we refer to electrons and positrons collectively as *electrons*.

We reject fake photons by considering $\sigma_{i\eta i\eta}$ and H/E [80]. Overlapping photons from a boosted π^0 decay yields a wide shower shape relative to a single prompt photon. Fake photons from neutral hadrons can be rejected by ensuring nearby HCAL signals are small relative to the ECAL energy deposits. Isolation is an observable that measures the degree of separation relative to nearby particles. We reject charged particle and hadronic fakes by imposing isolation requirements on the reconstructed photon.

4.9 Hadron Reconstruction

Hadrons can be either neutral or charged. Charged hadron signatures include tracks in the tracker, a small fraction of its energy deposited in the ECAL, and the bulk of its energy deposited in the HCAL. Neutral hadrons are almost exclusively detected in the HCAL. A charged track not identified as an electron or muon becomes a candidate charged hadron. Energy deposits in the HCAL associated with the unidentified charged track are also used in charged hadron identification.

4.10 Jet Reconstruction

Jets are formed from PF candidates with the anti-k_T algorithm [81]. The most widely adopted jet definition in CMS uses a distance parameter of 0.4, which roughly corresponds to a radius in the η-ϕ plane. We denote such jets as AK4 jets. To increase reconstruction speed, we use the FastJet package, described in Reference [82]. As described in Section 2.1.2, jets are the product of quarks and gluons creating showers of particles. The goal of jet reconstruction is to extract the initial parton four-momentum. All PF candidates are considered for jet clustering. Charged hadron subtraction reduces the effects of pileup by removing charged hadrons not originating from the vertex of interest from the list of PF candidates used in jet formation [83].

The anti-k_T algorithm proceeds in an iterative process. At each iteration, two distance parameters are calculated [84]. Every particle or existing cluster is indexed with i, and d_{iB}, representing the distance from the beam, is computed. Also computed during each iteration is the distance parameter d_{ij} for each pair of entities i and j. The distance parameters are defined as follows:

$$d_{iB} = 1/p_{\mathrm{T}i}^2, \tag{4.1}$$

$$d_{ij} = \mathrm{Min}(1/p_{\mathrm{T}i}^2, 1/p_{\mathrm{T}j}^2) \cdot \frac{(y_i - y_j)^2 + (\phi_i - \phi_j)^2}{R^2}, \tag{4.2}$$

where y_i is the rapidity of entity i and R is 0.4 for AK4 jets. If $d_{iB} > d_{ij}$, then entity i is a jet and is removed from subsequent iterations. Otherwise, entities i and j with smallest d_{ij} are clustered and the algorithm proceeds to the next iteration. This process continues until all particles have been clustered. The measured *raw* jet momenta are corrected for effects from secondary interactions of other partons in the proton, pileup, noise, and jet size [85].

4.10.1 Bottom-Quark Jets

While parton flavor identification in jets can be difficult, jets originating from b-quark hadronization can be discriminated from light-flavored quark jets with reasonable efficiency. The reason for this is b-hadrons have a relatively long lifetime compared to light-flavored hadrons [6, 86]. This results in a displaced secondary vertex and tracks with a large impact parameter from the decay products of the b-hadron.

Several algorithms for b-jet identification, called *b-taggers*, are supported by the CMS experiment. Some b-taggers use a single observable, while others use a combination of several observables [87, 88]. We adopt the CSVv2 algorithm to discriminate b-jets from light-flavor jets as shown in Figure 4.2. The analysis specific requirements on b-tagged jets are described in Section 5.1.1.

The CSVv2 algorithm is a multivariate discriminant that uses tracks in a given jet as inputs. In order for a jet to be considered, requirements on input tracks are imposed. Tracks are selected based on track p_{T}, angular separation from the jet direction, number of hits, number of hits in the pixel detector, and χ^2 per degree of freedom of the track fit. We reduce the effects of pileup by requiring that the distance of closest approach of the track be within 700 μm of the jet axis and 5 cm of the primary interaction vertex. Additionally, any combination of two tracks with invariant

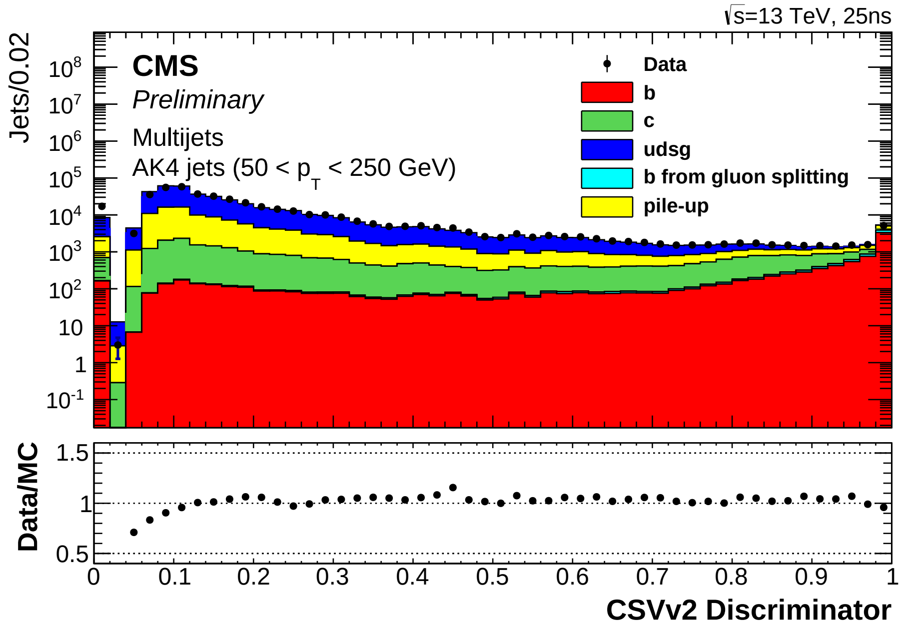

Figure 4.2: Output comparison of data and simulation from the CSVv2 b-tag discriminator [88].

mass within 30 MeV of the K_S^0 meson[2] are rejected. If at least two tracks satisfy these requirements, the CSVv2 algorithm is terminated and a negative value is assigned to the jet.

We use the Inclusive Vertex Finder (IVF) to reconstruct interaction vertices for b-tagging [89]. The IVF uses all tracks in the event instead of only the tracks associated with the jet. The CSVv2 algorithm proceeds by training three separate multilayer perceptron (MLP) artificial neural networks, each with one hidden layer using 12 input observables given as follows:

- the number of secondary vertices;
- the distance between the secondary vertex and the jet axis;
- the ratio of the transverse momentum of the summed tracks and the jet;
- the track decay length;
- the angle between the track and the jet;

[2] The K_S^0 meson lifetime ($\tau \approx 9 \times 10^{-11}$) is near enough to that of b-hadrons that the more numerous K_S^0 can fake b-jets.

- the flight distance significance;
- the vertex mass;
- the number of tracks associated with a vertex;
- the number of tracks in the jet;
- the transverse impact parameter significance of the first track (ordered by decreasing p_{T}); and
- the three-dimensional impact parameter significance of each track relative to the jet axis.

Jets fall into three categories for training the separate MLPs related to the interaction vertices in the event. These categories are given below.

- In the first category, at least one secondary vertex is reconstructed. When more than one secondary vertex is reconstructed, the secondary vertices are ranked in order of increasing uncertainty on the flight distance. In this case, most of the inputs to the MLP are from the tracks associated with the secondary vertex with the smallest uncertainty.
- In the second category, the *pseudo-vertex* category, at least two tracks have signed impact parameter significance greater than 2. The invariant mass of any combination of tracks cannot be within 50 MeV of the K^0_S mass.
- The third category is used if the jet satisfies neither of the above criteria. In which case, only the information on track displacement is used to train the MLP.

In general, the efficiency for tagging a b-quark jet is not the same in simulation as it is in data as shown in Figure 4.3a. To correct for this difference, we compute event-by-event weights that use generator level parton flavor, p_{T}, and η to determine the probability that a given event will be above a given CSVv2 threshold. To determine these weights, we use data events from multijet events, $\mathrm{Z} \to \mathrm{b\bar{b}}$, and $\mathrm{t\bar{t}}$ events, and we compare these events to simulation [88]. The result of the correction is shown in Figure 4.3b. We correct both signal and SM simulations for these differences.

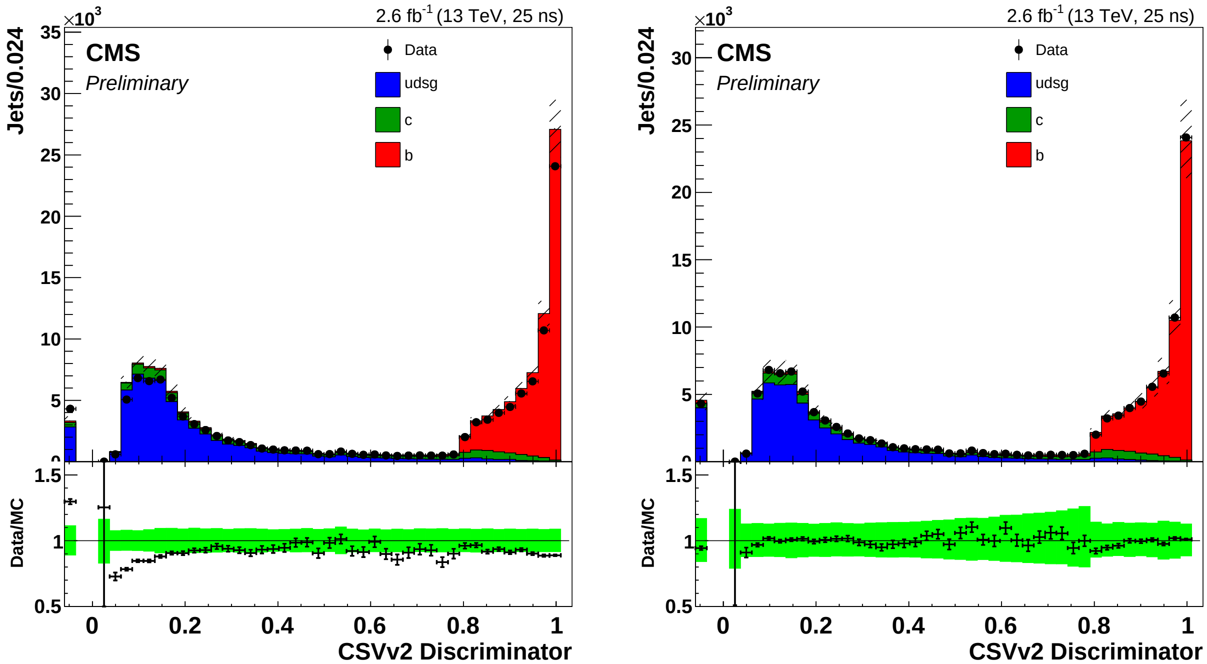

(a) (b)

Figure 4.3: Data vs simulation in the CSVv2 discriminator output before (a) and after (b) b-tag scale factor corrections [88].

4.11 Missing Transverse Energy

The net transverse momentum of particles resulting from interactions from pp LHC collisions is approximately zero. This allows us to infer the sum total of missing transverse momentum from undetected particles, called missing transverse energy or $\vec{p}_{\mathrm{T}}^{\mathrm{miss}}$, by measuring the sum total transverse momentum of visible particles in the event. In the situation where the transverse momenta of the detected particles are measured exactly, $\vec{p}_{\mathrm{T}}^{\mathrm{miss}}$ is simply the negative vector sum of the detected particle p_{T}. Since this precision and accuracy is not achievable in general, reconstruction and resolution imperfections can contribute to $\vec{p}_{\mathrm{T}}^{\mathrm{miss}}$. The formal definition of the missing transverse energy is given as

$$\vec{p}_{\mathrm{T}}^{\mathrm{miss}} = -\sum_{i} \vec{p}_{\mathrm{T}i}, \tag{4.3}$$

where i runs over all reconstructed particles in the event. Often we are only concerned with the magnitude of the missing transverse momentum, which we denote E_T^{miss}. The bulk of the scale and resolution degradation of E_T^{miss} is from limitations in our ability to measure the hadronic energy in the event. We can study the performance of E_T^{miss} reconstruction by using events with an identified Z boson or isolated photon [90]. The momentum of muons, electrons, and photons is typically resolved at the few percent level. We can then determine the E_T^{miss} resolution by studying the hadronic recoil in these events and applying conservation of momentum. Also, from these studies we develop filters to reject events with anomalous E_T^{miss}.

Chapter 5

Event Selection and Variable Definition

The SUSY models considered in this thesis often produce many jets and large transverse energy imbalances. Models with small mass splitting between the prompt SUSY particle and the LSP produce softer E_T^{miss} spectra. Choosing a relatively low jet p_T threshold will increase sensitivity for these models. With these considerations, as well as technical considerations such as trigger requirements, we define the baseline definition of events.

5.1 Signal Sample Definition

The following defines the baseline selection of events for this search:

(1) $\underline{N_{jet} \geq 2}$: Events are required to contain at least two jets, where each jet must satisfy

- $p_T > 30$ GeV,
- $|\eta| < 2.4$,
- Jets are clustered from PF candidates, using the anti-k_T algorithm with a distance parameter of 0.4 [81]. We choose jet quality criteria to maximize jet acceptance while still rejecting noise, reconstruction failures, and particles not resulting from hadronic activity [84]. We find $> 99\%$ efficiency in selecting jets with the quality criteria given below:
  - neutral hadron fraction < 0.99,
  - neutral EM fraction < 0.99,

- number of constituents > 1,
- charged hadron fraction > 0,
- charged multiplicity > 0,
- charged EM fraction < 0.99

We do not apply these jet ID criteria to jets that match isolated leptons, photons, and tracks (defined below). We reject any event containing a jet that satisfies the p_{T} requirement, but fails any of the above jet ID criteria.

(2) $\mathrm{H_T} > 700$ GeV: SUSY signatures considered in this search often have final states consisting of multiple jets with high transverse momentum. The variable, $\mathrm{H_T}$, quantifies this final state signature. The jets that define the $\mathrm{H_T}$ collection use the same definition as above, where

$$\mathrm{H_T} = \sum_{\mathrm{jets}} p_{\mathrm{T}}. \tag{5.1}$$

(3) $\mathrm{H_T^{miss}} > 300$ GeV: The neutral LSP escapes our detector and can be inferred as missing momentum in the transverse plane. The variable, $\mathrm{H_T^{miss}}$, is a measure of the missing transverse momentum from the recoiling jets in the event. The jet definition for the $\mathrm{H_T^{miss}}$ collection is a superset of the nominal jet collection defined above, where

$$\mathrm{H_T^{miss}} = \left| \sum_{\mathrm{jets}^*} \vec{p}_T \right|. \tag{5.2}$$

The additional jets included in the vector sum extend the η acceptance out to $|\eta| \leq 5.0$. As we extend beyond the tracker acceptance, we have less jet constituent information, and thus are required to reevaluate the jet identification criteria. The jet identification requirements for jets outside of tracker acceptance are given below.

- For jets with $2.4 \leq |\eta| \leq 2.7$:
  - neutral hadron fraction < 0.99,
  - neutral EM fraction < 0.99,

- number of constituents > 1

- For jets with $2.7 < |\eta| \leq 3.0$:
  - neutral EM fraction < 0.90,
  - number of particles > 2

- For jets with $3 < |\eta| < 5$:
  - neutral EM fraction < 0.90,
  - number of particles > 10

(4) Muon veto: Muon candidates are selected using the *Medium* muon ID [91], which balances muon efficiency with fake rate. A well-reconstructed inner track is required that must be identified as a global muon by the PF algorithm with strict requirements on χ^2, position matching, kinks, segment compatibility, and must be prompt with respect to the primary interaction vertex:

$$\begin{aligned} d_{xy}(\mu, \mathrm{PV}) &< 0.2 \text{ mm} \\ d_z(\mu, \mathrm{PV}) &< 0.5 \text{ mm}. \end{aligned} \tag{5.3}$$

Muon candidates are required to have $p_{\mathrm{T}} > 10$ GeV and $|\eta| < 2.4$. To avoid rejecting events with muons from b-hadron decays, muons are further required to satisfy an isolation requirement, $I_{\mathrm{mini}} < 0.2$, where I_{mini} is the mini-isolation variable with the property that the isolation cone is dependent on the p_{T} of the lepton. Any event with a muon satisfying all of the above criteria is vetoed.

(5) Electron veto: We choose an electron definition that results in a roughly 95% electron reconstruction efficiency. As with the muon definition, electron candidates are required to have $p_{\mathrm{T}} > 10$ GeV, but the range of the tracker and ECAL allow us to extend $|\eta|$ out to 2.5. Electron candidates are also required to satisfy an isolation requirement of $I_{\mathrm{mini}} < 0.1$. Any event with an electron satisfying all of the above criteria is vetoed.

(6) Angular cut: We rank the jets from the $\mathrm{H_T}$ collection in order of decreasing p_T, with j_1 as the leading (highest p_T) jet. We then apply the angular cut

$$\Delta\phi(\vec{\mathrm{H}}_\mathrm{T}^\mathrm{miss}, j_i) > 0.1, \text{ for } i = 1, 2, 3, 4. \tag{5.4}$$

The majority of QCD multijet events in our high-$\mathrm{H}_\mathrm{T}^\mathrm{miss}$ search region have jets with under measured momenta and thus a spurious momentum imbalance. A signature of such an event is a jet closely aligned in direction with the $\vec{\mathrm{H}}_\mathrm{T}^\mathrm{miss}$ vector in the ϕ direction. We therefore find that a relatively loose selection on $\Delta\phi(\vec{\mathrm{H}}_\mathrm{T}^\mathrm{miss}, j_i)$ for high momentum jets provides excellent background rejection, while preserving high signal efficiency. The discrimination power is degraded for lower p_T jets. We find empirically that background rejection is minimal after selecting on the fourth leading jet; thus, no such requirement is placed on other jets.

(7) Isolated track vetoes: A dominant source of background after applying the previous requirements is $\mathrm{t\bar{t}}$, single-top, and W events. In about half of these background events, the W boson decays to a τ lepton and the τ lepton decays hadronically, while in the other half, an electron or muon is not identified or does not satisfy the criteria for an isolated electron or muon candidate. To suppress these backgrounds, we reject events with one or more isolated charged tracks. To reduce the influence of tracks from pileup, only isolated tracks with impact parameter closest to the primary vertex are considered.

The isolated track definition depends on the PF algorithm identification. If identified as a muon or electron track, we require:

- $p_\mathrm{T} > 5$ GeV,
- $I_\mathrm{tk} < 0.2$.

To define I_tk, we take the scalar p_T sum of other charged tracks within the cone $\Delta R < 0.3$, where ΔR is defined as

$$\Delta R \equiv \sqrt{(\Delta\phi)^2 + (\Delta\eta)^2}. \tag{5.5}$$

Then, I_{tk} is defined as ΔR divided by the p_{T} of the primary track, itself. If the track is not identified as a muon or electron, the requirements become

- $p_{\mathrm{T}} > 10$ GeV,
- $I_{\mathrm{tk}} < 0.1$.

To retain more signal, and thus to improve the signal-to-background event discrimination, events with isolated tracks are vetoed only if the isolated track is consistent with originating from a W boson (with a mass of 80.1 GeV) by requiring $\mathrm{M_T}(\mathrm{tk}, \mathrm{E_T^{miss}}) < 100$ GeV, where

$$\mathrm{M_T}(\mathrm{tk}, \mathrm{E_T^{miss}}) \equiv \sqrt{2\, p_T^{\mathrm{tk}}\, \mathrm{E_T^{miss}}\, (1 - \cos \Delta\phi)}. \tag{5.6}$$

Here, p_T^{tk} is the transverse momentum of the track and $\Delta\phi$ is the azimuthal separation between the track and the missing momentum vector.

(8) Event cleaning:

To reject events with spurious $\mathrm{E_T^{miss}}$ signals [90], we apply event filters briefly summarized below.

- globalTightHaloFilter: Large radius machine induced particles form a beam halo that may interact with the CSC muon detectors or the ECAL. Events are discarded if CSC or ECAL deposits are consistent with halo shapes studied from out of time hits.
- HBHENoiseFilter and HBHEIsoNoiseFilter: Scintillator tiles in the HB and HE are subject to sporadic noise that may register as energy deposits. The geometrical patterns, channel multiplicities, and pulse shape information are used to reject these events.
- EcalDeadCellTriggerPrimitiveFilter: ECAL trigger primitives are used to recover data during reconstruction. However, trigger primitives are bounded and will saturate, leading to dead cells. Dead cells can lead to significant bias in the measurement of transverse momentum, and we flag events with trigger primitives at or near threshold.

- BadChargedHadronFilter: Charged pions can occasionally punch through the HCAL and mimic a high p_{T} muon, resulting in anomalously high missing transverse momentum. Events are filtered by comparing the angles of charged hadrons to low quality, high p_{T} muons.

- BadPFMuonFilter: Low quality hits in the muon system can lead to a high p_{T} muon track, which is subsequently rejected by the PF algorithm. The track persists, leading to large missing transverse momentum. Filtering these events involves matching rejected PF muons to high p_{T} tracks.

- goodVertexFilter: Events without a well defined vertex are often a source of anomalous $\mathrm{H}_{\mathrm{T}}^{\mathrm{miss}}$. To reject these events, we require at least one reconstructed vertex satisfying position requirements and a minimum number of associated degrees of freedom.

- HT5Filter: Events with anomalously energetic jets in the HF are observed in the data with $|\eta|$ between 3.0 and 3.1. To reject these events, we recalculate H_{T} using all jets within $|\eta| < 5$ and compare this to the nominal H_{T} value, such that passing events must satisfy

$$\mathrm{H}_{\mathrm{T}}(\text{jets with } |\eta| < 5)/\mathrm{H}_{\mathrm{T}}(\text{jets with } |\eta| < 2.4) < 2.0. \tag{5.7}$$

- PFoverCaloMETFilter: Particle flow failures can result in a large discrepancy between $\mathrm{E}_{\mathrm{T}}^{\mathrm{miss}}$ calculated with particle flow (PFMET) and $\mathrm{E}_{\mathrm{T}}^{\mathrm{miss}}$ calculated only from the calorimeters (CaloMET). To protect against such failures, we require

$$0.9 < \mathrm{PFMET}/\mathrm{CaloMET} < 5 \tag{5.8}$$

- customMuonFilter: Misreconstructed muons create artificial momentum imbalance. To avoid failures in muon reconstruction, we veto events if any jet in the event has
  - $p_{\mathrm{T}} > 200$ GeV

- muon energy fraction > 0.5
- $|\Delta\phi(\mathrm{jet}, \vec{p}_{\mathrm{T}}^{\mathrm{miss}})| > \pi - 0.4$

- fastsimJetFilter: Large jet energy mismeasurement can result from occasional failures in the FastSim approximations. We filter these events in FastSim by requiring that reconstructed jets be matched to generator level jets.

The impact of these filters on the signal efficiency has been determined to be negligible for all considered models.

5.1.1 Number of b-tagged Jets

While we do not apply a baseline selection on the number of jets that are tagged as b-jets ($\mathrm{N_{b\text{-}jet}}$) in our sample definition, estimating the heavy flavor content is an important tool for characterizing signal events. For each jet in the analysis we compute the CSVv2 discriminant described in Section 4.10.1. We tag a jet as a b-quark jet if it satisfies all the nominal jet criteria and the jet passes the CSVv2 medium working point, chosen to give a 1% mistag rate for light flavor quarks. Thus, $\mathrm{N_{jet}} \geq \mathrm{N_{b\text{-}jet}}$ is true for all events.

5.2 Signal Trigger

Signal events are recorded using triggers based on thresholds derived from missing transverse energy. Events in the search region are collected if the event passes one of the following trigger requirements:

- `HLT_PFMET100_PFMHT100_IDTight`, `HLT_PFMETNoMu100_PFMHTNoMu100_IDTight`
- `HLT_PFMET110_PFMHT110_IDTight`, `HLT_PFMETNoMu110_PFMHTNoMu110_IDTight`
- `HLT_PFMET120_PFMHT120_IDTight`, `HLT_PFMETNoMu120_PFMHTNoMu120_IDTight`

To measure the efficiency of these triggers, we select an unbiased single electron trigger, `HLT_Ele27_WPTight`, and measure the fraction of events passing the signal triggers after baseline selection. In the latter period of 2016 data taking, the rate of the lower E_T^{miss} threshold triggers (100 GeV) was manually reduced by a factor of 10 to accommodate the increase in instantaneous luminosity. The effective efficiency measurement takes this into account, as well as other varying conditions.

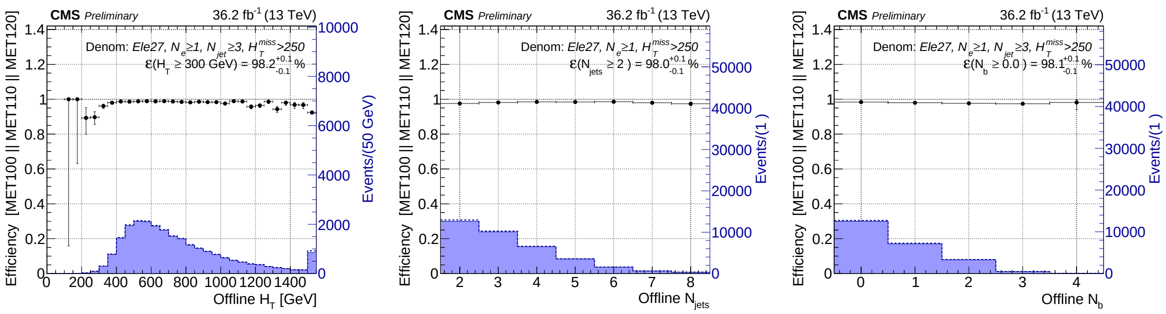

(a) (b) (c)

Figure 5.1: The trigger efficiency measurement of the `HLT_PFMETX_PFMHTX_IDTight` triggers vs H_T (a), N_{jet} (b) and $N_{b\text{-}jet}$ (c), where X = 100, 110, and 120 GeV [92]. The rightmost bin in each plot includes overflow.

Figure 5.1 shows the efficiency of the signal trigger as a function of H_T, N_{jet}, and $N_{b\text{-}jet}$. Overall, the signal trigger is very efficient ($> 98\%$), but at large H_T we see a slight degradation in trigger efficiency. We therefore measure the signal efficiency in two bins of H_T: less than 1500 GeV and greater than 1500 GeV. The turn-on curves as a function of H_T^{miss} are given in Figure 5.2. While the low H_T bin reaches 98% of the efficiency plateau at 231 GeV, we find that the turn-on is slower for the high-H_T bin. Therefore, in addition to binning the trigger efficiency in bins of H_T, we measure the trigger efficiency in three H_T^{miss} bins: $300 < H_T^{miss} \leq 350$, $350 < H_T^{miss} \leq 500$, and $H_T^{miss} > 500$ GeV.

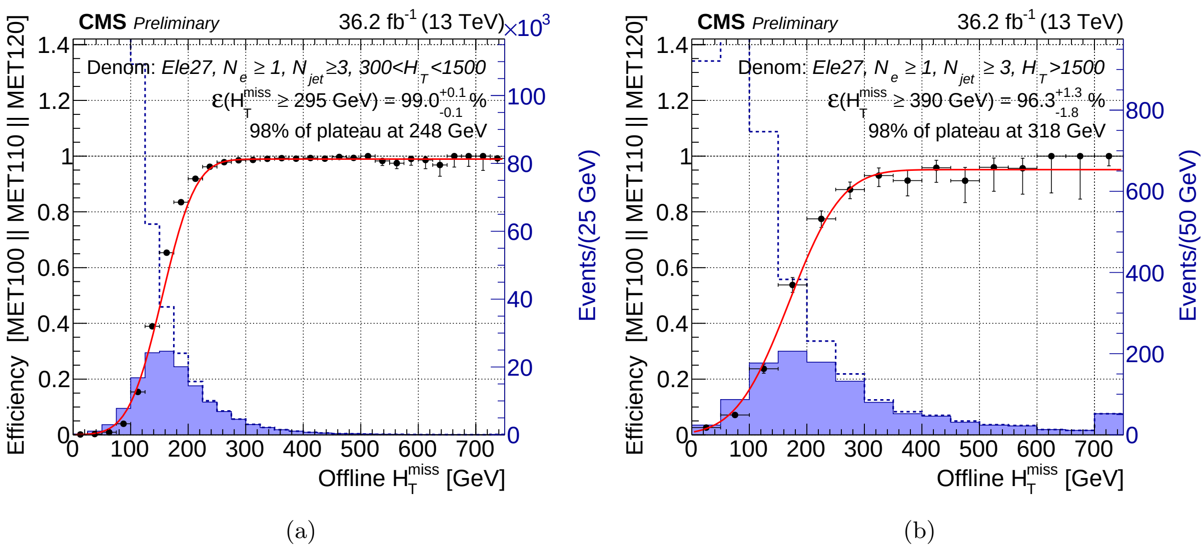

Figure 5.2: The trigger efficiency measurement of the `HLT_PFMETX_PFMHTX_IDTight` triggers vs H_T^{miss} for $300 \leq H_T \leq 1500$ (a) and for $H_T \geq 1500$ (b), where $\mathtt{X} = 100$, 110, and 120 GeV [92]. The rightmost bin in each plot includes overflow.

Chapter 6

Search for SUSY Using a Boosted Decision Tree Discriminant

We will now describe the main premise of this thesis, a search for gluino and stop pair production SUSY models. The search presented takes a somewhat different approach than a closely related analysis described in Chapter 7. The data for this search were collected from 13 TeV pp collisions at CMS during the 2016 run at the LHC, corresponding to 35.9 fb^{-1}.

6.1 Boosted Decision Tree Discriminant

After baseline selection, the observables $\mathrm{H_T}$, $\mathrm{H_T^{miss}}$, $\mathrm{N_{jet}}$, $\mathrm{N_{b\text{-}jet}}$, and $\Delta\phi(\vec{\mathrm{H}}_\mathrm{T}^{\mathrm{miss}}, j_i)$, with $i = 1, ..., 4$, all provide useful separation between signal and background. To further maximize separation, we use these eight variables as inputs to train a boosted decision tree (BDT) to discriminate signal from background. A decision tree is a set of rules (if-then statements) to classify data. BDT classification is accomplished by training an ensemble of weak decision trees that combine to form an efficient discriminant. The BDTs in this analysis are generated with the ROOT TMVA software package [93, 94].

A single decision tree begins with a node that separates data into two branches based on a splitting criterion that selects on an input variable. The data in each branch are then subjected to additional nodes. Through this process, we *grow* the tree until we reach a *leaf* node, in which data are categorized as signal or background. A node is determined to be a leaf node if one of two criteria are satisfied:

- The node has reached Max[Depth], defined as a positive integer assigned to control the maximum number of sequential cuts in a decision tree path.

- The fraction of events in the node relative to the total training sample size is below a predefined threshold, denoted as Min[Node Size].

These parameters are controlled to prevent overtraining around statistical fluctuations. The separation criterion for node splitting is chosen to be the selection that maximizes the *Gini index*, $G = p \cdot (1 - p)$, where p is the fraction of events in one of the two output nodes. Note that G is independent of the output node chosen to compute p and maximal separation is achieved with $G = 0.25$.

Relative to a single decision tree, better signal-to-background separation is achieved by using an ensemble of decision trees. We combine trees using the adaptive boosting (*AdaBoost*) algorithm. The AdaBoost algorithm is iterative. That is, at each tree indexed by i we determine the weights

$$\alpha_i = \left(\frac{1-\epsilon}{\epsilon}\right)^{\beta}, \tag{6.1}$$

where ϵ is the fraction of weighted events that were incorrectly categorized by the decision tree and $\beta = 0.5$. We then update the previous set of weights, applying α_i to events that were incorrectly categorized. All individual event weights, denoted by $\alpha_{i,j}$, are then rescaled by a normalization factor:

$$\alpha_{i,j} \rightarrow \left(\sum_{k}^{\mathrm{N_{events}}} \alpha_{i,k}\right)^{-1} \cdot \alpha_{i,j}, \tag{6.2}$$

where $j = 1, ..., \mathrm{N_{events}}$. We repeat this process over a predetermined number of individual decision trees, $\mathrm{N_{Trees}}$, updating the training event weights at each step until $\mathrm{N_{Trees}}$ is reached. Then we define the BDT output discriminant as

$$F_{\mathrm{BDT}} = \frac{1}{\mathrm{N_{Trees}}} \sum_{i}^{\mathrm{N_{Trees}}} \ln\left(\alpha_i\right) \cdot f_i(\mathbf{x}), \tag{6.3}$$

where $\mathbf{x}$ is the set of eight input variables of the event and $f_i(\mathbf{x})$ is the result of the i^{th} decision tree in the collection ($f_i(\mathbf{x}) = -1$ indicates the background hypothesis and $f_i(\mathbf{x}) = 1$ indicates the signal hypothesis). The output is then rescaled and offset such that $0 \leq F_{\mathrm{BDT}} \leq 1$.

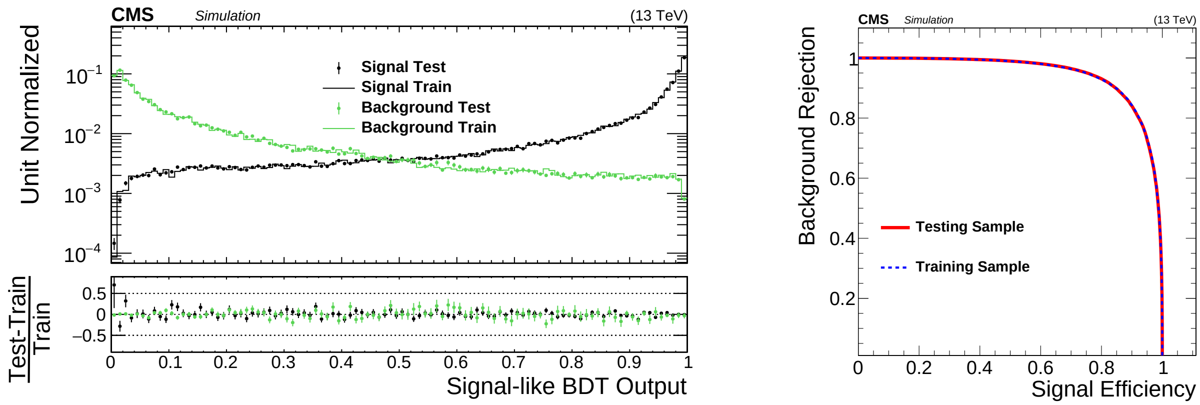

(a) (b)

Figure 6.1: Distribution of training and testing samples for both signal and background simulation (a) and the corresponding ROC curve (b).

We use the FullSim SUSY MC samples as our signal input and the SM MC samples as our background input to the BDT for training, and we refer to the result as the *signal-like BDT* output discriminant. Half of each MC sample is reserved for testing. A shape comparison between signal and background in the signal-like BDT discriminant is given in Figure 6.1a. A useful measurement of the signal-to-background separation is the receiver operating characteristic (ROC) curve, which is a two-dimensional contour that depicts the fraction of background rejected and the fraction of signal that remains for all values of selecting on the signal-like BDT output. The corresponding ROC curve for the signal-like BDT output is shown in Figure 6.1b. To optimize the efficiency of the BDT, we choose $\mathrm{N_{Trees}}$, Max[Depth], and Min[Node Size] to maximize the area under the ROC curve and to prevent overtraining. The area under the ROC curve becomes a proxy for signal-to-background separation. We can monitor the difference between the testing and training ROC curve area, $\Delta\mathrm{A_{ROC}} = \mathrm{A_{ROC}^{test}} - \mathrm{A_{ROC}^{train}}$, to determine the degree of overtraining. Figure 6.2 shows the one-dimensional variation in parameter values against the response in $\Delta\mathrm{A_{ROC}}$. We exclude parameter points that result in negative $\Delta\mathrm{A_{ROC}}$, which potentially indicate overtraining. The values chosen which optimize signal separation and avoid overtraining are given as follows:

$$\mathrm{N_{Trees}} = 2400, \quad \mathrm{Max[Depth]} = 2, \quad \mathrm{Min[Node\,Size]} = 1.8\%. \tag{6.4}$$

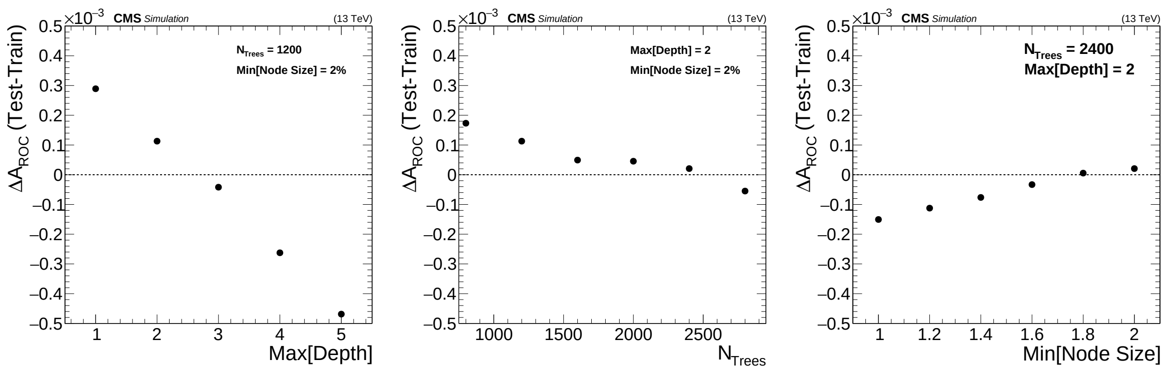

(a) (b) (c)

Figure 6.2: Difference in ROC curve area (test-train) as a function of varying the maximum node depth (a), number of trees (b), and minimum node size (c).

6.2 BDT Signal Region

We divide the signal-like BDT output discriminant into 50 bins of width 0.02. We define the signal region to be all events with signal-like BDT output discriminant of 0.5 or greater. The signal region remains *blind* until after background predictions are computed. This means that the data in the signal region, where we expect to find events with final states consistent with a SUSY signal, are concealed from the analysis until the complete set of predictions are made. The corresponding data with signal-like BDT output < 0.5 make up the *sideband.* In the sideband data, the yield from signal simulations are small and the background yields are large. We will use the sideband data to help understand the background predictions in the signal region.

As shown in Section 1.3, SUSY signatures of interest include multijet events with large jet energy and large missing transverse momentum. While ordinary processes with this characteristic topology are rare, there are three classes of standard model backgrounds that can mimic a SUSY signal. Each standard model background produces a unique distribution in our search variables and can be classified based on the nature of the H_T^{miss} produced:

- H_T^{miss} resulting from invisible Z decays,
- H_T^{miss} resulting from leptonic W decays, and

- H_T^{miss} resulting from jet p_T mismeasurement.

When a Z is produced, often through radiation off a hard scatter or from quark anti-quark annihilation, the boson decays to a pair of neutrinos 20% of the time [6]. This process represents an irreducible source of real H_T^{miss} and can only be accounted, not removed. Fortunately, we can define three independent control samples that directly, or indirectly, mimic this process. The procedure for estimating this background is described in Section 6.3.

Events where a W is produced, either through direct production or through the decay of a top quark, are suppressed by vetoing events with an identified lepton. Nevertheless, real leptons can fail any of our identification criteria and avoid our veto. The resulting event appears to be all hadronic and contains real H_T^{miss} from the neutrino. The estimation of this background is given in Section 6.4. Also note that hadronically decaying W production does not contribute to this background because this process does not yield H_T^{miss} from neutrinos.

Finally, it's possible that a reconstructed event gives rise to large H_T^{miss} without the direct production of neutrinos. While our jet energy resolution is quite good, the very large QCD cross section promotes rarely mismeasured jet events past our baseline H_T^{miss} selection. Other common mechanisms for producing this *fake* H_T^{miss} include jets out of our acceptance ($p_T < 30$ GeV or $|\eta| > 5$) and non-prompt neutrinos from semileptonic decays within a jet. Further details on this background, which we will refer to as QCD, are given in Section 6.4.

6.3 Background Arising from Z decays to neutrinos

The approach for estimating the $Z \to \nu\overline{\nu}$ background is to select events with the production of a visible prompt boson, either a photon or Drell-Yan events near the Z resonance, and remove the reconstructed boson from the event. Figure 6.3 illustrates an example diagram of the Z production background in this search and Figure 6.4 illustrates corresponding diagrams of γ and Drell-Yan processes with visible final states products.

After correcting for boson efficiencies and fake rates, the resulting event has identical kine-

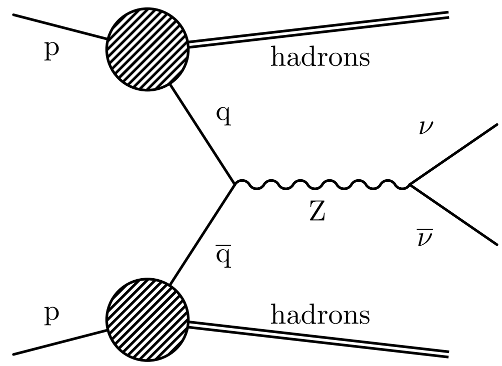

Figure 6.3: A tree level diagram of the $\mathrm{Z} \to \nu\overline{\nu}$ process resulting in genuine $\mathrm{H}_{\mathrm{T}}^{\mathrm{miss}}$.

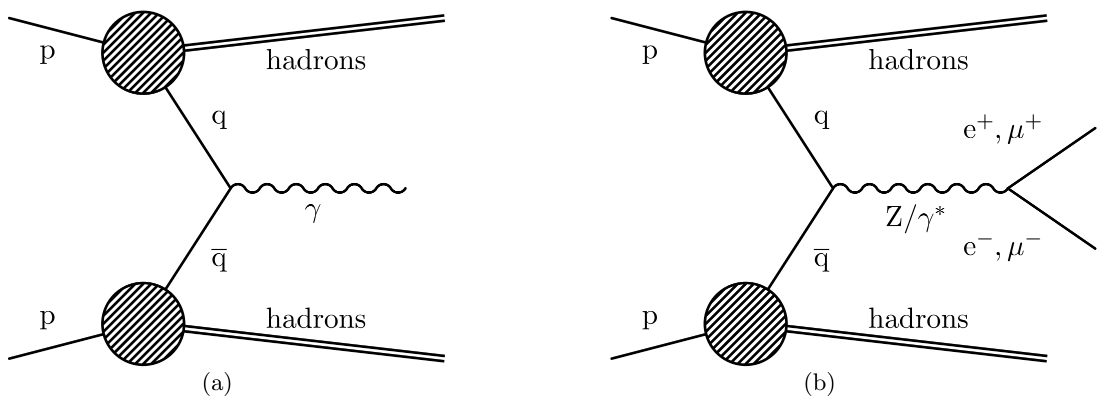

Figure 6.4: Diagram of direct photon (a) and Drell-Yan (b) production processes used to measure the $\mathrm{Z} \to \nu\overline{\nu}$ background.

matic properties to $\mathrm{Z} \to \nu\overline{\nu}$ in the case of $\mathrm{Z} \to \mu^+\mu^-$ or $\mathrm{Z} \to \mathrm{e}^+\mathrm{e}^-$, and nearly identical kinematic properties to $\mathrm{Z} \to \nu\overline{\nu}$ in the case of prompt γ production. We therefore define three independent control samples to estimate this background:

- **Single-γ control sample** has the benefit of large sample statistics, but care must be taken to understand the systematic uncertainties related to the mass and coupling differences between the photon and Z.

- **$\mathrm{Z} \to \mu^+\mu^-$ and $\mathrm{Z} \to \mathrm{e}^+\mathrm{e}^-$ control samples** each provide a direct handle on the physics of Z production, but the ratio of branching fractions, $\mathcal{B}_{\ell^+\ell^-/\nu\overline{\nu}}$, is small, leading to large statistical uncertainties [6].

The method presented will use both control samples to achieve good statistical precision with the

γ control sample while reducing systematic uncertainties by calibrating the γ control sample with data from $Z \rightarrow \mu^+\mu^-$ and $Z \rightarrow e^+e^-$ events.

6.3.1 Single-γ Control Sample

We select events with a single, well identified photon with $p_T > 200$ GeV. We do not consider photons outside the fiducial region of the ECAL ($1.444 < |\eta| < 1.566$ or $|\eta| > 2.5$). We use the `HLT_Photon175` trigger, with γ p_T requirement of 175 GeV, to select γ events in data. After offline γ p_T and H_T^{miss} selection, the trigger efficiency is found to be high, as shown in Figure 6.5a. For the purposes of photon definition and efficiency parameterization, we subdivide the control sample into barrel photons ($|\eta| < 1.444$) and endcap photons ($1.566 < |\eta| < 2.5$). Identification and isolation criteria used to identify photons in our sample are H/E, $\sigma_{i\eta i\eta}$, charged hadron isolation, neutral hadron isolation, and electromagnetic particle isolation. Corresponding values are given in Table 6.1. After removing the photon from the event, we apply the baseline selection as described in Section 5.1. Real photons in the control sample can be divided into three sources: *direct prompt*

Table 6.1: Criteria for barrel and endcap photons (in addition to the p_T requirement) that are used to define the Single-γ CS.

	Barrel photons	Endcap photons
H/E	< 0.028	< 0.093
$\sigma_{i\eta i\eta}$	< 0.0107	< 0.0272
charged hadron isolation	< 2.67	< 1.79
neutral hadron isolation	$< 7.23e^{0.0028 \cdot p_T + 0.5408}$	$< 8.89 + 0.01725 \cdot p_T$
electromagnetic particle isolation	$< 2.11 + 0.0014 \cdot p_T$	$< 3.09 + 0.0091 \cdot p_T$

photons, *fragmentation prompt photons*, and *non-prompt photons*. In simulation, we define the sources of photons as given below.

- **Direct prompt photons** are the result of a hard interaction from radiation directly from a quark or the incoming proton with $\Delta R > 0.4$, where ΔR is taken between the photon and any quark or gluon in the event.

- **Fragmentation prompt photons** are the result of a hard interaction from radiation directly from a quark or the incoming proton with $\Delta R < 0.4$ between the photon and any quark or gluon in the event. The fraction of direct prompt photons over the total number of prompt photons is denoted as $\mathcal{F}_{\text{dir}}$.

- **Non-prompt photons** are all other photons in the event, arising principally from π^0 and η decays.

Direct prompt photons, which make up about 85% of the control sample, are the most useful source of photons for predicting the $\mathrm{Z} \to \nu\overline{\nu}$ background for a couple of reasons. First, direct prompt photon production processes most neatly map onto the set of Z boson production processes, simplifying the translation into the signal region. Second, divergences in the matrix element computation of fragmentation photons enforce an artificial cutoff in simulated photon samples. The result is an increased reliance on parton shower simulation to recover fragmentation photons. To mitigate the problems associated with this, we categorize these sources in simulation and keep only the direct prompt photons for the $\mathrm{Z} \to \nu\overline{\nu}$ prediction. We then apply a correction factor to data to account for the fraction of events that are not from direct prompt photons.

The phenomenological ratio that translates the number of observed photon events in data into the number of expected $\mathrm{Z} \to \nu\overline{\nu}$ events is defined as

$$\mathcal{R}_{\mathrm{Z}(\nu\overline{\nu})/\gamma} = \frac{N^{\text{sim}}_{\nu\overline{\nu}}}{\mathcal{C}^{\gamma}_{\text{d/sim}} N^{\text{sim}}_{\gamma}}, \tag{6.5}$$

where, $N^{\text{sim}}_{\nu\overline{\nu}}$ is the bin-by-bin expectation of $\mathrm{Z} \to \nu\overline{\nu}$ events from simulation, N^{sim}_{γ} is the expectation of γ events from simulation, and $\mathcal{C}^{\gamma}_{\text{d/sim}}$ are a set of data driven scale factors to correct the modeling of γ efficiencies. Here, *bin* is being used generally to describe any independent search region with a $\mathrm{Z} \to \nu\overline{\nu}$ background contribution or a corresponding control region with identical kinematic selection. A bin may be one of the 50 segments of the signal-like BDT output discriminant defined in Section 6.2, or it may be a search region embedded in a multidimensional phase space. The

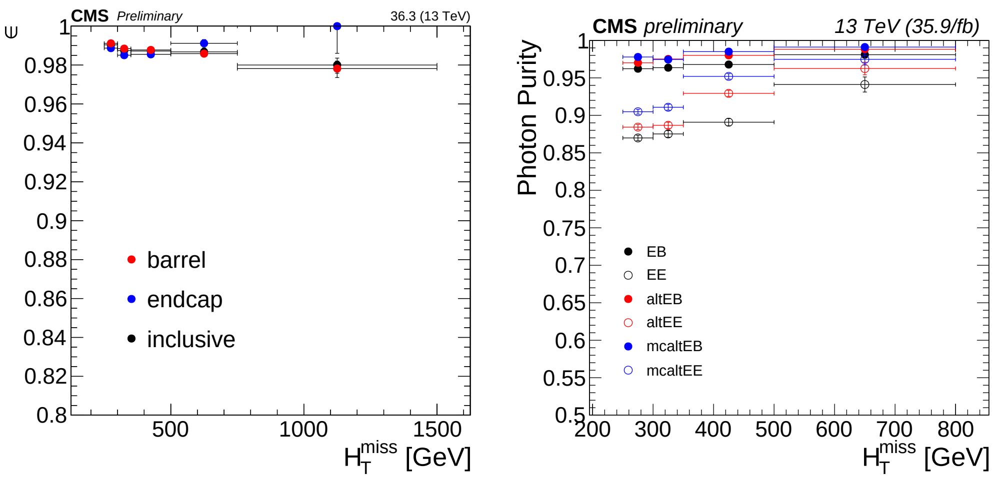

(a) (b)

Figure 6.5: Efficiency of the HLT_Photon175 trigger as a function H_T^{miss} (a) and the photon purity as a function of H_T^{miss} as measured with various non-prompt charged isolation templates (b) [92].

$\mathcal{R}_{Z(\nu\bar{\nu})/\gamma}$ ratio models the kinematic differences between γ events and $Z \to \nu\bar{\nu}$ events as well as the branching ratio. If we assumed no theoretical uncertainty on $\mathcal{R}_{Z(\nu\bar{\nu})/\gamma}$, we would simply apply this translation factor to a pure sample of photon events and we would obtain a $Z \to \nu\bar{\nu}$ prediction. While we expect many hadronic observables to cancel in the ratio, we do not explicitly assume this to be true. Likewise, known limitations in modeling of radiative processes suggest $\mathcal{R}_{Z(\nu\bar{\nu})/\gamma}$, as defined above with LO simulation, will require electroweak corrections for arbitrary accuracy [95]. Our inability to generate sufficient statistics in simulation at NLO restricts the effectiveness of this approach. Instead we describe a data calibration of $\mathcal{R}_{Z(\nu\bar{\nu})/\gamma}$ in the following sections.

6.3.2 Z Decay to Dilepton Control Samples

The lepton definitions given in Section 5.1 are the same as those used to build the $Z \to e^+e^-$ and $Z \to \mu^+\mu^-$ control samples. Instead of the lepton veto, we require that there be exactly two leptons of opposite charge with invariant mass within 15 GeV of the Z mass [6]. We also apply a Z p_T selection of > 200 GeV. This requirement is consistent with the γ offline selection and has the added benefit of rejecting a large fraction of the $t\bar{t}$ contamination.

The approach is the same as in the single-γ CS definition in that we apply the same baseline selection as that described in Section 5.1 after removing the leptons from the event. We use six single electron triggers and four single muon triggers with an array of p_{T}, $\mathrm{H_T}$, and isolation requirements. We find the efficiency to be high, but the single electron trigger efficiency is found to degrade slightly at large $\mathrm{H_T}$. We therefore correct the single electron trigger efficiency in two bins of $\mathrm{H_T}$ ($<$ 1000 GeV and $>$ 1000 GeV). The single electron trigger efficiency and single muon trigger efficiency are shown against $\mathrm{H_T}$ in Figure 6.6.

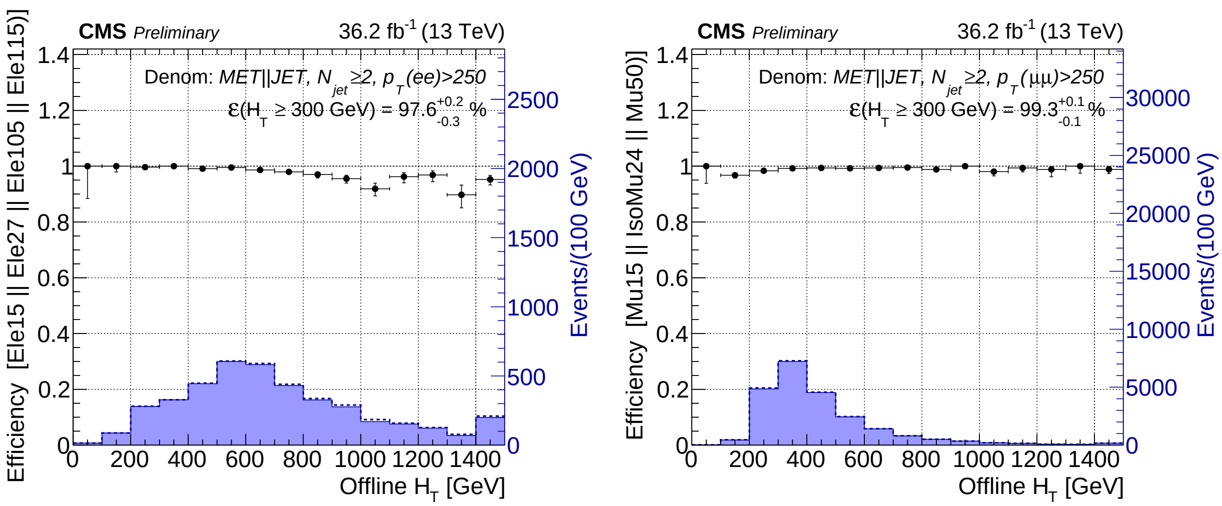

(a) (b)

Figure 6.6: Trigger efficiency for single lepton triggers used to select the $\mathrm{Z} \to \mathrm{e^+e^-}$ (a) and $\mathrm{Z} \to \mu^+\mu^-$ (b) samples as a function of $\mathrm{H_T}$ for events with $p_{\mathrm{T}}(\ell^+\ell^-) > 200$ GeV [92]. The rightmost bin in the plot includes overflow.

6.3.2.1 $\mathcal{R}_{\mathbf{Z}(\nu\overline{\nu})/\gamma}$ Double Ratio

As mentioned in Section 6.3.1, we wish to provide a data calibration of $\mathcal{R}_{\mathrm{Z}(\nu\overline{\nu})/\gamma}$ to reduce the uncertainties from the theory. This is accomplished through the double ratio:

$$\rho = \frac{\mathcal{R}^{\mathrm{obs}}_{\mathrm{Z}\to\ell^+\ell^-/\gamma}}{\mathcal{R}^{\mathrm{sim}}_{\mathrm{Z}\to\ell^+\ell^-/\gamma}} = \frac{N^{\mathrm{obs}}_{\mathrm{Z}\to\ell^+\ell^-}}{N^{\mathrm{sim}}_{\mathrm{Z}\to\ell^+\ell^-}} \cdot \frac{N^{\mathrm{MC}}_{\gamma}}{N^{\mathrm{obs}}_{\gamma}} \cdot \frac{\beta_{\ell\ell}}{\mathcal{C}^{\ell\ell}_{\mathrm{d/sim}}} \cdot \frac{\mathcal{C}^{\gamma}_{\mathrm{d/sim}}}{\mathcal{F}_{\mathrm{dir}}\beta_{\gamma}}, \tag{6.6}$$

where $N^{\rm obs}_{\rm Z\to\ell^+\ell^-}$ and $N^{\rm sim}_{\rm Z\to\ell^+\ell^-}$ are the number of $\rm Z \to \ell^+\ell^-$ events in data and simulation, $N^{\rm obs}_{\gamma}$ and $N^{\rm MC}_{\gamma}$ are the number of γ events in data and simulation, $\beta_{\ell\ell}$ is the $\rm Z \to \ell^+\ell^-$ purity estimation, $\mathcal{C}^{\ell\ell}_{\rm d/sim}$ are the data corrections to the $\rm Z \to \ell^+\ell^-$ efficiencies in simulation, and β_γ is the photon purity estimation. Here, purity describes the fraction of events that contain the physical process of interest. The value of ρ as a function of the signal-like BDT output is shown in Figure 6.7c. The following describes the full extent of the use of the double ratio in the $\rm Z \to \nu\overline{\nu}$ prediction.

- The central value, $\langle\rho\rangle = 0.996 \pm 0.036$ is applied as a scale factor to $\mathcal{R}_{\rm Z(\nu\overline{\nu})/\gamma}$, or equivalently, $\langle\rho\rangle$ scales the entire $\rm Z \to \nu\overline{\nu}$ prediction.
- If significant deviation from a flat ρ is observed, then a variable double ratio would be assigned as a function of the BDT output discriminant. However, assuming a linear ρ, the slope is consistent with zero. Therefore, no shape correction is applied.
- Error bands from the linear fit to the double ratio, given in Figure 6.7c, are used to derive a systematic uncertainty on the shape of $\mathcal{R}_{\rm Z(\nu\overline{\nu})/\gamma}$, as described in Section 6.3.3.

This leads to a general form for the full $\rm Z \to \nu\overline{\nu}$ prediction,

$$N^{\rm pred}_{\rm Z\to\nu\overline{\nu}} = \langle\rho\rangle \cdot \mathcal{R}_{\rm Z(\nu\overline{\nu})/\gamma} \cdot \mathcal{F}_{\rm dir} \cdot \beta_\gamma \cdot N^{\rm obs}_{\gamma}. \tag{6.7}$$

Here, $\mathcal{R}_{\rm Z(\nu\overline{\nu})/\gamma}$ and $N^{\rm obs}_{\gamma}$ are evaluated bin-by-bin, $\mathcal{F}_{\rm dir}$ is measured as a function of $\rm H_T$, $\rm H_T^{miss}$, $\rm N_{jet}$, and $\Delta\phi(\vec{\rm H}_{\rm T}^{\rm miss}, j_i)$, β_γ is measured as a function of $\rm H_T^{miss}$ and $|\eta|$, and $\langle\rho\rangle$ is the single value given above.

6.3.3 $\rm Z \to \nu\overline{\nu}$ Systematic Uncertainties

We identify all sources of uncertainty in the $\rm Z \to \nu\overline{\nu}$ prediction. The uncertainties are categorized by source and correlation structure. A systematic uncertainty is taken to be *correlated* if the difference between the best estimate of a parameter of interest, e.g. $\langle\rho\rangle$, and the parameter's true value can be characterized by a single *nuisance parameter* across a subset of independent search regions. In general, a nuisance parameter is any parameter that must be accounted for, e.g.

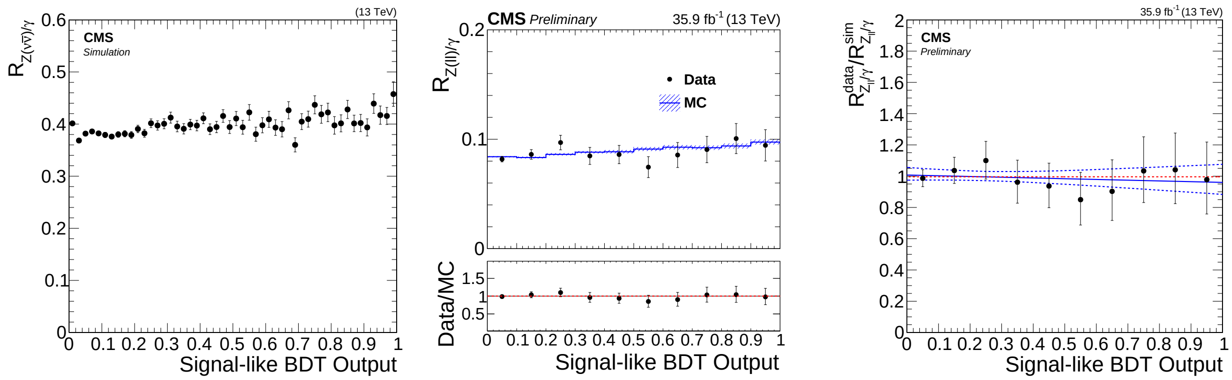

(a) (b) (c)

Figure 6.7: The $\mathcal{R}_{Z(\nu\overline{\nu})/\gamma}$ ratio in simulation (a) and $\mathcal{R}_{Z(\ell\ell)/\gamma}$ in data and simulation (b) all plotted against the signal-like BDT output with baseline selection applied. The double ratio (c) is used to calibrate $\mathcal{R}_{Z(\nu\overline{\nu})/\gamma}$ with data.

the spread of a distribution, but is not a parameter of interest, e.g. the distribution mean. In this analysis, nuisance parameters are taken to be the measurement uncertainties we derive at the one standard deviation level. The set of systematic uncertainties on the prediction of the $Z \to \nu\overline{\nu}$ background, with the uncertainty ranges corresponding to variations between bins of the signal-like BDT output, are as follows:

- **$\mathcal{R}_{Z(\nu\overline{\nu})/\gamma}$ statistics: 1-2%.** We include the statistical uncertainty on $\mathcal{R}_{Z(\nu\overline{\nu})/\gamma}$ from both $Z \to \nu\overline{\nu}$ and γ simulation. The bin-by-bin systematic uncertainties are uncorrelated.

- **b-tag scale factors: <1-5%.** We apply b-tag scale factors to simulation before calculating $\mathcal{R}_{Z(\nu\overline{\nu})/\gamma}$. Uncertainties in the b-tag scale factors are propagated and the resulting deviation in the prediction is considered as a systematic uncertainty. An uncorrelated uncertainty structure is assumed.

- **Signal region trigger efficiency: <1%.** Before calculating $\mathcal{R}_{Z(\nu\overline{\nu})/\gamma}$, we scale the simulated $Z \to \nu\overline{\nu}$ by the measured trigger efficiency in data described in Section 5.2. The trigger efficiency measurement is varied at $\pm 1\sigma$ in the distribution of the ensemble. The trigger efficiency uncertainty is small and is treated as fully correlated across the search bins.

- **Z $\rightarrow \nu\bar{\nu}$ normalization: 6.5%.** To find the overall Z $\rightarrow \nu\bar{\nu}$ scale uncertainty, we first consider the error on the intercept from a fit of a line with a slope of zero to the double ratio. From this, we obtain an uncertainty on the central value of $\langle\rho\rangle$. In addition, the net difference in lepton identification, reconstruction, and isolation efficiencies must be accounted for in the overall scale of the Z $\rightarrow \nu\bar{\nu}$ prediction. Scale factors are computed using the *Tag-and-Probe* technique, which exploits the dilepton resonance near the Z mass to extract lepton efficiencies in both data and simulation [96, 97]. The scale factors are binned in $\mathrm{H}_{\mathrm{T}}^{\mathrm{miss}}$ and the associated systematic uncertainty is 5%. We also include the uncertainty on the Z $\rightarrow \ell^{+}\ell^{-}$ purity, obtained from fits to the Z mass peak shown in Appendix C. The Z $\rightarrow \ell^{+}\ell^{-}$ purity and trigger efficiency uncertainties are small, but are also added in quadrature with the $\langle\rho\rangle$ and scale factor uncertainties. This uncertainty is correlated across all search bins.

- **Double ratio: 1-8%.** We subtract off the uncertainty on the central value of ρ from the error bands on the double ratio shown in Figure 6.7c. In quadrature, we add the difference between $\langle\rho\rangle$ and the line of best fit to the double ratio evaluated at the corresponding search region. The resulting uncertainty is taken to be uncorrelated across all bins.

- **Photon purity: 1%.** To obtain the prompt γ purity in the single-γ control sample, we fit shapes of prompt and non-prompt photons to the charged isolation distribution in data. The prompt shapes are taken from γ simulation and the non-prompt shapes are taken from QCD simulation. While the simulation-based templates are found to provide a reasonable description of both the prompt and non-prompt distributions, a data sideband is defined by inverting the $\sigma_{i\eta i\eta}$ requirement, giving a sample of predominantly non-prompt photons, from which a template is generated. The purity is taken to be the weighted average of the measurements from each template fit with the difference serving as the uncertainty on the purity. The prompt γ purity is measured in the barrel and endcap separately and found to be high, as shown in Figure 6.5b. Because of the double ratio calibration, we are insensitive to any overall scaling uncertainty from the photon purity. The bin-by-bin shape uncertainty is found to be small and is treated as an uncorrelated systematic uncertainty.

- **Photon identification efficiency: 0.5%.** Differences in photon identification efficiency between data and simulation are small but are accounted for in $\mathcal{R}_{\mathrm{Z}(\nu\overline{\nu})/\gamma}$. Tag-and-Probe studies are performed to derive scale factor corrections, binned in $\mathrm{H}_{\mathrm{T}}^{\mathrm{miss}}$. As with the photon purity, any overall normalization of the scale factors is divided out by the double ratio. The uncertainty on the shape of the scale factors is small and taken to be uncorrelated.

- **Photon trigger efficiency: 1%.** We use a combination of H_{T} reference triggers to measure the `HLT_Photon175` trigger efficiency. The photon trigger efficiency is found to be high with minimal dependence on the kinematic variables in the event as shown in Figure 6.5a. The effect of normalization cancels out, and the residual shape uncertainty is assumed to be uncorrelated.

- **Photon fragmentation fraction: 1.5%.** The fraction of fragmentation photons must be accounted for to remove any unmodeled dependence on $\mathcal{R}_{\mathrm{Z}(\nu\overline{\nu})/\gamma}$, as fragmentation photons are purposely removed in the simulation. Again, the overall normalization of $\mathcal{F}_{\mathrm{dir}}$ has no effect on the prediction. We bin $\mathcal{F}_{\mathrm{dir}}$ in $\mathrm{N}_{\mathrm{jet}}$, $\mathrm{H}_{\mathrm{T}}^{\mathrm{miss}}$, and H_{T}, and we consider the resulting spread to derive a 30% uncertainty on $1 - \mathcal{F}_{\mathrm{dir}}$ as an uncorrelated systematic uncertainty. With an average value of $\mathcal{F}_{\mathrm{dir}} \approx 0.95$, we derive an uncertainty of 1.5%.

- **Single-γ sample statistics: 2.5-5%.** The combined factor that multiplies the number of control region events in a given bin to determine the background estimation is called the *transfer factor.* While the uncertainties on the transfer factor are given above, the size of the transfer factor scales the control sample statistical uncertainty. Transfer factors less than one reduce the size of the statistical uncertainty; likewise, transfer factors larger than one expand the size of the statistical uncertainty. The single-γ control sample size ranges from 63 to 207 events with a corresponding transfer factor of around 0.37. The control sample statistical treatment is described in Section 6.6.1.1.

The full $Z \to \nu\overline{\nu}$ prediction in data in 50 bins of the signal-like BDT discriminant is shown in Figure 6.8. The prediction combines the above systematic uncertainties with the appropriate transfer factors described throughout Section 6.3 to translate the observed data yields in the single-γ CS into a $Z \to \nu\overline{\nu}$ prediction. For comparison, we plot the $Z \to \nu\overline{\nu}$ yields from simulation together with the data prediction.

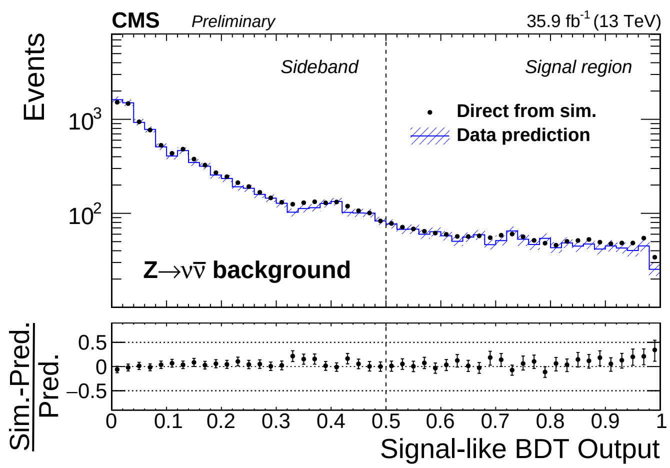

Figure 6.8: The data prediction of the $Z \to \nu\overline{\nu}$ background compared to simulation. Agreement between the data prediction and the simulation is not assumed, expected, or required.

6.4 Measurement of Multijet and Top+W Backgrounds

We define the signal region to include all events with signal-like BDT value of 0.5 and above. The remaining events define our sideband for use in constraining the backgrounds in our search. Section 6.3 describes a fully general procedure to obtain, not only the BDT shapes, but also the overall $Z \to \nu\overline{\nu}$ normalization with high confidence. For the two remaining backgrounds, we use data driven techniques to obtain the separate shapes in the analysis bins, and we use the sideband data to set the overall scale of each background. While the QCD and Top+W signal-like BDT shapes are different, separation is not readily achievable with high confidence. However, we can exploit the characteristics of these backgrounds to derive a new BDT discriminant to achieve separation between the two backgrounds in data.

- **Top+W Characteristics:** Large $N_{\text{b-jet}}$ with moderate to large H_T^{miss}, which is proportional to H_T.

- **QCD Characteristics:** Small H_T^{miss}, which is independent of H_T with $\Delta\phi(\vec{H}_T^{\text{miss}}, j_i)$ peaking at small values.

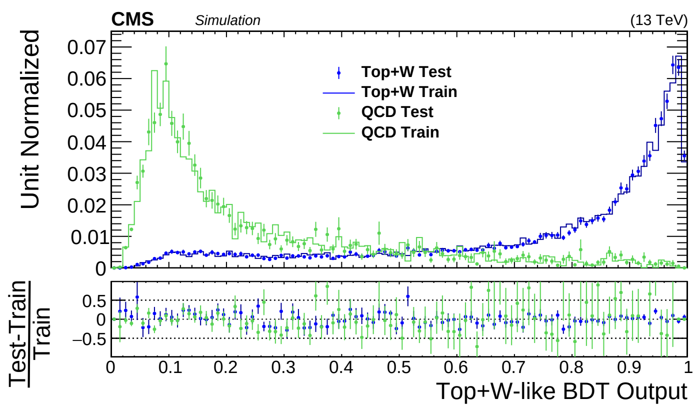

(a)

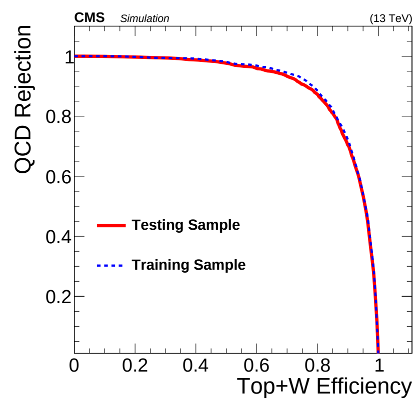

(b)

Figure 6.9: Distribution of training and testing samples for both top+W and QCD simulation (a) and the corresponding ROC curve (b).

With the same eight variables as those used to train the signal-like BDT discriminant, we train an additional BDT with the top+W simulation in place of the signal simulation. We also remove the $Z \to \nu\bar{\nu}$ simulation from training so that the *top+W-like* BDT discriminator is tasked with simply separating top+W events from QCD events. We apply the blinding criterion of signal-like BDT less than 0.5 to the training samples as we hope to achieve separation in the sideband data. Figure 6.9a shows QCD and top+W distributions in the top+W-like BDT output discriminant. The training and testing distributions of the top+W-like BDT and the corresponding ROC curves are given in Figure 6.9b. We find optimal values of $N_{\text{Trees}} = 3600$, Max[Depth] $= 3$, and Min[Node Size] $= 1.8\%$.

We use representative control samples, described in Sections 6.4.1 and 6.4.2, to provide shapes to fit the top+W-like BDT output. From the extracted fit parameters, we are then able to obtain the sideband normalization of the top+W and QCD backgrounds separately. However, before the sideband data can be fit with control sample shapes, we need to subtract off the Z $\rightarrow \nu\overline{\nu}$ background. We use the procedure described in Section 6.3.3 with the blinding criteria applied. The top+W-like shapes of $\mathcal{R}_{Z(\nu\overline{\nu})/\gamma}$ and ρ are given in Figure 6.10.

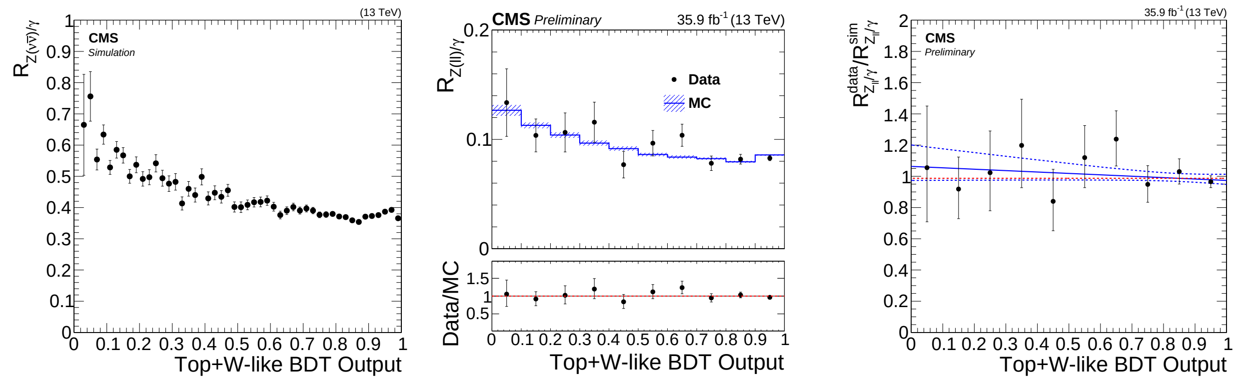

(a) (b) (c)

Figure 6.10: The $\mathcal{R}_{Z(\nu\overline{\nu})/\gamma}$ ratio in simulation (a) and $\mathcal{R}_{Z(\ell\ell)/\gamma}$ in data and simulation (b). The double ratio (c) is used to calibrate $\mathcal{R}_{Z(\nu\overline{\nu})/\gamma}$ with data. Each distribution is plotted against the top+W-like BDT output with the sideband selection (signal-like BDT < 0.5) applied.

6.4.1 Single-Lepton Control Sample and Lost Lepton Shape Determination

Top+W events enter our search region when a $W^{\pm} \rightarrow \ell^{\pm}\nu$ decay occurs and the charged lepton is not identified. Figure 6.11a shows one such example of semi-leptonic $t\bar{t}$ production. While $t\bar{t}$ is uniquely challenging because of the final state similarities with SUSY models associated with top quarks, direct W production in association with jets can also enter our search region as a background. All leptonically decaying W events, directly or through $t\bar{t}$ decays, that enter our search region will have a counterpart in events in which the charged lepton is successfully identified. Therefore, we choose a single-lepton (SL) control sample to derive an independent measurement of the top+W background. The SL control sample is defined as events with identical signal region selection but with exactly one isolated electron (single-electron CS) or exactly one isolated muon (single-muon CS). We use the same trigger requirements as for the signal data. Since SUSY signals associated with top quarks may also have one-lepton final states, we minimize the size of the signal contamination in the SL CS by imposing the requirement

$$M_T(\ell, E_T^{miss}) \equiv \sqrt{2\, p_T^{\ell}\, E_T^{miss}\, (1 - \cos\Delta\phi)} < 100 \text{ GeV} \tag{6.8}$$

where $\Delta\phi$ is the angular separation between the $\vec{p}_T$ of the lepton and $\vec{p}_T^{miss}$. If the neutrino in the W decay is the only source of true E_T^{miss} in the event, the M_T variable will peak at or below the W mass and therefore pass the event. However, additional sources of E_T^{miss}, such as the $\widetilde{\chi}_1^0$, will inflate M_T. This is shown in Figure 6.11b. The single-electron CS is approximately 95-96% pure, and the single-muon CS is >99% pure. A correction is applied to account for the CS impurity.

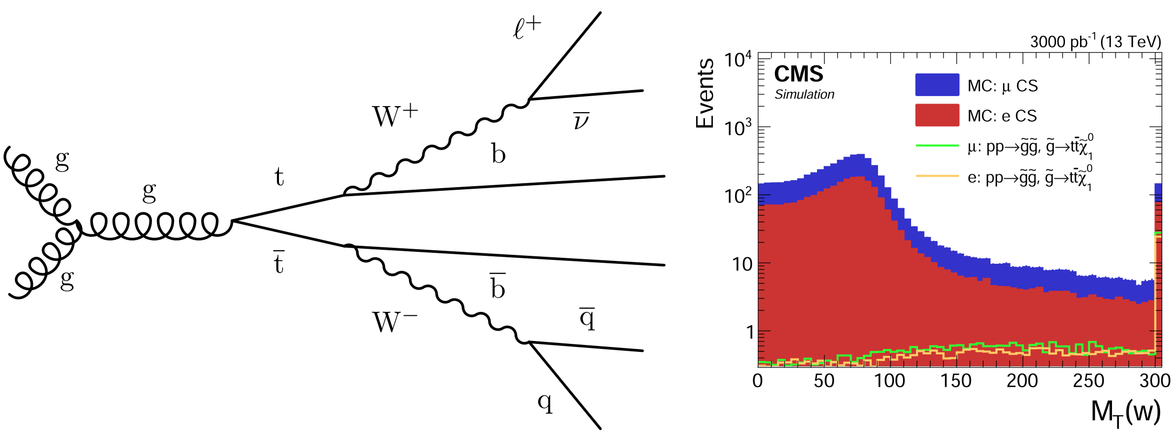

(a) (b)

Figure 6.11: An example diagram of the production of $t\bar{t}$ in the signal region (a), and the M_T distribution of the single-electron and -muon control samples for simulated $t\bar{t}$ and W+jets events together with a typical T1tttt signal distribution (b) [92]. For purposes of visibility, the T1tttt cross section is increased by a factor of 10 and the rightmost bin in the plot includes overflow.

The method for predicting the top+W background relies on BDT shape agreement between the control sample and background. In our analysis, leptons are included in the jet clustering procedure and thus in the calculation of H_T and H_T^{miss}. As a consequence, the distributions of the jet based kinematic variables, and hence the BDT output, are similar between the control and signal samples. Small differences might arise from out-of-acceptance lost-lepton events. However, the lepton p_T is small for those events because, by definition, either $p_T < 10$ GeV, or else $|\eta| > 2.5$ (electrons) or $|\eta| > 2.4$ (muons), which generally results in small p_T. Furthermore, high p_T leptons will almost always be reconstructed as some type of particle, even if it fails the lepton reconstruction or isolation requirements. Therefore, treating the control sample lepton as a jet will reproduce similar event kinematics as the top+W background. Nevertheless, shape corrections based on the probability a lepton might fail the veto requirements improves the performance when the method is applied to simulation. These corrections are typically based on event and/or lepton kinematics. Figure 6.12 schematically illustrates how events with leptons enter our search region. The three criteria for which leptons become lost are if the electron or muon fail:

- kinematic acceptance;
- reconstruction; or
- isolation.

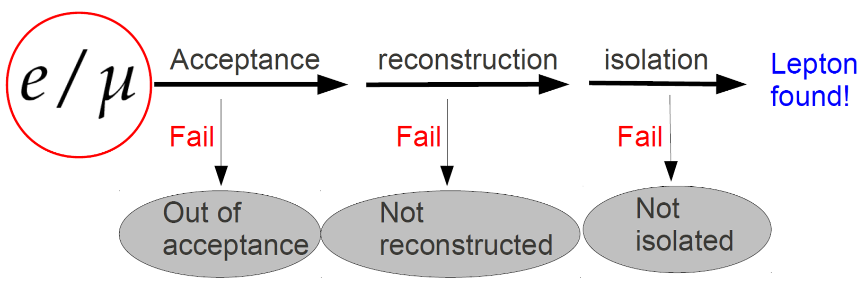

Figure 6.12: If an electron or muon does not satisfy one or more of the three indicated criteria, the lepton is considered to be *lost*.

The event weights used to correct the BDT shape difference between signal region top+W and SL top+W rely on determining the lepton efficiencies. The efficiencies are obtained from simulations of $t\bar{t}$, W, single-top, and exotic processes; the corresponding samples are given in Tables 3.1 and 3.3. We apply the baseline selection without any lepton identification or selection criteria and without the isolated-track veto. Generator information is used to select only events with exactly one hard lepton. From this information, we determine the acceptance by comparing the generated lepton p_{T} and η to our lepton acceptance requirements ($p_{\mathrm{T}} > 10$ GeV and $|\eta| < 2.5$ (e) or $|\eta| < 2.4$ (μ)). For generated leptons that pass acceptance, we define the reconstruction efficiency, ϵ_{reco}, as the fraction of them that are matched to an identified and reconstructed lepton. The fraction of these leptons that pass the isolation requirement define the isolation efficiency, ϵ_{iso}. The fraction of events that pass the $\mathrm{M_T}$ selection are denoted $\epsilon_{\mathrm{M_T}}$. Finally, there are two purity factors we consider in the top+W prediction. First, we have $\beta_{1\ell}$, which is the fraction of single generated leptons over the sum of generated single-lepton and dileptons in the single-lepton control sample. Second, we have β_{ℓ}, which is the fraction of single lepton events in which the generated lepton is prompt. Finally, once events in the control sample are weighted by the probability of becoming lost, we compute the fraction of the resulting events that will pass the isolated-track veto. These isolated-track efficiencies are computed separately for isolated-track veto isolation, reconstruction, and acceptance, denoted by $\epsilon^{!iso}_{\mathrm{isotrk}}$, $\epsilon^{!reco}_{\mathrm{isotrk}}$, and $\epsilon^{!acc}_{\mathrm{isotrk}}$, respectively. The lepton isolation and reconstruction efficiency maps are corrected for data/simulation differences using a Tag-and-Probe study, as described in Section 6.3.3. Also, the data/simulation agreement of the isolated track veto efficiencies are validated using Tag-and-Probe. Furthermore, dileptonic events can also contribute to the lost-lepton background when both leptons are lost.

To maintain reasonable statistical precision, we investigate the salient variables to bin the efficiency maps and integrate over other variables where necessary. Variables considered include event kinematics such as $\mathrm{H_T}$, $\mathrm{H_T^{miss}}$, $\mathrm{N_{jet}}$, $\mathrm{N_{b\text{-}jet}}$, and $\Delta\phi(\vec{\mathrm{H}}_\mathrm{T}^{\mathrm{miss}}, j_i)$. Additionally, we investigate lepton observables such as p_T, $|\eta|$, and the *activity*, around the lepton, which is defined as the sum of PF candidates in an annulus outside the standard isolation cone relative to the p_T of the lepton:

$$\mathcal{A} \equiv \left(\sum_{\mathtt{PFcands}}^{R_{\mathtt{miniIso}}<r<0.4} p_\mathrm{T} \right) / p_\mathrm{T}(\mathrm{lepton}) \tag{6.9}$$

The binning structure and efficiency definitions are summarized below:

- Acceptance efficiency (ϵ_{acc}): $\mathrm{H_T}$, $\mathrm{H_T^{miss}}$, $\mathrm{N_{jet}}$, $\mathrm{N_{b\text{-}jet}}$, and $\Delta\phi(\vec{\mathrm{H}}_\mathrm{T}^{\mathrm{miss}}, j_i)$;

- Reconstruction efficiency (ϵ_{reco}): lepton p_T and $|\eta|$;

- Isolation efficiency (ϵ_{iso}): lepton p_T and $\mathcal{A}$;

- Lepton purity (β_ℓ): $\mathrm{H_T^{miss}}$, $\mathrm{N_{jet}}$;
- $\mathrm{M_T}$ efficiency ($\epsilon_{\mathrm{M_T}}$): $\mathrm{H_T}$, $\mathrm{H_T^{miss}}$, $\mathrm{N_{jet}}$, $\mathrm{N_{b\text{-}jet}}$, and $\Delta\phi(\vec{\mathrm{H}}_\mathrm{T}^{\mathrm{miss}}, j_i)$;
- Dilepton purity ($\beta_{1\ell}$): $\mathrm{N_{jet}}$, $\mathrm{N_{b\text{-}jet}}$;
- Dilepton contribution to signal region (ϵ_{dilep}): $\mathrm{N_{jet}}$, $\mathrm{N_{b\text{-}jet}}$; and
- Isolated track veto efficiencies ($\epsilon_{\mathrm{isotrk}}^{!iso}$, $\epsilon_{\mathrm{isotrk}}^{!reco}$, $\epsilon_{\mathrm{isotrk}}^{!acc}$): $\mathrm{H_T}$, $\mathrm{H_T^{miss}}$, $\mathrm{N_{jet}}$, $\mathrm{N_{b\text{-}jet}}$, and $\Delta\phi(\vec{\mathrm{H}}_\mathrm{T}^{\mathrm{miss}}, j_i)$.

To model the number of non-isolated leptons in the signal region, we compute

$$N_{!iso} = \frac{N_{SL}}{\epsilon_{iso}} \cdot (1 - \epsilon_{iso}), \tag{6.10}$$

where the fractional term is the number of control region events, N_{SL}, corrected for isolation efficiency loss. The remaining factor in Equation 6.10 scales the corrected control region events to give us the number of leptons lost to isolation requirements, $N_{!iso}$. To model the number of unreconstructed leptons, we correct N_{SL} by both ϵ_{iso} and ϵ_{reco} to obtain

$$N_{!reco} = \frac{N_{SL}}{\epsilon_{iso} \cdot \epsilon_{reco}} \cdot (1 - \epsilon_{reco}). \tag{6.11}$$

The next step is to obtain the prediction for the number of leptons that are outside of acceptance,

$$N_{!acc} = \frac{N_{SL}}{\epsilon_{iso} \cdot \epsilon_{reco} \cdot \epsilon_{acc}} \cdot (1 - \epsilon_{acc}). \tag{6.12}$$

The last step is to obtain the number of dileptonic events that enter our search region,

$$N_{dilep} = N_{SL} \cdot (1 - \beta_{1\ell}) \cdot \epsilon_{dilep}. \tag{6.13}$$

Here, we apply the purity factor to N_{SL} to obtain the number of dileptonic events in the SL CS before applying the efficiency factor that represents the number of dilepton events that end up in our signal region.

Combining the above equations gives us the formula for determining the bin-by-bin number of leptons from top and W processes that become lost,

$$N_{LL} = \frac{\beta_\ell}{\epsilon_{\mathrm{M_T}}} \cdot \left[\beta_{1\ell}\left(\epsilon_{\mathrm{isotrk}}^{!iso} \cdot N_{!iso} + \epsilon_{\mathrm{isotrk}}^{!reco} \cdot N_{!reco} + \epsilon_{\mathrm{isotrk}}^{!acc} \cdot N_{!acc}\right) + N_{dilep}\right]. \tag{6.14}$$

We do this separately for the muon and electron CS and obtain an average value for N_{LL}/N_{SL} for each bin of the BDT output discriminant. The resulting BDT shape agrees well with the signal region when tested on simulation. This test, as well as additional simulation closure tests of methods described below, is documented in Figure 6.18a. However, to proceed with the explanation of the top+W and QCD backgrounds, we must first describe the low Min[$\Delta\phi$] control sample.

6.4.2 Low Min[$\Delta\phi$] Control Sample and QCD Shape Determination

The dominant mechanism for QCD events passing the baseline selection is through the mismeasurement of one of the leading jets in the event. This process is illustrated in Figure 6.13a. To select a rich sample of QCD events, we invert the selection on $\Delta\phi(\vec{\mathrm{H}}_{\mathrm{T}}^{\mathrm{miss}}, j_i)$. As shown in Figure 6.13b, events with Min[$\Delta\phi$] < 0.1 have a large fraction of QCD events according to simulation.

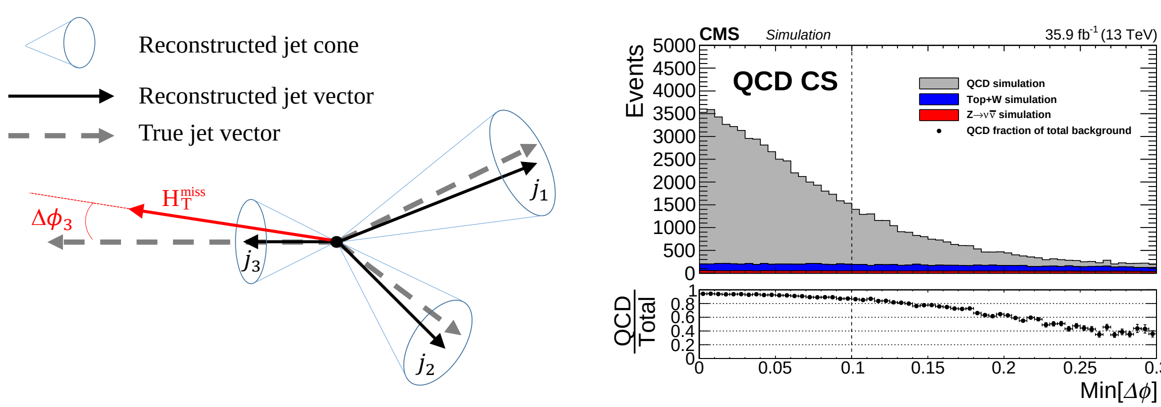

(a) (b)

Figure 6.13: Illustration of a typical multi-jet event, in the transverse plane, with no real missing momentum but poor measurement of a high p_{T} jet resulting in large $\mathrm{H}_{\mathrm{T}}^{\mathrm{miss}}$ (a). Data compared to simulation of the minimum $\Delta\phi$ between $\mathrm{H}_{\mathrm{T}}^{\mathrm{miss}}$ and the four leading jets (b). The QCD control sample consists of events with $\Delta\phi(\vec{\mathrm{H}}_{\mathrm{T}}^{\mathrm{miss}}, j_i) < 0.1$.

Non-QCD contamination is measured and subtracted from the control sample. For Z contamination, we invert the selection on Min[$\Delta\phi$] in data and simulation and proceed using the Z $\rightarrow \nu\bar{\nu}$ estimation procedure described in Section 6.3. We measure the top+W contamination in the low Min[$\Delta\phi$] control sample by fitting QCD shapes from simulation and top+W shapes from the SL

CS, with efficiency corrections, to the low Min[$\Delta\phi$] data in the top+W like BDT output discriminant. The result of these fits applied to simulation, as a closure test, and to data is shown in Figures 6.14a and 6.14b, respectively.

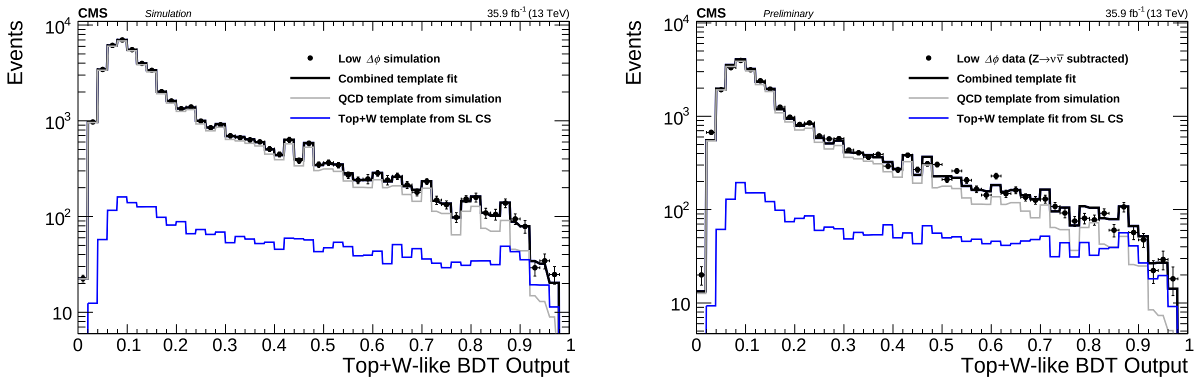

(a) (b)

Figure 6.14: Fit of top+W contamination in the low $\Delta\phi(\vec{\mathrm{H}}_{\mathrm{T}}^{\mathrm{miss}}, j_i)$ using template fits in straight simulation (a) and in data (b). The QCD templates originate from simulation while the top+W templates are from the single lepton control sample.

While the low Min[$\Delta\phi$] control sample has high QCD purity, a natural challenge arises from using events with, by definition, a subset of biased BDT inputs. This will lead to shape differences between the control sample and signal region BDT output. We correct this shape difference by computing the ratio in simulation

$$\mathcal{R}_{\Delta\phi} = \frac{N_{\mathrm{QCD}}(\mathrm{Min}[\Delta\phi] > 0.1)}{N_{\mathrm{QCD}}(\mathrm{Min}[\Delta\phi] < 0.1)}, \tag{6.15}$$

where $N_{\mathrm{QCD}}(\mathrm{Min}[\Delta\phi] > 0.1)$ is the bin-by-bin number of events from QCD in the signal region and $N_{\mathrm{QCD}}(\mathrm{Min}[\Delta\phi] < 0.1)$ is the bin-by-bin number of events in the control sample. The shapes of $\mathcal{R}_{\Delta\phi}$ in the top+W-like BDT and signal-like BDT discriminators, given in Figures 6.15a and 6.15b, are smooth and steadily rising in the signal region.

We wish to validate $\mathcal{R}_{\Delta\phi}$ in data. To do so, we select events failing the PFoverCaloMETFilter filter with PFMET/CaloMET < 0.9. Events satisfying this criterion typically have large fake-$\mathrm{H}_{\mathrm{T}}^{\mathrm{miss}}$ and are empirically found to be very pure in QCD events ($> 95\%$). This validation region is limited by statistics, but can be used to constrain mismodeling of $\mathcal{R}_{\Delta\phi}$. Similar to how

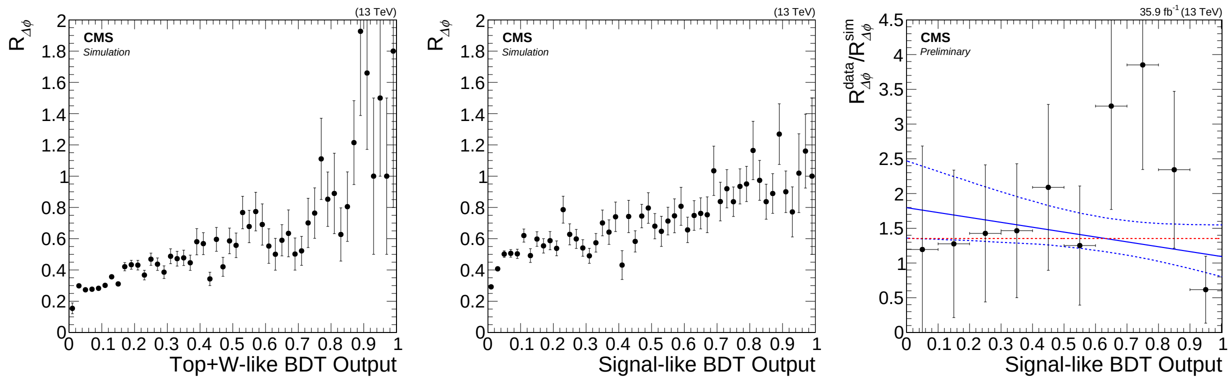

(a) (b) (c)

Figure 6.15: The $\mathcal{R}_{\Delta\phi}$ ratio in simulation for the Top+W-like BDT discriminant (a) and the signal-like BDT discriminant (b). The double ratio using the low PF/Calorimeter $\mathrm{E}_{\mathrm{T}}^{\mathrm{miss}}$ (c) is used to calibrate $\mathcal{R}_{\Delta\phi}$ in data.

we calibrate the $\mathrm{Z} \to \nu\overline{\nu}$ background, a double ratio can be defined as

$$\rho_{\mathrm{QCD}} = \frac{\mathcal{R}^{\mathrm{data}}_{\Delta\phi}}{\mathcal{R}^{\mathrm{sim}}_{\Delta\phi}}, \tag{6.16}$$

where each term is evaluated using the low PFMET/CaloMET selection. In the signal-like BDT output, ρ_{QCD} is found to be flat within statistical uncertainty as shown in Figure 6.15c. Since the QCD normalization is obtained using a more precise method described below, we do not scale the QCD prediction by the central value of ρ_{QCD}. However, we do use the uncertainties from the linear fit to ρ_{QCD} as described in Section 6.4.4.

With the shape corrections to both the single-lepton and low Min[$\Delta\phi$] control samples in place, we can now extract the normalizations of the QCD and top+W backgrounds from the $\mathrm{Z} \to \nu\overline{\nu}$ subtracted sideband data. The shape-corrected low Min[$\Delta\phi$] control data becomes the QCD shape, and the efficiency corrected single lepton data becomes the top+W shape. We fit these shapes to the $\mathrm{Z} \to \nu\overline{\nu}$ subtracted sideband data in the top+W-like BDT output discriminant. The result of this procedure applied to simulation is shown in Figure 6.16a, and the test is found to be accurate to about 1%. The fit-based normalization determination in data is shown in Figure 6.16b.

With BDT shapes and background normalizations determined, the only remaining step is to

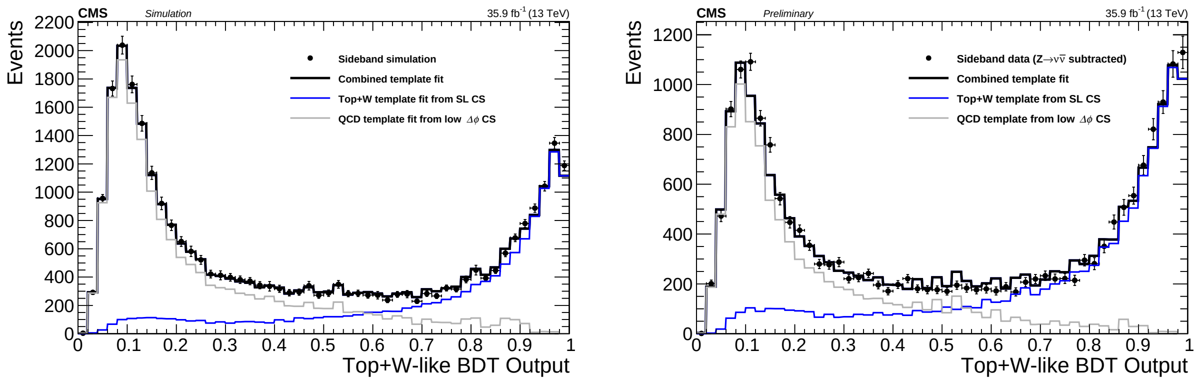

(a) (b)

Figure 6.16: Fit of top+W and QCD to obtain sideband normalization of each background in simulation (a) and in data (b). The QCD templates originate from the low $\Delta\phi(\vec{\mathrm{H}}_{\mathrm{T}}^{\mathrm{miss}}, j_i)$ control sample while the top+W templates are from the single-lepton control sample. Error bars shown represent only the statistical uncertainty on the $\mathrm{Z} \rightarrow \nu\bar{\nu}$ subtracted sideband data.

measure the associated systematic uncertainties. Sections 6.4.3 and 6.4.4 list the top+W and QCD systematic uncertainties, respectively. Section 6.5 gives the signal systematic uncertainties.

6.4.3 Top+W Systematic Uncertainties

The following sources of systematic uncertainties are included for the top+W background prediction:

- **Lepton isolation efficiency: 1-4%.** The muon and electron isolation efficiencies are obtained from simulated events. To account for isolation efficiency differences in data and simulation, the Tag-and-Probe method described in Section 6.3.3 is used to obtain data/simulation scale factors (SFs). The efficiency maps from simulation are corrected by these SFs and the recommended uncertainties on the SFs are propagated. Separate nuisance parameters are assigned for muon and electron isolation efficiency. The individual lepton uncertainties are taken to be fully correlated across all search bins.

- **Lepton reconstruction/ID efficiency: 3-6%.** As above, the muon and electron reconstruction and ID efficiencies are obtained from simulated events, and scale factors are derived from differences between efficiencies measured in data and simulation. A fully correlated uncertainty structure is assumed for each lepton.

- **Lepton acceptance: 1-3%.** Leptons lost from being out of acceptance cannot be measured directly in data. Therefore, the acceptance correction is determined from simulation with no supporting scale factor. The uncertainty of the acceptance efficiency is derived from studies of the parton distribution functions (PDF) and the renormalization and factorization scale. We vary the PDF sets and scale uncertainties and take the corresponding bin-by-bin deviations in the acceptance as a systematic uncertainty. The acceptance uncertainty is assumed to be uncorrelated across all bins.

- **Lepton purity: <1%.** The purity is expected to be very high ($> 99\%$ for muons, $> 95\%$ for electrons as determined from simulation). The small impurity leads to a minor systematic uncertainty on the total prediction. A conservative uncertainty of 20% on the impurity is assigned and is taken to be uncorrelated in all search bins.

- **Dilepton correction: 1-3%.** Dileptonic corrections are small compared to the single lepton fraction and are obtained directly from simulation. A conservative systematic uncertainty of 50% is assigned on the dileptonic contribution and is assumed to be uncorrelated bin-by-bin.

- **$\mathrm{M_T}$ cut efficiency: 0.5-1%.** The uncertainty associated with the $\mathrm{M_T}$ cut is found from varying the jet energy corrections (JECs). The $\mathrm{E_T^{miss}}$ and $\mathrm{M_T}$ are recalculated and the subsequent uncertainty is derived bin-by-bin, where it is assumed to be uncorrelated.

- **Isolated-track vetoes: 2-3%.** We perform Tag-and-Probe studies to determine this uncertainty. We find that it dominantly depends on $\mathrm{N_{jet}}$ and is parametrized in this way. The isolated-track veto uncertainty is assumed to be fully correlated across all search bins.

- **Hadronic-τ non-closure: 1-46%** An implicit assumption in the top+W background estimation is that the BDT shape for events containing a lepton that is lost is the same as for events with a τ that decays hadronically. We test this assumption directly in simulation as shown in Figure 6.17. We assign an uncorrelated uncertainty based on the bin-by-bin difference observed in simulation shapes.

- **Top+W normalization: 1.4%.** The uncertainty from the fit to the top+W-like BDT discriminant is added in quadrature to the non-closure uncertainty in the normalization determination when applied to simulation. This uncertainty is taken to be correlated across all search bins.

- **Single-lepton sample statistics: 6-12%.** The control sample size ranges from 38 to 114 single-lepton events with a corresponding transfer factor of around 0.7. The control sample statistical treatment is described in Section 6.6.1.1.

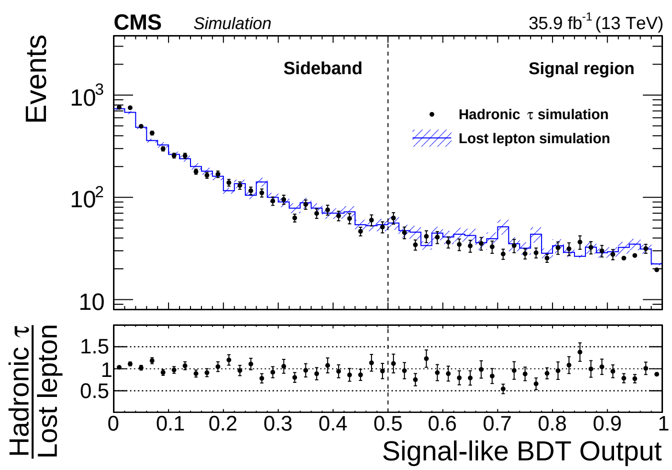

Figure 6.17: The ratio of hadronically decaying τ background to lost-lepton type background in the signal region as given by simulation. The deviation from unity in the ratio is used as a systematic on the top+W background prediction.

6.4.4 QCD Systematic Uncertainties

The following sources of systematic uncertainty are considered for the QCD background prediction.

- $\mathcal{R}_{\Delta\phi}$ **statistics: 12-50%.** While the QCD simulation generally lacks statistical precision, the high $\mathrm{H_T}$ cut combined with the coarse granularity of the analysis bins mitigates the size of the uncertainty. The $\mathcal{R}_{\Delta\phi}$ statistics are taken to be an uncorrelated nuisance parameter in all bins.

- **Double ratio: 18-33%.** Since the normalization for the QCD background is obtained from the sideband fits, we do not apply the central value of ρ_{QCD} as a scaling factor. However, we do consider the shape uncertainty by extracting the error bands in Figure 6.15c. In quadrature, we add the deviation from flatness in the line of best fit to the QCD double ratio. The resulting uncertainty is taken to be uncorrelated across all bins.

- **b-tag scale factors: <1-5%.** We apply b-tag scale factors to simulation before calculating $\mathcal{R}_{\Delta\phi}$. Uncertainties in the b-tag scale factors are propagated and the resulting deviation in the prediction is considered as a systematic uncertainty. An uncorrelated uncertainty structure is assumed.

- **Electroweak background contamination: 4-60%.** The non-QCD contamination in the low $\Delta\phi(\vec{\mathrm{H}}_{\mathrm{T}}^{\mathrm{miss}}, j_i)$ control sample is varied by 50% and the resulting change in the QCD prediction is propagated as an uncorrelated systematic uncertainty in all search bins.

- **QCD normalization: 1.2%.** The uncertainty from the fit to the top+W-like BDT discriminant is added in quadrature from the non-closure uncertainty in the normalization determination when applied to simulation. This uncertainty is correlated across all search bins.

- **Low Min[$\Delta\phi$] sample statistics: 7-100%.** The number of low $\Delta\phi(\vec{\mathrm{H}}_{\mathrm{T}}^{\mathrm{miss}}, j_i)$ control sample events ranges from 0 to 53 events. The bin-by-bin central value of the transfer factor ranges between 0.37 and 1.21 and has an average value of 0.77. The control sample statistical treatment is described in Section 6.6.1.1.

We test the full procedure for the top+W and QCD background prediction by selecting control sample events from simulation and comparing the prediction to yields from simulation in the signal region. In this test we treat simulation like data and expect to get back a result which is consistent with the direct yields. The result of this closure test is shown in Figure 6.18.

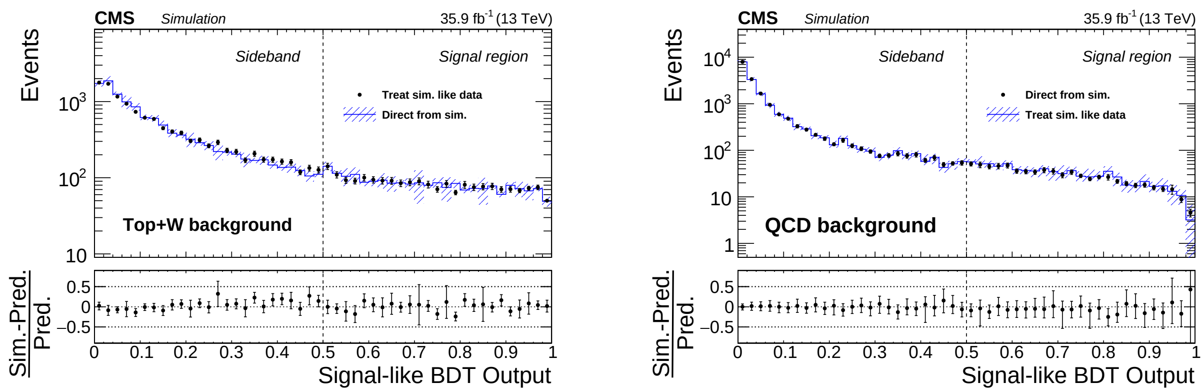

(a) (b)

Figure 6.18: Validation of the data-driven methods to measure top+W (a) and QCD (b) by treating the simulation as if it were data and comparing the result to the simulation directly.

6.5 Signal Systematic Uncertainties

We account for the following signal systematic uncertainties:

- **Luminosity: 2.5%.** The integrated luminosity estimation is based on data from five sub-detectors and the use of five luminosity algorithms [70]. The sub-detectors used include the CMS pixel detector, barrel DTs, and HF calorimeter described in Sections 2.3.3, 2.3.6 and 2.3.5, respectively. Also utilized are the Pixel Detector Telescope (PLT) and the Fast Beam Conditions Monitor (BCM1F) diamond sensors [98, 99]. The algorithms used are the Pixel Cluster Counting (PCC) method and the vertex, PLT, BCM1F diamond, and HF zero counting methods [70, 98, 99, 100]. Since our signal samples are scaled to match the data at 35.9 fb^{-1}, we must account for the uncertainty in this measurement. We find the uncertainty in the luminosity to be 2.5% [70]. We treat this as a correlated nuisance parameter across the entire search binning.

- **Isolated track veto: 2%.** We are sensitive to differences between data and simulation in the isolated-track veto efficiencies. This systematic uncertainty is only non-negligible for signal models where we expect isolated tracks from leptonic W decays: T1tttt and T2tt. We validate the isolated track veto, ϵ_{isotrk}, using Tag-and-Probe methods in data. The value of ϵ_{isotrk} is found to be independent of the search variables and has an average value of 32%, 40%, and 35% for isolated muon, isolated electron, and isolated pion tracks, respectively. We find differences in simulation and data to be small, and we assign a 2% systematic uncertainty correlated across the entire search binning to account for our degree of accuracy in measuring this scale factor.

- **PF Jet ID: 1%.** The jet ID criteria of N(constituents), charged multiplicity, and neutral multiplicity, defined in Section 4.10, are not well modeled in fast simulation. Thus we do not apply the jet ID criteria to the fast simulation signal samples. In full simulation, we measure the jet ID efficiency to be $\geq$ 99%. We apply a flat 99% efficiency to the fast simulation MC and assign a fully correlated 1% systematic uncertainty to this scale factor.

- b**-tag efficiency: <1%-5%.** As noted in Sections 4.10.1 and 5.1.1, differences between data and simulation in b-tag efficiency are corrected for by using weights. We reassign the b-tagged jet multiplicity according to the output of a random number compared to the event's probability of having $\text{N}_{\text{b-jet}}$. This procedure is repeated after varying the b-tagging, charm-mistagging, and light flavor-mistagging scale factors independently. This gives us nine additional values for $\text{N}_{\text{b-jet}}$ for which we take the maximum and minimum deviation as three separate bin-by-bin uncorrelated uncertainties, with no net effect on signal efficiency.

- b**-tag FastSim corrections: <1-4%.** Despite the differences between FastSim and FullSim, the overall performance of FastSim is quite good and differences in b-tagging of jets is small [60]. However, as with the scale factors above, any differences between data and simulation need to be properly accounted for by deriving the appropriate corrections. Accordingly, uncertainties in the b-tagging, charm-mistagging, and light flavor-mistagging rates are varied independently and are propagated as migrations in the independent signal regions.

- **Signal sample statistics: <1-5%.** After event selection, the absolute number of simulated events, combined with the appropriate transfer factor, are treated as a bin-by-bin systematic uncertainty. The details of this treatment are described in Section 6.6.1.1. A benefit of binning the data in an MVA discriminant is that the most sensitive bins also tend to have the largest signal statistics. Therefore, sample statistics generally have negligible impact on the sensitivity of the search.

- **Trigger efficiency: 0.2-0.8%.** We scale the simulated signal by the measured trigger efficiency in data, using a Bayesian Neural Network (BNN). This efficiency is corrected for as a function of $\mathrm{H_T^{miss}}$ and the output of the BNN is varied at $\pm 1\sigma$ in the distribution of the ensemble. The trigger efficiency uncertainty is small and is treated as fully correlated across the search bins.

- **Pileup re-weighting: <1-5%.** The effects of pileup differences between data and simulation appear to be tiny. We apply a systematic uncertainty to cover any potential effect on the signal efficiency. To do this, we split the sample in equal parts about the mean value of the pileup distribution. From this sample we derive a linear parameterization of the change in signal efficiency as a function of mean pileup. We then take the change in efficiency, evaluated at the mean pileup as measured in data, as the systematic uncertainty. The pileup systematic uncertainty is correlated across all search bins.

- **Theory Scales: <1-3%.** As described in Section 2.1.1, the parton distribution function of the proton depends on the renormalization and factorization scales, μ_R and μ_F. We vary these scales by a factor of 2 and derive the uncertainty from the subsequent envelope [101, 102]. This uncertainty is taken to be correlated across all search bins.

- **ISR: <1-10%.** ISR mismodeling in simulation is corrected for using a data-driven approach. To derive an ISR correction, we select a pure $t\bar{t}$ sample by choosing events with two leptons (electrons or muons) and two b-tagged jets. In this sample, any other jets in the event arise from ISR. The correction factors are 1.000, 0.920, 0.821, 0.715, 0.662, 0.561, 0.511 for $N_{\mathrm{jet}}^{\mathrm{ISR}} = 0, 1, 2, 3, 4, 5, 6+$, respectively. To ensure the overall sample cross section is unchanged, we apply a factor to preserve normalization, which is typically around 1.15. We take 50% of the deviation from unity as the systematic uncertainty and recalculate the bin-by-bin signal yields with the $\pm 1\sigma$ ISR corrections. The effect on the yield is fully correlated across all signal bins.

- **Jet Energy Corrections: <1-4%.** We apply simulation level jet energy corrections (JECs) to scale to the appropriate jet response in data. The JECs are measured by comparing data from an unbiased trigger against simulation using the missing transverse energy projection fraction (MPF) method on dijet events [103, 104]. The MPF method exploits the lack of $\mathrm{E}_{\mathrm{T}}^{\mathrm{miss}}$ and subsequent balance observed by the hadronic recoil in the transverse plane in γ and $\mathrm{Z} \rightarrow \ell^+\ell^-$ events. These corrections are typically 1–20% in size and vary with jet p_{T} and $|\eta|$. We propagate the variations in the JECs and recalculate any jet dependent observable, including $\mathrm{N}_{\mathrm{jet}}$, $\mathrm{N}_{\mathrm{b\text{-}jet}}$, H_{T}, $\mathrm{H}_{\mathrm{T}}^{\mathrm{miss}}$, and $\Delta\phi(\vec{\mathrm{H}}_{\mathrm{T}}^{\mathrm{miss}}, j_i)$. The resulting bin-by-bin uncertainties are taken to be uncorrelated.

- **Jet Energy Resolution: ≤1%.** As with the JECs, jet energy resolution (JER) studies are performed to correct the simulated detector response. Simulated jet momenta are smeared to match the resolution in data. For low-p_{T} jets ($p_{\mathrm{T}} < 100$ GeV), the JER is pileup dependent and jets are typically resolved at the 20% level. For jets with $p_{\mathrm{T}} = 100$ GeV and $p_{\mathrm{T}} = 1$ TeV the JER is 10% and 5%, respectively [104]. We, again, propagate the uncertainties as variations in jet dependent observables. The overall effect is small, and we treat these uncertainties as uncorrelated.

- **Parton Distribution Functions:** The production cross section of a signal sample depends on the assumed parton distribution function (PDF), described in Section 2.1.1. The PDF4LHC group provides a prescription for determining a given model's PDF uncertainty [105, 106, 107, 108]. We evaluate these uncertainties and give them as $\pm 1\sigma$ bands in the limits shown in Figure 6.21.

- **Signal contamination:** Contamination of SUSY signal in the background predictions can manifest in three possible modalities. We account for signal contamination using the *reduced efficiency* method, whereby, contamination measured in simulation is subtracted from signal yields in the signal bins. The three sources are given as follows:

  (1) *Sideband contamination* results when signal events fall below the BDT signal selection cut of 0.5. Generally, this source is small and is least important in the most sensitive BDT bins, but its relative importance grows for signal sources with a soft $\mathrm{E}_{\mathrm{T}}^{\mathrm{miss}}$ spectrum. The consequence of sideband contamination is an overestimation of the normalization of one of the two backgrounds obtained from sideband data. We find that the sideband signal reliably peaks at large values of the top+W-like BDT output discriminant. The result is that any signal in the sideband gets absorbed into the top+W background normalization. We therefore use the signal-like BDT shape of the top+W background as the shape of the sideband contamination. We normalize the fraction of the shape below 0.5 to the total signal yield in the sideband and consider the result as contamination.

  (2) *Low Min*[$\Delta\phi$] *CS contamination* occurs when signal events appear in the low Min[$\Delta\phi$] control sample. Since the selection on $\Delta\phi(\vec{\mathrm{H}}_{\mathrm{T}}^{\mathrm{miss}}, j_i)$ is very restrictive in the control sample definition, the low Min[$\Delta\phi$] CS contamination is small. Nevertheless, we account for the contamination by considering the few signal events below the Min[$\Delta\phi$] threshold. We propagate these events with the exact transfer factors applied to the control sample to extract the yield of signal events from contamination.

(3) *SL CS contamination* are signal events in the single-lepton control sample. The M_T cut, shown in Figure 6.11b, reduces the size of the SL CS contamination. Furthermore, signal models without prompt lepton production, such as T1bbbb and T1qqqq, have negligible yields in the SL CS and contamination is not considered. For the remaining signal models, events in the SL CS surviving the M_T cut are propagated using the same transfer factors as those applied to the SL CS to extract the yield of signal events from contamination.

The H_T^{miss} in the single-γ and $Z \to \ell^+\ell^-$ control regions is artificial, as we manually remove the relevant particles from the event. Therefore, no signal contamination is considered from the $Z \to \nu\overline{\nu}$ background prediction.

6.6 Results

We perform the data-driven background estimations described with the blinding criteria applied to the signal data. After a full prediction is made, complete with all associated uncertainties, we unblind the signal data and compare to the SM expectation. As shown in Figure 6.19, no significant deviation with the SM expectation is observed. Table 6.2 also gives the prediction compared to observation in each of the 25 signal bins. Appendix A contains Table A.1 with the corresponding sideband yields. Overall, agreement between prediction and observation is good. We appear to see a mild deficit in data in the region with signal-like BDT value between around 0.7 and 0.88. Three of the four most sensitive bins show a slight underprediction, but each of these bins is within one standard deviation of the background expectation. In Figure 6.20, we overlay signal from the four separate SMS models considered. Each mass point shown in Figure 6.20 was at or just beyond the reach of searches performed on the first 2.3 fb^{-1} of 13 TeV data taken during 2015 [109, 110, 111].

Table 6.2: Observed number of events compared to prediction in the search bins. The upper and lower uncertainties on the prediction are given separately, formatted as STAT + SYST, and the absolute number of observed events are given in the rightmost column. The corresponding table of sideband yields (Table A.1) is given in Appendix A.

Analysis Bin	QCD Pred.	Top+W Pred.	$Z \to \nu\bar{\nu}$ Pred.	Total Pred.	Observation
26	$31.7^{+4.7+9.7}_{-4.1-8.5}$	$77^{+7.6+11}_{-7.0-11}$	$77.1^{+5.5+6.2}_{-5.2-5.4}$	$186^{+11+16}_{-9.6-15}$	184
27	$31^{+4.6+16}_{-4.0-7.9}$	$73.0^{+7.2+6.1}_{-6.6-5.8}$	$67.6^{+5.1+5.0}_{-4.7-4.7}$	$172^{+10.0+18}_{-9.1-11}$	154
28	$31.8^{+4.8+9.4}_{-4.2-8.2}$	$70^{+7.8+18}_{-7.1-18}$	$67.9^{+5.3+5.1}_{-4.9-5.0}$	$170^{+11+21}_{-9.6-20}$	144
29	$30.7^{+4.9+9.1}_{-4.2-7.5}$	$52^{+6.3+13}_{-5.6-13}$	$59.9^{+4.7+4.4}_{-4.4-4.7}$	$143^{+9.3+16}_{-8.3-15}$	156
30	$23^{+3.7+11}_{-3.2-11}$	$60.2^{+6.8+6.7}_{-6.1-6.5}$	$63.8^{+5.0+4.8}_{-4.6-5.2}$	$147^{+9.2+14}_{-8.3-14}$	180
31	$17.4^{+3.0+7.2}_{-2.6-6.9}$	$53.3^{+6.6+6.9}_{-5.8-6.8}$	$57.7^{+4.8+4.4}_{-4.4-4.1}$	$128^{+8.7+11}_{-7.8-10}$	122
32	$30.3^{+5.1+9.0}_{-4.4-6.3}$	$58^{+7.0+13}_{-6.2-13}$	$50.4^{+4.4+4.1}_{-4.1-3.6}$	$139^{+9.7+16}_{-8.6-14}$	105
33	$13.3^{+2.9+5.3}_{-2.4-5.4}$	$52^{+6.4+12}_{-5.7-12}$	$55.8^{+4.6+4.4}_{-4.3-4.5}$	$121^{+8.4+14}_{-7.5-14}$	119
34	$17.0^{+3.2+7.0}_{-2.7-7.5}$	$39.1^{+5.3+3.0}_{-4.7-2.8}$	$59.2^{+5.0+4.7}_{-4.6-4.7}$	$115.3^{+8.0+9.0}_{-7.1-9.3}$	129
35	$25.2^{+5.3+7.6}_{-4.4-9.2}$	$55.3^{+6.6+9.9}_{-5.9-9.8}$	$46.4^{+4.1+4.6}_{-3.7-3.3}$	$126^{+9.4+13}_{-8.3-14}$	140
36	$30^{+5.7+16}_{-4.8-6.8}$	$53^{+6.6+25}_{-5.9-25}$	$51.3^{+4.5+4.2}_{-4.2-3.9}$	$135^{+9.9+30}_{-8.7-26}$	105
37	$26.1^{+5.6+7.0}_{-4.6-5.7}$	$46.4^{+5.8+3.8}_{-5.2-3.6}$	$65.0^{+5.1+5.4}_{-4.7-5.2}$	$137.4^{+9.6+9.7}_{-8.4-8.6}$	102
38	$20.8^{+4.3+7.0}_{-3.6-5.7}$	$41.0^{+5.4+5.7}_{-4.8-5.5}$	$53.0^{+4.8+4.5}_{-4.4-6.4}$	$114^{+8.4+10}_{-7.4-10}$	118
39	$17.8^{+4.0+9.9}_{-3.3-5.3}$	$45^{+5.9+16}_{-5.2-16}$	$46.6^{+4.4+4.1}_{-4.0-3.7}$	$109^{+8.4+19}_{-7.3-17}$	88
40	$18.4^{+4.2+6.8}_{-3.4-5.1}$	$45.7^{+5.9+5.8}_{-5.2-5.7}$	$54.2^{+4.7+4.8}_{-4.4-4.9}$	$118^{+8.7+10}_{-7.6-9.1}$	96
41	$34^{+7.1+11}_{-5.9-8.9}$	$41.8^{+5.7+3.4}_{-5.0-3.2}$	$43.1^{+4.1+4.6}_{-3.7-3.3}$	$119^{+10+13}_{-8.6-10}$	100
42	$17.0^{+4.4+5.7}_{-3.5-7.0}$	$45.8^{+6.0+5.0}_{-5.3-4.9}$	$48.4^{+4.4+4.9}_{-4.0-3.7}$	$111.3^{+8.6+9.0}_{-7.5-9.3}$	115
43	$13.0^{+3.5+4.6}_{-2.7-4.4}$	$41^{+5.8+16}_{-5.1-16}$	$44.8^{+4.4+4.2}_{-4.0-4.0}$	$99^{+8.0+17}_{-7.0-17}$	89
44	$16.7^{+4.2+6.0}_{-3.3-4.9}$	$42.3^{+5.7+3.0}_{-5.0-2.8}$	$47.2^{+4.3+4.6}_{-3.9-3.7}$	$106.2^{+8.3+8.1}_{-7.2-6.7}$	92
45	$11.8^{+4.4+5.5}_{-3.2-3.5}$	$37.6^{+5.4+3.2}_{-4.7-3.0}$	$41.7^{+4.1+4.1}_{-3.7-3.3}$	$91.1^{+8.1+7.6}_{-6.8-5.7}$	111
46	$3.1^{+1.4+2.2}_{-0.96-2.1}$	$42.3^{+5.8+3.9}_{-5.1-3.7}$	$45.0^{+4.2+5.0}_{-3.8-3.6}$	$90.4^{+7.3+6.7}_{-6.4-5.6}$	83
47	$13.0^{+4.0+6.9}_{-3.0-4.2}$	$33.3^{+5.0+7.5}_{-4.3-7.5}$	$42.8^{+4.3+4.3}_{-3.9-3.5}$	$89^{+7.7+11}_{-6.6-9.3}$	102
48	$2.7^{+1.2+2.7}_{-0.83-2.8}$	$35.9^{+5.4+8.5}_{-4.7-8.4}$	$40.3^{+4.1+4.2}_{-3.7-3.9}$	$78.8^{+6.9+9.8}_{-6.0-9.7}$	93
49	$10.6^{+4.2+4.5}_{-3.0-4.0}$	$40.5^{+5.7+3.0}_{-5.0-2.8}$	$45.0^{+4.3+4.8}_{-3.9-4.1}$	$96.1^{+8.2+7.2}_{-7.0-6.4}$	83
50	$0^{+1.0+0.63}_{-0-0}$	$28.8^{+5.1+4.2}_{-4.3-4.1}$	$25.4^{+3.4+2.8}_{-3.0-2.2}$	$54.2^{+6.2+5.1}_{-5.3-4.7}$	63

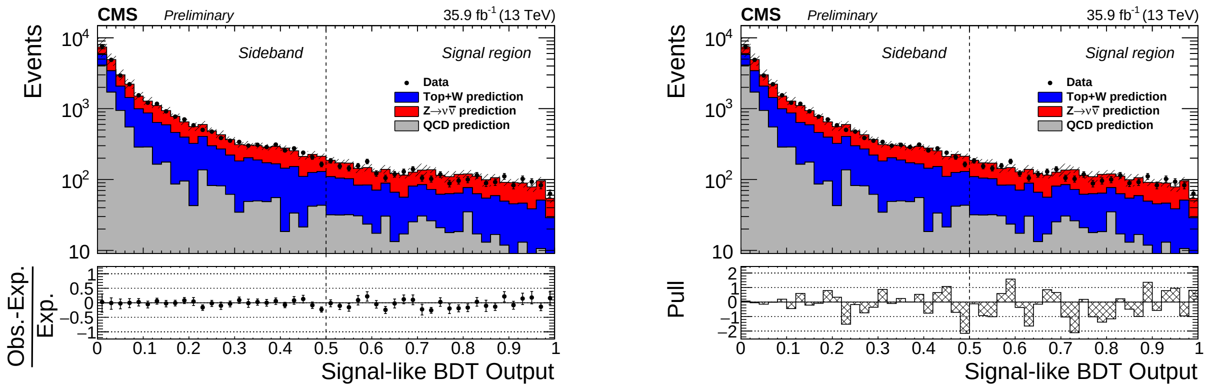

(a)

(b)

Figure 6.19: The observed data yields compared to the expected background in the sideband and signal region. The pull in the bottom plot of (b) is defined as $(\mathrm{N_{Obs.}} - \mathrm{N_{Exp.}})/\sqrt{\mathrm{N_{Obs.}} + (\delta\mathrm{N_{Exp.}})^2}$ where $\delta\mathrm{N_{Exp.}}$ is the total uncertainty on the background prediction.

6.6.1 Statistical Treatment

We wish to quantify the level of incompatibility of the data with the background plus signal hypothesis relative to the background only hypothesis and express it as a 95% confidence level (CL). The choice of 95% as threshold is convention. We set limits using the CL$_s$ criterion, a modified frequentist method [112, 113, 114, 115]. First, we construct the likelihood function which is a product of Poisson probabilities to observe N events in each bin. We use the test statistic

$$q_\mu = -2\ln\left(\mathcal{L}_\mu/\mathcal{L}_{\max}\right), \tag{6.17}$$

where $\mathcal{L}_\mu$ is the likelihood for a given signal strength μ and $\mathcal{L}_{\max}$ is the maximum likelihood determined by allowing all parameters to vary, including μ. Under the background only hypothesis with nonzero signal strength, we are more likely to observe a set of data with $q_\mu > 0$. A grid of several model points in the $m_{\tilde{\mathrm{g}}}$ (or $m_{\tilde{\mathrm{t}}}$) vs. $m_{\tilde{\chi}^0_1}$ plane are considered for setting upper limits on signal strength. We say that the model point is excluded when the 95% CL upper limit on μ drops to one.

Using classical frequentist inference, we can use toy pseudo-datasets with observation from a Poisson probability assuming background and a given signal strength. We can then determine

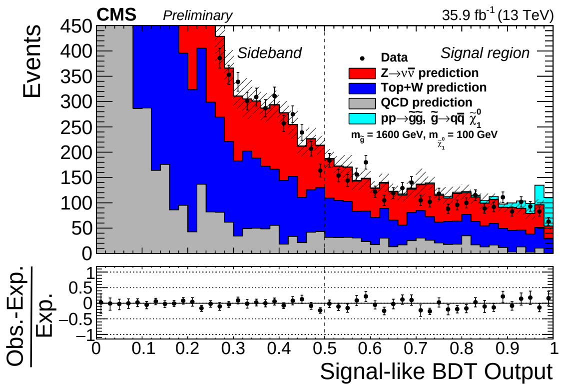

(a)

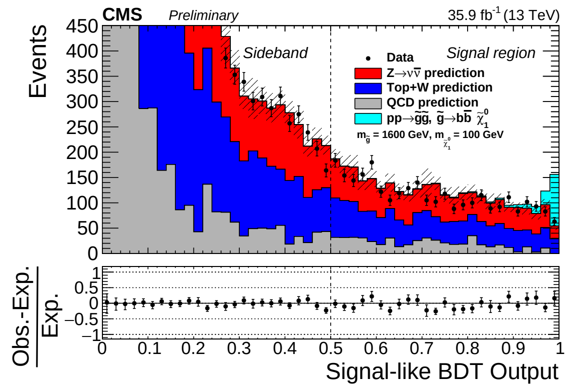

(b)

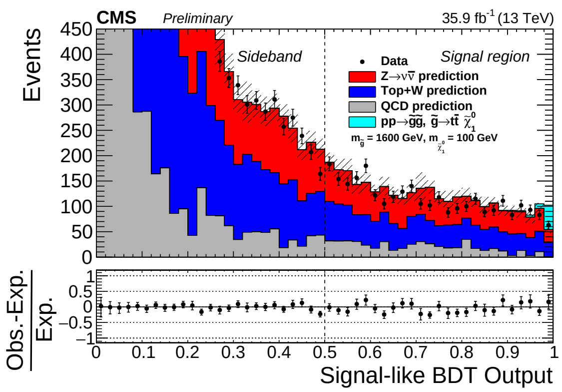

(c)

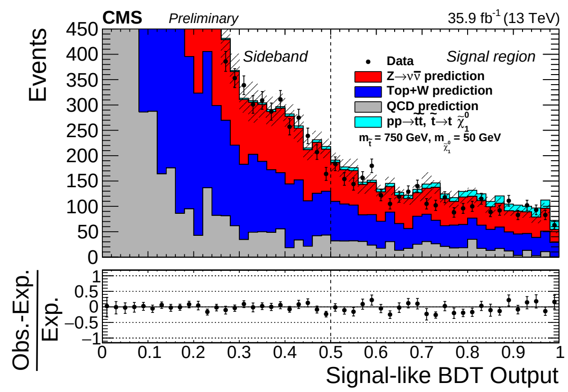

(d)

Figure 6.20: The observed data yields compared to the expected background in the sideband and signal region with signal model points stacked on the background for comparison. The difference plots compare only background prediction to observed data.

the fraction of toy datasets that produce a test statistic, q_μ^{toy}, that is less than q_μ. We could then exclude the signal at 95% confidence if the computed fraction, which we call CL_{s+b}, is < 0.05. However, to guard against downward fluctuations in the observation (or upward fluctuations in the background prediction) producing an exclusion limit of zero signal strength, we introduce a modification to the classical frequentist method. In this so-called CL_s method, we also calculate the fraction of toy datasets with $q_{\mu=0}^{\text{toy}} > q_{\mu=0}$, which we call CL_b. The ratio of these two quantities,

$$\text{CL}_s = \frac{\text{CL}_{s+b}}{\text{CL}_b}, \tag{6.18}$$

is what we require to be < 0.05 in order to exclude a signal at 95% confidence. This modified frequentist method is advantageous because it protects against overestimating our upper limits when we have weak signals and a downward background fluctuation.

All uncertainties in the background prediction and signal expectation enter the statistical analysis as nuisance parameters. Signal and background nuisance parameters, $s(\theta)$ and $b(\theta)$, are described with probability density functions (*pdf*'s) written as $\rho(\theta|\tilde{\theta})$. Here, θ is the nuisance parameter itself and $\tilde{\theta}$ is the best estimate of the nuisance parameter. The full likelihood used in Equation 6.17 includes constraints given by the nuisance parameter *pdf*'s. The nature of the systematic uncertainty determines the *pdf* chosen to describe the parameter. Uncertainties on event rates are discussed in Section 6.6.1.1. The remaining nuisance parameters are described in Section 6.6.1.2.

6.6.1.1 Control Region and Simulated Event Statistics

The gamma function is used to described the statistical uncertainties on the rate of events from data control regions and from signal simulation. Let N be either the total number of events in the data control region or the total number of generated events in simulation. Then the event rate in the signal region can be expressed as $n = \alpha \cdot N$. Here, α has its own set of uncertainties which are treated separately with log-normal *pdf*'s described below, but we describe the statistical uncertainty on n with

$$\rho(n|N) = \frac{1}{\alpha}\frac{(n/\alpha)^N}{N!}e^{-n/\alpha}. \tag{6.19}$$

This results in a mean value for n of $\alpha(N+1)$, the most probable value of αN, and a dispersion of $\alpha\sqrt{N^2+1}$. Since all observations, N, are independent, uncertainties modeled by the gamma *pdf* are never correlated.

6.6.1.2 Systematic Uncertainties

For a nuisance parameter θ, with corresponding best estimate of $\tilde{\theta}$, we describe all remaining systematic uncertainties with a log-normal probability density function (*pdf*) expressed as

$$\rho(\theta|\tilde{\theta}) = \frac{1}{\sqrt{2\pi}\ln\kappa}\frac{1}{\theta}\exp\left(-\frac{\ln(\theta/\tilde{\theta})^2}{2(\ln\kappa)^2}\right), \tag{6.20}$$

where κ characterizes the width of the log-normal *pdf*. It can be shown that the log-normal *pdf* is asymptotically identical to the Gaussian *pdf* with small relative uncertainty ϵ and $\kappa = 1 + \epsilon$ [115]. For large uncertainties, the log-normal *pdf* is a more appropriate choice as the log-normal *pdf* goes to zero at $\theta = 0$, a desirable property for evaluating positively defined observables. Asymmetric uncertainties are handled by stitching together two log-normal *pdf*'s at $\tilde{\theta}$, each with its own unique κ estimate. Systematic uncertainties are divided into fully correlated and uncorrelated parts, each becoming an additional nuisance parameter. Fully correlated systematic uncertainties are handled by linking the associated width parameters of two fully correlated systematic uncertainties in such a way that the size of each uncertainty need not be the same but the relative deviations are identical.

6.6.2 Upper Limits on SUSY Model Production Cross Section

We proceed to set upper limits on simplified model production cross sections. Cross section upper limits are evaluated at 95% confidence level. Figure 6.21 shows the upper limits in the two-dimensional mass plane of the prompt SUSY particle, $m_{\widetilde{\mathrm{g}}}$ or $m_{\widetilde{\mathrm{t}}}$, and the lightest SUSY particle, $m_{\widetilde{\chi}^0_1}$. Drawn as solid curves are the contours representing the intersection between the observed upper limit and the cross section obtained from NLO+NLL theory with PDF uncertainty bands. Also plotted with dashed lines are the expected cross section upper limit intersection contours. Good compatibility is observed between the expected and observed upper limits. Uncompressed gluino model points peak more strongly at high BDT discriminant values, where we see a mild excess. This results in slightly weaker observed limits for small $m_{\widetilde{\chi}^0_1}$. T2tt, as well as compressed gluino model points, produce more evenly distributed BDT output in the signal region, where we see a mild deficit in data. The outcome is a slightly stronger set of observed limits compared to expectation. The expected and observed upper limit contours are always compatible within uncertainties.

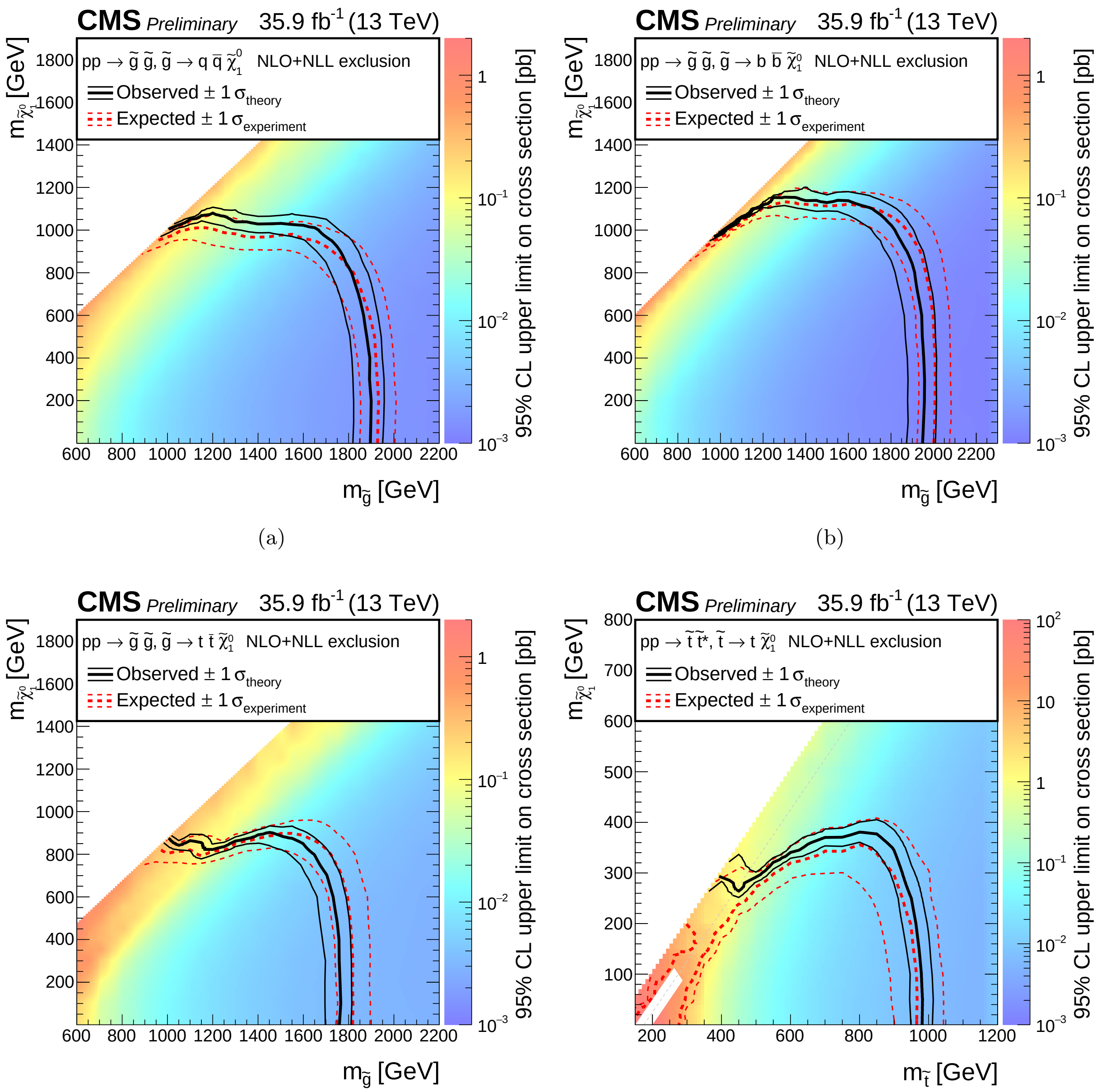

(a) (b)

(c) (d)

Figure 6.21: Cross section upper limits in the two dimensional mass plane for T1qqqq (a), T1bbbb (b), T1tttt (c), and T2tt (d). The intersection of the expected upper limit (red) and observed upper limit (black) are drawn as exclusion curves. In the diagonal region near $m_{\tilde{t}} - m_{\tilde{\chi}_1^0} = m_{\mathrm{t}}$, labeled with a dashed line in (d), the $\tilde{\chi}_1^0$ receives a boost which is proportional to m_{t}. When $m_{\tilde{t}}$ is also near m_{t}, the event kinematics become nearly identical to $\mathrm{t\bar{t}}$ and we lose sensitivity. This region is indicated by the white box in the lower left corner of (d).

Chapter 7

Search for SUSY in Multidimensional Fit

Here we describe a similar analysis targeting gluino and stop mediated SUSY production. A key difference is the use of a multidimensional binning structure in place of the multivariate technique described in Chapter 6. The content of this chapter is also the subject of Reference [116]. It represents an evolution of an analysis on data collected in 2011 [117], 2012 [118], and 2015 [109]. The search variables and corresponding binning are as follows:

- $\mathrm{N_{jet}}$: 2, 3-4, 5-6, 7-8, $\geq$9;
- $\mathrm{N_{b\text{-}jet}}$: 0, 1, 2, $\geq$3; and
- $\mathrm{H_T^{miss}}$ and $\mathrm{H_T}$: a total of 10 orthogonal 2D-intervals, illustrated in Figure 7.1.

Note that we exclude search regions in which $\mathrm{H_T} < \mathrm{H_T^{miss}}$, as $\mathrm{H_T^{miss}}$ should not exceed $\mathrm{H_T}$ in a physical event. Likewise, since $\mathrm{N_{b\text{-}jet}}$ cannot exceed $\mathrm{N_{jet}}$, we drop $\mathrm{N_{b\text{-}jet}} \geq 3$ for the $\mathrm{N_{jet}} = 2$ bins. In addition, we define a low-$\mathrm{H_T^{miss}}$ sideband, $250 < \mathrm{H_T^{miss}} < 300$ GeV with the same $\mathrm{H_T}$ boundaries as the bins with $300 < \mathrm{H_T^{miss}} < 350$ GeV. This sideband is used to validate the QCD background estimation. For $\mathrm{N_{jet}} \geq 7$, with jet $p_\mathrm{T} > 30$ GeV, it is kinematically improbable for events to populate the C1, 1, and 4 bins in the $\mathrm{H_T}$-$\mathrm{H_T^{miss}}$ plane. The total number of independent search bins then becomes 174.[1] Likewise, the total number of sideband bins is 49.

To remove QCD background from our search region, we impose tighter rectangular cuts on $\Delta\phi(\vec{\mathrm{H}}_\mathrm{T}^\mathrm{miss}, j_i)$ than those of the analysis of Chapters 5 and 6. For the two leading jets in the event,

[1] Bin counting by $\mathrm{N_{jet}}$ is given as follows: $\mathrm{N_{jet}} = 2$: $(1 \times 3 \times 10)$; $\mathrm{N_{jet}} =$ 3-6: $(2 \times 4 \times 10)$; $\mathrm{N_{jet}} \geq 7$: $(2 \times 4 \times 8)$.

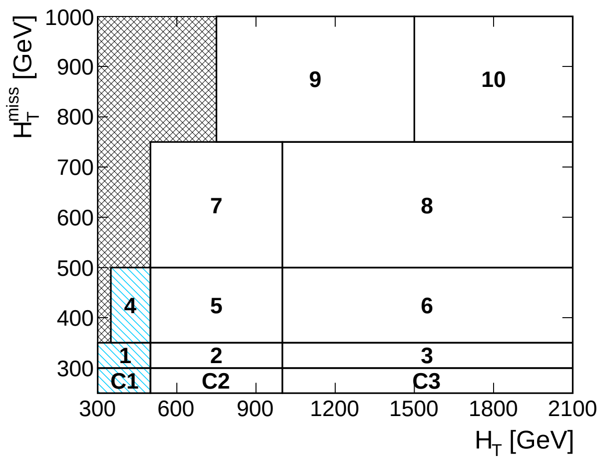

Figure 7.1: Two-dimensional plane in $\mathrm{H_T}$ and $\mathrm{H_T^{miss}}$ showing the signal bins and the QCD sideband bins. The same $\mathrm{H_T}$ and $\mathrm{H_T^{miss}}$ regions are used for each $\mathrm{N_{jet}}$ and $\mathrm{N_{b\text{-}jet}}$ bin, except for the bins with teal shading, which are excluded for $\mathrm{N_{jet}} \geq 7$.

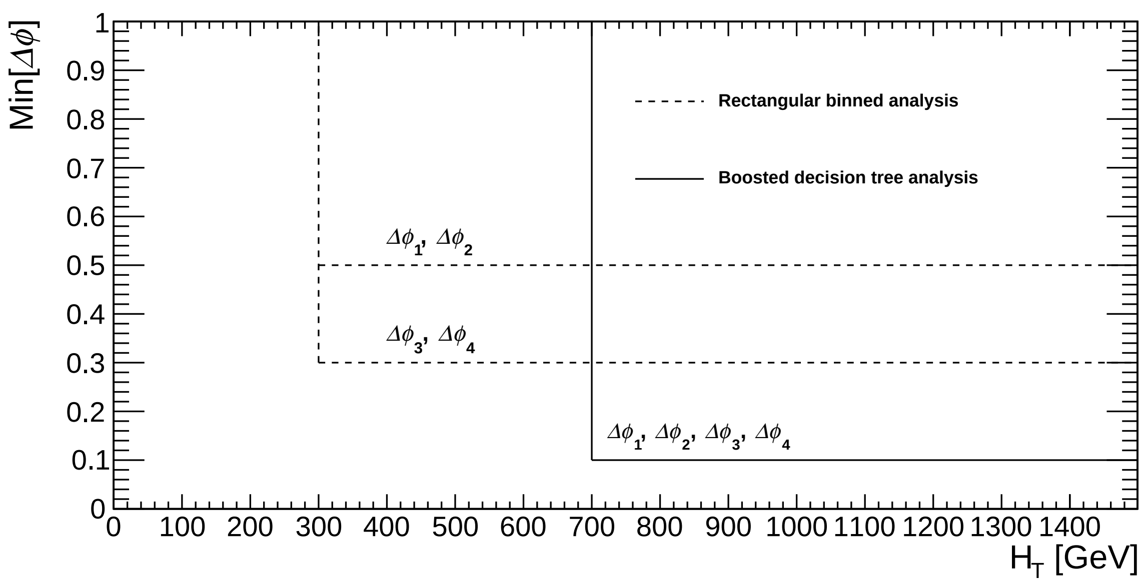

Figure 7.2: Two-dimensional plane in $\mathrm{H_T}$ and $\Delta\phi(\vec{\mathrm{H}}_\mathrm{T}^{\mathrm{miss}}, j_i)$ showing the differences in the baseline selection for signal region events between the multidimensional rectangular binned analysis with the boosted decision tree analysis.

we require the angular separation in ϕ to be at least 0.5, and we require separation of 0.3 for the third and fourth leading jets. We also soften the $\mathrm{H_T}$ requirement from $\mathrm{H_T} > 700$ GeV to $\mathrm{H_T} > 300$ GeV. A comparison of the baseline selection with the search presented in Chapter 6 is given in Figure 7.2. The rest of the event selection is identical to what was presented in Chapters 5 and 6. Likewise, no changes are made in variable definition and triggering of the signal region.

7.1 QCD Estimation

The QCD background is measured using the *rebalance and smear* (R+S) method. We also use a $\Delta\phi(\vec{\mathrm{H}}_{\mathrm{T}}^{\mathrm{miss}}, j_i)$ extrapolation technique, similar to what was presented in Section 6.4.2, to validate the R+S prediction. The method of rebalance and smear involves two steps. In the rebalance step, we select a pure sample of QCD events using the set of inclusive $\mathrm{H_T}$ triggers with the following $\mathrm{H_T}$ thresholds

- `HLT_PFHT[x]_v* ([x] = 250,300,350,400,475,600,650,800).`

Each event in the sample is modified to approximately undo the effects of the detector smearing of the jets. We define a posterior density representing the probability of various configurations of parton-level jet four-vectors, $\vec{J}_{\mathrm{part}}$. This posterior density is maximized with respect to the transverse momenta of the jets, given the set of measured jet four-vectors, $\vec{J}_{\mathrm{meas}}$. During the maximization procedure, the magnitudes of the jet four-vectors are free parameters, subject to two priors: the detector response associated with each jet response template and a low-$\mathrm{H}_{\mathrm{T}}^{\mathrm{miss}}$ constraint introduced via the prior $\pi(\vec{J}_{\mathrm{part}})$, which depends on the parton-level jets. The posterior density is given as

$$\mathrm{P}(\vec{J}_{\mathrm{part}}|\vec{J}_{\mathrm{meas}}) \sim \mathrm{P}(\vec{J}_{\mathrm{meas}}|\vec{J}_{\mathrm{part}}) \cdot \pi(\vec{J}_{\mathrm{part}}). \tag{7.1}$$

The prior depends only on the probability density for the parton-level $\mathrm{H}_{\mathrm{T}}^{\mathrm{miss}}$, which we take from simulation. The prior is binned in $\mathrm{N}_{\text{b-jet}}$ and $\mathrm{H_T}$, as shown in Figure 7.3. The binning in $\mathrm{N}_{\text{b-jet}}$ accommodates $\mathrm{H}_{\mathrm{T}}^{\mathrm{miss}}$ arising from B decays with neutrinos, and the binning in $\mathrm{H_T}$ accommodates $\mathrm{H}_{\mathrm{T}}^{\mathrm{miss}}$ that can arise from jets that fail the selection criteria. The result of this procedure is a set of rebalanced jets, the first of the two step process.

The second step in the procedure for estimating QCD is to smear the jets according to the jet response of the detector. The jet response is the ratio of the reconstructed jet p_{T} to the true jet p_{T}.

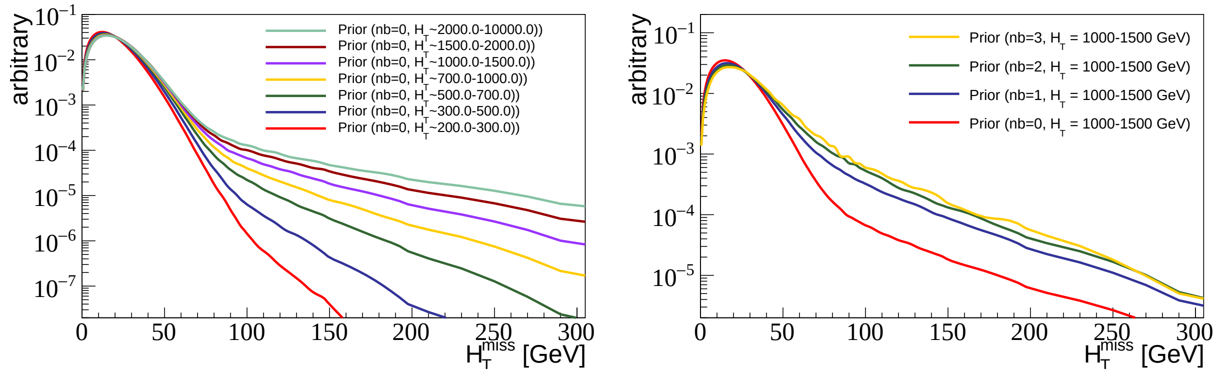

(a) (b)

Figure 7.3: Distributions of the $\mathrm{H_T^{miss}}$ component of the prior for various ranges of $\mathrm{H_T}$ (a) and $\mathrm{N_{b\text{-}jet}}$ (b).

It is obtained from simulation, with corrections from the jet energy resolution scale factors. The response is binned in p_T and η. The p_T binning accounts for the intrinsic calorimeter resolution and varies as a function of jet energy. The η binning accounts for changes in the amount of material between the interaction point and the calorimeters, which varies with pseudorapidity. The jet response is shown in Figure 7.4 for two ranges of p_T and η. We randomly sample the response templates to smear the rebalanced jets before obtaining a smeared prediction. This process is repeated, and each event is smeared $\mathcal{O}(100)$ times to obtain a prediction in all 174 search bins.

7.1.1 QCD R+S Systematic Uncertainties

- **Jet response template core: 20-70%.** The uncertainty in the core of the jet response is found to be well described by a gaussian function. We evaluate this uncertainty by taking the difference between the nominal prediction and a set of predictions using alternate response templates. We obtain the alternate templates by varying the JEC and JER scale factors by the respective uncertainties and recomputing the response. An example jet response template is shown in Figure 7.4.

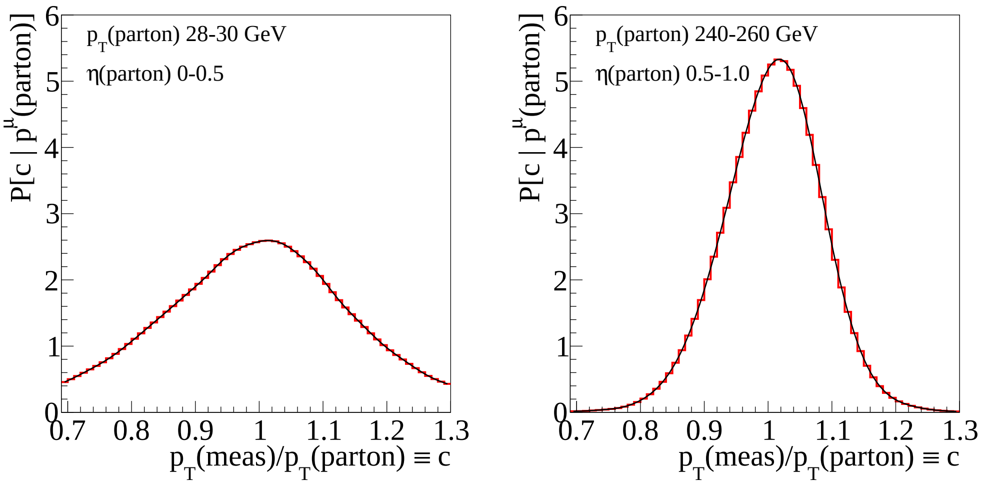

Figure 7.4: The likelihood function for the jet energy response (response templates) in two regions of the phase space of the parton-level jet four-vector [92].

- **Jet response template tail: 32%.** We subtract the gaussian component of the jet response core from the response template to isolate the jet response template tail. We analyze back-to-back di-jet events in data ($|\Delta\phi| > 2.7$ and in the same region of $|\eta|$), and the non-gaussian component of the asymmetry in the di-jet events provides a data driven handle on our jet response in the tails. We compute the tail asymmetry also in simulation and determine appropriate scale factors. The uncertainties in the scale factors are propagated to the final prediction.

- **Prior: 5%.** The prediction is relatively insensitive to the choice of prior. However, we apply a data-to-simulation reweighting procedure to the prior distributions. The resulting change in the prediction is small compared to the uncertainty on the prediction, but we include this deviation as a separate systematic uncertainty.

- **Electroweak background contamination: <1-20%.** QCD dominates the R+S data control sample. We take the non-QCD contamination from electroweak simulation. We scale the normalization of the simulation by 50% and use the difference in the prediction as a systematic uncertainty.

- **b-tag reweighting: (0, 0, 30, 100)%.** For the two largest $\mathrm{N_{b\text{-}jet}}$ bins, we observe an under-prediction of the QCD background when tested on simulation. The source of this under-prediction is a result of a non-trivial correlation between the b-tagging efficiency and the p_T of the rebalanced and smeared jets. However, the under-prediction is not found to depend on any of the other search variables, so we apply a single normalization correction to $\mathrm{N_{b\text{-}jet}} = 2$ and $\mathrm{N_{b\text{-}jet}} \geq 3$, separately. The systematic uncertainty applied to these bins is equal to the size of the correction.

- **Trigger efficiency: 1-3%.** The R+S prediction is insensitive to control sample trigger inefficiencies. However, the QCD prediction in the signal region must account for inefficiencies in the signal trigger. The inefficiency and uncertainty is measured using a Bayesian Neural Network technique.

- **R+S Statistical Uncertainty: 5-100%.** The statistical uncertainty on the method is obtained by dividing the sample into five independent subsets. We repeat the QCD estimation procedure on each of the five sub-samples, resulting in 5 independent predictions. The square root of the variance of the bin-by-bin prediction is taken as the statistical uncertainty.

7.1.2 Cross Check with $\Delta\phi(\vec{\mathrm{H}}_\mathrm{T}^\mathrm{miss}, j_i)$ Extrapolation

To validate the R+S method, we compare the prediction to a method which relies on extrapolation from the sample with an inverted $\Delta\phi(\vec{\mathrm{H}}_\mathrm{T}^\mathrm{miss}, j_i)$ selection. The search presented in Reference [109] utilizes this method as the main QCD background estimation procedure. Here, we briefly summarize the main features of the cross check.

We use the inverted $\Delta\phi(\vec{\mathrm{H}}_\mathrm{T}^\mathrm{miss}, j_i)$ selection to obtain a QCD enriched control sample. To translate the control sample data into the individual search bins, we use a high/low $\Delta\phi(\vec{\mathrm{H}}_\mathrm{T}^\mathrm{miss}, j_i)$ ratio which assumes the $\mathrm{H}_\mathrm{T}^\mathrm{miss}$ dependence factorizes from $\mathrm{H_T}$ and $\mathrm{N_{jet}}$. The $\mathrm{H_T}$ and $\mathrm{N_{jet}}$ dependence is measured using a likelihood fit to the low $\mathrm{H}_\mathrm{T}^\mathrm{miss}$ sideband ($250 < \mathrm{H}_\mathrm{T}^\mathrm{miss} < 300$ GeV) data. The

$\mathrm{H}_{\mathrm{T}}^{\mathrm{miss}}$ dependence of the high/low ratio is obtained from simulation. Uncertainties on the prediction are derived from the covariance matrix in the likelihood fit, $\mathrm{H}_{\mathrm{T}}^{\mathrm{miss}}$ scaling in simulation, statistical precision in the closure test, contamination from non-QCD backgrounds, and low $\Delta\phi(\vec{\mathrm{H}}_{\mathrm{T}}^{\mathrm{miss}}, j_i)$ control sample statistics. A closure test of the $\Delta\phi(\vec{\mathrm{H}}_{\mathrm{T}}^{\mathrm{miss}}, j_i)$ extrapolation procedure is given in Figure 7.9b.

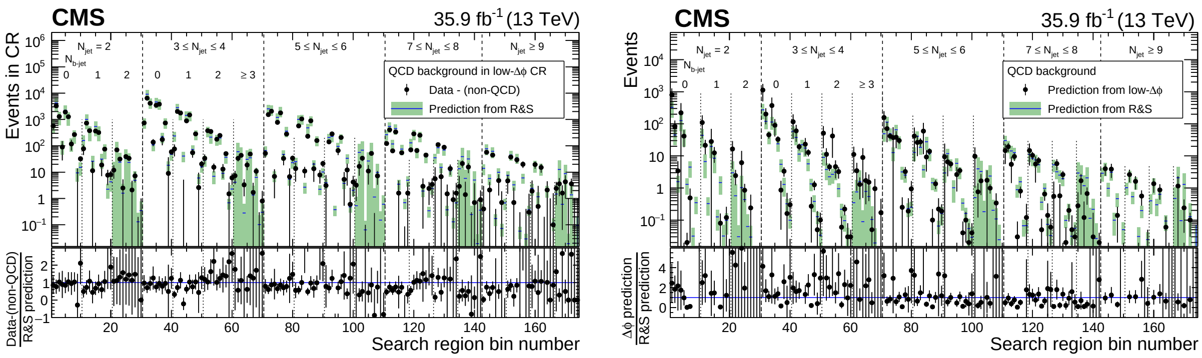

(a) (b)

Figure 7.5: A validation of the R+S procedure for estimating the QCD background in the inverted $\Delta\phi(\vec{\mathrm{H}}_{\mathrm{T}}^{\mathrm{miss}}, j_i)$ control sample (a) and by direct comparison to the $\Delta\phi(\vec{\mathrm{H}}_{\mathrm{T}}^{\mathrm{miss}}, j_i)$ extrapolation prediction in the signal search bins (b).

An R+S cross check is performed in two separate samples. By inverting the selection on $\Delta\phi(\vec{\mathrm{H}}_{\mathrm{T}}^{\mathrm{miss}}, j_i)$, we can test the QCD prediction on an independent sample in data. A relatively small amount of non-QCD contamination is subtracted using data prediction before the comparison is made. We find good agreement between the background subtracted low $\Delta\phi(\vec{\mathrm{H}}_{\mathrm{T}}^{\mathrm{miss}}, j_i)$ control data and the R+S prediction. This comparison is shown in Figure 7.5a. A second cross check is performed by comparing the R+S prediction directly to the $\Delta\phi(\vec{\mathrm{H}}_{\mathrm{T}}^{\mathrm{miss}}, j_i)$ extrapolation prediction in the signal search bins shown in Figure 7.5b. The two methods predict consistent results within uncertainties.

7.2 Top Quark and W Estimation

Unlike the approach described in Section 6.4, we cannot measure the background arising from the top quark and W processes together by extracting the normalization from a sideband and shapes from a single lepton control sample. Instead, we carefully consider two separate cases:

- W decays to e, μ, or τ, where the τ decays leptonically and we fail to identify and reconstruct the lepton.
- W decays to τ, which in turn decays hadronically: $\tau \rightarrow \nu_\tau$(hadrons).

The first of these cases is described in Section 7.2.1 and the other is described in Section 7.2.2

7.2.1 Lost Lepton Background Estimation

The method for determining the lost lepton background is nearly identical to the procedure described in Section 6.4. The main difference is that we use Equation 6.14 to give us the absolute number of lost lepton events, instead of using it to determine the shape of the entire top+W background. Therefore, the types of systematic uncertainties are the same as those presented in Section 6.4.3 except for the uncertainty on the hadronic τ shape differences and the top+W normalization. The size of each individual systematic uncertainty can vary in the four-dimensional binning structure, but the typical size is approximately unchanged. However, control region statistics can be as large 100% for many of the bins with small background prediction. We see good closure, shown in Figure 7.9d, when treating the simulation like data.

7.2.2 Hadronically Decaying τ Lepton Background Estimation

To measure the hadronic τ background (τ_h), we select events from a single-muon CS and smear the muon p_T according to simulated τ response templates. All analysis variables are then recomputed before obtaining a prediction of the background arising from hadronic τ events.

The single-muon data control sample for the τ_h estimation is defined by the following criteria:

- Exactly one isolated muon as defined in Section 5.1 except with additional muon criteria of $|\eta| < 2.1$, $p_\mathrm{T} > 25$ GeV for $300 < \mathrm{H_T} < 500$ GeV, and $p_\mathrm{T} > 20$ GeV for $\mathrm{H_T} > 500$ GeV;
- No isolated electron candidate; and

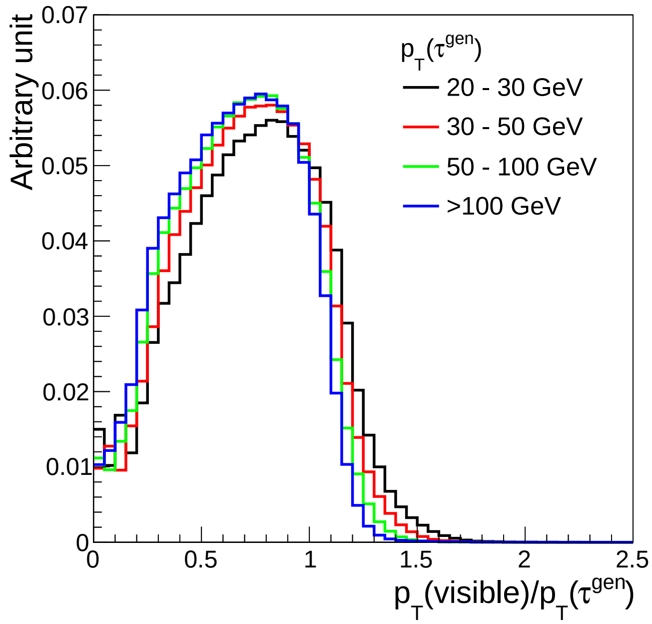

Figure 7.6: Response templates from hadronically decaying taus [92].

- $M_T < 100$ GeV.

The last criterion is chosen to reduce signal contamination.

The measured muon transverse momentum, $p_{T\mu}$, in the CS is smeared according to the τ_h response functions given in Figure 7.6. We derive the response templates by taking the ratio of p_T of an AK4 jet matched with that of the generated hadronically decaying τ particle. The excellent muon momentum resolution of the CMS detector allows us to treat the value of $p_{T\mu}$ as a proxy for the generator-level value of the τ particle, $p_{T,\tau_h\text{-gen}}$. Separate τ_h response templates are computed in four intervals: $20 < p_{T\mu} < 30$ GeV; $30 < p_{T\mu} < 50$ GeV; $50 < p_{T\mu} < 100$ GeV; and $p_{T\mu} > 100$ GeV.

Once the appropriate template is determined, $p_{T\mu}$ is subtracted from the jet associated with the muon.[2] Then, along the direction of the muon we add in the hadronic τ reconstructed transverse momentum, $p_{T,\tau_h\text{-reco}}$, which we obtain from sampling the τ response templates. For each event we take 250 samples of $p_{T,\tau_h\text{-reco}}$, uniformly binned across the entire hadronic τ response template, weighted by the probability to observe $p_{T,\tau_h\text{-reco}}$ given as $P^{\text{resp}}_{\tau_h}$. For each of these samples, we

[2] Recall that isolated leptons automatically pass jet definition (see Section 5.1).

recalculate $\mathrm{N_{jet}}$, $\mathrm{H_T}$, $\mathrm{H_T^{miss}}$, and $\Delta\phi(\vec{\mathrm{H}}_\mathrm{T}^\mathrm{miss}, j_i)$. An additional weight, $w_{\text{b-mistag}}^{\tau_\mathrm{h}}$, is applied for each $\mathrm{N_{b\text{-}jet}}$ bin which accounts for the $\mathrm{N_{b\text{-}jet}}$ content of the CS event and the probability that the τ_h jet is misidentified as a b-jet.

The following corrections are also incorporated:

- The ratio of branching fractions $\mathcal{B}(\mathrm{W} \to \tau_\mathrm{h}\nu)/\mathcal{B}(\mathrm{W} \to \mu\nu) = 0.6476 \pm 0.0024$ [6];
- The muon reconstruction efficiency ($\epsilon^\mu_\mathrm{reco}$), binned in $p_{\mathrm{T}\mu}$ and muon $|\eta|$;
- The muon isolation efficiency ($\epsilon^\mu_\mathrm{ISO}$), binned in $p_{\mathrm{T}\mu}$ and activity;
- The muon acceptance ($\epsilon^\mu_\mathrm{Acc}$) binned in $\mathrm{N_{jet}}$, $\mathrm{H_T}$, $\mathrm{H_T^{miss}}$ and $\mathrm{N_{b\text{-}jet}}$;
- The $\mathrm{M_T}$ selection efficiency ($\epsilon_{\mathrm{M_T}}$), binned in $\mathrm{N_{jet}}$, $\mathrm{H_T}$, and $\mathrm{H_T^{miss}}$;
- CS contamination from $\mathrm{W} \to \tau\nu_\tau \to \mu\nu_\mu\bar{\nu}_\tau\nu_\tau$, binned in $\mathrm{N_{jet}}$, $\mathrm{H_T}$, and $\mathrm{H_T^{miss}}$, expressed as a purity factor $\beta_{\tau\to\mu}$;
- CS contamination from dileptonic events, binned in $\mathrm{N_{jet}}$, $\mathrm{H_T}$, $\mathrm{H_T^{miss}}$ and $\mathrm{N_{b\text{-}jet}}$, expressed as a purity factor $\beta_{\ell\ell}$; and
- The isolated track veto efficiency (ϵ_isotrk), binned in $\mathrm{N_{jet}}$, $\mathrm{H_T}$, $\mathrm{H_T^{miss}}$, and $\mathrm{N_{b\text{-}jet}}$.

The formula for calculating the hadronically decaying τ background is

$$N_{\tau_\mathrm{h}} = \sum_i^{N^\mu_\mathrm{CS}} \left(\sum_j^{\text{Template bins}} \left(P^\mathrm{resp}_{\tau_\mathrm{h}} \sum_k w^{\tau_\mathrm{h}}_{\text{b-mistag}} \right) \frac{\beta_{\tau\to\mu}}{\epsilon^\mu_\mathrm{Trig}\epsilon^\mu_\mathrm{Reco}\epsilon^\mu_\mathrm{ISO}} \frac{\beta_{\ell\ell}}{\epsilon^\mu_\mathrm{Acc}\epsilon^\mu_{\mathrm{M_T}}} \frac{\mathcal{B}(\mathrm{W}\to\tau_\mathrm{h}\nu)}{\mathcal{B}(\mathrm{W}\to\mu\nu)} \epsilon_\mathrm{isotrk} \right). \quad (7.2)$$

7.2.2.1 Hadronic-τ Systematic Uncertainties

- **Hadronic tau response template:** We vary the τ_h jet energy scale and propagate the corresponding uncertainty in the prediction.
- **Mistagging rate of hadronic tau jet:** We vary the b-jet mistag rate by 50% and propagate the corresponding uncertainty.

- **Muon reconstruction/ID/isolation efficiency:** The Tag-and-Probe method described in Section 6.3.3 is used to obtain the data/simulation scale factors, and recommended uncertainties on the SFs are propagated.

- **Acceptance:** The uncertainty from the acceptance is computed by varying the PDFs and the renormalization and factorization scales within uncertainties. In quadrature, we include the statistical precision of the simulation.

- **Dilepton correction:** This contamination is determined from simulation and is found to be small (about 2% across all search regions). We consider 100% of this subtraction as a systematic uncertainty.

- **$\mathrm{M_T}$ cut efficiency:** We vary the uncertainty on the $\mathrm{E_T^{miss}}$ scale by 30% and include the statistical uncertainty of determining this efficiency from simulation in quadrature.

- **Isolated track vetoes:** We take the isolated track veto efficiency from simulation and derive the associated systematic uncertainty from Tag-and-Probe studies.

- **MC closure:** In most search bins, the method closes to within about 10% as shown in Figure 7.9c. We take the larger of the bin-by-bin difference from the closure test and the MC sample statistics as a systematic uncertainty. This uncertainty is taken to be uncorrelated across all search bins.

7.3 $\mathrm{Z} \rightarrow \nu\bar{\nu}$ Estimation

The background resulting from Z bosons decaying to a pair of neutrinos is the largest background after the baseline selection criteria are applied. The method for measuring $\mathrm{Z} \rightarrow \nu\bar{\nu}$ nearly mimics the estimation procedure presented in Section 6.3. One complication results from the loss of control sample statistics in some of the 174 search bins. The single-γ control sample distribution falls most rapidly in the $\mathrm{N_{jet}}$ and $\mathrm{N_{b\text{-}jet}}$ dimensions. To manage this, we find that we can smooth our prediction in the $\mathrm{N_{b\text{-}jet}}$ dimension without losing accuracy.

7.3.1 $\mathbf{N_{b\text{-}jet}} = 0$

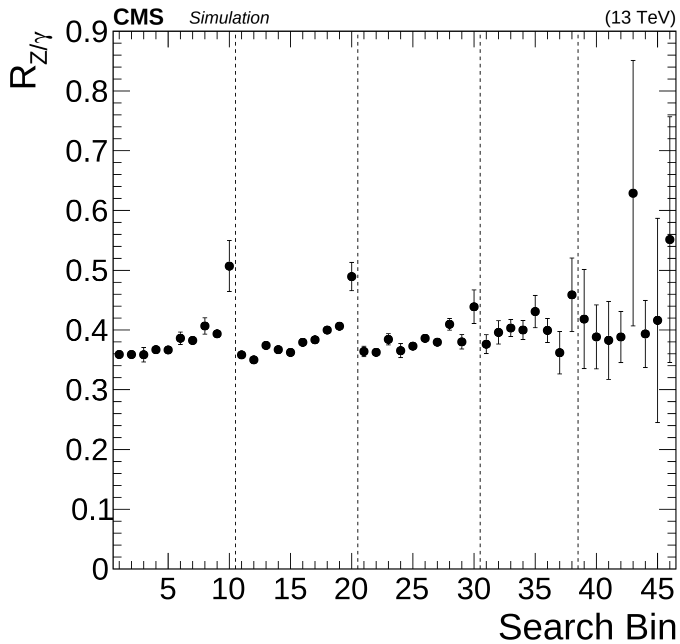

Figure 7.7: The $\mathcal{R}_{Z(\nu\overline{\nu})/\gamma}$ in each of the 46 search bins with $N_{\text{b-jet}} = 0$. The vertical dashed lines separate N_{jet}.

In the 46 bins with $N_{\text{b-jet}} = 0$, the $Z \rightarrow \nu\overline{\nu}$ estimation procedure is nearly identical to that presented in Section 6.3, including the systematic uncertainty determination. We compute $\mathcal{R}_{Z(\nu\overline{\nu})/\gamma}$ in all 46 bins with $N_{\text{b-jet}} = 0$ as shown in Figure 7.7. Since these bins do not represent a continuous function, it would not be particularly useful to consider the double ratio as a function of the analysis bins. Instead, we calibrate $\mathcal{R}_{Z(\nu\overline{\nu})/\gamma}$ by measuring the double ratio in each of the three 1D distributions of $\mathcal{R}_{Z(\nu\overline{\nu})/\gamma}$: H_T, H_T^{miss}, and N_{jet}. We find a trend at low H_T. We correct for this trend using the linear best fit for values below $H_T = 900$ GeV. The correction enters the prediction as weights applied to the γ simulation, given functionally as $\rho(H_T) = 0.91 + \left(9.6 \times 10^{-5}\,\text{GeV}^{-1}\right) \min\left(H_T, 900\,\text{GeV}\right)$. Before correction, we find an average value of $\langle\rho\rangle = 0.95 \pm 0.02$, where the uncertainty given is statistical in nature. The 1-dimensional distributions of the double ratio, before and after applying the H_T correction, are given in Figure 7.8. For each of the 46 $N_{\text{b-jet}} = 0$ bins, we use the corresponding double ratio fit with maximum error band width evaluated at the corresponding value in each distribution as the set of error bands used to determine the double ratio systematic uncertainty.

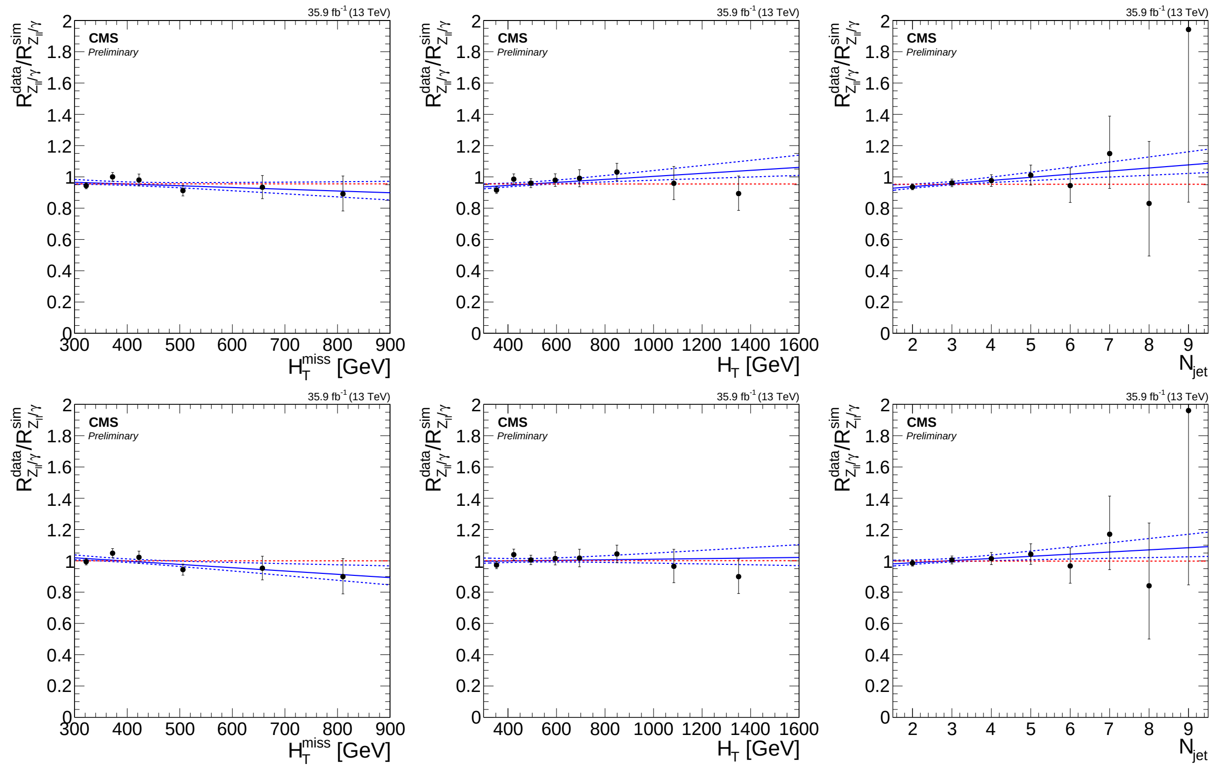

Figure 7.8: ρ vs $\mathrm{H_T^{miss}}$, $\mathrm{H_T}$, and $\mathrm{N_{jet}}$. The solid blue line shows the straight-line fit to ρ in each plot, with the uncertainties propagated as blue dashed lines. The average value of 0.95 is drawn as a red dashed line on each plot (top). The plots on the bottom show ρ after applying the $\mathrm{H_T}$ dependent scale factor.

7.3.2 $\mathbf{N_{b\text{-}jet}} > 0$

We find for $\mathrm{Z} \to \nu\bar{\nu}$ that the kinematic variables ($\mathrm{H_T}$ and $\mathrm{H_T^{miss}}$) are strongly correlated with $\mathrm{N_{jet}}$ but not with $\mathrm{N_{b\text{-}jet}}$. We exploit this feature by copying the $\mathrm{N_{b\text{-}jet}} = 0$ kinematic shape (the shape vs $\mathrm{H_T}$ and $\mathrm{H_T^{miss}}$) in each $\mathrm{N_{jet}}$ bin and extrapolating the shape to the corresponding set of bins with $\mathrm{N_{b\text{-}jet}} = b$, where $b = 1, 2, \geq 3$. This can be formally expressed as

$$\left(N^{\mathrm{pred}}_{\nu\bar{\nu}}\right)_{j,b,k} = \left(N^{\mathrm{pred}}_{\nu\bar{\nu}}\right)_{j,0,k} \mathcal{F}_{j,b}, \tag{7.3}$$

where $\mathcal{F}_{j,b}$ is the extrapolation factor, and the j, b, and k indices (numbered from zero) refer to the $\mathrm{N_{jet}}$, $\mathrm{N_{b\text{-}jet}}$, and kinematic variables, respectively. We measure $\mathcal{F}_{j,b}$ by taking a ratio of $\mathrm{Z} \to \ell^+\ell^-$ events in data, corrected for purity, after baseline selection. This is expressed as

$$\mathcal{F}_{j,b} = \left(N_{\ell\ell}^{\mathrm{data}} \beta_{\ell\ell}\right)_{j,b} / \left(N_{\ell\ell}^{\mathrm{data}} \beta_{\ell\ell}\right)_{j,0}, \tag{7.4}$$

with $j = 1, 2, 3, 4$. For $j = 5$, which corresponds to $\mathrm{N_{jet}} \geq 9$, we run out of statistics in data and we use simulation to augment our extrapolation factor

$$\mathcal{F}_{4,b} = \mathcal{F}_{3,b} \left(\mathcal{F}_{4,b}^{\mathrm{sim}} / \mathcal{F}_{3,b}^{\mathrm{sim}}\right), \tag{7.5}$$

where $\mathcal{F}_{j,b}^{\mathrm{sim}}$ is the corresponding extrapolation factor as calculated in $\mathrm{Z} \to \ell^+\ell^-$ simulation. The rare background of $\mathrm{t\bar{t}Z}$, with fully hadronic top decays, can become significant for large jet and b-tagged jet multiplicity, and so we include this sample in $\mathcal{F}_{j,b}^{\mathrm{sim}}$ as well as the other rare backgrounds of di- and tri-boson production. We consider several sources of systematic uncertainty on $\mathcal{F}_{j,b}$. These include the statistical uncertainty on the number of $\mathrm{Z} \to \ell^+\ell^-$ events from data, the uncertainty on the purity of the dilepton control sample, the simulation statistical uncertainty on $\mathcal{F}_{j,b}^{\mathrm{sim}}$, and a scale factor uncertainty on the relative importance of $\mathrm{t\bar{t}Z}$. The latter two sources are only included in the largest $\mathrm{N_{jet}}$ bin since we use data for all other bins. Also, in the bins which rely on simulation for extrapolation, we derive an upper and lower bound estimate on the extrapolation factor from two separate models. The lower bound model assumes that the $\mathrm{N_{b\text{-}jet}}$ distribution for $\mathrm{N_{jet}} \geq 9$ is identical to the $\mathrm{N_{b\text{-}jet}}$ distribution for $7 \leq \mathrm{N_{jet}} \leq 8$. The upper bound model is derived from a ratio of binomial expectations and assumes the probability of any additional jets to be tagged as a b-jet is independent of jet multiplicity. To obtain the 68% CL, we divide the fractional difference between the (upper or lower) bound and the central value by $\sqrt{3}$. Finally, the assumption that the kinematic shape is constant vs $\mathrm{N_{b\text{-}jet}}$ is tested as shown in Figure 7.9a. We find that adding a systematic uncertainty of 7%, 10%, and 20% for $\mathrm{N_{b\text{-}jet}} = 1, 2$, and ≥ 3, respectively, yields a χ^2 per degree of freedom of around 1. We take these kinematic variation uncertainties, σ_{kin}, to be uncorrelated across all bins. Table 7.1 gives the systematic uncertainties on the $\mathrm{N_{b\text{-}jet}}$ extrapolation of the $\mathrm{Z} \to \nu\overline{\nu}$ prediction.

Table 7.1: Extrapolation factors for $\mathrm{N_{b\text{-}jet}} > 0$ with uncertainties. All uncertainties are given as percentages. Uncertainties that are statistical in nature are denoted with prefix σ, and uncertainties that are systematic in nature are denoted with prefix δ. In the first column, bin $\equiv 4(j-1)+b$, where j (n) is the index of the $\mathrm{N_{jet}}$ ($\mathrm{N_{b\text{-}jet}}$) bin. Here, $\mathcal{J} = \left(\mathcal{F}^{\mathrm{sim}}_{4,b}/\mathcal{F}^{\mathrm{sim}}_{3,b}\right)$.

bin	$N_{\mu^+\mu^-}$	$N_{e^+e^-}$	$\mathcal{F}_{j,b}$	σ_{stat}	$\delta\beta_{\ell\ell}$	$\delta\mathcal{J}$	$\sigma_{t\bar{t}Z\ \mathrm{SF}}$	σ_{kin}
1	3436	2460	1.0	0	0	$\pm0^{+0}_{-0}$	0	0
2	360	255	0.103	4	2	$\pm0^{+0}_{-0}$	0	7
3	17	9	0.004	20	27	$\pm0^{+0}_{-0}$	0	10
4	2982	2099	1.0	0	0	$\pm0^{+0}_{-0}$	0	0
5	445	344	0.153	4	2	$\pm0^{+0}_{-0}$	0	7
6	65	38	0.02	10	9	$\pm0^{+0}_{-0}$	0	10
7	2	2	0.001	50	9	$\pm0^{+0}_{-0}$	0	20
8	423	309	1.0	0	0	$\pm0^{+0}_{-0}$	0	0
9	118	94	0.282	8	5	$\pm0^{+0}_{-0}$	0	7
10	30	15	0.05	15	22	$\pm0^{+0}_{-0}$	0	10
11	1	4	0.005	45	22	$\pm0^{+0}_{-0}$	0	20
12	43	26	1.0	0	0	$\pm0^{+0}_{-0}$	0	0
13	15	15	0.428	21	5	$\pm0^{+0}_{-0}$	0	7
14	4	4	0.101	34	22	$\pm0^{+0}_{-0}$	0	10
15	2	3	0.061	46	22	$\pm0^{+0}_{-0}$	0	20
16	5	2	1.0	0	0	$\pm0^{+0}_{-0}$	0	0
17	0	1	0.686	21	5	$\pm10^{+7}_{-18}$	4	7
18	0	0	0.257	34	22	$\pm19^{+0}_{-23}$	10	10
19	0	0	0.182	46	22	$\pm39^{+12}_{-39}$	3	20

7.4 Background Estimation Closure

For each of the four backgrounds, we compare the simulated MC directly to the background derived from the simulation. This allows us to directly test the closure of the method in the 174 bin search space. Results of this test on each of the sources of background are shown in Figure 7.9.

7.5 Results

A comparison between the observations and the background predictions in all 174 bins of the multidimensional search space is given in Figure 7.10. The data in the search region agree with background predictions.

To illuminate signal distributions, we overlay the data against the background predictions

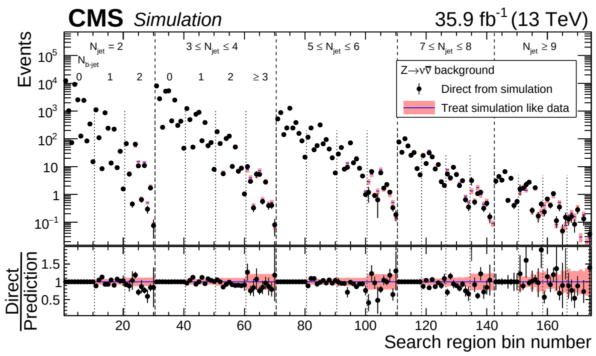

(a)

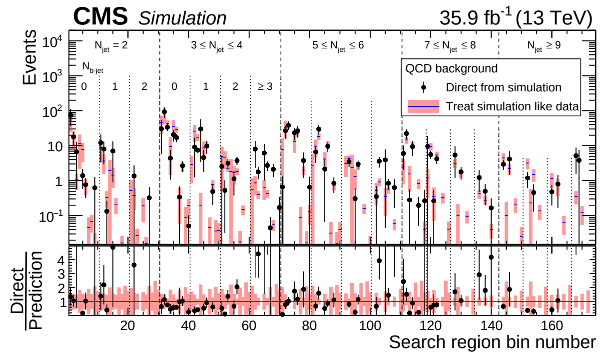

(b)

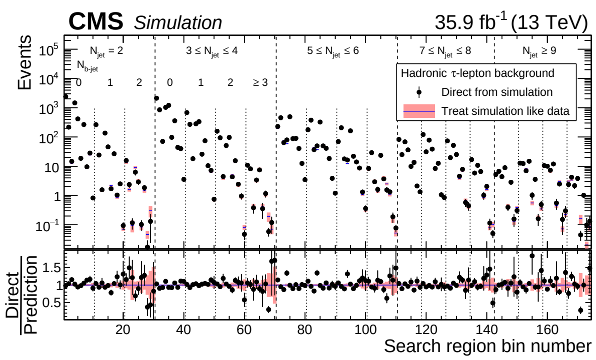

(c)

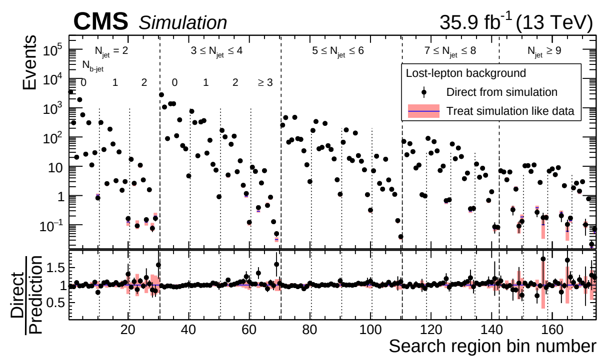

(d)

Figure 7.9: For the individual backgrounds, we compare the direct simulation (data points) to instead treating the simulation like data (histogram) for $Z \to \nu\bar{\nu}$ (a), QCD (b), hadronic τ (c), and lost-lepton (d).

in one-dimensional projections of the search bins in Figure 7.11. We enhance the relative signal strength in each of these plots by excluding bins with overwhelming background predictions.

We proceed to set limits, treating each of the 174 bins as independent search regions. The statistical treatment, including the nuisance parameter *pdf*'s and CL$_s$ definition, is identical to that which is presented in Sections 6.6.1 and 6.6.2. Likewise, the same signal systematic uncertainties as those described in Section 6.5 are considered. Upper limits are set in the context of the presented gluino and stop pair production models. The two-dimensional cross section upper limits and corresponding exclusion curves are shown in Figure 7.12. Additional interpretations are given in Appendix B. Expected and observed limits agree to within uncertainties.

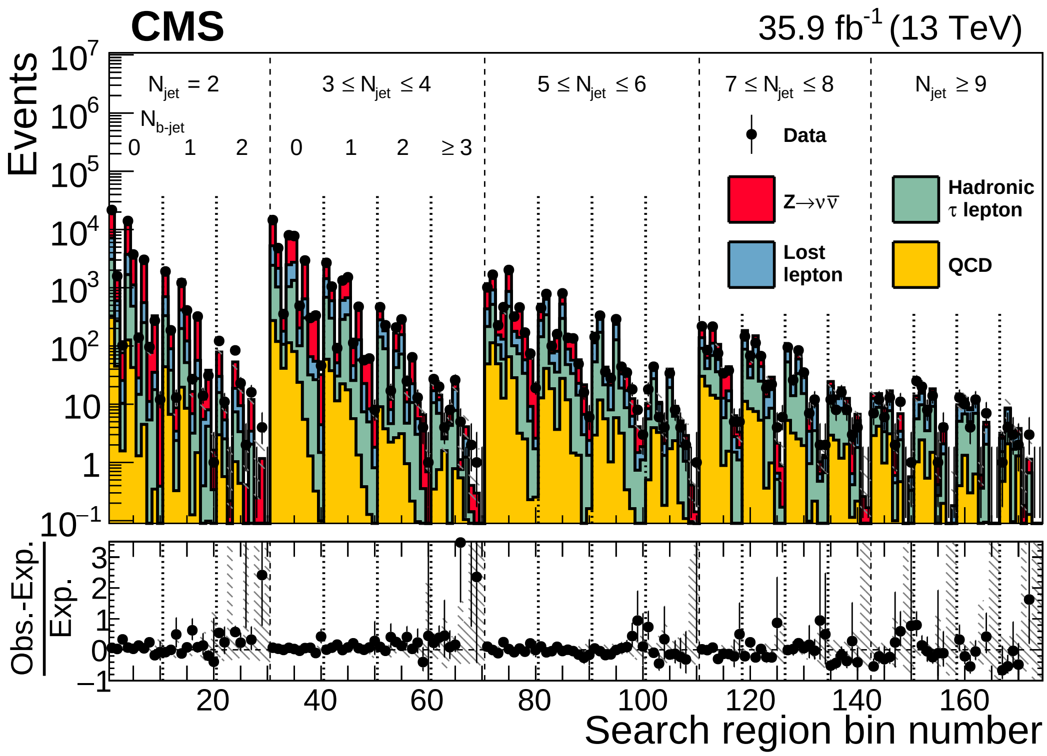

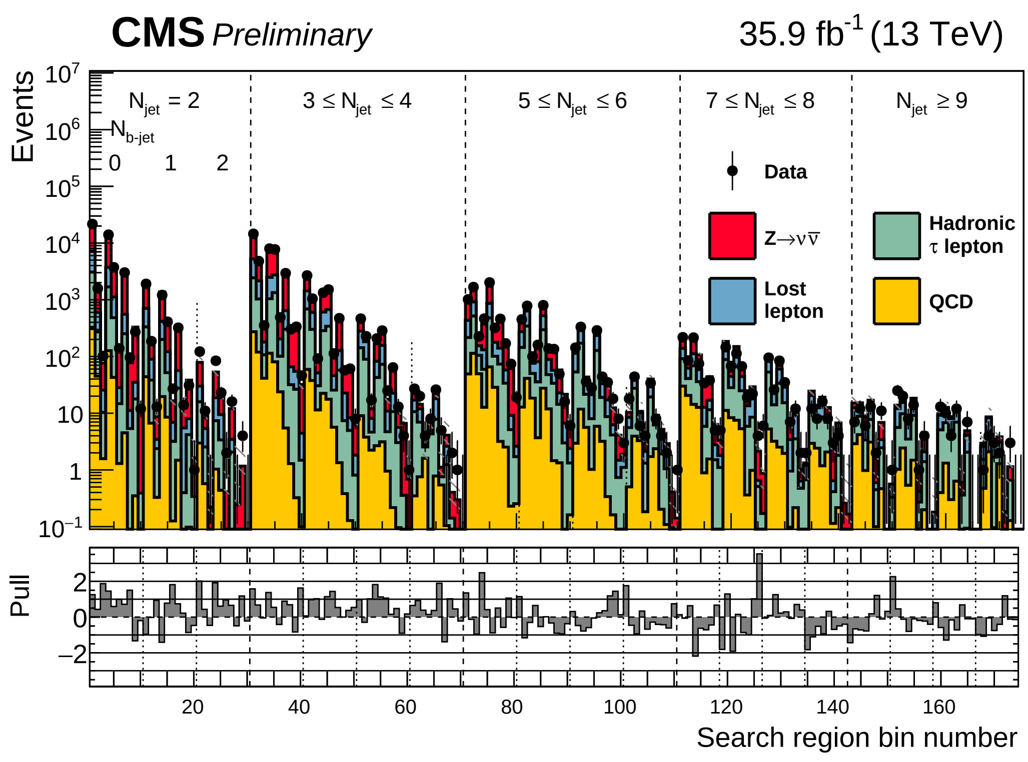

Figure 7.10: Observed number of events and pre-fit background predictions in all search bins. The lower panel of the top plot shows the relative difference between the observed data and estimated background, while the lower panel of the bottom plot shows the pull, defined as $(N_{\text{Obs.}} - N_{\text{Exp.}})/\sqrt{N_{\text{Obs.}} + (\delta N_{\text{Exp.}})^2}$, where $\delta N_{\text{Exp.}}$ is the total uncertainty on the pre-fit background prediction, for each bin.

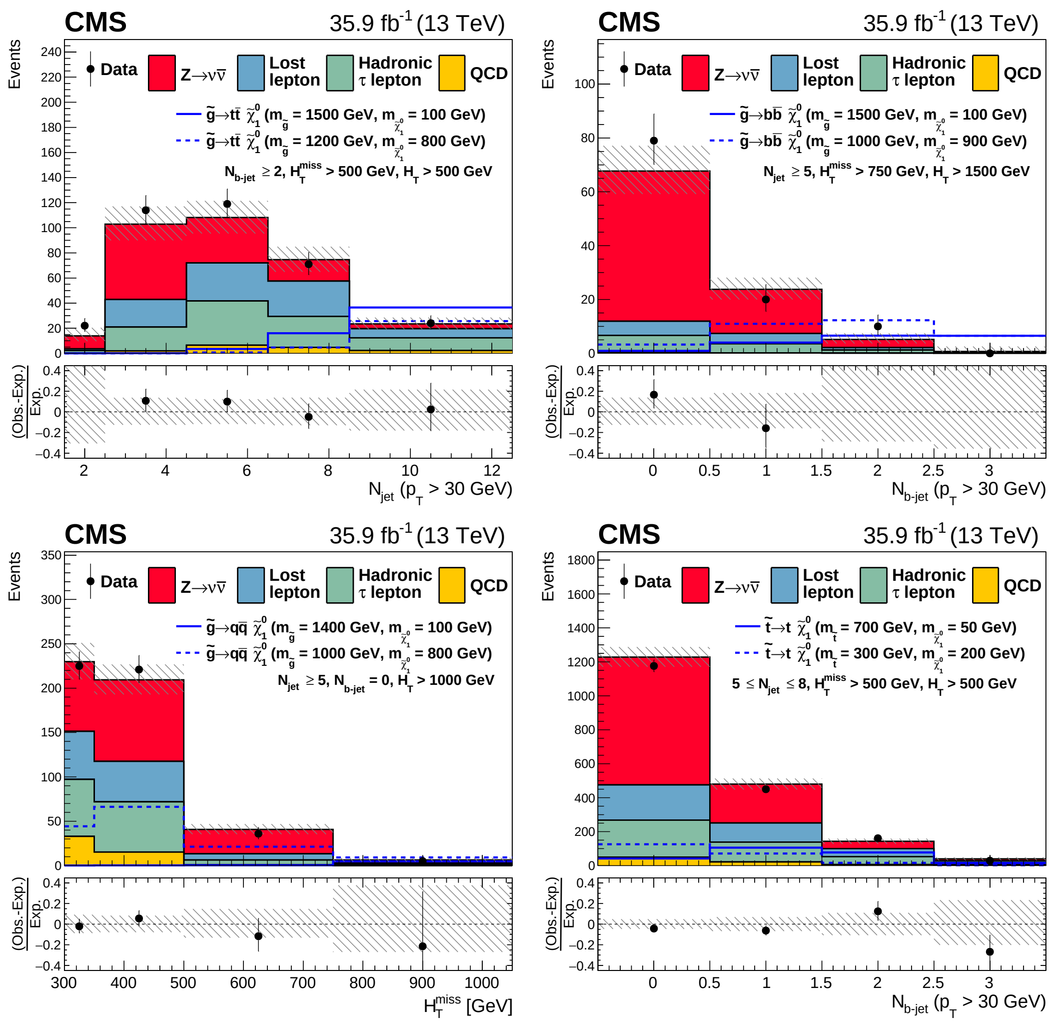

Figure 7.11: One-dimensional projections of various kinematic regions with sensitive SUSY signal models overlaid.

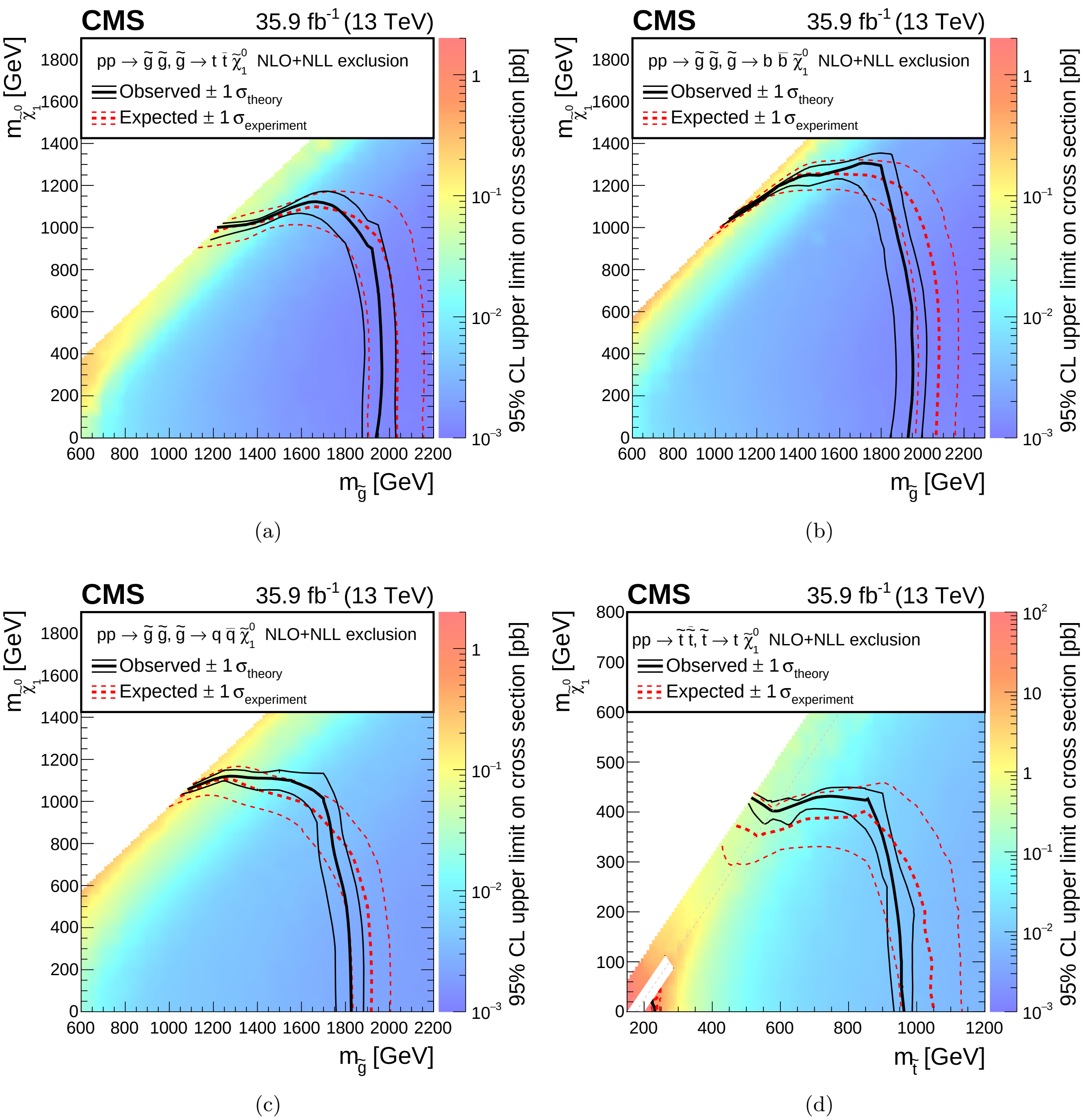

Figure 7.12: The 95% CL upper limits using the multidimensional binning analysis method for T1tttt (a), T1bbbb (b), T1qqqq (c), and T2tt (d). In the diagonal region near $m_{\tilde{t}} - m_{\tilde{\chi}_1^0} = m_{t}$, labeled with a dashed line in (d), the $\tilde{\chi}_1^0$ receives a boost which is proportional to m_{t}. When $m_{\tilde{t}}$ is also near m_{t}, the event kinematics become nearly identical to $t\bar{t}$ and we lose sensitivity. This region is indicated by the white box in the lower left corner of (d).

Chapter 8

Summary and Outlook

The tremendously successful standard model, a theory which describes the electromagnetic, weak, and strong interactions, continues to withstand the critical examination of our experimental probes. Despite the success, concerns of naturalness and gauge unification suggest that a deeper theory awaits discovery. Furthermore, a precise description of dark matter is very much incomplete. Supersymmetry has the potential to solve these problems in a very economical way, provided a subset of the super partners are relatively light. If SUSY is an accurate description of nature, the LHC could see evidence for its existence.

Two searches for SUSY are presented with 35.9 fb^{-1} of data from 13 TeV pp collisions using the CMS detector. The results are interpreted using generic SUSY models that assume three body gluino decays and two body top squark decays, each with a neutral lightest supersymmetric particle observed as missing momentum in the event. The searches consider hadronic events with large jet energies and large missing momentum. The first search makes use of event kinematics and heavy flavor multiplicity to train a boosted decision tree to discriminate standard model processes from SUSY signals. Training is performed on simulated events, and data control regions are used to predict the expected background. An independent set of simulated signal events is used to interpret the data.

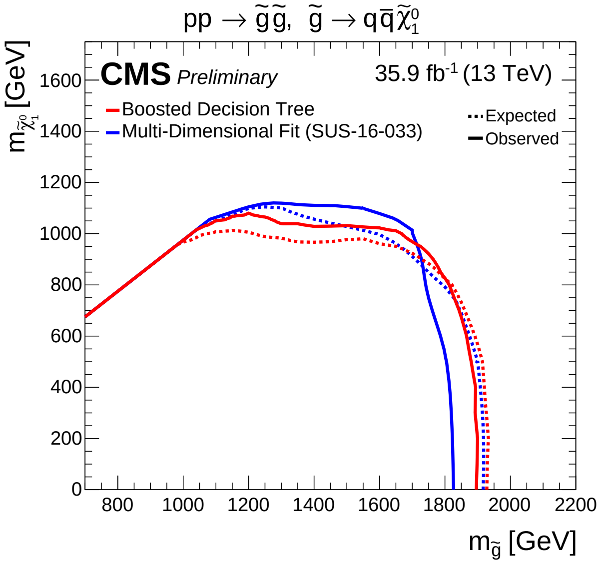

(a)

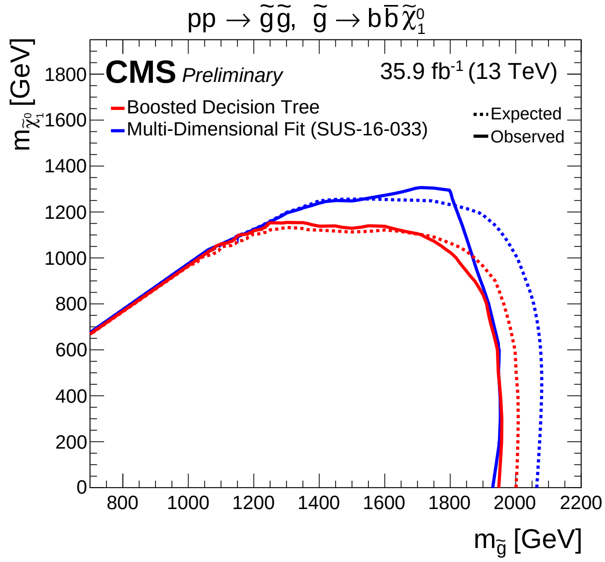

(b)

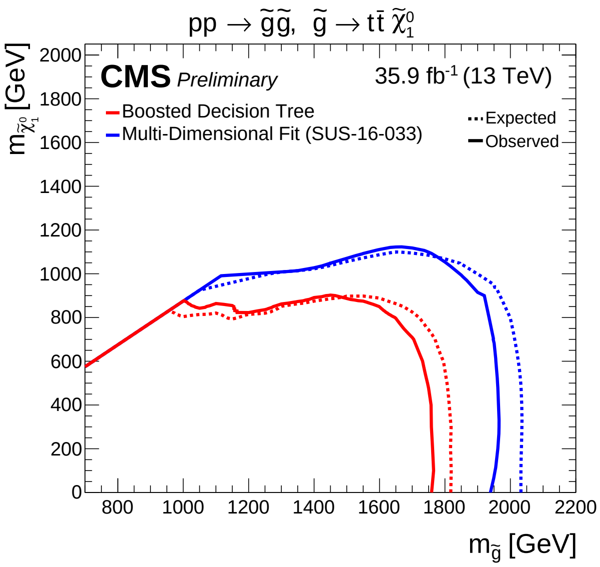

(c)

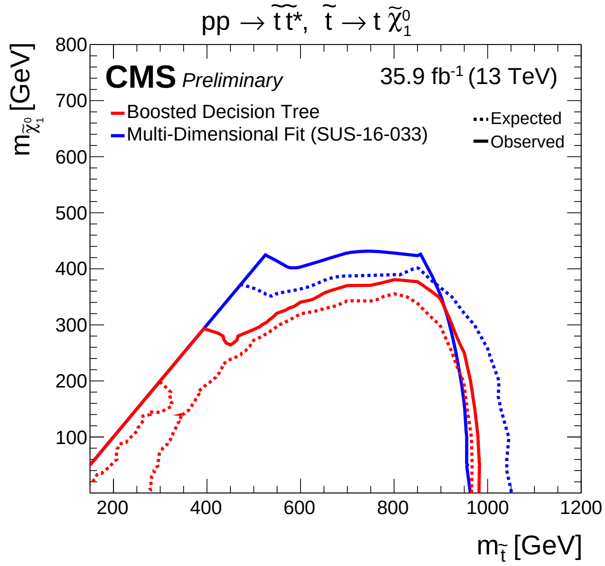

(d)

Figure 8.1: The 95% CL upper limits comparison between the boosted decision tree analysis described in Chapter 6 and the multidimensional binning method for T1qqqq (a), T1bbbb (b), T1tttt (c), and T2tt (d).

The second search is presented on a separate but overlapping dataset that bins the search region with rectangular cuts on H_T^{miss}, H_T, N_{jet}, and $N_{b\text{-}jet}$. The analyses presented have comparable sensitivity for models in which the LSP mass is much less than the mass of the produced SUSY particle. A comparison of the cross section upper limits between the two separate searches is given in Figure 8.1.

The observed data are consistent with the expected background from standard model processes. This results in improved limits on gluino and stop masses in the context of simplified SUSY models. We set lower limits on gluino masses of 1900–1960 GeV and stop masses of 960–980 GeV. These exclusions put significant constraints on natural SUSY, suggesting that the problem of fine-tuning might not be entirely solved with SUSY alone.

8.1 Outlook

The first sets of data at 13 TeV from the experiments at the LHC are just now being analyzed. We are less than midway through the run timeline including a projected 150 fb^{-1} of collected data by the end of 2018. We hope to increase the center–of–mass collision energy to the LHC design of 14 TeV before Run 3, when we expect to collect an additional 300 fb^{-1}. Additionally, development of the High–Luminosity LHC (HL-LHC) is underway, a project that intends to increase the instantaneous luminosity by up to seven times the original design. The HL-LHC projects upwards of 3,000 fb^{-1} of data collected by 2037. The full LHC timeline is given in Figure 8.2.

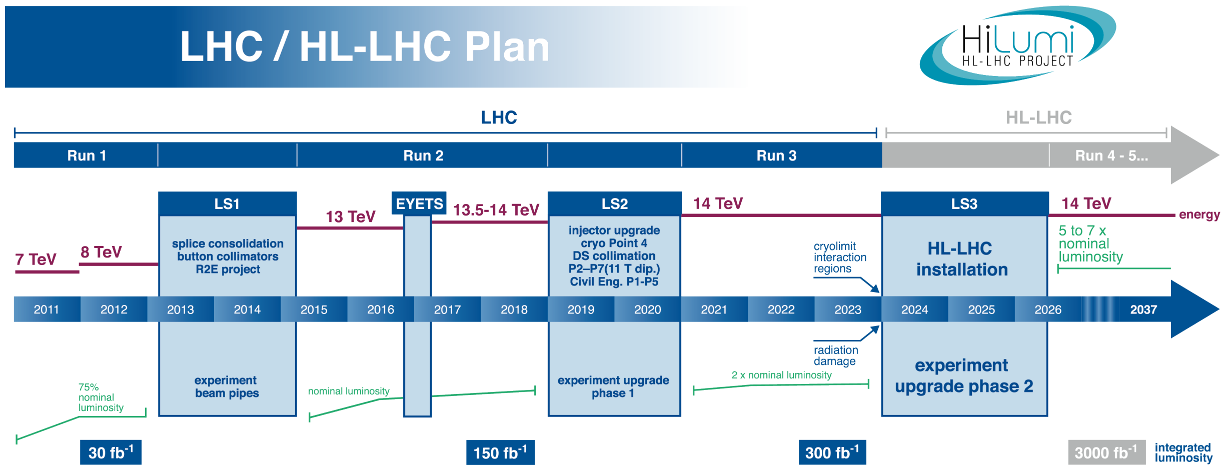

Figure 8.2: The long term program of the LHC showing delivered energies and projected integrated luminosities for different phases of the experiment [119].

Despite only collecting a fraction of the data in the LHC long term schedule, the experiments at the LHC have enjoyed tremendous success, having discovered the Higgs boson, ruling out a wide range of mass scales for new physics scenarios, and providing precision tests of rare standard model processes. However, fundamental questions remain unanswered including a solution to the hierarchy problem and an explanation for dark matter. The future plans for the LHC will provide many challenges for the experiments that collect the collision data and will also provide opportunities to pursue fundamental questions on the nature of particle interactions.

Bibliography

[1] R. Bruce, G. Arduini, H. Bartosik, R. de Maria, M. Giovannozzi, G. Iadarola, J. Jowett, K. Li, M. Lamont, A. Lechner, E. Metral, D. Mirarchi, T. Pieloni, S. Redaelli, G. Rumolo, B. Salvant, R. Tomas, and J. Wenninge, "LHC run 2: Results and challenges," in ICFA Advanced Beam Dynamics Workshop, 2016. High-Intensity, High Brightness and High Power Hadron Beams.

[2] CMS Collaboration, "Observation of a new boson at a mass of 125 GeV with the CMS experiment at the LHC," Phys. Lett. B, vol. 716, pp. 30–61, 2012.

[3] ATLAS Collaboration, "Observation of a new particle in the search for the Standard Model Higgs boson with the ATLAS detector at the LHC," Phys. Lett. B, vol. 716, pp. 1–29, 2012.

[4] CMS Collaboration, "Measurements of properties of the Higgs boson and search for an additional resonance in the four-lepton final state at $\sqrt{s} = 13$ TeV," Tech. Rep. CMS-PAS-HIG-16-033, CERN, Geneva, 2016.

[5] C. Burgess and G. Moore, The Standard Model: A Primer. Cambridge University Press, 2007.

[6] Particle Data Group, "Review of Particle Physics," Chin. Phys. C, vol. 38, p. 090001, 2014.

[7] S. L. Glashow, "Partial Symmetries of Weak Interactions," Nucl. Phys., vol. 22, pp. 579–588, 1961.

[8] S. Weinberg, "A Model of Leptons," Phys. Rev. Lett., vol. 19, pp. 1264–1266, 1967.

[9] A. Salam, "Weak and Electromagnetic Interactions," Conf. Proc., vol. C680519, pp. 367–377, 1968.

[10] CMS Collaboration, "Summaries of CMS cross section measurements." `http://cern.ch/go/pNj7`, 2017.

[11] D. Hanneke, S. Fogwell, and G. Gabrielse, "New Measurement of the Electron Magnetic Moment and the Fine Structure Constant," Phys. Rev. Lett., vol. 100, no. 12, p. 120801, 2008.

[12] L. Susskind, "The gauge hierarchy problem, technicolor, supersymmetry, and all that," Phys. Rept., vol. 104, pp. 181–193, 1984.

[13] R. Adam et al., "Planck 2015 results. I. Overview of products and scientific results," Astron. Astrophys., vol. 594, p. A1, 2016.

[14] E. Gildener, "Gauge-symmetry hierarchies," Phys. Rev. D, vol. 14, p. 1667, 1976.

[15] S. P. Martin, "A Supersymmetry primer," Adv. Ser. Direct. High Energy Phys, vol. 18, p. 1, 1997.

[16] M. Papucci, J. T. Ruderman, and A. Weiler, "Natural SUSY Endures," JHEP, vol. 09, p. 035, 2012.

[17] C. F. Kolda and H. Murayama, "The Higgs mass and new physics scales in the minimal standard model," JHEP, vol. 07, p. 035, 2000.

[18] J. L. Feng, "Naturalness and the status of supersymmetry," Ann. Rev. Nucl. Part. Sci., vol. 63, pp. 351–382, 2013.

[19] C. Borschensky, M. Krämer, A. Kulesza, M. Mangano, S. Padhi, T. Plehn, and X. Portell, "Squark and gluino production cross sections in pp collisions at $\sqrt{s} = 13$, 14, 33 and 100 TeV," Eur. Phys. J., vol. C74, no. 12, p. 3174, 2014.

[20] H. Georgi and S. L. Glashow, "Unity of all elementary-particle forces," Phys. Rev. Lett., vol. 32, pp. 438–441, 1974.

[21] J. Terning, Modern Supersymmetry: Dynamics and Duality. Oxford Science Publications, 2006.

[22] A. Redelbach, "Searches for prompt R-parity-violating supersymmetry at the LHC," Advances in High Energy Physics, vol. 2015, p. 35, 2015.

[23] P. S. B. Dev, D. K. Ghosh, and W. Rodejohann, "r-parity violating supersymmetry at Ice-Cube," Phys. Lett. B, vol. 762, p. 116, 2016.

[24] P. Binétruy, Supersymmetry: Theory, Experiment, and Cosmology. Oxford Graduate Texts, 2006.

[25] T. Falk, K. A. Olive, and M. Srednicki, "Heavy sneutrinos as dark matter," Phys. Lett. B, vol. 339, pp. 248–251, 1994.

[26] D. Alves, "Simplified Models for LHC New Physics Searches," J. Phys., vol. G39, p. 105005, 2012.

[27] CMS Collaboration, "Interpretation of Searches for Supersymmetry with Simplified Models," Phys. Rev. D, vol. 88, no. 5, p. 052017, 2013.

[28] G. Dissertori, I. Knowles, and M. Schmelling, Quantum Chromodynamics: High Energy Experiments and Theory. International series of monographs on physics, Oxford University Press, 2009.

[29] R. Ellis, W. Stirling, and B. Webber, QCD and Collider Physics. Cambridge Monographs on Particle Physics, Nuclear Physics and Cosmology, Cambridge University Press, 2003.

[30] R. Placakyte, "Parton Distribution Functions," in 31st International Conference on Physics, 2011. arXiv:1111.5452.

[31] A. D. Martin, "Proton structure, Partons, QCD, DGLAP and beyond," Acta Phys. Polon., vol. B39, pp. 2025–2062, 2008.

[32] M. E. Peskin, "Beyond the standard model," in European School of High-Energy Physics, 1996. hep-ph/9705479.

[33] O. S. Bruning, P. Collier, P. Lebrun, S. Myers, R. Ostojic, J. Poole, and P. Proudlock, "LHC Design Report Vol.1: The LHC Main Ring," 2004.

[34] CERN, "The CERN accelerator complex." `http://cds.cern.ch/record/1260465`, 2008.

[35] S. Tavernier, Experimental Techniques in Nuclear and Particle Physics. Springer-Verlag Berlin Heidelberg, 2010.

[36] V. Kain, "Beam Transfer and Machine Protection," in Proceedings, 2014 Joint International Accelerator School, pp. 137–158, 2016.

[37] L. Evans and P. Bryant, "LHC Machine," JINST, vol. 3, p. S08001, 2008.

[38] CMS Collaboration, "The CMS Experiment at the CERN LHC," JINST, vol. 3, p. S08004, 2008.

[39] CMS Collaboration, "Description and performance of track and primary-vertex reconstruction with the CMS tracker," JINST, vol. 9, no. 10, p. P10009, 2014.

[40] CMS Collaboration, "Commissioning and performance of the CMS pixel tracker with cosmic ray muons," JINST, vol. 5, no. 03, p. T03007, 2010.

[41] CMS Collaboration, "Commissioning and performance of the cms silicon strip tracker with cosmic ray muons," JINST, vol. 5, no. 03, p. T03008, 2010.

[42] L. L. Jones, M. J. French, Q. R. Morrissey, A. Neviani, M. Raymond, G. Hall, P. Moreira, and G. Cervelli, "The APV25 deep submicron readont chip for CMS detectors." `"https://cds.cern.ch/record/432224`, 1999.

[43] A. Benaglia, "The CMS ECAL performance with examples," JINST, vol. 9, p. C02008, 2014.

[44] CMS Collaboration, "CMS: The hadron calorimeter technical design report," 1997.

[45] Saint-Gobain Ceramics and Plastics, "Premium plastic scintillators." `http://www.crystals.saint-gobain.com/sites/imdf.crystals.com/files/documents/sgc-bc400-404-408-412-416-data-sheet.pdf`, 2017.

[46] Kuraray, "Kuraray's plastic scintillating fibers." `http://kuraraypsf.jp/pdf/all.pdf`, 2017.

[47] CMS Collaboration, "The performance of the CMS muon detector in proton-proton collisions at $\sqrt{s} = 7$ TeV at the LHC," JINST, vol. 8, p. P11002, 2013.

[48] CMS Collaboration, CMS TriDAS project: Technical Design Report, Volume 1. Technical Design Report CMS, CERN, 2000.

[49] CMS Collaboration, CMS TriDAS Project: Technical Design Report, Volume 2. Technical Design Report CMS, Geneva: CERN, 2002.

[50] CMS Collaboration, "The CMS trigger system," JINST, vol. 12, no. 01, p. P01020, 2017.

[51] B. Kreis et al., "Run 2 Upgrades to the CMS Level-1 Calorimeter Trigger," JINST, vol. 11, no. 01, p. C01051, 2016.

[52] CMS Collaboration, "The upgrade of the CMS trigger system," JINST, vol. 9, no. 08, p. C08002, 2014.

[53] J. Alwall, R. Frederix, S. Frixione, V. Hirschi, F. Maltoni, O. Mattelaer, H. S. Shao, T. Stelzer, P. Torrielli, and M. Zaro, "The automated computation of tree-level and next-to-leading order differential cross sections, and their matching to parton shower simulations," JHEP, vol. 07, p. 079, 2014.

[54] S. Alioli, P. Nason, C. Oleari, and E. Re, "A general framework for implementing NLO calculations in shower Monte Carlo programs: the POWHEG BOX," JHEP, vol. 06, p. 043, 2010.

[55] T. Sjöstrand, S. Ask, J. R. Christiansen, R. Corke, N. Desai, P. Ilten, S. Mrenna, S. Prestel, C. O. Rasmussen, and P. Z. Skands, "An Introduction to PYTHIA 8.2," Comput. Phys. Commun., vol. 191, pp. 159–177, 2015.

[56] S. Agostinelli et al., "GEANT4: A Simulation toolkit," Nucl. Instrum. Meth., vol. A506, pp. 250–303, 2003.

[57] S. Mrenna and P. Richardson, "Matching matrix elements and parton showers with HERWIG and PYTHIA," JHEP, vol. 2004, no. 05, p. 040, 2004.

[58] R. D. Ball et al., "Parton distributions for the LHC Run II," JHEP, vol. 04, p. 040, 2015.

[59] T. Melia, P. Nason, R. Rontsch, and G. Zanderighi, "W^+W^-, WZ and ZZ production in the POWHEG BOX," JHEP, vol. 11, p. 078, 2011.

[60] S. Sekmen, "Recent Developments in CMS Fast Simulation," in 38th International Conference on High Energy Physics (ICHEP), p. 181, 2016.

[61] S. Abdullin, P. Azzi, F. Beaudette, P. Janot, A. Perrotta, and the CMS Collaboration, "The fast simulation of the CMS detector at LHC," Journal of Physics: Conference Series, vol. 331, no. 3, p. 032049, 2011.

[62] A. Giammanco, "The fast simulation of the CMS experiment," Journal of Physics: Conference Series, vol. 513, no. 2, p. 022012, 2014.

[63] CMS Collaboration, "Comparison of the Fast Simulation of CMS with the first LHC data," Tech. Rep. CMS-DP-2010-039, CERN, 2010.

[64] W. Beenakker, S. Brensing, M. Kramer, A. Kulesza, E. Laenen, and I. Niessen, "Soft-gluon resummation for squark and gluino hadroproduction," JHEP, vol. 12, p. 041, 2009.

[65] W. Beenakker, S. Brensing, M. Kramer, A. Kulesza, E. Laenen, L. Motyka, and I. Niessen, "Squark and Gluino Hadroproduction," Int. J. Mod. Phys., vol. A26, pp. 2637–2664, 2011.

[66] A. Kulesza and L. Motyka, “Threshold resummation for squark-antisquark and gluino-pair production at the LHC,” Phys. Rev. Lett., vol. 102, p. 111802, 2009.

[67] A. Kulesza and L. Motyka, “Soft gluon resummation for the production of gluino-gluino and squark-antisquark pairs at the LHC,” Phys. Rev. D, vol. 80, p. 095004, 2009.

[68] F. De Guio, “The CMS data quality monitoring software: experience and future prospects,” J. Phys. Conf. Ser., vol. 513, p. 032024, 2014.

[69] L. Tuura, A. Meyer, I. Segoni, and G. Della Ricca, “CMS data quality monitoring: Systems and experiences,” J. Phys. Conf. Ser., vol. 219, p. 072020, 2010.

[70] CMS Collaboration, “CMS Luminosity Measurement for the 2016 Data Taking Period,” Tech. Rep. CMS-PAS-LUM-17-001, CERN, Geneva, 2017.

[71] BRIL Group, “BRIL Work Suite.” `http://cms-service-lumi.web.cern.ch/cms-service-lumi/brilwsdoc.html`, 2017.

[72] CMS Collaboration, “Description and performance of track and primary-vertex reconstruction with the CMS tracker,” JINST, vol. 9, no. 10, p. P10009, 2014.

[73] R. Frühwirth, “Application of Kalman filtering to track and vertex fitting,” Nucl. Instrum. Meth., vol. A262, pp. 444–450, 1987.

[74] CMS Collaboration, “Performance of CMS muon reconstruction in cosmic-ray events,” JINST, vol. 5, no. 03, p. T03022, 2010.

[75] K. Rose, “Deterministic annealing for clustering, compression, classification, regression, and related optimization problems,” Proceedings of the IEEE, vol. 86, no. 11, pp. 2210–2239, 1998.

[76] R. Frühwirth, W. Waltenberger, and P. Vanlaer, “Adaptive Vertex Fitting,” Tech. Rep. CMS-NOTE-2007-008, CERN, Geneva, 2007.

[77] CMS Collaboration, “Particle-Flow Event Reconstruction in CMS and Performance for Jets, Taus, and MET,” Tech. Rep. CMS-PAS-PFT-09-001, CERN, 2009. Geneva, 2009.

[78] CMS Collaboration, “Commissioning of the Particle-flow Event Reconstruction with the first LHC collisions recorded in the CMS detector,” Tech. Rep. CMS-PAS-PFT-10-001, CERN, 2010.

[79] CMS Collaboration, “Performance of Electron Reconstruction and Selection with the CMS Detector in Proton-Proton Collisions at $\sqrt{s} = 8$ TeV,” JINST, vol. 10, no. 06, p. P06005, 2015.

[80] CMS Collaboration, “Performance of Photon Reconstruction and Identification with the CMS Detector in Proton-Proton Collisions at $\sqrt{s} = 8$ TeV,” JINST, vol. 10, no. 08, p. P08010, 2015.

[81] M. Cacciari, G. P. Salam, and G. Soyez, “The anti-k_T jet clustering algorithm,” JHEP, vol. 04, p. 063, 2008.

[82] M. Cacciari, G. P. Salam, and G. Soyez, "FastJet User Manual," Eur. Phys. J., vol. C72, p. 1896, 2012.

[83] CMS Collaboration, "Pileup Removal Algorithms," Tech. Rep. CMS-PAS-JME-14-001, CERN, Geneva, 2014.

[84] CMS Collaboration, "Jet algorithms performance in 13 TeV data," Tech. Rep. CMS-PAS-JME-16-003, CERN, Geneva, 2017.

[85] CMS Collaboration, "Jet Performance in pp Collisions at 7 TeV," Tech. Rep. CMS-PAS-JME-10-003, CERN, Geneva, 2010.

[86] MAC Collaboration, "Lifetime of Particles Containing b Quarks," Phys. Rev. Lett., vol. 51, pp. 1022–1025, 1983.

[87] CMS collaboration, "Identification of b-quark jets with the CMS experiment," JINST, vol. 8, no. 04, p. P04013, 2013.

[88] CMS Collaboration, "Identification of b-quark jets at the CMS Experiment in the LHC Run 2," Tech. Rep. CMS-PAS-BTV-15-001, CERN, Geneva, 2016.

[89] CMS Collaboration, "Measurement of $B\bar{B}$ Angular Correlations based on Secondary Vertex Reconstruction at $\sqrt{s} = 7$ TeV," JHEP, vol. 03, p. 136, 2011.

[90] CMS Collaboration, "Performance of missing energy reconstruction in 13 TeV pp collision data using the CMS detector," Tech. Rep. CMS-PAS-JME-16-004, CERN, Geneva, 2016.

[91] CMS Collaboration, "Performance of the CMS muon detector and reconstruction with p+p collisions at $\sqrt{s} = 13$ TeV," Tech. Rep. CMS-PAS-MUO-16-001, CERN, 2017. Geneva, 2017.

[92] CMS Collaboration, "Search for supersymmetry in multijet final states in proton-proton collisions at 13 TeV," Tech. Rep. CMS-AN-SUS-16-350, CERN, Geneva, 2017.

[93] A. Hoecker, P. Speckmayer, J. Stelzer, J. Therhaag, E. von Toerne, H. Voss, M. Backes, T. Carli, O. Cohen, A. Christov, D. Dannheim, K. Danielowski, S. Henrot-Versille, M. Jachowski, K. Kraszewski, A. Krasznahorkay, Jr., M. Kruk, Y. Mahalalel, R. Ospanov, X. Prudent, A. Robert, D. Schouten, F. Tegenfeldt, A. Voigt, K. Voss, M. Wolter, and A. Zemla, "TMVA - Toolkit for Multivariate Data Analysis," arXiv:0703039, 2007.

[94] A. Hoecker, P. Speckmayer, J. Stelzer, J. Therhaag, E. von Toerne, and V. E., "TMVA 4 toolkit for multivariate data analysis with ROOT." `http://tmva.sourceforge.net/docu/TMVAUsersGuide.pdf`, 2016.

[95] S. Kallweit, J. M. Lindert, S. Pozzorini, M. Schnherr, and P. Maierhfer, "NLO QCD+EW automation and precise predictions for V+multijet production," in Proceedings, 50th Rencontres de Moriond, pp. 121–124, 2015.

[96] CMS Collaboration, "Measuring Electron Efficiencies at CMS with Early Data," 2008.

[97] CMS Collaboration, "Tag and probe." `https://twiki.cern.ch/twiki/bin/view/CMSPublic/TagAndProbe`, 2014.

[98] A. Kornmayer, “The CMS Pixel Luminosity Telescope,” Tech. Rep. CMS-CR-2015-121, CERN, Geneva, 2015.

[99] M. Hempel, T. Baer, W. Lange, N. J. Odell, D. P. Stickland, and E. Griesmayer, “Performance of detectors using diamond sensors at the LHC and CMS,” in International Beam Instrumentation Conference, 2013.

[100] CMS Collaboration, “CMS Luminosity Based on Pixel Cluster Counting - Summer 2013 Update,” Tech. Rep. CMS-PAS-LUM-13-001, CERN, 2013.

[101] M. Cacciari, S. Frixione, M. L. Mangano, P. Nason, and G. Ridolfi, “The $t\bar{t}$ cross-section at 1.8 TeV and 1.96 TeV: A Study of the systematics due to parton densities and scale dependence,” JHEP, vol. 04, p. 068, 2004.

[102] S. Catani, D. de Florian, M. Grazzini, and P. Nason, “Soft gluon resummation for Higgs boson production at hadron colliders,” JHEP, vol. 07, p. 028, 2003.

[103] CMS Experiment, “Determination of Jet Energy Calibration and Transverse Momentum Resolution in CMS,” JINST, vol. 6, p. P11002, 2011.

[104] CMS Collaboration, “Jet energy scale and resolution performances with 13 TeV data,” Tech. Rep. CMS-DP-2016-020, CERN, 2016.

[105] M. Botje et al., “The PDF4LHC Working Group Interim Recommendations,” 2011. arXiv:1101.0538.

[106] S. Alekhin et al., “The PDF4LHC Working Group Interim Report,” 2011. arXiv:1101.0536.

[107] A. D. Martin, W. J. Stirling, R. S. Thorne, and G. Watt, “Update of parton distributions at NNLO,” Phys. Lett. B, vol. 652, pp. 292–299, 2007.

[108] J. Butterworth et al., “PDF4LHC recommendations for LHC Run II,” J. Phys. G, vol. 43, p. 023001, 2016.

[109] CMS Collaboration, “Search for supersymmetry in the multijet and missing transverse momentum final state in pp collisions at 13 TeV,” Phys. Lett. B, vol. 758, pp. 152–180, 2016.

[110] CMS Collaboration, “Search for new physics in the all-hadronic final state with the MT2 variable,” Tech. Rep. CMS-PAS-SUS-15-003, CERN, 2015.

[111] CMS Collaboration, “Search for supersymmetry in pp collisions at $\sqrt{s} = 13$ TeV in the single-lepton final state using the sum of masses of large-radius jets,” JHEP, vol. 08, p. 122, 2016.

[112] G. Cowan, K. Cranmer, E. Gross, and O. Vitells, “Asymptotic formulae for likelihood-based tests of new physics,” Eur. Phys. J., vol. C71, p. 1554, 2011. [Erratum: Eur. Phys. J.C73,2501(2013)].

[113] T. Junk, “Confidence level computation for combining searches with small statistics,” Nucl. Instrum. Meth., vol. A434, pp. 435–443, 1999.

[114] A. L. Read, “Presentation of search results: the CL_s technique,” J. Phys. G, vol. 28, no. 10, p. 2693, 2002.

[115] The ATLAS Collaboration, The CMS Collaboration, The LHC Higgs Combination Group, "Procedure for the LHC Higgs boson search combination in Summer 2011," Tech. Rep. CMS-NOTE-2011-005. ATL-PHYS-PUB-2011-11, CERN, Geneva, 2011.

[116] CMS Collaboration, "Search for supersymmetry in multijet events with missing transverse momentum in proton-proton collisions at 13 TeV," 2017. arXiv:1704.07781.

[117] CMS Collaboration, "Search for supersymmetry in events with b-quark jets and missing transverse energy in pp collisions at 7 TeV," Phys. Rev., vol. D86, p. 072010, 2012.

[118] CMS Collaboration, "Search for gluino mediated bottom- and top-squark production in multijet final states in pp collisions at 8 TeV," Phys. Lett. B, vol. 725, pp. 243–270, 2013.

[119] A. Szeberenyi, "A luminous future for the LHC," CERN Courier, 2015.

[120] CMS Collaboration, "Physics analysis oriented event display." `https://twiki.cern.ch/twiki/bin/view/CMSPublic/WorkBookFireworks`, 2017.

Appendix A

Supporting Material for the Boosted Decision Tree Analysis

A comparison between FullSim and FastSim for a benchmark SUSY model point is shown in Figure A.1. Expected and observed yields in the BDT sideband region (signal-like BDT < 0.5) are given in Table A.1.

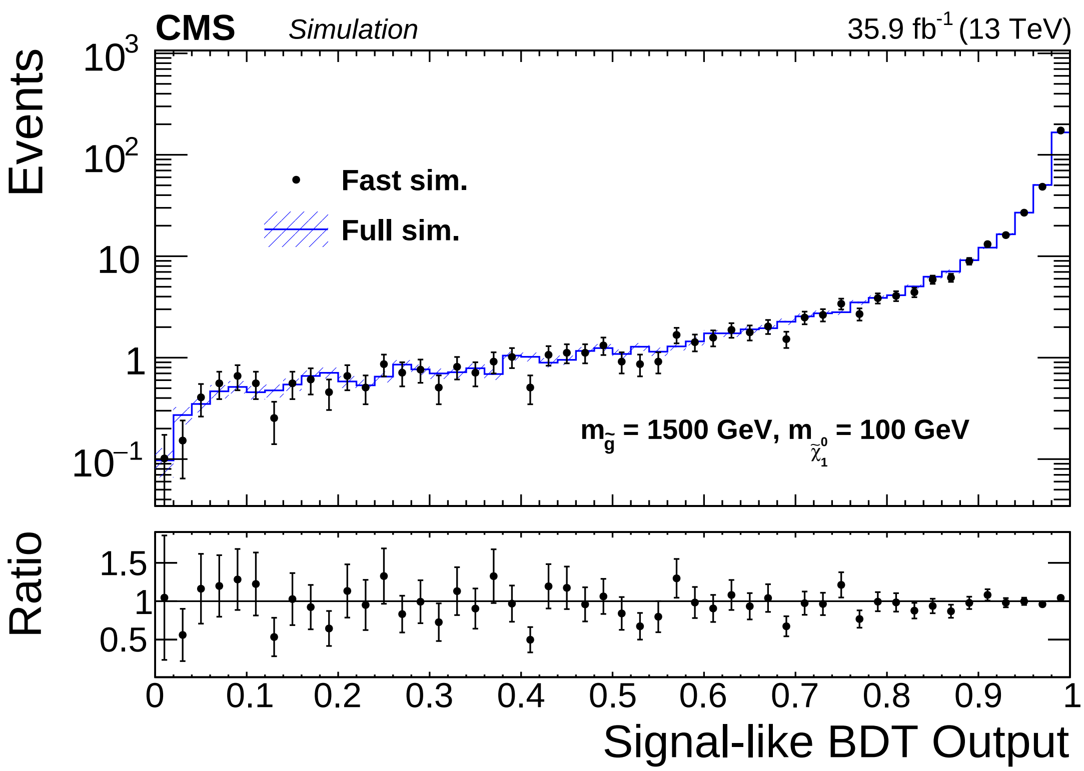

Figure A.1: Comparison of FastSim and FullSim in the signal-like BDT output discriminant for a single mass point. The BDT is trained using a few FullSim benchmark points while the SUSY SMS models are interpreted in the context of the FastSim mass scans.

Table A.1: Observed number of events compared to the prediction in the sideband bins (signal-like BDT<0.5). The upper and lower uncertainties on the prediction are given separately, formatted as STAT + SYST, and the absolute number of observed events are given in the rightmost column. The corresponding table of signal yields (Table 6.2) is given in Chapter 6.

Analysis Bin	QCD Pred.	Top+W Pred.	Z $\to \nu\bar{\nu}$ Pred.	Total Pred.	Observation
1	$4108^{+32+2500}_{-31-2000}$	$1689^{+28+160}_{-28-140}$	$1617^{+25+110}_{-24-110}$	$7414^{+49+2500}_{-48-2000}$	7589
2	$1708^{+24+1000}_{-23-850}$	$1718^{+31+230}_{-31-220}$	$1498^{+23+110}_{-22-110}$	$4925^{+45+1100}_{-44-890}$	4883
3	$943^{+20+550}_{-19-450}$	1132^{+27+86}_{-26-79}	927^{+18+65}_{-18-65}	$3003^{+38+560}_{-37-470}$	2934
4	$550^{+15+320}_{-15-260}$	$884^{+24+170}_{-23-170}$	781^{+17+54}_{-16-53}	$2216^{+33+360}_{-32-320}$	2212
5	$286^{+10+170}_{-9.9-140}$	708^{+22+77}_{-21-75}	510^{+13+35}_{-13-35}	$1505^{+28+190}_{-27-170}$	1544
6	$287^{+12+160}_{-12-130}$	582^{+20+42}_{-20-39}	407^{+12+28}_{-12-28}	$1277^{+26+160}_{-26-140}$	1212
7	$164^{+8.1+90}_{-7.7-76}$	475^{+19+45}_{-18-44}	464^{+13+32}_{-12-32}	$1103^{+24+110}_{-23-93}$	1171
8	$175^{+9.7+89}_{-9.2-73}$	414^{+18+53}_{-17-52}	347^{+11+24}_{-11-24}	$938^{+23+110}_{-22-92}$	917
9	$86^{+5.5+54}_{-5.2-47}$	375^{+17+41}_{-16-42}	316^{+11+22}_{-10-22}	778^{+21+71}_{-20-67}	772
10	$95^{+6.6+50}_{-6.1-43}$	300^{+15+25}_{-14-24}	$255^{+9.5+18}_{-9.1-18}$	651^{+19+59}_{-18-52}	704
11	$42^{+3.6+31}_{-3.3-27}$	280^{+14+59}_{-14-59}	$234^{+9.2+16}_{-8.9-16}$	558^{+17+69}_{-17-67}	583
12	$136^{+11+60}_{-9.8-49}$	268^{+14+21}_{-14-20}	$191^{+8.3+13}_{-7.9-13}$	597^{+20+65}_{-19-54}	502
13	$82^{+7.1+36}_{-6.5-29}$	216^{+13+28}_{-12-27}	$184^{+8.3+13}_{-8.0-13}$	483^{+17+47}_{-16-42}	475
14	$81^{+7.1+33}_{-6.5-27}$	188^{+12+43}_{-12-43}	$159^{+7.7+11}_{-7.3-11}$	428^{+16+55}_{-15-52}	386
15	$61^{+5.9+26}_{-5.4-20}$	159^{+11+16}_{-10-16}	$145^{+7.4+10}_{-7.0-10}$	365^{+15+32}_{-14-27}	353
16	$34^{+3.5+18}_{-3.1-16}$	$148^{+10+13}_{-9.8-13}$	$127.9^{+7.1+8.8}_{-6.7-8.9}$	310^{+13+24}_{-12-22}	339
17	$48^{+5.0+20}_{-4.5-18}$	153^{+11+32}_{-10-32}	$102.8^{+6.2+7.1}_{-5.9-7.2}$	305^{+13+39}_{-12-37}	301
18	$49^{+5.6+21}_{-5.0-18}$	$138^{+10+11}_{-9.6-9.9}$	$112.4^{+6.5+8.0}_{-6.1-7.8}$	300^{+13+25}_{-12-22}	309
19	$48^{+5.3+19}_{-4.8-18}$	$123^{+9.8+16}_{-9.1-16}$	$114.8^{+6.6+8.3}_{-6.3-8.0}$	286^{+13+26}_{-12-25}	287
20	$55^{+6.3+20}_{-5.7-17}$	$110^{+9.2+11}_{-8.5-11}$	$127.3^{+7.0+9.5}_{-6.6-8.8}$	293^{+13+25}_{-12-22}	311
21	$18^{+2.2+13}_{-2.0-10}$	$125^{+9.9+11}_{-9.2-11}$	$133.6^{+7.3+9.3}_{-6.9-9.5}$	277^{+13+19}_{-12-18}	257
22	$33^{+4.5+14}_{-3.9-15}$	$118^{+9.7+18}_{-8.9-18}$	$102.4^{+6.2+7.2}_{-5.9-7.1}$	254^{+12+24}_{-11-25}	275
23	$21.3^{+3.2+8.8}_{-2.8-7.7}$	$89^{+8.6+14}_{-7.9-14}$	$101.0^{+6.2+7.1}_{-5.8-7.3}$	211^{+11+18}_{-10-17}	239
24	$41^{+5.7+13}_{-5.0-13}$	$83^{+7.9+13}_{-7.2-13}$	$100.4^{+6.4+7.1}_{-6.0-8.0}$	226^{+12+19}_{-11-20}	207
25	$43^{+6.2+13}_{-5.5-10.0}$	$86.5^{+8.3+7.3}_{-7.6-7.0}$	$83.0^{+5.6+5.9}_{-5.3-5.8}$	212^{+12+16}_{-11-14}	164

Appendix B

Supporting Material for Multidimensional Binned Analysis

Yields in all 172 bins of the multidimensional binned analysis are given in Tables B.1-B.5.

B.1 Additional Interpretations

In addition to the targeted scenarios presented in Figure 7.12, we present alternative simplified model exclusion interpretations. The diagrams corresponding to these models are shown in Figure B.1, and the corresponding cross section upper limit plots are shown in Figure B.2.

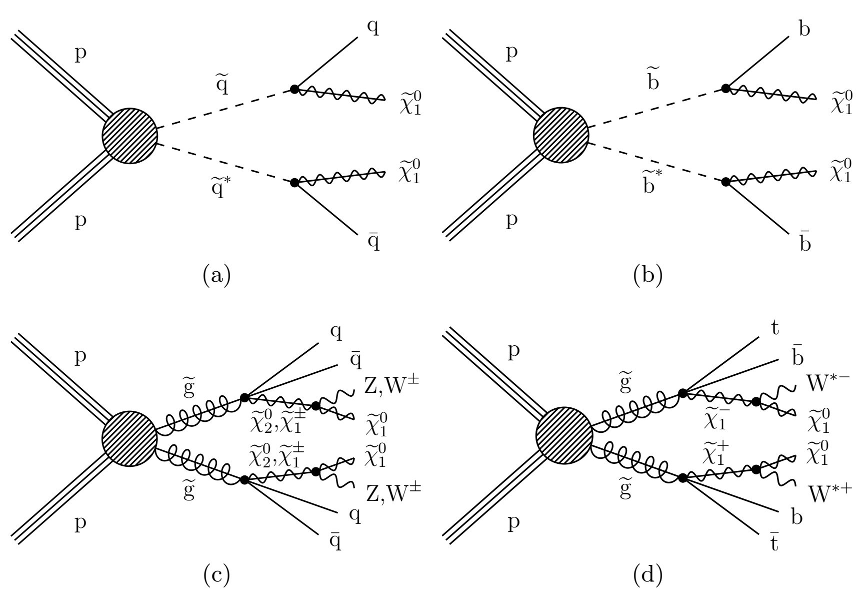

Figure B.1: Simplified SUSY diagrams for additional interpretations: T2qq (a), T2bb (b), T1qqqqVV (c), and T1tbtb (d).

Table B.1: Observed number of events and pre-fit background predictions in the $\mathrm{N_{jet}} = 2$ search bins.

Bin	$\mathrm{H_T^{miss}}$ [GeV]	$\mathrm{H_T}$ [GeV]	$\mathrm{N_{jet}}$	$\mathrm{N_{b\text{-}jet}}$	Lost-e/μ	$\tau \to$ had	$Z \to \nu\bar{\nu}$	QCD	Total Pred.	Obs.
1	300-350	300-500	2	0	$4069^{+67+320}_{-67-320}$	$2744^{+37+510}_{-37-500}$	$13231^{+67+760}_{-66-740}$	$326^{+12+170}_{-12-120}$	$20370^{+120+980}_{-120-960}$	21626
2	300-350	500-1000	2	0	326^{+22+36}_{-22-36}	226^{+11+43}_{-11-42}	944^{+18+55}_{-18-54}	45^{+2+24}_{-2-17}	1541^{+37+82}_{-37-79}	1583
3	300-350	1000+	2	0	$15.2^{+5.8+2.3}_{-5.1-2.3}$	$8.7^{+2.1+2.1}_{-2.0-2.1}$	$50.9^{+4.5+4.4}_{-4.1-3.8}$	$1.57^{+0.16+0.84}_{-0.16-0.61}$	$76.3^{+9.1+5.5}_{-8.2-5.0}$	102
4	350-500	350-500	2	0	$2049^{+46+160}_{-46-160}$	$1553^{+27+290}_{-27-290}$	$9347^{+57+540}_{-57-520}$	126^{+4+67}_{-4-48}	$13076^{+93+630}_{-93-620}$	14019
5	350-500	500-1000	2	0	631^{+25+54}_{-25-54}	439^{+14+84}_{-14-84}	$2502^{+30+150}_{-30-140}$	43^{+7+22}_{-7-16}	$3615^{+49+180}_{-49-170}$	3730
6	350-500	1000+	2	0	$13.5^{+4.9+1.9}_{-4.3-1.9}$	$13.4^{+2.4+2.6}_{-2.3-2.6}$	$94.0^{+6.2+7.9}_{-5.8-6.9}$	$1.30^{+0.06+0.68}_{-0.06-0.49}$	$122.1^{+9.5+8.6}_{-8.8-7.6}$	139
7	500-750	500-1000	2	0	303^{+17+29}_{-17-29}	247^{+10+48}_{-10-47}	$2328^{+30+170}_{-29-160}$	$4.5^{+0.1+2.4}_{-0.1-1.7}$	$2883^{+40+180}_{-40-170}$	3018
8	500-750	1000+	2	0	$5.8^{+2.7+1.5}_{-2.2-1.5}$	$5.3^{+1.4+1.3}_{-1.3-1.3}$	$66.2^{+5.4+5.3}_{-5.0-5.1}$	$0.03^{+0.02+0.02}_{-0.02-0.01}$	$77.3^{+6.8+5.7}_{-6.1-5.4}$	96
9	750+	750-1500	2	0	$17.3^{+4.5+3.0}_{-4.1-3.0}$	$17.4^{+2.5+4.5}_{-2.4-4.5}$	295^{+11+41}_{-11-38}	$0.35^{+0.06+0.18}_{-0.06-0.13}$	330^{+13+42}_{-12-38}	272
10	750+	1500+	2	0	$0.0^{+1.8+0.0}_{-0.0-0.0}$	$0.38^{+0.54+0.09}_{-0.29-0.09}$	$12.6^{+3.0+2.1}_{-2.4-1.9}$	$0.01^{+0.01+0.00}_{-0.01-0.00}$	$13.0^{+3.8+2.1}_{-2.5-1.9}$	12
11	300-350	300-500	2	1	370^{+21+31}_{-21-31}	288^{+11+63}_{-11-63}	1361^{+7+140}_{-7-140}	44^{+6+25}_{-6-17}	$2063^{+33+160}_{-33-160}$	1904
12	300-350	500-1000	2	1	51^{+10+7}_{-10-7}	$31.6^{+4.2+7.2}_{-4.2-7.2}$	97^{+2+10}_{-2-10}	$6.7^{+2.7+3.7}_{-2.7-2.5}$	186^{+15+15}_{-14-14}	186
13	300-350	1000+	2	1	$1.1^{+2.3+0.2}_{-1.1-0.0}$	$2.0^{+1.1+0.5}_{-1.0-0.5}$	$5.23^{+0.46+0.63}_{-0.42-0.59}$	$0.33^{+0.02+0.18}_{-0.02-0.13}$	$8.7^{+3.4+0.9}_{-2.1-0.8}$	13
14	350-500	350-500	2	1	215^{+16+19}_{-16-19}	179^{+9+39}_{-9-39}	962^{+6+99}_{-6-98}	20^{+2+11}_{-2-8}	$1376^{+26+110}_{-26-110}$	1212
15	350-500	500-1000	2	1	$69.8^{+9.9+7.5}_{-9.8-7.5}$	$43.3^{+4.4+9.7}_{-4.4-9.6}$	257^{+3+27}_{-3-26}	$8.5^{+3.0+4.8}_{-3.0-3.2}$	379^{+15+30}_{-15-29}	409
16	350-500	1000+	2	1	$3.7^{+2.5+0.7}_{-1.9-0.7}$	$3.1^{+1.1+0.9}_{-1.0-0.9}$	$9.7^{+0.6+1.2}_{-0.6-1.1}$	$0.13^{+0.04+0.07}_{-0.04-0.05}$	$16.6^{+3.7+1.6}_{-3.0-1.6}$	27
17	500-750	500-1000	2	1	$28.9^{+5.8+3.3}_{-5.6-3.3}$	$26.0^{+2.9+5.8}_{-2.9-5.8}$	240^{+3+27}_{-3-26}	$1.48^{+0.18+0.83}_{-0.18-0.56}$	296^{+9+28}_{-9-27}	321
18	500-750	1000+	2	1	$5.1^{+6.2+1.6}_{-4.1-1.6}$	$0.36^{+0.55+0.12}_{-0.30-0.12}$	$6.81^{+0.56+0.80}_{-0.52-0.78}$	$0.03^{+0.03+0.02}_{-0.03-0.00}$	$12.3^{+6.8+1.8}_{-4.5-1.7}$	14
19	750+	750-1500	2	1	$3.8^{+2.2+0.8}_{-1.7-0.8}$	$4.1^{+1.5+1.1}_{-1.4-1.1}$	$30.4^{+1.1+5.0}_{-1.1-4.7}$	$0.10^{+0.03+0.06}_{-0.03-0.04}$	$38.4^{+3.9+5.1}_{-3.3-4.8}$	31
20	750+	1500+	2	1	$0.0^{+1.4+0.0}_{-0.0-0.0}$	$0.34^{+0.51+0.13}_{-0.22-0.13}$	$1.29^{+0.31+0.24}_{-0.25-0.23}$	$0.00^{+0.01+0.00}_{-0.00-0.00}$	$1.6^{+2.0+0.3}_{-0.3-0.3}$	1
21	300-350	300-500	2	2	$14.1^{+4.5+2.6}_{-4.0-2.6}$	$12.9^{+2.3+2.8}_{-2.2-2.8}$	49^{+0+17}_{-0-17}	$3.0^{+0.8+3.6}_{-0.8-2.1}$	79^{+7+18}_{-6-18}	122
22	300-350	500-1000	2	2	$2.8^{+2.4+0.9}_{-1.7-0.9}$	$2.0^{+1.1+1.0}_{-0.9-1.0}$	$3.5^{+0.1+1.2}_{-0.1-1.2}$	$0.57^{+0.17+0.69}_{-0.17-0.40}$	$8.9^{+3.5+2.0}_{-2.6-1.9}$	11
23	300-350	1000+	2	2	$0.0^{+2.2+0.0}_{-0.0-0.0}$	$0.00^{+0.46+0.00}_{-0.00-0.00}$	$0.19^{+0.02+0.07}_{-0.01-0.07}$	$0.03^{+0.01+0.04}_{-0.01-0.02}$	$0.2^{+2.6+0.1}_{-0.0-0.1}$	0
24	350-500	350-500	2	2	$11.4^{+4.5+2.5}_{-3.9-2.5}$	$6.3^{+1.7+2.1}_{-1.6-2.1}$	35^{+0+12}_{-0-12}	$1.0^{+0.5+1.2}_{-0.5-0.6}$	53^{+6+13}_{-6-13}	84
25	350-500	500-1000	2	2	$6.1^{+2.9+1.5}_{-2.4-1.5}$	$2.9^{+1.2+0.8}_{-1.1-0.8}$	$9.3^{+0.1+3.3}_{-0.1-3.3}$	$0.44^{+0.05+0.52}_{-0.05-0.39}$	$18.7^{+4.1+3.8}_{-3.5-3.7}$	23
26	350-500	1000+	2	2	$0.0^{+1.1+0.0}_{-0.0-0.0}$	$0.00^{+0.46+0.00}_{-0.00-0.00}$	$0.35^{+0.02+0.13}_{-0.02-0.13}$	$0.06^{+0.04+0.08}_{-0.04-0.02}$	$0.4^{+1.5+0.1}_{-0.0-0.1}$	2
27	500-750	500-1000	2	2	$1.4^{+2.9+0.4}_{-1.4-0.0}$	$2.03^{+0.84+0.61}_{-0.70-0.61}$	$8.6^{+0.1+3.1}_{-0.1-3.1}$	$0.03^{+0.01+0.04}_{-0.01-0.03}$	$12.1^{+3.7+3.2}_{-2.1-3.2}$	16
28	500-750	1000+	2	2	$0.0^{+2.2+0.0}_{-0.0-0.0}$	$0.00^{+0.46+0.00}_{-0.00-0.00}$	$0.24^{+0.02+0.09}_{-0.02-0.09}$	$0.00^{+0.01+0.00}_{-0.00-0.00}$	$0.2^{+2.7+0.1}_{-0.0-0.1}$	0
29	750+	750-1500	2	2	$0.0^{+1.6+0.0}_{-0.0-0.0}$	$0.07^{+0.46+0.07}_{-0.04-0.06}$	$1.09^{+0.04+0.41}_{-0.04-0.41}$	$0.01^{+0.01+0.01}_{-0.01-0.00}$	$1.2^{+2.1+0.4}_{-0.1-0.4}$	4
30	750+	1500+	2	2	$0.0^{+2.0+0.0}_{-0.0-0.0}$	$0.00^{+0.46+0.00}_{-0.00-0.00}$	$0.05^{+0.01+0.02}_{-0.01-0.02}$	$0.00^{+0.01+0.00}_{-0.00-0.00}$	$0.0^{+2.5+0.0}_{-0.0-0.0}$	0

Table B.2: Observed number of events and pre-fit background predictions in the $3 \leq N_{jet} \leq 4$ search bins.

Bin	H_T^{miss} [GeV]	H_T [GeV]	N_{jet}	$N_{b\text{-}jet}$	Lost-e/μ	$\tau \to$ had	$Z \to \nu\bar{\nu}$	QCD	Total Pred.	Obs.
31	300-350	300-500	3-4	0	$2830^{+45+200}_{-45-200}$	$2152^{+29+160}_{-29-150}$	$8353^{+52+480}_{-52-470}$	$273^{+68+120}_{-68-100}$	$13608^{+110+560}_{-110-540}$	14520
32	300-350	500-1000	3-4	0	$1125^{+25+120}_{-25-120}$	$909^{+18+100}_{-18-100}$	$2487^{+29+140}_{-28-140}$	119^{+8+51}_{-8-45}	$4640^{+52+220}_{-52-210}$	4799
33	300-350	1000+	3-4	0	$72.7^{+7.1+6.1}_{-7.1-6.1}$	$65.3^{+5.2+6.4}_{-5.2-6.3}$	176^{+8+14}_{-8-12}	41^{+2+18}_{-2-16}	356^{+15+24}_{-15-22}	354
34	350-500	350-500	3-4	0	$1439^{+37+110}_{-37-110}$	$930^{+19+120}_{-19-110}$	$5014^{+41+280}_{-41-280}$	114^{+6+48}_{-6-43}	$7496^{+70+330}_{-69-320}$	7973
35	350-500	500-1000	3-4	0	$1402^{+27+140}_{-27-140}$	$1253^{+22+120}_{-22-120}$	$4811^{+40+270}_{-40-260}$	80^{+9+34}_{-9-31}	$7547^{+65+330}_{-64-320}$	7735
36	350-500	1000+	3-4	0	103^{+8+11}_{-8-11}	$77.0^{+5.9+7.6}_{-5.9-7.5}$	303^{+11+24}_{-10-21}	24^{+1+10}_{-1-9}	506^{+18+30}_{-17-26}	490
37	500-750	500-1000	3-4	0	339^{+15+33}_{-15-33}	297^{+10+26}_{-10-26}	$2143^{+28+150}_{-28-140}$	$5.5^{+0.2+2.3}_{-0.2-2.1}$	$2785^{+37+160}_{-37-150}$	2938
38	500-750	1000+	3-4	0	$33.8^{+4.4+3.6}_{-4.3-3.6}$	$30.5^{+3.4+2.9}_{-3.4-2.9}$	219^{+10+16}_{-9-15}	$1.29^{+0.53+0.55}_{-0.53-0.49}$	284^{+12+17}_{-12-16}	303
39	750+	750-1500	3-4	0	$28.2^{+4.4+3.7}_{-4.3-3.7}$	$26.0^{+2.9+3.4}_{-2.9-3.4}$	319^{+11+44}_{-11-40}	$0.32^{+0.03+0.14}_{-0.03-0.12}$	373^{+14+44}_{-13-41}	334
40	750+	1500+	3-4	0	$2.9^{+2.0+0.7}_{-1.5-0.7}$	$1.38^{+0.66+0.17}_{-0.48-0.17}$	$27.8^{+3.9+4.1}_{-3.5-3.8}$	$0.10^{+0.01+0.04}_{-0.01-0.04}$	$32.2^{+4.8+4.2}_{-4.0-3.9}$	46
41	300-350	300-500	3-4	1	746^{+25+55}_{-25-55}	627^{+15+48}_{-15-47}	1235^{+8+130}_{-8-120}	59^{+4+24}_{-4-22}	$2667^{+41+150}_{-41-150}$	2677
42	300-350	500-1000	3-4	1	296^{+15+25}_{-15-25}	262^{+9+27}_{-9-27}	385^{+4+39}_{-4-39}	38^{+4+15}_{-4-14}	981^{+24+56}_{-24-56}	1048
43	300-350	1000+	3-4	1	$20.8^{+4.1+2.1}_{-4.0-2.1}$	$19.0^{+2.6+1.8}_{-2.5-1.8}$	$27.6^{+1.3+3.2}_{-1.2-3.0}$	$11.4^{+0.8+4.7}_{-0.8-4.4}$	$78.8^{+6.9+6.3}_{-6.6-6.0}$	92
44	350-500	350-500	3-4	1	321^{+17+25}_{-17-25}	263^{+10+22}_{-10-21}	738^{+6+74}_{-6-74}	$22.3^{+1.4+9.1}_{-1.4-8.5}$	1343^{+28+82}_{-28-81}	1332
45	350-500	500-1000	3-4	1	329^{+14+26}_{-14-26}	324^{+11+26}_{-11-26}	737^{+6+74}_{-6-74}	$17.6^{+3.4+7.2}_{-3.4-6.7}$	1407^{+26+83}_{-26-83}	1515
46	350-500	1000+	3-4	1	$20.4^{+4.0+2.0}_{-3.8-2.0}$	$19.9^{+2.9+1.8}_{-2.9-1.7}$	$47.5^{+1.7+5.5}_{-1.6-5.1}$	$5.7^{+0.5+2.3}_{-0.5-2.2}$	$93.4^{+7.1+6.5}_{-6.9-6.2}$	113
47	500-750	500-1000	3-4	1	$69.7^{+7.4+6.6}_{-7.3-6.6}$	$56.0^{+4.1+5.0}_{-4.1-4.9}$	322^{+4+35}_{-4-35}	$1.34^{+0.10+0.55}_{-0.10-0.51}$	449^{+12+36}_{-12-36}	472
48	500-750	1000+	3-4	1	$15.3^{+3.4+1.9}_{-3.3-1.9}$	$7.0^{+1.4+0.7}_{-1.4-0.7}$	$34.4^{+1.5+3.8}_{-1.4-3.8}$	$0.38^{+0.14+0.16}_{-0.14-0.15}$	$57.0^{+5.1+4.4}_{-4.9-4.3}$	57
49	750+	750-1500	3-4	1	$3.3^{+1.5+0.5}_{-1.3-0.5}$	$4.8^{+1.3+0.8}_{-1.2-0.8}$	$48.5^{+1.7+7.9}_{-1.7-7.3}$	$0.13^{+0.01+0.05}_{-0.01-0.05}$	$56.8^{+3.3+7.9}_{-3.0-7.4}$	61
50	750+	1500+	3-4	1	$1.0^{+1.2+0.3}_{-0.7-0.3}$	$0.77^{+0.75+0.16}_{-0.59-0.16}$	$4.40^{+0.62+0.75}_{-0.55-0.71}$	$0.03^{+0.01+0.01}_{-0.01-0.01}$	$6.2^{+2.0+0.8}_{-1.4-0.8}$	8
51	300-350	300-500	3-4	2	137^{+11+11}_{-11-11}	133^{+7+11}_{-7-11}	145^{+1+26}_{-1-26}	$9.0^{+1.1+3.9}_{-1.1-3.4}$	424^{+18+31}_{-17-31}	464
52	300-350	500-1000	3-4	2	$92.3^{+9.1+9.5}_{-9.0-9.5}$	$85.6^{+5.7+7.5}_{-5.7-7.4}$	$53.0^{+0.6+9.6}_{-0.6-9.6}$	$3.8^{+1.2+1.6}_{-1.2-1.4}$	235^{+15+16}_{-15-15}	227
53	300-350	1000+	3-4	2	$3.4^{+2.2+0.8}_{-1.7-0.8}$	$2.41^{+0.91+0.50}_{-0.78-0.50}$	$3.95^{+0.18+0.75}_{-0.17-0.73}$	$2.23^{+0.18+0.96}_{-0.18-0.86}$	$12.0^{+3.1+1.6}_{-2.5-1.5}$	17
54	350-500	350-500	3-4	2	$39.6^{+6.1+3.8}_{-5.9-3.8}$	$39.8^{+3.9+3.8}_{-3.8-3.8}$	84^{+1+15}_{-1-15}	$2.7^{+0.6+1.1}_{-0.6-1.0}$	166^{+10+16}_{-10-16}	208
55	350-500	500-1000	3-4	2	$83.9^{+8.2+7.8}_{-8.1-7.8}$	$69.4^{+4.9+5.9}_{-4.9-5.8}$	97^{+1+18}_{-1-17}	$3.1^{+0.2+1.3}_{-0.2-1.2}$	254^{+13+20}_{-13-20}	286
56	350-500	1000+	3-4	2	$6.2^{+4.0+1.0}_{-3.6-1.0}$	$3.8^{+1.1+0.6}_{-1.0-0.6}$	$6.8^{+0.2+1.3}_{-0.2-1.3}$	$0.95^{+0.16+0.41}_{-0.16-0.36}$	$17.7^{+5.2+1.8}_{-4.6-1.8}$	25
57	500-750	500-1000	3-4	2	$11.8^{+3.3+2.0}_{-3.1-2.0}$	$10.5^{+1.8+1.6}_{-1.7-1.6}$	$39.7^{+0.5+7.4}_{-0.5-7.3}$	$0.22^{+0.04+0.09}_{-0.04-0.08}$	$62.1^{+5.1+7.8}_{-4.8-7.7}$	64
58	500-750	1000+	3-4	2	$2.6^{+2.3+0.6}_{-1.6-0.6}$	$2.9^{+1.5+0.6}_{-1.5-0.6}$	$4.90^{+0.21+0.92}_{-0.21-0.91}$	$0.10^{+0.03+0.04}_{-0.03-0.04}$	$10.5^{+3.8+1.2}_{-3.1-1.2}$	13
59	750+	750-1500	3-4	2	$0.0^{+1.1+0.0}_{-0.0-0.0}$	$0.32^{+0.48+0.09}_{-0.13-0.09}$	$6.3^{+0.2+1.4}_{-0.2-1.3}$	$0.03^{+0.02+0.01}_{-0.02-0.01}$	$6.6^{+1.6+1.4}_{-0.3-1.3}$	4
60	750+	1500+	3-4	2	$0.0^{+1.1+0.0}_{-0.0-0.0}$	$0.03^{+0.46+0.01}_{-0.02-0.01}$	$0.65^{+0.09+0.15}_{-0.08-0.14}$	$0.01^{+0.01+0.01}_{-0.01-0.00}$	$0.7^{+1.6+0.1}_{-0.1-0.1}$	1
61	300-350	300-500	3-4	3+	$6.4^{+2.8+0.7}_{-2.3-0.7}$	$10.3^{+1.9+2.7}_{-1.9-2.7}$	$5.0^{+0.0+2.8}_{-0.0-2.8}$	$0.35^{+0.18+0.42}_{-0.18-0.16}$	$22.0^{+4.7+3.9}_{-4.2-3.9}$	27
62	300-350	500-1000	3-4	3+	$4.9^{+2.7+0.6}_{-2.2-0.6}$	$6.2^{+1.4+1.7}_{-1.3-1.7}$	$2.5^{+0.0+1.4}_{-0.0-1.4}$	$0.75^{+0.52+0.90}_{-0.52-0.24}$	$14.4^{+4.2+2.4}_{-3.6-2.2}$	20
63	300-350	1000+	3-4	3+	$0.0^{+1.1+0.0}_{-0.0-0.0}$	$0.94^{+0.87+0.44}_{-0.74-0.44}$	$0.21^{+0.01+0.12}_{-0.01-0.12}$	$1.6^{+0.2+1.9}_{-0.2-1.4}$	$2.7^{+2.0+2.0}_{-0.8-1.5}$	4
64	350-500	350-500	3-4	3+	$0.6^{+1.2+0.1}_{-0.6-0.0}$	$4.2^{+1.5+1.3}_{-1.4-1.3}$	$2.5^{+0.0+1.4}_{-0.0-1.4}$	$0.09^{+0.04+0.11}_{-0.04-0.05}$	$7.4^{+2.6+1.9}_{-1.9-1.9}$	8
65	350-500	500-1000	3-4	3+	$10.2^{+6.3+2.1}_{-5.7-2.1}$	$7.0^{+1.5+1.9}_{-1.5-1.9}$	$4.3^{+0.0+2.4}_{-0.0-2.4}$	$0.78^{+0.18+0.94}_{-0.18-0.60}$	$22.3^{+7.9+3.8}_{-7.2-3.7}$	26
66	350-500	1000+	3-4	3+	$0.0^{+1.1+0.0}_{-0.0-0.0}$	$0.21^{+0.49+0.13}_{-0.16-0.13}$	$0.36^{+0.01+0.20}_{-0.01-0.20}$	$0.54^{+0.15+0.65}_{-0.15-0.39}$	$1.1^{+1.6+0.7}_{-0.2-0.5}$	5
67	500-750	500-1000	3-4	3+	$1.4^{+2.9+0.4}_{-1.4-0.0}$	$1.13^{+0.74+0.45}_{-0.58-0.45}$	$1.50^{+0.02+0.83}_{-0.02-0.83}$	$0.10^{+0.10+0.13}_{-0.10-0.00}$	$4.1^{+3.6+1.0}_{-2.0-0.9}$	0
68	500-750	1000+	3-4	3+	$0.00^{+0.95+0.00}_{-0.00-0.00}$	$0.12^{+0.46+0.09}_{-0.06-0.09}$	$0.26^{+0.01+0.15}_{-0.01-0.15}$	$0.02^{+0.03+0.02}_{-0.02-0.00}$	$0.4^{+1.4+0.2}_{-0.1-0.2}$	2
69	750+	750-1500	3-4	3+	$0.00^{+0.97+0.00}_{-0.00-0.00}$	$0.00^{+0.46+0.00}_{-0.00-0.00}$	$0.29^{+0.01+0.16}_{-0.01-0.16}$	$0.01^{+0.02+0.01}_{-0.01-0.00}$	$0.3^{+1.4+0.2}_{-0.0-0.2}$	1
70	750+	1500+	3-4	3+	$0.0^{+1.4+0.0}_{-0.0-0.0}$	$0.00^{+0.46+0.00}_{-0.00-0.00}$	$0.04^{+0.01+0.02}_{-0.00-0.02}$	$0.01^{+0.03+0.02}_{-0.01-0.00}$	$0.0^{+1.8+0.0}_{-0.0-0.0}$	0

Table B.3: Observed number of events and pre-fit background predictions in the $5 \leq \mathrm{N_{jet}} \leq 6$ search bins.

Bin	$\mathrm{H_T^{miss}}$ [GeV]	$\mathrm{H_T}$ [GeV]	$\mathrm{N_{jet}}$	$\mathrm{N_{b\text{-}jet}}$	Lost-e/μ	$\tau \to$ had	$Z \to \nu\bar{\nu}$	QCD	Total Pred.	Obs.
71	300-350	300-500	5-6	0	217^{+11+22}_{-11-22}	166^{+6+27}_{-6-27}	489^{+12+42}_{-12-39}	49^{+5+21}_{-5-19}	922^{+21+58}_{-21-56}	1015
72	300-350	500-1000	5-6	0	397^{+13+37}_{-13-37}	403^{+9+36}_{-9-36}	772^{+16+61}_{-15-57}	113^{+4+47}_{-4-43}	1686^{+27+93}_{-27-88}	1673
73	300-350	1000+	5-6	0	$49.6^{+4.5+5.4}_{-4.5-5.4}$	$55.1^{+3.8+8.3}_{-3.8-8.3}$	$100.0^{+6.4+8.2}_{-6.0-7.1}$	49^{+1+21}_{-1-19}	254^{+11+24}_{-10-22}	226
74	350-500	350-500	5-6	0	71^{+7+11}_{-6-11}	47^{+3+16}_{-3-16}	242^{+9+20}_{-9-19}	$12.7^{+2.3+5.3}_{-2.3-4.8}$	372^{+13+29}_{-13-28}	464
75	350-500	500-1000	5-6	0	384^{+12+33}_{-12-33}	412^{+11+32}_{-11-32}	1110^{+19+84}_{-19-78}	65^{+2+27}_{-2-25}	1971^{+30+99}_{-29-93}	2018
76	350-500	1000+	5-6	0	$76.9^{+6.4+8.9}_{-6.4-8.9}$	$72.4^{+4.8+9.3}_{-4.8-9.3}$	170^{+8+14}_{-8-12}	28^{+1+12}_{-1-11}	347^{+14+22}_{-14-21}	320
77	500-750	500-1000	5-6	0	$66.7^{+5.1+7.3}_{-5.0-7.3}$	$70.1^{+4.3+6.1}_{-4.2-6.0}$	302^{+10+23}_{-10-22}	$3.2^{+0.1+1.3}_{-0.1-1.2}$	442^{+14+25}_{-14-24}	460
78	500-750	1000+	5-6	0	$23.9^{+2.9+4.5}_{-2.9-4.5}$	$31.2^{+3.1+4.0}_{-3.1-4.0}$	$123.5^{+7.3+9.4}_{-6.9-8.9}$	$2.5^{+0.1+1.1}_{-0.1-1.0}$	181^{+10+11}_{-9-11}	170
79	750+	750-1500	5-6	0	$4.0^{+1.2+0.7}_{-1.1-0.7}$	$4.90^{+0.89+0.52}_{-0.76-0.52}$	$52.2^{+4.6+7.5}_{-4.2-6.8}$	$0.23^{+0.04+0.10}_{-0.04-0.09}$	$61.3^{+5.0+7.5}_{-4.6-6.9}$	74
80	750+	1500+	5-6	0	$0.90^{+0.61+0.19}_{-0.45-0.19}$	$1.46^{+0.67+0.16}_{-0.49-0.16}$	$16.5^{+2.9+2.7}_{-2.5-2.5}$	$0.25^{+0.06+0.11}_{-0.06-0.10}$	$19.1^{+3.2+2.7}_{-2.7-2.5}$	19
81	300-350	300-500	5-6	1	130^{+8+11}_{-8-11}	131^{+6+17}_{-6-17}	133^{+3+19}_{-3-19}	$12.8^{+2.8+5.2}_{-2.8-4.9}$	407^{+15+29}_{-15-28}	450
82	300-350	500-1000	5-6	1	290^{+11+25}_{-11-25}	302^{+8+25}_{-8-25}	218^{+4+31}_{-4-30}	41^{+4+17}_{-4-16}	851^{+20+50}_{-20-49}	781
83	300-350	1000+	5-6	1	$25.8^{+3.4+2.5}_{-3.4-2.5}$	$31.6^{+2.9+5.9}_{-2.9-5.9}$	$29.0^{+1.8+4.1}_{-1.7-4.0}$	$18.4^{+0.8+7.5}_{-0.8-7.1}$	105^{+7+11}_{-6-10}	100
84	350-500	350-500	5-6	1	$45.4^{+5.5+5.4}_{-5.4-5.4}$	32^{+3+11}_{-3-11}	$65.1^{+2.4+9.3}_{-2.3-9.1}$	$3.7^{+0.5+1.5}_{-0.5-1.4}$	146^{+9+16}_{-8-16}	160
85	350-500	500-1000	5-6	1	228^{+10+20}_{-10-20}	269^{+8+21}_{-8-21}	310^{+5+43}_{-5-42}	28^{+3+11}_{-3-11}	834^{+19+53}_{-19-52}	801
86	350-500	1000+	5-6	1	$40.5^{+5.5+4.2}_{-5.4-4.2}$	$36.0^{+3.3+4.3}_{-3.3-4.2}$	$49.4^{+2.3+7.0}_{-2.2-6.7}$	$11.9^{+0.7+4.8}_{-0.7-4.5}$	138^{+9+10}_{-9-10}	138
87	500-750	500-1000	5-6	1	$23.4^{+3.5+2.6}_{-3.4-2.6}$	$32.1^{+2.8+3.3}_{-2.8-3.3}$	84^{+3+12}_{-3-12}	$1.45^{+0.11+0.59}_{-0.11-0.55}$	141^{+7+13}_{-7-12}	135
88	500-750	1000+	5-6	1	$8.5^{+1.8+1.1}_{-1.7-1.1}$	$13.0^{+1.8+1.5}_{-1.7-1.5}$	$35.3^{+2.1+4.9}_{-2.0-4.8}$	$1.33^{+0.17+0.54}_{-0.17-0.51}$	$58.0^{+4.1+5.3}_{-3.9-5.2}$	49
89	750+	750-1500	5-6	1	$3.7^{+1.4+0.7}_{-1.2-0.7}$	$2.9^{+1.0+0.4}_{-0.9-0.4}$	$14.9^{+1.3+2.8}_{-1.2-2.6}$	$0.07^{+0.01+0.03}_{-0.01-0.03}$	$21.6^{+2.8+2.9}_{-2.5-2.7}$	16
90	750+	1500+	5-6	1	$1.06^{+0.74+0.26}_{-0.56-0.26}$	$1.16^{+0.73+0.18}_{-0.57-0.18}$	$4.79^{+0.85+0.96}_{-0.73-0.92}$	$0.16^{+0.07+0.07}_{-0.07-0.06}$	$7.2^{+1.7+1.0}_{-1.3-1.0}$	6
91	300-350	300-500	5-6	2	$60.1^{+7.1+6.0}_{-7.0-6.0}$	$50.2^{+3.3+4.9}_{-3.3-4.9}$	$23.8^{+0.6+7.1}_{-0.6-7.1}$	$2.9^{+0.9+1.1}_{-0.9-1.1}$	137^{+10+11}_{-10-11}	143
92	300-350	500-1000	5-6	2	137^{+9+13}_{-9-13}	160^{+6+14}_{-6-14}	39^{+1+12}_{-1-11}	$11.8^{+1.8+4.6}_{-1.8-4.5}$	347^{+15+22}_{-15-22}	332
93	300-350	1000+	5-6	2	$16.9^{+3.8+2.0}_{-3.7-2.0}$	$15.9^{+2.1+2.1}_{-2.1-2.1}$	$5.1^{+0.3+1.5}_{-0.3-1.5}$	$5.6^{+0.4+2.2}_{-0.4-2.2}$	$43.5^{+5.9+3.9}_{-5.8-3.9}$	36
94	350-500	350-500	5-6	2	$13.3^{+3.1+1.9}_{-2.9-1.9}$	$7.0^{+1.1+2.3}_{-1.0-2.3}$	$11.7^{+0.4+3.5}_{-0.4-3.5}$	$1.02^{+0.54+0.40}_{-0.54-0.39}$	$32.9^{+4.3+4.6}_{-4.0-4.6}$	28
95	350-500	500-1000	5-6	2	$107.5^{+7.6+9.6}_{-7.6-9.6}$	$121.2^{+5.8+9.9}_{-5.8-9.8}$	55^{+1+16}_{-1-16}	$5.9^{+1.0+2.3}_{-1.0-2.2}$	290^{+14+22}_{-13-21}	288
96	350-500	1000+	5-6	2	$14.2^{+2.8+1.8}_{-2.7-1.8}$	$15.7^{+2.2+2.0}_{-2.1-2.0}$	$8.7^{+0.4+2.6}_{-0.4-2.6}$	$3.2^{+0.1+1.2}_{-0.1-1.2}$	$41.8^{+5.0+4.0}_{-4.8-3.9}$	44
97	500-750	500-1000	5-6	2	$8.4^{+2.3+1.1}_{-2.2-1.1}$	$8.3^{+1.3+1.0}_{-1.2-1.0}$	$15.0^{+0.5+4.4}_{-0.5-4.4}$	$0.34^{+0.05+0.13}_{-0.05-0.13}$	$32.1^{+3.7+4.7}_{-3.4-4.7}$	35
98	500-750	1000+	5-6	2	$2.1^{+1.3+0.3}_{-1.0-0.3}$	$4.0^{+1.1+0.6}_{-1.0-0.6}$	$6.2^{+0.4+1.9}_{-0.3-1.8}$	$0.16^{+0.05+0.06}_{-0.05-0.06}$	$12.5^{+2.4+2.0}_{-2.0-2.0}$	18
99	750+	750-1500	5-6	2	$0.74^{+0.87+0.22}_{-0.53-0.22}$	$0.68^{+0.64+0.16}_{-0.45-0.16}$	$2.64^{+0.23+0.85}_{-0.21-0.83}$	$0.05^{+0.05+0.02}_{-0.05-0.00}$	$4.1^{+1.5+0.9}_{-1.0-0.9}$	8
100	750+	1500+	5-6	2	$0.77^{+0.65+0.24}_{-0.45-0.24}$	$1.07^{+0.72+0.33}_{-0.56-0.33}$	$0.84^{+0.15+0.28}_{-0.13-0.27}$	$0.03^{+0.03+0.01}_{-0.03-0.00}$	$2.7^{+1.4+0.5}_{-1.0-0.5}$	3
101	300-350	300-500	5-6	3+	$2.8^{+1.5+0.3}_{-1.2-0.3}$	$5.1^{+1.0+0.8}_{-0.9-0.8}$	$2.0^{+0.0+1.1}_{-0.0-1.1}$	$0.50^{+0.37+0.57}_{-0.37-0.13}$	$10.4^{+2.5+1.5}_{-2.1-1.4}$	18
102	300-350	500-1000	5-6	3+	$17.0^{+3.2+1.6}_{-3.1-1.6}$	$23.5^{+2.4+3.2}_{-2.3-3.2}$	$4.2^{+0.1+2.3}_{-0.1-2.3}$	$3.9^{+2.3+4.5}_{-2.3-1.6}$	$48.7^{+6.0+6.2}_{-5.9-4.5}$	44
103	300-350	1000+	5-6	3+	$4.4^{+2.1+0.6}_{-1.8-0.6}$	$2.50^{+0.86+0.47}_{-0.73-0.47}$	$0.65^{+0.04+0.35}_{-0.04-0.35}$	$3.3^{+0.4+3.7}_{-0.4-2.8}$	$10.8^{+3.0+3.8}_{-2.6-3.0}$	6
104	350-500	350-500	5-6	3+	$0.8^{+1.7+0.2}_{-0.8-0.0}$	$1.14^{+0.75+0.33}_{-0.59-0.33}$	$0.87^{+0.03+0.47}_{-0.03-0.47}$	$0.18^{+0.08+0.21}_{-0.08-0.10}$	$3.0^{+2.4+0.6}_{-1.4-0.6}$	4
105	350-500	500-1000	5-6	3+	$15.2^{+2.6+1.5}_{-2.6-1.5}$	$17.6^{+2.2+2.7}_{-2.1-2.7}$	$5.7^{+0.1+3.1}_{-0.1-3.1}$	$1.7^{+0.1+1.9}_{-0.1-1.6}$	$40.2^{+4.8+4.8}_{-4.7-4.6}$	34
106	350-500	1000+	5-6	3+	$1.9^{+1.1+0.3}_{-0.8-0.3}$	$3.8^{+1.1+0.7}_{-1.0-0.7}$	$1.14^{+0.05+0.62}_{-0.05-0.62}$	$2.4^{+0.3+2.7}_{-0.3-2.1}$	$9.2^{+2.2+2.8}_{-1.9-2.3}$	8
107	500-750	500-1000	5-6	3+	$1.8^{+1.1+0.3}_{-0.8-0.3}$	$1.71^{+0.77+0.67}_{-0.61-0.67}$	$1.48^{+0.05+0.81}_{-0.05-0.80}$	$0.20^{+0.04+0.23}_{-0.04-0.17}$	$5.2^{+1.8+1.1}_{-1.5-1.1}$	4
108	500-750	1000+	5-6	3+	$1.13^{+0.96+0.25}_{-0.66-0.25}$	$0.94^{+0.67+0.27}_{-0.49-0.27}$	$0.73^{+0.04+0.40}_{-0.04-0.40}$	$0.11^{+0.03+0.12}_{-0.03-0.08}$	$2.9^{+1.6+0.6}_{-1.1-0.6}$	2
109	750+	750-1500	5-6	3+	$0.00^{+0.72+0.00}_{-0.00-0.00}$	$0.07^{+0.46+0.04}_{-0.06-0.04}$	$0.31^{+0.03+0.17}_{-0.03-0.17}$	$0.02^{+0.04+0.03}_{-0.02-0.00}$	$0.4^{+1.2+0.2}_{-0.1-0.2}$	0
110	750+	1500+	5-6	3+	$0.00^{+0.63+0.00}_{-0.00-0.00}$	$0.03^{+0.46+0.01}_{-0.02-0.01}$	$0.11^{+0.02+0.06}_{-0.02-0.06}$	$0.00^{+0.02+0.01}_{-0.00-0.00}$	$0.1^{+1.1+0.1}_{-0.0-0.1}$	1

Table B.4: Observed number of events and pre-fit background predictions in the $7 \leq N_{\mathrm{jet}} \leq 8$ search bins.

Bin	H_T^{miss} [GeV]	H_T [GeV]	N_{jet}	$N_{b\text{-}jet}$	Lost-e/μ	$\tau \to$ had	$Z \to \nu\bar{\nu}$	QCD	Total Pred.	Obs.
111	300-350	500-1000	7-8	0	$48.0^{+3.9+5.4}_{-3.8-5.4}$	$60.8^{+3.4+6.0}_{-3.4-6.0}$	76^{+5+11}_{-5-10}	30^{+2+12}_{-2-11}	215^{+9+18}_{-9-17}	218
112	300-350	1000+	7-8	0	$21.2^{+2.9+2.3}_{-2.9-2.3}$	$20.3^{+2.2+2.8}_{-2.1-2.8}$	$23.9^{+3.3+2.8}_{-2.9-2.5}$	$20.5^{+0.5+8.5}_{-0.5-7.8}$	$85.9^{+6.1+9.6}_{-5.8-9.0}$	85
113	350-500	500-1000	7-8	0	$43.2^{+3.9+4.9}_{-3.9-4.9}$	$54.2^{+3.6+5.7}_{-3.5-5.7}$	89^{+6+11}_{-5-10}	$14.3^{+1.9+5.9}_{-1.9-5.4}$	201^{+10+14}_{-9-14}	215
114	350-500	1000+	7-8	0	$22.5^{+2.8+2.7}_{-2.7-2.7}$	$23.3^{+2.5+2.3}_{-2.4-2.3}$	$48.3^{+4.7+5.4}_{-4.3-4.8}$	$12.6^{+0.7+5.2}_{-0.7-4.8}$	$106.7^{+7.1+8.3}_{-6.7-7.7}$	75
115	500-750	500-1000	7-8	0	$6.9^{+1.8+1.4}_{-1.7-1.4}$	$4.96^{+0.95+0.77}_{-0.84-0.77}$	$26.5^{+3.6+3.3}_{-3.2-3.0}$	$0.88^{+0.10+0.36}_{-0.10-0.34}$	$39.2^{+4.5+3.7}_{-4.1-3.5}$	34
116	500-750	1000+	7-8	0	$5.4^{+1.1+0.9}_{-1.0-0.9}$	$9.9^{+1.6+1.7}_{-1.5-1.7}$	$27.2^{+3.7+3.1}_{-3.2-2.8}$	$1.56^{+0.12+0.64}_{-0.12-0.59}$	$44.1^{+4.5+3.7}_{-4.1-3.5}$	38
117	750+	750-1500	7-8	0	$1.26^{+0.70+0.50}_{-0.58-0.50}$	$1.44^{+0.74+0.24}_{-0.57-0.24}$	$3.6^{+1.4+0.7}_{-1.0-0.6}$	$0.07^{+0.02+0.03}_{-0.02-0.03}$	$6.4^{+2.0+0.9}_{-1.5-0.8}$	5
118	750+	1500+	7-8	0	$0.69^{+0.47+0.16}_{-0.35-0.16}$	$1.03^{+0.69+0.15}_{-0.51-0.15}$	$1.5^{+1.2+0.3}_{-0.7-0.3}$	$0.07^{+0.01+0.03}_{-0.01-0.03}$	$3.3^{+1.7+0.4}_{-1.1-0.4}$	5
119	300-350	500-1000	7-8	1	$64.7^{+5.1+6.4}_{-5.1-6.4}$	$77.0^{+3.9+7.5}_{-3.8-7.4}$	$31.7^{+2.1+8.6}_{-1.9-8.4}$	$11.2^{+0.5+4.7}_{-0.5-4.3}$	184^{+9+14}_{-9-14}	146
120	300-350	1000+	7-8	1	$16.3^{+2.4+1.7}_{-2.4-1.7}$	$19.9^{+2.2+2.1}_{-2.1-2.1}$	$10.3^{+1.4+2.7}_{-1.2-2.6}$	$8.3^{+0.2+3.5}_{-0.2-3.2}$	$54.8^{+4.8+5.2}_{-4.7-5.0}$	68
121	350-500	500-1000	7-8	1	$46.9^{+4.4+5.0}_{-4.4-5.0}$	$58.6^{+3.7+5.7}_{-3.7-5.7}$	$37.0^{+2.4+9.7}_{-2.2-9.5}$	$7.5^{+0.4+3.2}_{-0.4-2.9}$	150^{+8+13}_{-8-12}	113
122	350-500	1000+	7-8	1	$19.5^{+2.5+2.1}_{-2.4-2.1}$	$19.5^{+2.3+2.0}_{-2.3-2.0}$	$21.0^{+2.0+5.4}_{-1.9-5.3}$	$5.3^{+0.5+2.2}_{-0.5-2.0}$	$65.3^{+5.2+6.5}_{-5.1-6.4}$	67
123	500-750	500-1000	7-8	1	$7.6^{+2.0+1.4}_{-1.9-1.4}$	$5.5^{+1.1+0.8}_{-1.1-0.8}$	$11.5^{+1.6+3.0}_{-1.4-3.0}$	$0.36^{+0.04+0.15}_{-0.04-0.14}$	$24.9^{+3.5+3.4}_{-3.3-3.4}$	19
124	500-750	1000+	7-8	1	$9.3^{+2.1+1.3}_{-2.0-1.3}$	$7.5^{+1.5+0.8}_{-1.4-0.8}$	$11.4^{+1.5+3.0}_{-1.4-2.9}$	$0.98^{+0.12+0.41}_{-0.12-0.37}$	$29.2^{+3.9+3.3}_{-3.7-3.3}$	22
125	750+	750-1500	7-8	1	$0.14^{+0.30+0.05}_{-0.14-0.00}$	$0.44^{+0.51+0.10}_{-0.22-0.10}$	$1.48^{+0.56+0.44}_{-0.42-0.43}$	$0.07^{+0.03+0.03}_{-0.03-0.03}$	$2.14^{+0.99+0.46}_{-0.56-0.45}$	4
126	750+	1500+	7-8	1	$0.00^{+0.47+0.00}_{-0.00-0.00}$	$0.14^{+0.47+0.02}_{-0.08-0.02}$	$0.70^{+0.55+0.22}_{-0.34-0.21}$	$0.03^{+0.01+0.01}_{-0.01-0.01}$	$0.9^{+1.1+0.2}_{-0.3-0.2}$	6
127	300-350	500-1000	7-8	2	$34.7^{+3.5+3.6}_{-3.5-3.6}$	$47.7^{+3.0+4.4}_{-3.0-4.4}$	$8.1^{+0.5+3.6}_{-0.5-3.5}$	$5.3^{+0.5+2.1}_{-0.5-2.1}$	$95.8^{+6.6+7.1}_{-6.5-7.0}$	95
128	300-350	1000+	7-8	2	$9.0^{+2.1+1.2}_{-2.1-1.2}$	$10.8^{+1.4+1.3}_{-1.4-1.3}$	$2.4^{+0.3+1.0}_{-0.3-1.0}$	$3.2^{+0.1+1.3}_{-0.1-1.3}$	$25.4^{+3.6+2.4}_{-3.4-2.4}$	26
129	350-500	500-1000	7-8	2	$26.2^{+3.0+2.9}_{-3.0-2.9}$	$31.0^{+2.5+3.3}_{-2.5-3.2}$	$9.6^{+0.6+4.1}_{-0.6-4.1}$	$2.5^{+0.2+1.0}_{-0.2-1.0}$	$69.3^{+5.6+6.1}_{-5.5-6.1}$	84
130	350-500	1000+	7-8	2	$13.3^{+2.5+1.5}_{-2.4-1.5}$	$13.3^{+1.8+1.3}_{-1.7-1.3}$	$4.7^{+0.5+2.0}_{-0.4-2.0}$	$1.95^{+0.13+0.78}_{-0.13-0.75}$	$33.3^{+4.3+3.0}_{-4.2-2.9}$	35
131	500-750	500-1000	7-8	2	$2.5^{+1.4+0.5}_{-1.2-0.5}$	$0.86^{+0.50+0.21}_{-0.18-0.21}$	$2.6^{+0.3+1.1}_{-0.3-1.1}$	$0.10^{+0.01+0.04}_{-0.01-0.04}$	$6.0^{+1.9+1.3}_{-1.4-1.3}$	7
132	500-750	1000+	7-8	2	$6.0^{+2.3+1.0}_{-2.2-1.0}$	$3.3^{+1.0+0.6}_{-0.9-0.6}$	$2.9^{+0.4+1.2}_{-0.3-1.2}$	$0.22^{+0.06+0.09}_{-0.06-0.08}$	$12.4^{+3.4+1.7}_{-3.1-1.7}$	12
133	750+	750-1500	7-8	2	$0.16^{+0.34+0.08}_{-0.16-0.00}$	$0.44^{+0.56+0.15}_{-0.32-0.15}$	$0.39^{+0.15+0.18}_{-0.11-0.18}$	$0.03^{+0.01+0.01}_{-0.01-0.01}$	$1.03^{+0.91+0.25}_{-0.49-0.23}$	2
134	750+	1500+	7-8	2	$0.53^{+0.62+0.20}_{-0.38-0.20}$	$0.61^{+0.57+0.22}_{-0.33-0.22}$	$0.13^{+0.10+0.06}_{-0.06-0.06}$	$0.06^{+0.02+0.02}_{-0.02-0.02}$	$1.3^{+1.2+0.3}_{-0.7-0.3}$	2
135	300-350	500-1000	7-8	3+	$8.1^{+1.8+1.0}_{-1.7-1.0}$	$9.4^{+1.4+1.3}_{-1.3-1.3}$	$4.1^{+0.3+2.3}_{-0.2-2.3}$	$2.9^{+0.6+3.3}_{-0.6-2.3}$	$24.6^{+3.2+4.3}_{-3.1-3.7}$	12
136	300-350	1000+	7-8	3+	$4.7^{+2.0+0.7}_{-1.8-0.7}$	$5.4^{+1.2+0.8}_{-1.1-0.8}$	$1.51^{+0.21+0.85}_{-0.18-0.84}$	$2.4^{+0.3+2.7}_{-0.3-2.1}$	$13.9^{+3.2+3.0}_{-2.9-2.5}$	8
137	350-500	500-1000	7-8	3+	$5.9^{+1.9+0.8}_{-1.7-0.8}$	$7.4^{+1.4+1.2}_{-1.3-1.2}$	$4.7^{+0.3+2.7}_{-0.3-2.7}$	$1.2^{+0.1+1.3}_{-0.1-1.1}$	$19.2^{+3.2+3.3}_{-3.1-3.2}$	16
138	350-500	1000+	7-8	3+	$2.6^{+1.1+0.3}_{-1.0-0.3}$	$4.8^{+1.3+0.7}_{-1.2-0.7}$	$3.1^{+0.3+1.8}_{-0.3-1.8}$	$2.1^{+0.3+2.3}_{-0.3-1.8}$	$12.6^{+2.5+3.0}_{-2.2-2.6}$	8
139	500-750	500-1000	7-8	3+	$0.23^{+0.48+0.08}_{-0.23-0.00}$	$0.30^{+0.48+0.10}_{-0.13-0.10}$	$1.70^{+0.23+0.96}_{-0.20-0.96}$	$0.11^{+0.04+0.12}_{-0.04-0.08}$	$2.34^{+0.99+0.98}_{-0.41-0.96}$	3
140	500-750	1000+	7-8	3+	$3.4^{+2.4+0.7}_{-2.1-0.7}$	$1.59^{+0.83+0.49}_{-0.69-0.49}$	$1.51^{+0.20+0.85}_{-0.18-0.85}$	$0.22^{+0.08+0.24}_{-0.08-0.14}$	$6.7^{+3.2+1.2}_{-2.7-1.2}$	4
141	750+	750-1500	7-8	3+	$0.00^{+0.56+0.00}_{-0.00-0.00}$	$0.05^{+0.46+0.02}_{-0.03-0.02}$	$0.19^{+0.07+0.11}_{-0.05-0.11}$	$0.03^{+0.04+0.03}_{-0.03-0.00}$	$0.3^{+1.0+0.1}_{-0.1-0.1}$	0
142	750+	1500+	7-8	3+	$0.00^{+0.72+0.00}_{-0.00-0.00}$	$0.04^{+0.46+0.02}_{-0.02-0.02}$	$0.12^{+0.10+0.07}_{-0.06-0.07}$	$0.01^{+0.03+0.01}_{-0.01-0.00}$	$0.2^{+1.2+0.1}_{-0.1-0.1}$	0

Table B.5: Observed number of events and pre-fit background predictions in the $N_{jet} \geq 9$ search bins.

Bin	H_T^{miss} [GeV]	H_T [GeV]	N_{jet}	$N_{b\text{-}jet}$	Lost-e/μ	$\tau \to$ had	$Z \to \nu\bar{\nu}$	QCD	Total Pred.	Obs.
143	300-350	500-1000	9+	0	$6.2^{+2.7+1.7}_{-2.6-1.7}$	$3.46^{+0.89+0.59}_{-0.77-0.59}$	$2.6^{+1.2+0.7}_{-0.9-0.7}$	$2.9^{+0.3+1.3}_{-0.3-1.1}$	$15.1^{+3.8+2.3}_{-3.5-2.2}$	7
144	300-350	1000+	9+	0	$3.5^{+1.2+0.6}_{-1.1-0.6}$	$4.6^{+1.0+0.6}_{-0.9-0.6}$	$3.0^{+1.4+0.6}_{-1.0-0.6}$	$4.2^{+0.3+1.9}_{-0.3-1.6}$	$15.2^{+2.7+2.1}_{-2.3-1.9}$	12
145	350-500	500-1000	9+	0	$2.39^{+0.99+0.69}_{-0.89-0.69}$	$2.39^{+0.86+0.48}_{-0.73-0.48}$	$2.9^{+1.3+0.7}_{-0.9-0.6}$	$0.97^{+0.08+0.43}_{-0.08-0.37}$	$8.6^{+2.3+1.2}_{-1.9-1.1}$	6
146	350-500	1000+	9+	0	$3.7^{+1.1+0.6}_{-1.1-0.6}$	$4.6^{+1.0+0.6}_{-0.9-0.6}$	$5.5^{+1.9+1.0}_{-1.5-0.9}$	$3.1^{+0.2+1.4}_{-0.2-1.2}$	$17.0^{+2.9+1.9}_{-2.5-1.7}$	13
147	500-750	500-1000	9+	0	$0.15^{+0.32+0.10}_{-0.15-0.00}$	$0.35^{+0.55+0.12}_{-0.30-0.12}$	$1.0^{+1.3+0.4}_{-0.7-0.4}$	$0.10^{+0.05+0.04}_{-0.05-0.04}$	$1.6^{+1.6+0.5}_{-0.8-0.4}$	2
148	500-750	1000+	9+	0	$0.98^{+0.50+0.26}_{-0.41-0.26}$	$1.98^{+0.74+0.30}_{-0.58-0.30}$	$3.5^{+1.6+0.7}_{-1.1-0.7}$	$0.47^{+0.05+0.21}_{-0.05-0.18}$	$6.9^{+2.0+0.8}_{-1.5-0.8}$	11
149	750+	750-1500	9+	0	$0.00^{+0.44+0.00}_{-0.00-0.00}$	$0.00^{+0.46+0.00}_{-0.00-0.00}$	$0.00^{+0.64+0.00}_{-0.00-0.00}$	$0.01^{+0.02+0.00}_{-0.01-0.00}$	$0.0^{+1.1+0.0}_{-0.0-0.0}$	0
150	750+	1500+	9+	0	$0.23^{+0.27+0.16}_{-0.17-0.16}$	$0.28^{+0.50+0.08}_{-0.21-0.08}$	$0.00^{+0.82+0.00}_{-0.00-0.00}$	$0.05^{+0.03+0.02}_{-0.03-0.02}$	$0.6^{+1.1+0.2}_{-0.4-0.2}$	1
151	300-350	500-1000	9+	1	$6.5^{+1.8+1.1}_{-1.7-1.1}$	$4.57^{+0.93+0.77}_{-0.81-0.77}$	$1.83^{+0.84+0.68}_{-0.60-0.74}$	$1.02^{+0.06+0.42}_{-0.06-0.40}$	$13.9^{+2.8+1.5}_{-2.6-1.6}$	25
152	300-350	1000+	9+	1	$5.7^{+1.6+0.7}_{-1.5-0.7}$	$7.3^{+1.3+1.1}_{-1.2-1.1}$	$2.08^{+0.95+0.69}_{-0.68-0.77}$	$2.43^{+0.06+0.99}_{-0.06-0.94}$	$17.5^{+3.0+1.8}_{-2.8-1.8}$	20
153	350-500	500-1000	9+	1	$2.92^{+0.94+0.57}_{-0.84-0.57}$	$2.96^{+0.77+0.60}_{-0.61-0.60}$	$2.00^{+0.91+0.71}_{-0.65-0.78}$	$0.53^{+0.05+0.22}_{-0.05-0.21}$	$8.4^{+1.9+1.1}_{-1.6-1.2}$	8
154	350-500	1000+	9+	1	$5.4^{+1.4+0.7}_{-1.3-0.7}$	$7.7^{+1.4+1.1}_{-1.3-1.1}$	$3.9^{+1.3+1.3}_{-1.0-1.4}$	$1.48^{+0.05+0.60}_{-0.05-0.57}$	$18.4^{+3.1+1.9}_{-2.8-2.0}$	14
155	500-750	500-1000	9+	1	$0.14^{+0.30+0.08}_{-0.14-0.00}$	$0.24^{+0.49+0.21}_{-0.18-0.16}$	$0.71^{+0.94+0.35}_{-0.46-0.36}$	$0.03^{+0.03+0.01}_{-0.03-0.00}$	$1.1^{+1.2+0.4}_{-0.6-0.4}$	1
156	500-750	1000+	9+	1	$0.68^{+0.58+0.12}_{-0.41-0.12}$	$1.20^{+0.64+0.21}_{-0.44-0.21}$	$2.4^{+1.1+0.8}_{-0.8-0.9}$	$0.20^{+0.02+0.08}_{-0.02-0.07}$	$4.5^{+1.6+0.8}_{-1.2-0.9}$	4
157	750+	750-1500	9+	1	$0.00^{+0.73+0.00}_{-0.00-0.00}$	$0.04^{+0.46+0.02}_{-0.04-0.00}$	$0.00^{+0.45+0.00}_{-0.00-0.00}$	$0.01^{+0.01+0.00}_{-0.01-0.00}$	$0.1^{+1.3+0.0}_{-0.0-0.0}$	0
158	750+	1500+	9+	1	$0.13^{+0.27+0.06}_{-0.13-0.00}$	$0.03^{+0.46+0.01}_{-0.02-0.01}$	$0.00^{+0.57+0.00}_{-0.00-0.00}$	$0.02^{+0.01+0.01}_{-0.01-0.01}$	$0.18^{+0.93+0.06}_{-0.15-0.01}$	0
159	300-350	500-1000	9+	2	$4.1^{+1.3+0.7}_{-1.2-0.7}$	$4.68^{+0.92+0.85}_{-0.80-0.85}$	$0.64^{+0.29+0.34}_{-0.21-0.36}$	$0.40^{+0.06+0.24}_{-0.06-0.21}$	$9.8^{+2.2+1.2}_{-2.0-1.2}$	13
160	300-350	1000+	9+	2	$5.2^{+1.6+0.7}_{-1.5-0.7}$	$5.5^{+1.2+1.0}_{-1.1-1.0}$	$0.73^{+0.33+0.37}_{-0.24-0.39}$	$1.32^{+0.15+0.68}_{-0.15-0.58}$	$12.7^{+2.8+1.4}_{-2.6-1.4}$	10
161	350-500	500-1000	9+	2	$3.01^{+0.91+0.63}_{-0.82-0.63}$	$4.7^{+1.1+0.9}_{-1.0-0.9}$	$0.70^{+0.32+0.36}_{-0.23-0.39}$	$0.30^{+0.08+0.14}_{-0.08-0.12}$	$8.7^{+2.0+1.1}_{-1.8-1.1}$	4
162	350-500	1000+	9+	2	$4.4^{+1.1+0.6}_{-1.1-0.6}$	$6.3^{+1.4+0.8}_{-1.3-0.8}$	$1.35^{+0.47+0.67}_{-0.36-0.72}$	$0.63^{+0.03+0.32}_{-0.03-0.27}$	$12.7^{+2.6+1.3}_{-2.4-1.3}$	12
163	500-750	500-1000	9+	2	$0.00^{+0.39+0.00}_{-0.00-0.00}$	$0.35^{+0.49+0.17}_{-0.18-0.17}$	$0.25^{+0.33+0.15}_{-0.16-0.16}$	$0.01^{+0.01+0.01}_{-0.01-0.00}$	$0.61^{+0.95+0.23}_{-0.24-0.23}$	0
164	500-750	1000+	9+	2	$2.0^{+1.1+0.4}_{-0.9-0.4}$	$1.95^{+0.87+0.45}_{-0.73-0.45}$	$0.84^{+0.39+0.43}_{-0.28-0.46}$	$0.09^{+0.02+0.04}_{-0.02-0.04}$	$4.9^{+2.0+0.7}_{-1.7-0.7}$	7
165	750+	750-1500	9+	2	$0.00^{+0.60+0.00}_{-0.00-0.00}$	$0.01^{+0.46+0.01}_{-0.00-0.00}$	$0.00^{+0.16+0.00}_{-0.00-0.00}$	$0.00^{+0.01+0.00}_{-0.00-0.00}$	$0.0^{+1.1+0.0}_{-0.0-0.0}$	0
166	750+	1500+	9+	2	$0.00^{+0.38+0.00}_{-0.00-0.00}$	$0.00^{+0.46+0.00}_{-0.00-0.00}$	$0.00^{+0.20+0.00}_{-0.00-0.00}$	$0.01^{+0.02+0.00}_{-0.01-0.00}$	$0.01^{+0.87+0.00}_{-0.01-0.00}$	0
167	300-350	500-1000	9+	3+	$1.06^{+0.63+0.27}_{-0.50-0.27}$	$1.06^{+0.57+0.29}_{-0.34-0.29}$	$0.37^{+0.17+0.26}_{-0.12-0.28}$	$0.47^{+0.13+0.56}_{-0.13-0.34}$	$3.0^{+1.2+0.7}_{-0.9-0.6}$	1
168	300-350	1000+	9+	3+	$3.5^{+1.7+0.5}_{-1.5-0.5}$	$2.6^{+1.0+0.7}_{-0.9-0.7}$	$0.42^{+0.19+0.29}_{-0.14-0.31}$	$2.1^{+0.3+2.4}_{-0.3-1.8}$	$8.6^{+2.7+2.6}_{-2.4-2.0}$	4
169	350-500	500-1000	9+	3+	$1.03^{+0.60+0.30}_{-0.47-0.30}$	$1.58^{+0.71+0.43}_{-0.55-0.43}$	$0.40^{+0.18+0.28}_{-0.13-0.31}$	$0.10^{+0.03+0.11}_{-0.03-0.07}$	$3.1^{+1.3+0.6}_{-1.0-0.6}$	3
170	350-500	1000+	9+	3+	$0.81^{+0.56+0.14}_{-0.41-0.14}$	$0.96^{+0.54+0.16}_{-0.27-0.16}$	$0.77^{+0.27+0.53}_{-0.20-0.58}$	$1.3^{+0.2+1.5}_{-0.2-1.1}$	$3.8^{+1.1+1.6}_{-0.7-1.3}$	2
171	500-750	500-1000	9+	3+	$0.00^{+0.43+0.00}_{-0.00-0.00}$	$0.03^{+0.46+0.03}_{-0.02-0.03}$	$0.14^{+0.19+0.11}_{-0.09-0.11}$	$0.01^{+0.02+0.01}_{-0.01-0.00}$	$0.18^{+0.91+0.11}_{-0.09-0.11}$	0
172	500-750	1000+	9+	3+	$0.00^{+0.48+0.00}_{-0.00-0.00}$	$0.53^{+0.56+0.13}_{-0.31-0.13}$	$0.48^{+0.22+0.33}_{-0.16-0.37}$	$0.13^{+0.14+0.15}_{-0.13-0.00}$	$1.1^{+1.1+0.4}_{-0.4-0.4}$	3
173	750+	750-1500	9+	3+	$0.00^{+0.50+0.00}_{-0.00-0.00}$	$0.00^{+0.46+0.00}_{-0.00-0.00}$	$0.00^{+0.09+0.00}_{-0.00-0.00}$	$0.01^{+0.05+0.02}_{-0.01-0.00}$	$0.01^{+0.97+0.02}_{-0.01-0.00}$	0
174	750+	1500+	9+	3+	$0.00^{+0.42+0.00}_{-0.00-0.00}$	$0.00^{+0.46+0.00}_{-0.00-0.00}$	$0.00^{+0.11+0.00}_{-0.00-0.00}$	$0.02^{+0.05+0.02}_{-0.02-0.00}$	$0.02^{+0.89+0.02}_{-0.02-0.00}$	0

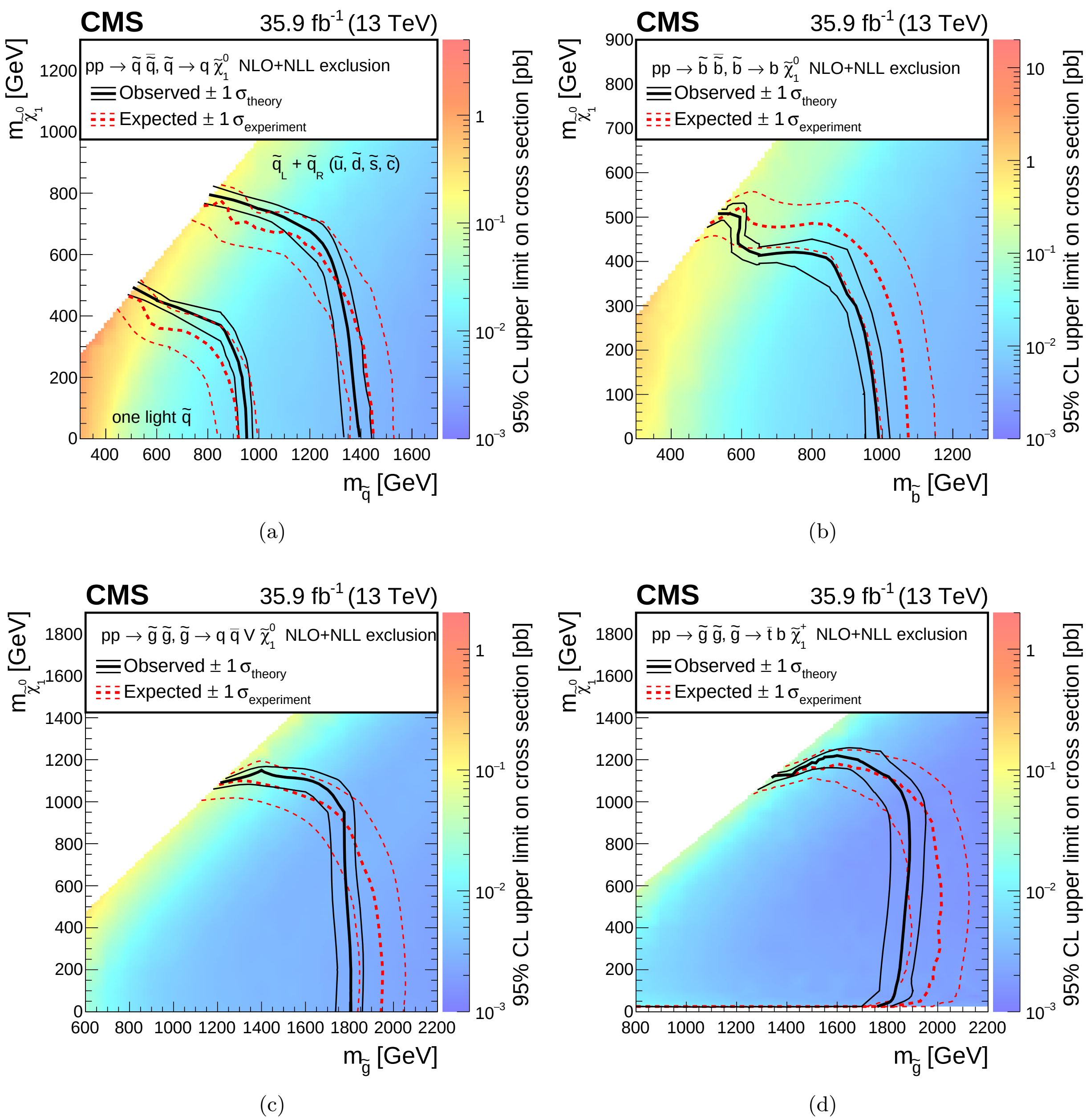

Figure B.2: The 95% CL upper limits on the T2qq (a), T2bb (b), T5qqqqVV (c), and T1tbtb (d) simplified SUSY models.

Appendix C

Supporting material for the $Z \to \nu\bar{\nu}$ estimation

Measurements of the $\mathrm{Z} \to \ell^+\ell^-$ control sample purity in bins of $\mathrm{N_{jet}}$ and $\mathrm{N_{b\text{-}jet}}$ are shown in Table C.1. These measurements are obtained from fits to data assuming a combinatorial background. These fits are shown in Figures C.1-C.3 with simulation overlaid for comparison purposes. Figure C.4 is showing the $\mathrm{Z} \to \mathrm{e^+e^-}$ and $\mathrm{Z} \to \mu^+\mu^-$ trigger efficiencies as a function of Z p_T.

Table C.1: Purity of the $\mathrm{Z} \to \mu^+\mu^-$ and $\mathrm{Z} \to \mathrm{e^+e^-}$ control samples, with absolute uncertainties. MC simulation indicate that the sample purity is constant across the two samples for $\mathrm{N_{b\text{-}jet}} >= 2$. We combine these bins for the Z purity estimate.

sample		0 $\mathrm{N_{b\text{-}jet}}$	1 $\mathrm{N_{b\text{-}jet}}$	≥ 2 $\mathrm{N_{b\text{-}jet}}$
$\mathrm{Z} \to \mu^+\mu^-$	$\mathrm{N_{jet}} = 2$	1.0 ± 0.006	0.981 ± 0.024	0.851 ± 0.154
	$3 \leq \mathrm{N_{jet}} \leq 4$	1.0 ± 0.007	0.96 ± 0.025	0.924 ± 0.079
	$\mathrm{N_{jet}} \geq 5$	0.99 ± 0.019	0.932 ± 0.051	0.851 ± 0.119
$\mathrm{Z} \to \mathrm{e^+e^-}$	$\mathrm{N_{jet}} = 2$	0.993 ± 0.008	0.996 ± 0.024	0.815 ± 0.302
	$3 \leq \mathrm{N_{jet}} \leq 4$	0.988 ± 0.009	0.97 ± 0.024	0.867 ± 0.095
	$\mathrm{N_{jet}} \geq 5$	0.976 ± 0.025	0.966 ± 0.048	0.678 ± 0.205

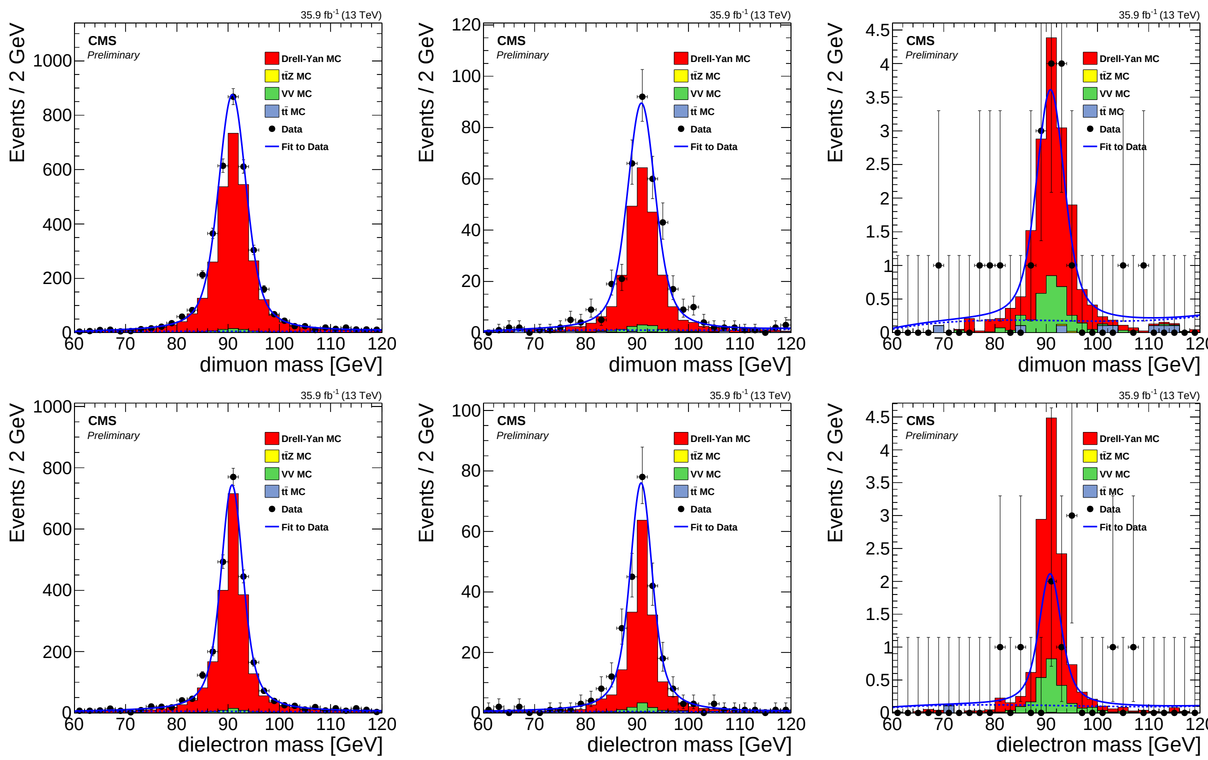

Figure C.1: Fits to the data dilepton invariant mass distribution with $N_{\text{jet}} = 2$ to obtain the $Z \to \ell^+\ell^-$ purity for muons (top), electrons (bottom), with 0 (left), 1 (middle), and ≥ 2 (right) b-tagged jets. Histograms show expected contributions from MC simulation.

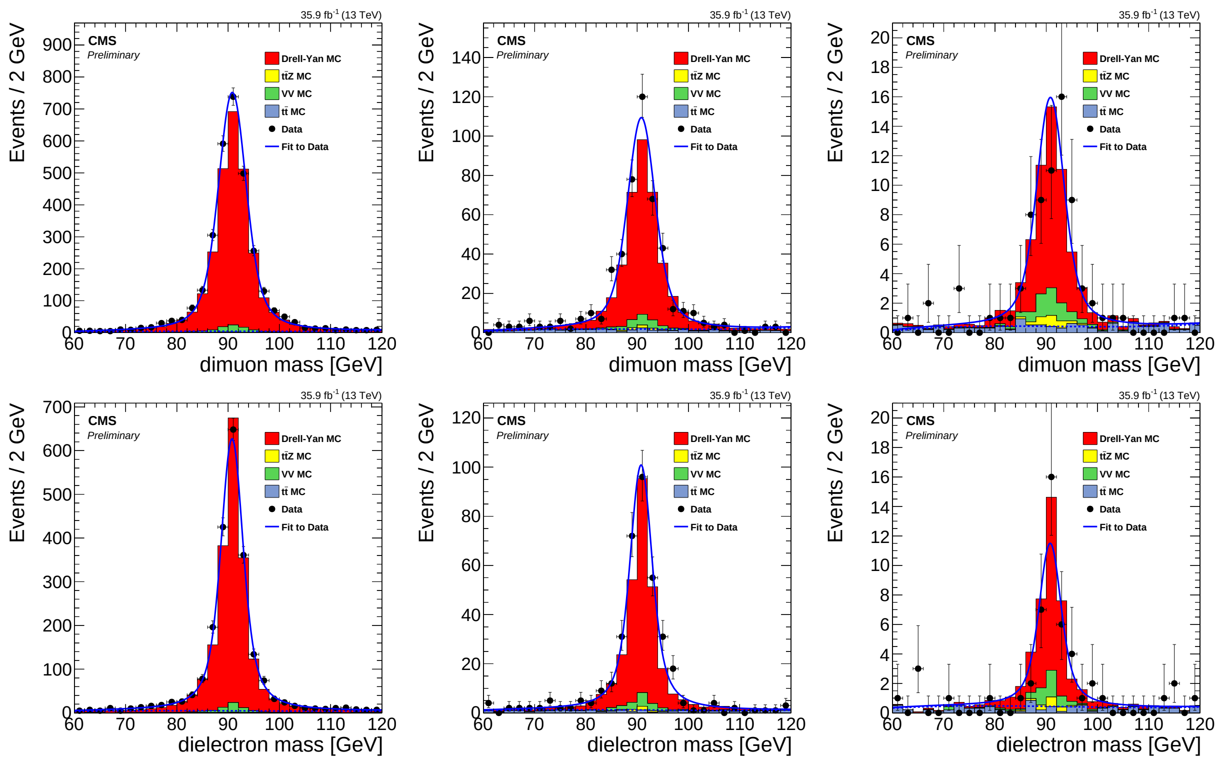

Figure C.2: Fits to the data dilepton invariant mass distribution with $3 \leq \mathrm{N_{jet}} \leq 4$ to obtain the $\mathrm{Z} \rightarrow \ell^+\ell^-$ purity for muons (top), electrons (bottom), with 0 (left), 1 (middle), and ≥ 2 (right) b-tagged jets. Histograms show expected contributions from MC simulation.

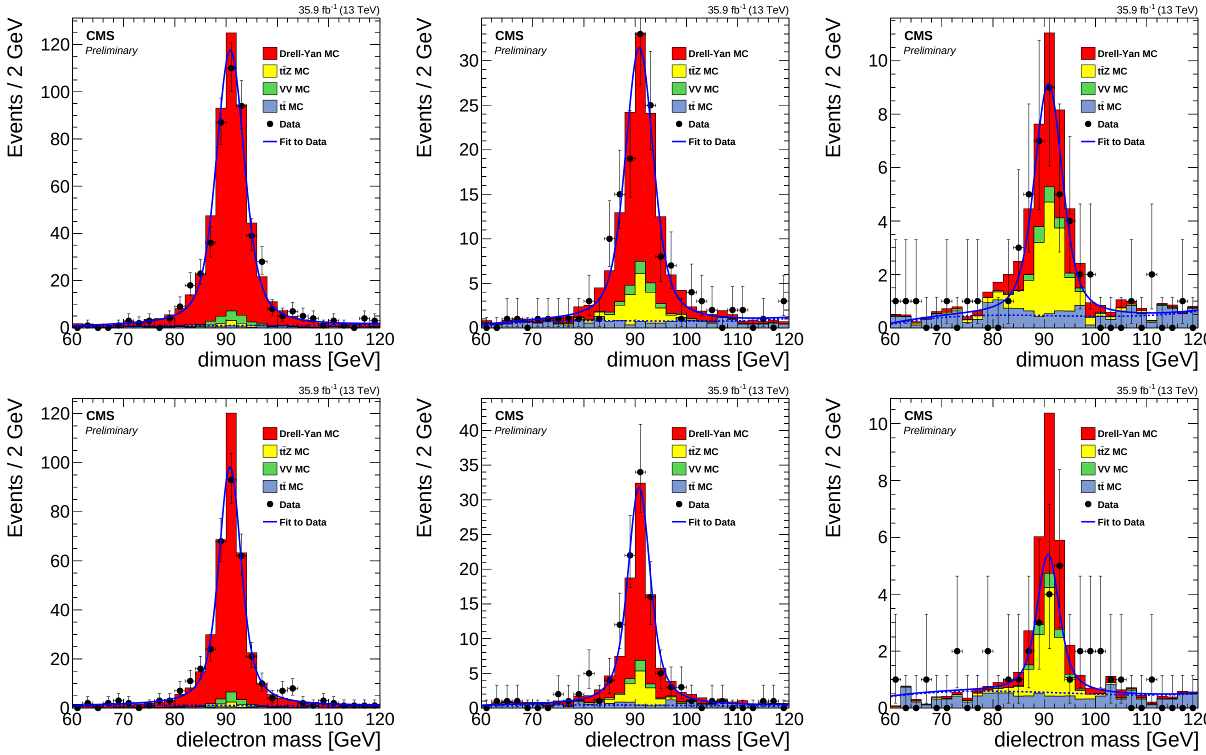

Figure C.3: Fits to the data dilepton invariant mass distribution with $N_{jet} \geq 5$ to obtain the $Z \to \ell^+\ell^-$ purity for muons (top), electrons (bottom), with 0 (left), 1 (middle), and ≥ 2 (right) b-tagged jets. Histograms show expected contributions from MC simulation.

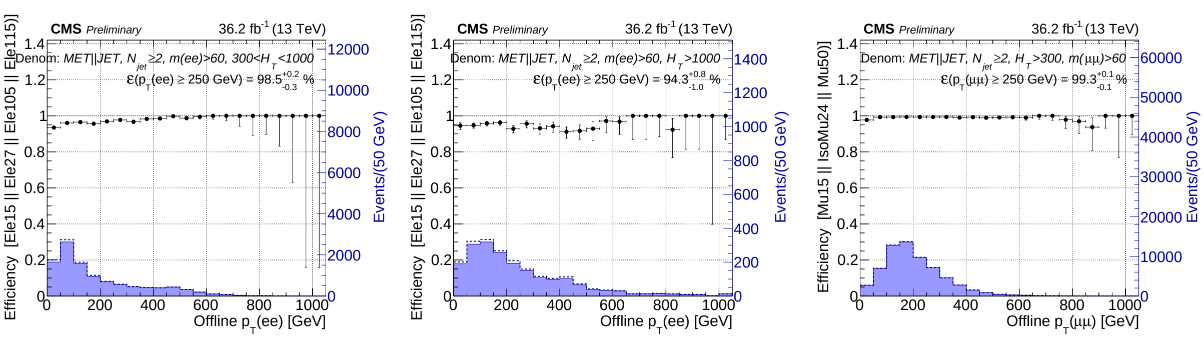

(a) (b) (c)

Figure C.4: Trigger efficiency of single lepton triggers used to select the di-electron (a) and (b) and $Z \to \mu^+\mu^-$ (c) samples as a function of the p_T of the $\ell^+ \ \ell^-$ system for events with $m(\ell^+\ell^-) > 60$ GeV. The plots in (a) and (b) compare the trigger efficiency in the $Z \to e^+e^-$ sample for $H_T < 1000$ GeV and $H_T > 1000$ GeV, respectively.

Appendix D

Event Displays

The following event displays are taken from events in the signal region for this analysis [120]. The $\vec{\mathrm{H}}_{\mathrm{T}}^{\mathrm{miss}}$ vector is drawn in purple and the jets in the event are drawn as yellow cones in the r–ϕ plane with jet p_{T} labels. Blue and red towers give the HCAL and ECAL energy deposits, respectively. Green tracks show particle flow candidates in the event. The muon system and ECAL boundary geometry are superimposed in the event display.

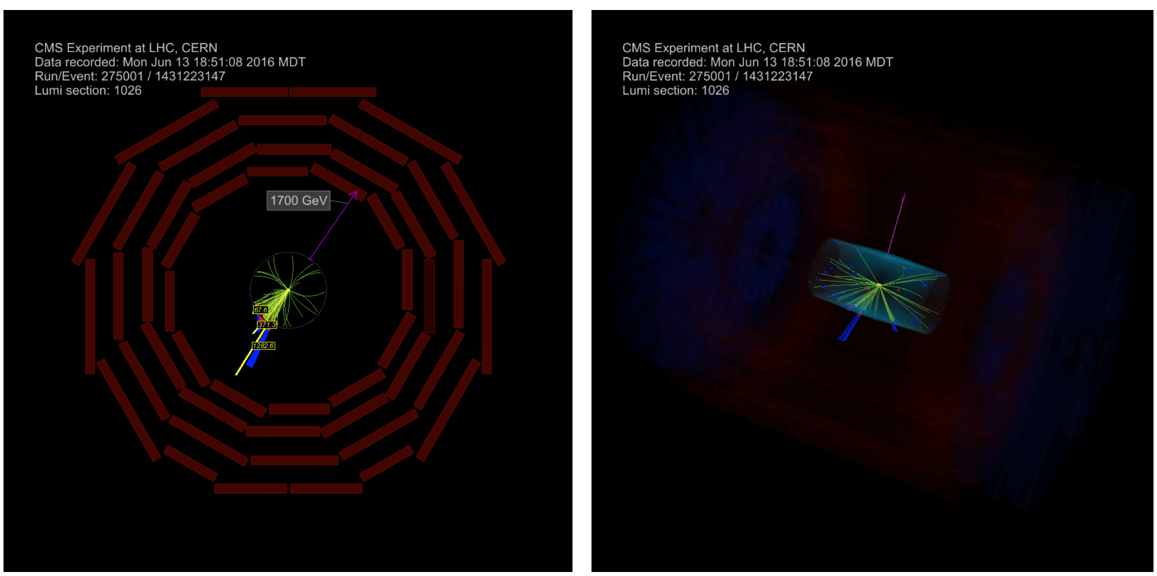

(a) (b)

Figure D.1: A display of an event in the signal region with $\mathrm{H}_{\mathrm{T}}^{\mathrm{miss}} = 1700$ GeV, $\mathrm{N}_{\mathrm{jet}} = 3$, and $\mathrm{Min}[\Delta\phi] = 2.73$ in the r–ϕ plane (a) and 3D perspective view (b). None of the jets in the event are tagged as a b–jet. The above event yields a signal-like BDT output value of 0.688 which corresponds to the 35th analysis bin.

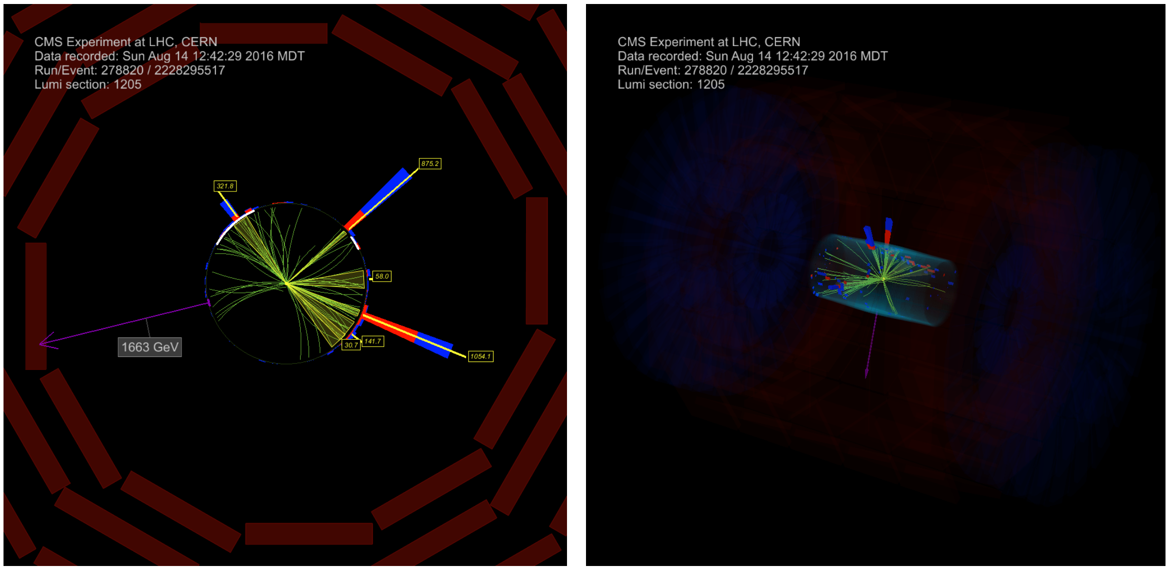

(a) (b)

Figure D.2: A display of an event in the signal region with H_T^{miss} = 1663 GeV, N_{jet} = 6, and Min[$\Delta\phi$] = 1.14 in the r–ϕ plane (a) and 3D perspective view (b). None of the jets in the event are tagged as a b–jet. The above event yields a signal-like BDT output value of 0.990 which corresponds to the 50th analysis bin.

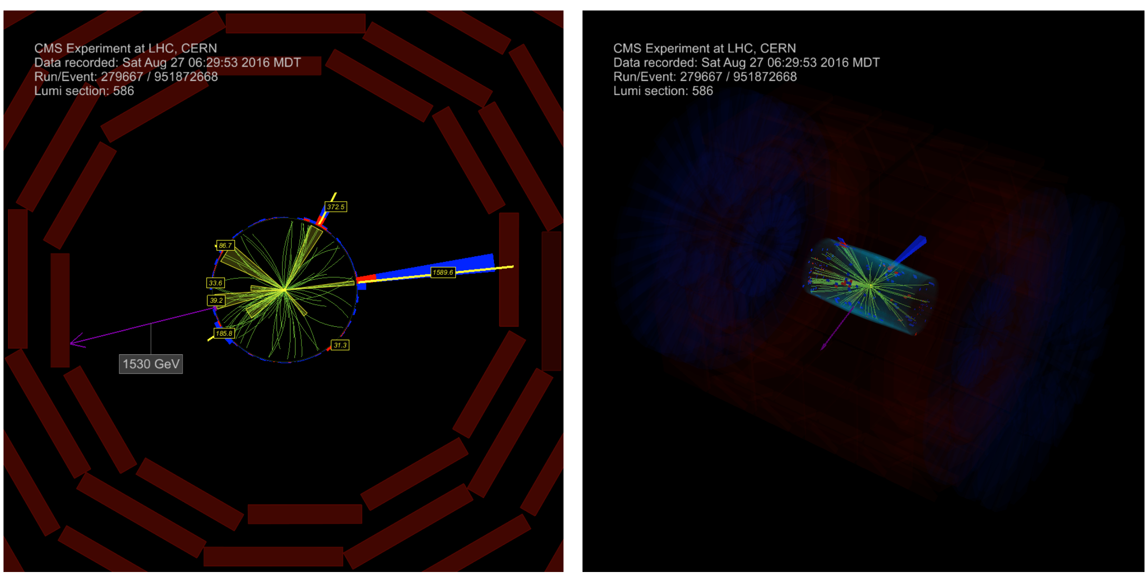

(a) (b)

Figure D.3: A display of an event in the signal region with H_T^{miss} = 1530 GeV, N_{jet} = 7, and Min[$\Delta\phi$] = 0.314 in the r–ϕ plane (a) and 3D perspective view (b). Two of the jets in the event are tagged as b–jets. The above event yields a signal-like BDT output value of 0.981 which corresponds to the 50th analysis bin.

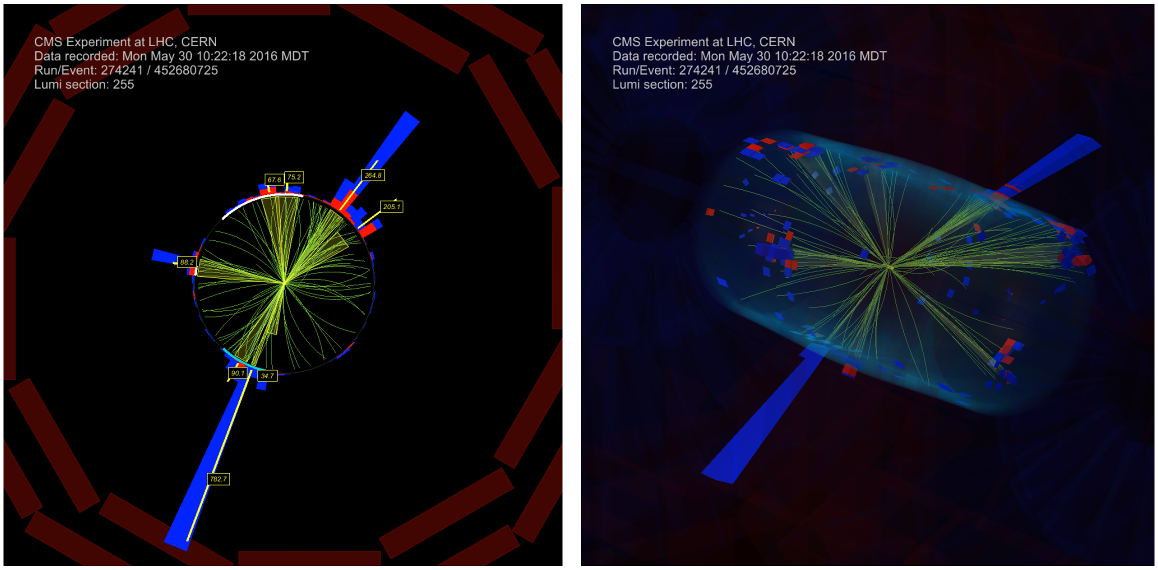

(a) (b)

Figure D.4: A display of an event in the signal region with $\mathrm{N_{b\text{-}jet}} = 6$, $\mathrm{N_{jet}} = 8$, $\mathrm{H_T^{miss}} = 368.5$ GeV and $\mathrm{Min}[\Delta\phi] = 0.370$ in the r–ϕ plane (a) and 3D perspective view (b). The above event yields a signal-like BDT output value of 0.572 which corresponds to the 28th analysis bin.

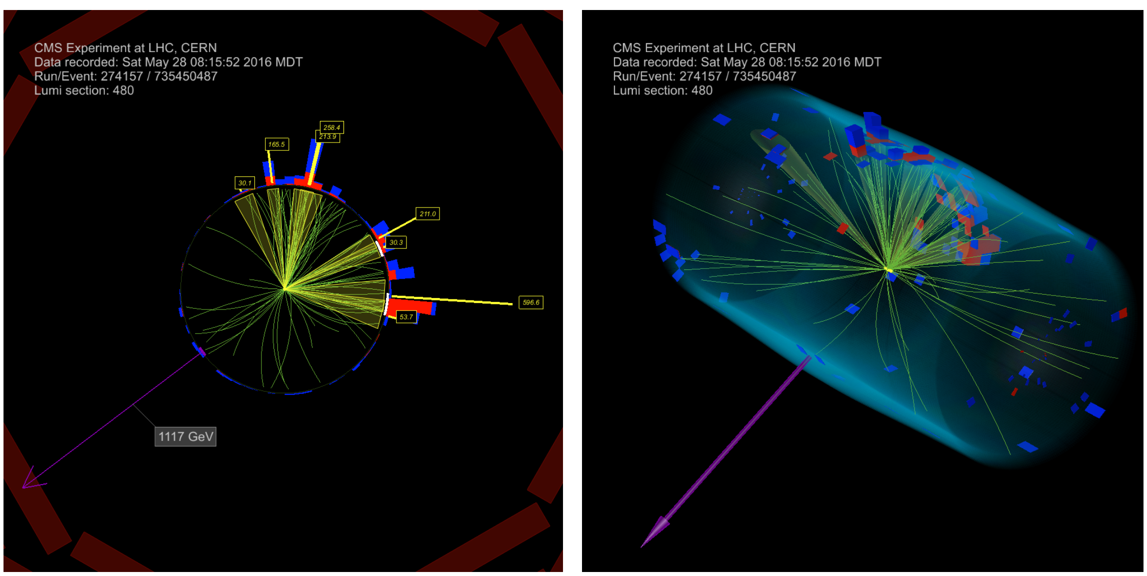

(a) (b)

Figure D.5: A display of an event in the signal region with $\mathrm{H_T^{miss}} = 1117$ GeV, $\mathrm{N_{jet}} = 8$, and $\mathrm{Min}[\Delta\phi] = 2.43$ in the r–ϕ plane (a) and 3D perspective view (b). One jet in the event is tagged as a b–jet. The above event yields a signal-like BDT output value of 0.991 which corresponds to the 50th analysis bin.

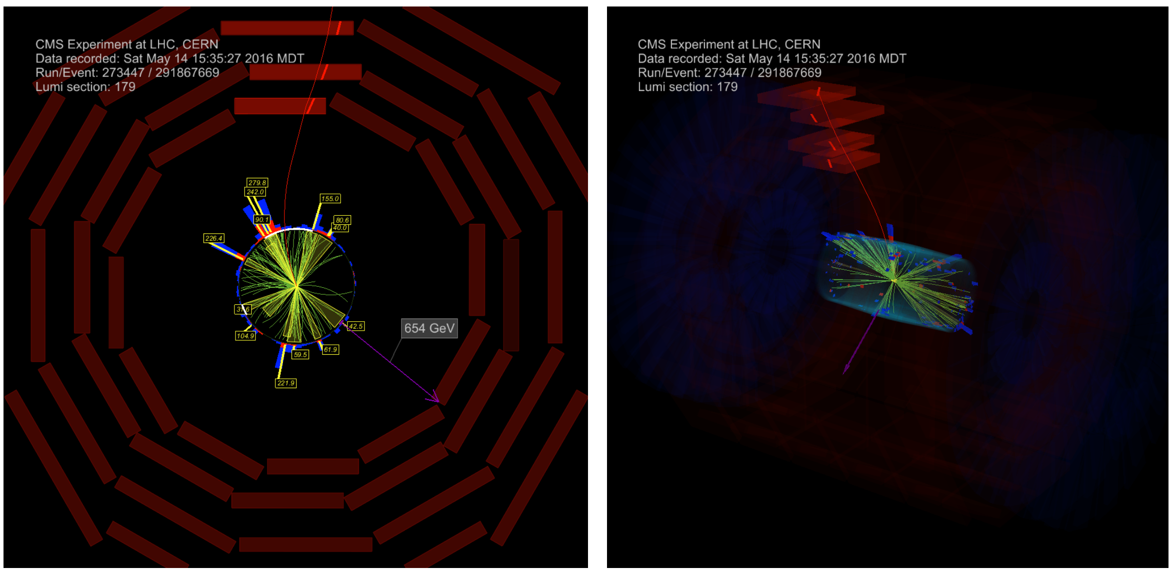

(a) (b)

Figure D.6: A display of an event in the signal region with $H_T^{miss} = 654$ GeV, $N_{jet} = 12$, and $\mathrm{Min}[\Delta\phi] = 1.0$ in the r–ϕ plane (a) and 3D perspective view (b). Two of the jets in the event are tagged as a b–jet. The above event yields a signal-like BDT output value of 0.993 which corresponds to the 50th analysis bin.